

# **RFI Mitigation for VLBI and Arrays Water Megamasers in Active Galaxies**

INAUGURAL-DISSERTATION

zur

Erlangung des Doktorgrades  
der Mathematisch-Naturwissenschaftlichen Fakultät  
der Universität zu Köln



vorgelegt von

**Jan Florian Wagner**  
aus Helsinki, Finnland

Köln 2014

Berichtersteller: Prof. Dr. Andreas Eckart  
Prof. Dr. J. Anton Zensus

Tag der mündlichen Prüfung: 26. Juni 2014



*To Yoon and Lumi and my beloved parents and sister.*

# Abstract

This thesis studies the central parsec in active galaxies via spectral line observations of OH and water megamasers and millimeter-wave interferometry. The aims are four-fold: 1) measure the mass of the supermassive black hole in active galactic nuclei (AGN) through circumnuclear water maser observations, 2) measure the Hubble constant through circumnuclear water maser observations, 3) mitigate the radio frequency interference that degrades spectral line observations, and 4) probe the innermost regions of AGN by expanding a mm-wavelength interferometer.

The AGN is a compact region at the center of active galaxies and can reach extremely high luminosities. The current paradigm conjectures that AGN contain a supermassive black hole (SMBH) fed by matter from a rotating accretion disk, and that this sub-parsec SMBH/disk system is partially enshrouded in a “torus” of obscuring material within 10 parsec (pc) of the SMBH. Some AGN also launch a pair of relativistic jets via mechanisms that are still debated, partly due to the high frequency and extreme resolution required to resolve the jet launching region.

The high spatial resolution of very long baseline radio interferometry (VLBI) allows to track jet components over pc to kilo-pc scales outside an AGN. Within AGN, water megamaser emission mapped by VLBI is an excellent tracer of the sub-pc structure, in particular of the accretion disk. Its rotation curve, traced by water masers, allows an accurate SMBH mass measurement, important for constraining the empirical relation between black hole mass and stellar velocity dispersion in the galactic bulge – current evidence suggest that this  $M_{\text{BH}}-\sigma_{\star}$  -relation is not universal, indicating differences in SMBH feeding, accretion history and AGN evolution.

Disk masers further yield accurate distances to nearby maser galaxies by an almost purely geometric means. This allows measuring the current rate of expansion of the Universe, described by the Hubble constant,  $H_0$ , an important cosmological parameter that can constrain competing Dark Energy (DE) -like models. The maser-based  $H_0$  is an important complement to other techniques as it does not rely on not yet fully understood astrophysics. To constrain DE models the key goal of the Megamaser Cosmology Project (MCP) is to measure  $H_0$  to at least 3 % precision.

Relatively few ( $\lesssim 5\%$ ) active galaxies have been detected in water masers. In this thesis I carried out a water maser survey in nearby galaxies, some with AGN, some also detected in the dissociation product of water, the neutral hydroxyl radical (OH). Four new water masers were detected, including OH-detected galaxies, such as NGC 4261 famous for its dusty torus.

---

The MCP project by J. Braatz et al. conducts 22 GHz VLBI and single-dish observations of disk maser galaxies. I analyzed the data of three quite different maser galaxies with putative AGN (NGC 23, UGC 3193 and IC 2560). The maser data for NGC 23 suggest either an association with a possibly truncated low-luminosity jet, or exceptionally luminous nuclear/extranuclear star formation masers. The AGN disk water masers in UGC 3193 reveal a large accretion disk with two rings suggestive of a disrupted disk around a low central SMBH mass of about  $0.6 \pm 0.2 \times 10^6 M_{\odot}$ . The disk masers in IC 2560 on the other hand indicate a SMBH mass of  $5.4^{+0.9}_{-0.6} \times 10^6 M_{\odot}$ , which in light of the  $134 \pm 12 \text{ km s}^{-1}$  stellar velocity dispersion in the (pseudo)bulge and the common  $M_{\text{BH}}-\sigma_{\star}$ -relation is undermassive, consistent with the trend seen in other water maser galaxies. The IC 2560 disk masers also allowed the Hubble constant to be measured, resulting in an  $H_0$  of  $67.7^{+11.6}_{-8.9} \text{ km s}^{-1} \text{ Mpc}^{-1}$ . Combined with recent MCP results (UGC 3789, NGC 6264) this yields a new maser-based Hubble constant of  $68.4 \pm 5.3 \text{ km s}^{-1} \text{ Mpc}^{-1}$  (8%). Additional galaxies are analyzed in the MCP project and the 3% precision on  $H_0$  necessary to constrain the DE may soon be reached.

The above observations of low flux density spectral lines, and especially lines at lower frequencies, are often degraded by man-made radio frequency interference (RFI). Thus I also discuss two techniques for mitigating RFI. The first method was implemented in a popular VLBI software correlator. I evaluate the theoretical and practical performance, also in a VLBI search for 1.6 GHz OH in tori of Cygnus A and NGC 1068. I find the mitigation method to be effective but limited in practice due to the particular software correlator architecture. The second method improves over two existing approaches for antenna arrays, including focal plane arrays. While current instrumentation did not allow an immediate application, e.g., in my maser survey, I find that the method shows great potential for future spectral line observations in presence of RFI.

Finally, our recent work on expanding a global sub-millimeter VLBI array has enabled extreme angular resolution, sufficient to resolve the SMBH/disk system and the jet launching region. At the end of this thesis I present the first 230 GHz VLBI observation of the core region of blazar 3C 279. The work also allowed extreme-resolution observations of Sgr A\* and the SMBHs in M 87, recently carried out, with emission detected at a scale shorter than 10 gravitational radii. These latter data are being analyzed, in a post-thesis time frame, and will lead to a better understanding of SMBH spin, accretion, and jet launching.

This thesis contributes on multiple fronts, both to instrumentation and to RFI mitigation, and increases the current knowledge of individual maser galaxies and observational cosmology.

**Keywords:** RFI, arrays, VLBI, AGN, extragalactic water masers, observational cosmology.

# Zusammenfassung

Diese Arbeit untersucht die inneren Parsec (pc) aktiver Galaxien anhand Spektrallinienbeobachtungen und Radiointerferometrie. Aktive Galaxien beherbergen eines der leuchtkräftigsten Objekte des Universums, den Aktiven Galaktischen Kern (engl. AGN), eine kompakte zentrale Region die extreme Leuchtstärken erreichen kann. Die aktuelle Lehrmeinung vermutet ein supermassives Schwarzes Loch (engl. SMBH) im inneren sub-pc-Bereich eines AGN, mit Materiezuffluss aus einer das SMBH umgebenden rotierenden Akkretionsscheibe (AS). Man vermutet außerdem, dass das SMBH/AS-System teilweise durch einen äußeren sub-10 pc Materie-“Torus” verdeckt wird. In einigen AGN stößt die innere Region auch einen relativistischen Materiestrom aus. Die Mechanismen die diesen “Jet” bilden sind umstritten, da die Region bisher nicht direkt beobachtet und bildgebend aufgelöst werden konnte.

Mit Radiointerferometrie auf langen Basislinien (engl. VLBI) kann man z.B. der Jet-Materiefluss außerhalb des AGN über mehrere (kilo-)pc verfolgen. Die innere sub-pc -Region kann wiederum durch VLBI-Beobachtungen leuchtstarker Wassermaser ( $\text{H}_2\text{O}$ -Emissionslinien) erfasst werden. Wassermaser werden oft in Jet-Nähe, aber auch in der sub-pc AS beobachtet. Die durch “Disk-Maser” abgetastete Rotationskurve der AS erlaubt eine genaue Bestimmung der Masse des zentralen SMBH. Dies liefert wichtige Daten zur empirischen Relation zwischen der SMBH-Masse und der stellaren Geschwindigkeitsdispersion im Zentralbereich der Galaxie (der sog.  $M_{\text{BH}}-\sigma_*$ -Relation). Die Relation scheint bekanntermaßen nicht universell zu sein und dies deutet auf Unterschiede in der AGN- und SMBH-Evolution in verschiedenen Galaxientypen hin.

Disk-Maser ermöglichen auch eine präzise und nahezu rein geometrische Entfernungsmessung zu Masergalaxien. Anhand der Distanz lässt sich die Expansionsrate des Universums bestimmen, also die Hubble-Konstante,  $H_0$ , einem wichtigen kosmologischen Parameter. Anders als bei populären Methoden hängt die maserbasierte  $H_0$ -Messung nicht von teils noch umstrittenen Details der Astrophysik ab. Mit einem exakten Wert für  $H_0$  lassen sich konkurrierende Dark Energy (DE) -ähnliche Modelle der theoretischen Physik ausschließen. Deshalb ist das Hauptziel des Megamaser Cosmology Project, für das ich drei recht verschiedene Masergalaxien analysiert haben, die Bestimmung von  $H_0$  auf eine Genauigkeit von mindestens 3 %.

Noch sind relativ wenige Masergalaxien bekannt. In dieser Arbeit habe ich eine Masersuche in aktiven Galaxien, und Galaxien mit Hydroxyl-Radikal (OH) -Spektrallinien (einem Dissoziationsprodukt von Wasser) durchgeführt. Vier neue Detektionen enthielten u.a. einen Disk-Maser,

---

und einen Jet-Maser in der Galaxie NGC 4261, bekannt für ihren Torus.

Unter dem MCP-Projekt von J. Braatz et al. habe ich drei recht verschiedene Masergalaxien mit möglichen AGN niedriger Leuchtstärke (NGC 23, UGC 3193 und IC 2560) analysiert. Die Maser in NGC 23 sind entweder mit einem gekürzten Jet von sehr niedriger Leuchtkraft assoziiert, oder sind ungewöhnlich leuchtstarke Maser in inneren Sternformationregionen in NGC 23. Die Disk-Maser in UGC 3193 andererseits beschreiben eine weite, gewölbte und unterbrochene AS mit zwei Ringen, die eine SMBH-Masse von nur  $0.6 \pm 0.2 \times 10^6 M_{\odot}$  umgeben. Die Disk-Maser in IC 2560 deuten wiederum auf eine SMBH-Masse von  $5.4_{-0.6}^{+0.9} \times 10^6 M_{\odot}$  hin. Mit einer  $\sigma_{\star}$  von  $134 \pm 12 \text{ km s}^{-1}$  ist auch dieses SMBH untermassiv im Vergleich zu der  $M_{\text{BH}}-\sigma_{\star}$ -Relation. Dieser Trend ist auch in anderen Masergalaxien sichtbar. Zusätzlich erlaubten die Disk-Maser in IC 2560 eine Messung der Hubble-Konstante, in diesem Fall  $67.7_{-8.9}^{+11.6} \text{ km s}^{-1} \text{ Mpc}^{-1}$ . Mit den Resultaten des MCP zu zwei weiteren Galaxien (UGC 3789, NGC 6264) aktualisiert dies den maserbasierten Wert von  $H_0$  auf  $68.4 \pm 5.3 \text{ km s}^{-1} \text{ Mpc}^{-1}$  (8 %). Das MCP-Projekt analysiert noch weitere Galaxien und wird bald eine Genauigkeit von 3 % erreichen.

Die obigen Beobachtungen, und besonders Spektrallinienbeobachtungen auf noch niedrigeren Frequenzen, leiden oft unter terrestrischen Störsignalen (engl. RFI). Diese Arbeit enthält deshalb auch zwei Methoden zur RFI-Abwehrung (engl. RFI mitigation). Die erste Methode wurde in einem bekannten VLBI-Softwarekorrelator implementiert und die theoretischen und praktischen Leistung wurde evaluiert, auch in einer VLBI-Suche nach 1.6 GHz OH in den Tori von Cygnus A und NGC 1068. Die Methode an sich ist effektiv, aber wegen der Softwarearchitektur des Korrelators konnte die volle Leistungsfähigkeit nicht erreicht werden. Die zweite Methode, RFI-Subtraktion für Antennenarrays, stellt eine Verbesserung zweier Ansätze dar. Die aktuelle Antenneinstrumentation erlaubte zwar keine sofortige Anwendung der Methode, sie zeigte jedoch großes Potential für Beobachtungen mit zukünftigen Arrays und Multi-pixel-Empfängern in der Präsenz von RFI.

Um zukünftig auch die innerste AGN-Region um das SMBH bildgebend aufzulösen, das Ziel der Event Horizon Telescope (EHT) -Kollaboration, arbeiteten wir an einer Erweiterung eines globalen Sub-Millimeter-VLBI-Arrays. Im letzten Kapitel werden die Ergebnisse einer ersten extrem hochauflösenden Beobachtung von 3C 279 vorgestellt. Vor kurzem beobachteten wir bzw. das EHT auch Sgr A\* und das SMBH in M 87. Es wurde hierbei Emission innerhalb von 10 Schwarzschild-Radii detektiert. Diese frischen noch auszuwertenden Daten und zukünftige Beobachtungen mit dem erweiterten EHT werden, im Anschluss an die hier vorliegende Arbeit, zu einem besseren Verständnis des SMBH-Spins, Akkretion und der Jet-Entstehung beitragen.

Mit der vorliegenden Arbeit werden sowohl Beiträge im Bereich der Instrumentation und RFI-Abwehrung, als auch Beiträge zu mehreren Masergalaxien und der Kosmologie geleistet.

**Schlüsselwörter:** RFI, Arrays, VLBI, AGN, Maser, beobachtungsorientierte Kosmologie.

# Contents

<b>Glossary</b>	<b>viii</b>
<b>1 Introduction</b>	<b>3</b>
1.1 Active Galaxies and Jets . . . . .	4
1.2 The Active Galaxy Zoo . . . . .	4
1.3 The AGN Unification Scheme . . . . .	5
1.4 Astrophysical Masers . . . . .	7
1.5 Water Masers in AGN Accretion Disks . . . . .	11
<b>2 Radio Interferometry</b>	<b>13</b>
2.1 Modern Arrays . . . . .	15
2.2 The Principle of Synthesis Imaging . . . . .	17
2.3 The Coherence Function . . . . .	18
2.4 The Intensity Distribution . . . . .	18
2.5 The Complex Visibility . . . . .	19
2.6 Derived Observables . . . . .	21
<b>3 Radio Frequency Interference and Interference Mitigation</b>	<b>23</b>
3.1 Overview of RFI Mitigation . . . . .	24
3.2 Interference Mitigation for Arrays . . . . .	28
3.3 A Fringe Rate Filter Implementation for DiFX-2 . . . . .	34
3.4 Fringe Rate Filter Tests and Results . . . . .	39
3.5 EVN VLBI Test Observation for RFI Mitigation . . . . .	46
3.6 Conclusions for VLBI RFI Mitigation in DiFX . . . . .	54
3.7 RFI Mitigation for Arrays . . . . .	56
3.8 Array RFI Mitigation Tests and Results . . . . .	64
3.9 Summary and Conclusions for Array RFI Mitigation . . . . .	76

<b>4</b>	<b>Water Megamaser Survey</b>	<b>77</b>
4.1	Source Sample . . . . .	78
4.2	Observations . . . . .	79
4.3	Data Reduction . . . . .	79
4.4	Detections and Discussion . . . . .	82
4.5	Dual Maser Species . . . . .	86
4.6	Conclusions and Summary . . . . .	88
<b>5</b>	<b>Jet Water Masers in NGC 23</b>	<b>91</b>
5.1	Abstract . . . . .	91
5.2	Introduction . . . . .	92
5.3	Observations and Data Reduction . . . . .	93
5.4	Results . . . . .	95
5.5	Discussion . . . . .	101
5.6	Summary and Conclusions . . . . .	103
<b>6</b>	<b>A Black Hole Mass Measurement for Megamaser Galaxy UGC 3193</b>	<b>104</b>
6.1	The Megamaser Galaxy UGC 3193 . . . . .	105
6.2	Single Dish Observations . . . . .	106
6.3	Fitting of Maser Accelerations . . . . .	107
6.4	Maser Accelerations in UGC 3193 . . . . .	109
6.5	Interferometric Observations . . . . .	111
6.6	VLBI Data Reduction . . . . .	113
6.7	VLBI Results . . . . .	115
6.8	Geometric Keplerian Disk and Plummer Cluster Models . . . . .	118
6.9	Model Fit Results and Discussion . . . . .	119
6.10	Summary and Conclusions . . . . .	121
<b>7</b>	<b>An Angular Diameter Distance to Megamaser Galaxy IC 2560</b>	<b>122</b>
7.1	Abstract . . . . .	122
7.2	Introduction . . . . .	123
7.3	The Water Maser Galaxy IC 2560 . . . . .	126
7.4	Single-Dish Observations and Data Reduction . . . . .	127
7.5	Single-Dish Results . . . . .	128
7.6	Maser Acceleration Fitting . . . . .	130
7.7	Maser Accelerations Results . . . . .	130
7.8	VLBI Observations and Data Reduction . . . . .	133
7.9	VLBI Results . . . . .	134

7.10 Geometric Models Fit to IC 2560 Maser Data . . . . .	136
7.11 Model Fit Results and Discussion . . . . .	138
7.12 Summary and Conclusions . . . . .	146
<b>8 Deeper into AGN: <math>\lambda</math>1.3 mm-VLBI</b>	<b>147</b>
8.1 Abstract . . . . .	148
8.2 Introduction . . . . .	149
8.3 Zero Spacing Flux Density . . . . .	151
8.4 VLBI Observation . . . . .	151
8.5 VLBI Data Reduction . . . . .	155
8.6 Results . . . . .	161
8.7 Discussion . . . . .	172
8.8 Conclusions . . . . .	173
8.9 Future Outlook . . . . .	174
<b>Bibliography</b>	<b>177</b>
<b>List of Figures</b>	<b>193</b>
<b>List of Tables</b>	<b>197</b>
<b>Acknowledgements</b>	<b>199</b>
<b>A Appendix</b>	<b>201</b>
A.1 DiFX Configuration Files for Fringe Rate Filtering . . . . .	201
A.2 Summary of the RFI Mitigation Source Code . . . . .	205
A.3 Spectra of the Water Maser Non-Detections . . . . .	207
A.4 Geometric Models for the Maser Distribution . . . . .	211
A.5 Water Megamaser Epochs on IC 2560 . . . . .	223
A.6 Water Megamaser Positions in NGC 23, UGC 3193 and IC 2560 . . . . .	224
A.7 Parameter Posteriors for the IC 2560 Disk Maser Model Fit . . . . .	232
<b>Erklärung</b>	<b>248</b>
<b>Curriculum Vitae</b>	<b>249</b>



# Glossary

AGN	active galactic nucleus.
AP	averaging period.
APEX	Atacama Pathfinder Experiment telescope.
EHT	Event Horizon Telescope.
EVN	European VLBI Network.
FWHM	full width at half maximum.
GBT	Robert C. Byrd Green Bank Telescope.
GMVA	Global mm-VLBI Array.
INR	interference to noise power ratio.
IVS	International VLBI Service.
LOS	line of sight.
LSR	local standard of rest reference frame.
MCP	Megamaser Cosmology Project.
NED	the NASA/IPAC Extragalactic Database.
RFI	radio frequency interference.
SMBH	supermassive black hole.
SNR	signal-to-noise ratio.
VLA	Karl G. Jansky Very Large Array.
VLBA	Very Long Baseline Array.
VLBI	very long baseline interferometry.

# Structure of this Work

This thesis covers a range of studies on active galactic nuclei, combining technical improvements with observational astronomical applications. To help orient the reader the general outline and structure of the thesis is described here.

The main theme of this thesis is the central region in active galaxies at scales shorter than a few parsec. The thesis started out as a technical project for mitigating man-made radio frequency interference that is detrimental to radio astronomical observations, and in particular to spectral line observations. The technical work was followed by spectral line observations, observations of the extremely luminous astrophysical megamasers found near the core of active galaxies, partly with implications to observational cosmology, and finally, the first ultra-high resolution observation of the core region of an active galaxy.

The first part of this thesis presents the general background and technical matter. The second part then moves towards progressively higher resolution and finer scales in active galaxies. The chapters are organized as follows:

- Chapter 1 introduces the reader to active galaxies and astrophysical masers, and in particular to water megamasers that trace accretion disks around the supermassive black hole in the center of these active galaxies. The Chapter sets the context for the observations of active galaxies carried out under this thesis.
- Chapter 2 presents the fundamentals of the classic radio interferometric technique that is related to very long baseline interferometry (VLBI), phased arrays, and focal-plane arrays. Radio interferometry was used in VLBI observations of active galaxies at frequencies from 1.6 GHz to 230 GHz. Interferometry is also the underlying principle of the radio interference mitigation techniques under this thesis.
- Chapter 3 begins with an introduction to radio frequency interference in relation to astronomy. The Chapter then discusses the technical aspects of the particular interference mitigation techniques that were implemented, improved, and tested under this thesis. Results for synthetic and actual data are presented.

- 
- The topic of Chapter 4 is a short water megamaser survey conducted with the Green Bank Telescope in 2013. Four new water megamaser galaxies were detected and radio interferometric follow-ups are pending. The following Chapters instead concentrate on the first observations of water megamasers previously detected by in three other galaxies.
  - Chapter 5 presents observations of the putative “jet” water megamasers in the galaxy NGC 23, carried out under the Megamaser Cosmology Project.
  - Chapter 6 discusses observations of the water megamasers in a large accretion disk around the core of the active galaxy UGC 3193. The masers were first detected by the Megamaser Cosmology Project and this Chapter presents the results of the first VLBI observations, including a maser-based estimate of the mass of the supermassive black hole in UGC 3193.
  - Chapter 7 discusses another “disk” maser galaxy, IC 2560, for which both a black hole mass as well as an accurate distance are derived. The main goal of the Megamaser Cosmology Project is to measure the cosmological parameter related to Dark Energy and the accelerated expansion of the Universe, the Hubble constant, by measuring distances to several galaxies similar to IC 2560. This Chapter provides a new estimate of the Hubble constant based on the water maser distance to IC 2560.
  - Finally, Chapter 8 discusses the future ultra-high resolution interferometry with a telescope network that now includes the APEX telescope in Chile. The Chapter shows the results of a fringe finder observation and tentative results on the fine-scale structure in the blazar 3C 279.

# 1 Introduction

The building blocks of our Universe are galaxies, also known as “dust” to cosmologists. Galaxies are massive gravitationally bound objects of star systems, star clusters, interstellar medium, and a hypothetical component, a halo of dark matter that appears to affect the motion of the stars and gas in a galaxy. In addition to ordinary galaxies like our own, there exists a category of galaxies that have an exceptionally high luminosity across a wide range of the spectrum (Fig. 1.1). Most of the energetic activity in these *active galaxies* is concentrated to a single central region, the *active galactic nucleus* (AGN).

This central region is bright, extremely compact, and often outshines the host galaxy by several orders of magnitude. Its spectral energy distribution indicates radiative processes that are thermal (e.g., heated gas and dust, thermal bremsstrahlung) and non-thermal (e.g., synchrotron and inverse-Compton emission). Unlike in other galaxies the spectrum is not dominated by stellar radiation.

The emission by AGN is thought to be powered by the gravitational energy dissipated through accretion onto a *supermassive black hole* (SMBH; over  $10^5$  solar masses). Most of the radiated energy comes from very close to the event horizon of the SMBH. While SMBHs are found in the nucleus of both active and non-active galaxies (Kormendy & Richstone 1995), and both galaxies have the same

morphological properties, only active galaxies appear to have sufficient matter transport towards the core region to fuel the AGN (see, e.g., Joglee 2006; Hopkins & Quataert 2010 and references therein). Depending on the radiative efficiency and the nature of the accretion disk and the gas accretion, relatively low fueling rates of between  $10^{-5}$  and 10 solar masses per year are sufficient to explain the observed luminosity.

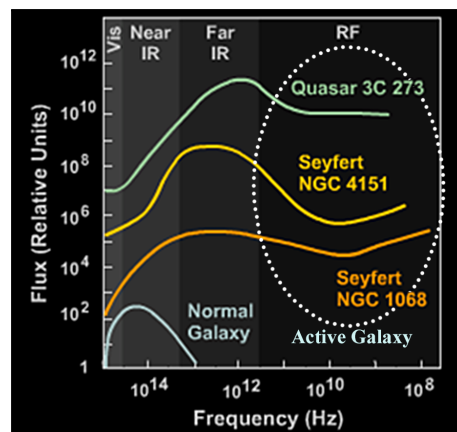


**Fig. 1.1:** A typical spectral energy distribution for normal and active galaxies across radio frequency (RF), infrared (IR) and visible light wavelengths. (Image credit: Cengage Learning.)

## 1.1 Active Galaxies and Jets

Approximately 10% of AGN are known to launch a diametrically opposed pair of *relativistic jets*. The jets are detected as linear radio structure in interferometric images, and with apparent superluminal motion due to viewing angle effects (e.g., Lister et al. 2013). Due to relativistic Doppler de-boosting the receding jet is usually not detected unless the jet axis is closely aligned with the plane of the sky.

Jets have been the subject of extensive study for several decades, yet there is no consensus on the mechanism that leads to the creation, launching, and collimation of the jet in the innermost region of an AGN. With a dramatic improvement in the angular resolution of radio interferometers, however, a work that is currently in progress, sufficiently high resolution will be reached to probe accretion mechanisms and directly observe the jet launching region in nearby AGN (e.g., Doeleman et al. 2012). It also becomes possible to constrain the spin of certain SMBHs such as the black hole in the center of our Galaxy (e.g., Dexter & Fragile 2013).

## 1.2 The Active Galaxy Zoo

There are several types of active galaxy, divided into radio-quiet and radio-loud objects, and classified as Seyfert galaxies, radio-quiet quasars, radio-loud quasars, blazars or BL Lac type objects and optically violently variable quasars, and radio galaxies (e.g., Antonucci 1993).

The most luminous active galaxies, blazars, and their slightly less energetic relative, quasars, are thought to be the result of beamed emission by a jet that is pointed towards the observer (Fig. 1.2). Recently quasars have been detected up to high redshifts, as far back as the epoch of reionization, an epoch in the evolution of the Universe (Fan et al. 2006). A common characteristic of most active galaxies is their optical spectral line emission. Depending on the presence of broad or narrow optical emission lines, the AGN in an active galaxy is often classified as a Type 1 AGN (Seyfert 1) or a Type 2 AGN (Seyfert 2), or neither. Quasars and Seyfert 1 galaxies have *broad* optical permitted *lines* such as H $\alpha$  and H $\beta$ , with a  $> 500 \text{ km s}^{-1}$  full width half maximum (FWHM) line width. In Seyfert 2 galaxies these lines are not detected. On the other hand, quasars and both Seyfert types are detected in *narrow* high and low ionization forbidden *lines*, such as [O III] and others, with  $< 500 \text{ km s}^{-1}$  FWHM line widths. Quasars and Seyferts are also detected in very high ionization coronal lines ([Fe X] and others), with similar line ratios (Bianchi et al. 2012).

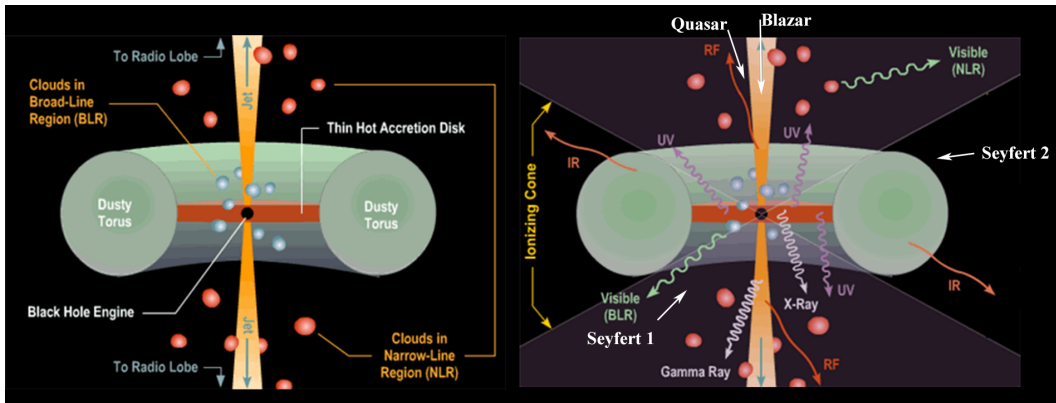


**Fig. 1.2:** The structure of an active galactic nucleus (AGN) under the AGN Unification scheme. (Image credit: Cengage Learning.)

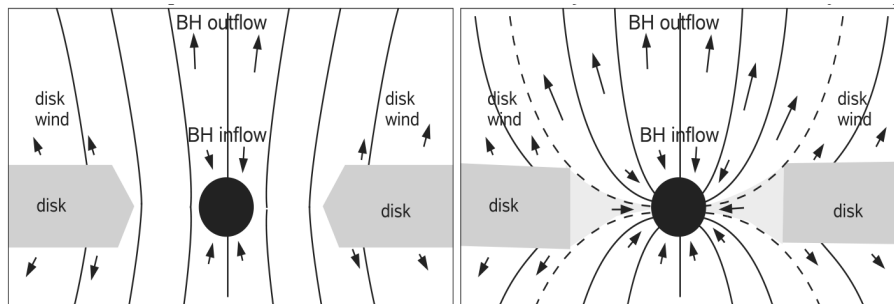


**Fig. 1.3:** A close-up view of Fig. 1.2 on the structure of the accretion disk and the inner magnetosphere in the region where the disk terminates at the black hole’s innermost stable circular orbit (left), or with the accretion flow extending beyond this orbit (right). Image from Komissarov (2012).

### 1.3 The AGN Unification Scheme

Under the Seyfert or AGN unification model, a model that has been debated for the last two decades, the apparent different classes of AGN mentioned above are explained by an orientation-dependent obscuration of a basically similar central object (Antonucci 1993).

The structure of an AGN under the unification model is shown in the left of Fig. 1.2. The emission that is dominant in different parts of this structure is shown in the right of Fig. 1.2. For example, the narrow line region (NLR) with narrow optical spectral lines is thought to reside at a larger distance from the SMBH and its surrounding accretion disk. In contrast, the broad line region (BLR) that emits broad optical spectral lines, possibly from a deep gravitational potential well, is thought to reside near the SMBH. The accretion disk around the SMBH produces strong

ultraviolet (UV) emission that is typical of Seyfert galaxies.

From certain viewing angles an obscuring region of material (the “*dusty torus*” of Fig. 1.2) coincides with the line of sight towards the SMBH and obscures the view to the broad line region. The region of obscuring material is often thought to be clumpy and composed of clouds, and is often thought to have the shape of a torus, although other geometries are also possible.

An AGN in which the obscuring torus is seen edge-on will have an obscured BLR and will be subsequently undetected in broad optical lines, leading to its optical classification as a Seyfert 2.

Current evidence for a torus is indirect, and its structure and formation are uncertain or largely unknown. Even its existence is debated. If it exists, the torus is likely not larger than 100 pc, may be clumpy, perhaps molecular, and may arise from outflow of clouds embedded in a hydromagnetic disk wind (indicated in Fig. 1.3), with clouds uplifted from the accretion disk (Blandford & Payne 1982). It may also consist of clouds accreted from the host galaxy (Krolik & Begelman 1988), or in some galaxies even only a single cloud (Aretxaga et al. 1999).

For an overview of the past and current understanding of the unification scheme and the obscuring torus, the reader is referred to Antonucci (1993) and the reviews by Urry & Padovani (1995) and Bianchi et al. (2012), but also see Ramos Almeida et al. (2011) and Elitzur (2012).

Recently, clouds in a putative torus may have been detected in spectral line emission, and in spectral line absorption against the core, although such detections have been highly elusive in the past. Elitzur & Shlosman (2006) consider the water megamaser emission seen at parsec scales in the Seyfert 2 galaxy NGC 3079 to be associated with a torus. A similar association has also been suggested for masers in Circinus A (Greenhill et al. 2003) and NGC 1052 (Sawada-Satoh et al. 2008). In addition, hydroxyl has been seen in absorption at sub-parsec scales in NGC 1052 and tentatively in Cygnus A (Impellizzeri 2008).

In all cases, however, a torus association is not definite. Also other evidence of the existence of a torus and the ability of a torus to explain the sometimes quite different properties even of Seyfert galaxies (e.g., the recently detected “unobscured” Seyfert 2 galaxies, with a possible explanation given by Tan et al. 2012) remains inconclusive.

Currently only the black-hole/accretion-disk paradigm is well-established. The structure of the accretion disk at less than ten gravitational radii from the black hole (Fig. 1.3) – and the relation of the disk structure to jet launching and black hole spin – can soon be observed directly owing to the advancements in high resolution radio interferometry (e.g., Doeleman et al. 2012).

The structure and conditions in the accretion disk can, in fact, already be probed through water maser emission at sub-parsec scales and at a few thousand gravitational radii.

## 1.4 Astrophysical Masers

Astrophysical “masers” (microwave amplification by stimulated emission of radiation; cf. Elitzur 1992, 2007) are the result of *stimulated radiative transitions* from a higher to a lower energy level in molecules in some medium (Fig. 1.4). Some of the energy levels of water vapour ( $\text{H}_2\text{O}$ ) and some of the radiative transitions between these levels are shown in Fig. 1.5.

Masers operate by the same principle as terrestrial optical lasers. Maser emission occurs when the medium is out of thermal equilibrium and when there is an energy source available that *pumps* the maser emission by maintaining a population inversion, a greater occupancy of the higher energy level in the molecular gas. To allow a radiative rather than collisional de-excitation the density of the medium must be below a certain *critical volume density*.

In addition, for an incident photon to produce a second photon (Fig. 1.4), its wavelength must be within the thermal line width of the inverted molecules, without a significant Doppler shift. The latter requires the molecules to have the same radial velocity i.e. the medium must be

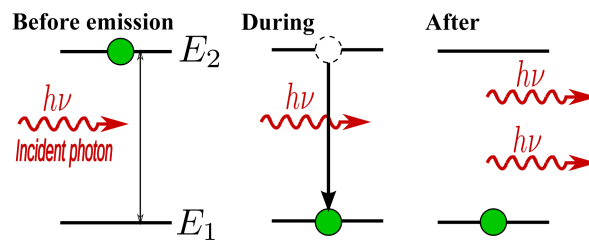


**Fig. 1.4:** Stimulated emission in a masing molecule.

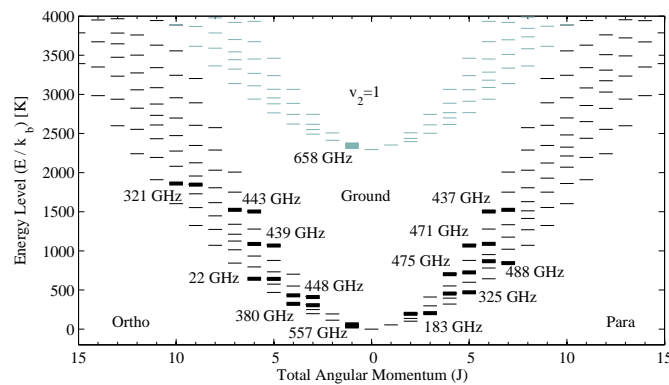


**Fig. 1.5:** The energy levels and some radiative transitions of ortho and para isomers of water. The nuclear spins of the hydrogen atoms are either parallel (total spin  $I = 1$ ) or antiparallel (total spin  $I = 0$ ) for the ortho and para isomers, respectively. Data from Tennyson (2011).



*velocity coherent* along the line of sight. When the *column density* is sufficiently high, a growing cascade of stimulated photons will be generated along this path, producing a maser.

Maser emission by OH, H<sub>2</sub>O, H<sub>2</sub>CO, CH<sub>3</sub>OH, SiO, and other molecules has been detected in our Galaxy, but the most luminous *extragalactic masers* are hydroxyl (OH) and water vapour (H<sub>2</sub>O) masers. They have been detected at kilomaser ( $\lesssim 1 L_{\odot}$ ) and megamaser luminosities ( $\gtrsim 1 L_{\odot}$ ). However, currently Arp 299 (IC 694) is the only galaxy with both OH and H<sub>2</sub>O megamasers detected in their lowest frequency radiative transition.

Extragalactic OH masers at 1665 MHz and 1667 MHz, first detected in NGC 253 (Whiteoak & Gardner 1974) and at a megamaser luminosity first in Arp 220 (Baan et al. 1982), are generally found in the inner 100 pc of luminous infrared galaxies. The masers are associated with starbursts and AGN and often shows disk/ring-like structure (Klöckner & Baan 2004; Pihlström 2005).

Extragalactic H<sub>2</sub>O masers on the other hand, first found in M 33 by Churchwell et al. (1977), are generally detected in the  $6_{16} \rightarrow 5_{23}$  ( $J_{KaKc}$ ) rotational energy level transition with a corresponding rest frequency of 22.23508 GHz ( $\lambda 1.3$  cm). While several of the other transitions in Fig. 1.5 have been detected in our Galaxy in, e.g., star formation regions and circumstellar envelopes of stars, the detection of extragalactic water masers at frequencies higher than 22 GHz appears to be limited by sensitivity. In fact, currently only two extragalactic masers have been found at 183 GHz, in NGC 3079 and Arp 220, with one tentative maser detection at 439 GHz in NGC 3079 (Humphreys et al. 2005). Future high-sensitivity high-frequency arrays are likely to increase the number of these detections.

The currently known  $\lambda 1.3$  cm water masers are predominantly found in nearby radio-quiet Seyfert 2s and low-ionization nuclear emission-line region (LINER) galaxies (Greenhill 2007). The population inversion necessary for masing is thought to be the result of purely collisional pumping. The water masers favour large hydrogen densities,  $10^7 \leq n(\text{H}_2) \leq 10^{11} \text{ cm}^{-3}$ , and large gas phase water abundances of  $x(\text{H}_2\text{O}) = n(\text{H}_2\text{O})/n(\text{H}_2) > 10^{-4}$ . The abundance of water

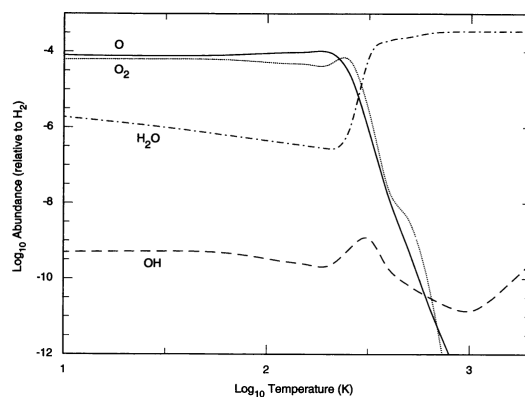
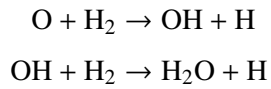


**Fig. 1.6:** Abundances of O, O<sub>2</sub>, OH, and H<sub>2</sub>O as a function of temperature. Abundances are relative to a density  $n(\text{H}_2)$  of  $10^6 \text{ cm}^{-3}$  and are sensitive to temperature (Neufeld et al. 1995).

is significantly enhanced at  $> 300$  K temperatures by the neutral-neutral reaction,



that produce but also deplete OH, depending on the temperature (Fig. 1.6; also see, e.g., Elitzur & de Jong 1978; Neufeld et al. 1995). Gas kinetic temperatures of 300 K up to the dissociation of the water molecule at about 1000 K are typical for the environment of water masers.

To date, over 4000 galaxies have been searched for 22 GHz water masers, resulting in 150 masers detections (e.g., Braatz & Gugliucci 2008; Braatz et al. 1997; Henkel et al. 2005; Kondratko et al. 2006; Nakai et al. 1995).

The water masers known so far may be subdivided into five categories with masers associated with: 1) late-type stars, 2) star forming regions, 3) AGN “outflow masers” in outflow impinging onto dense molecular clouds and collisionally pumped in the shocked interface, 4) “*jet*” masers in jet-cloud or jet-interstellar medium interactions within a few 10 parsec of the SMBH and also related to a shocked region, and 5) *disk masers* that trace a sometimes warped accretion disk around the SMBH at sub-parsec scales (Figs. 1.7 and 1.8).

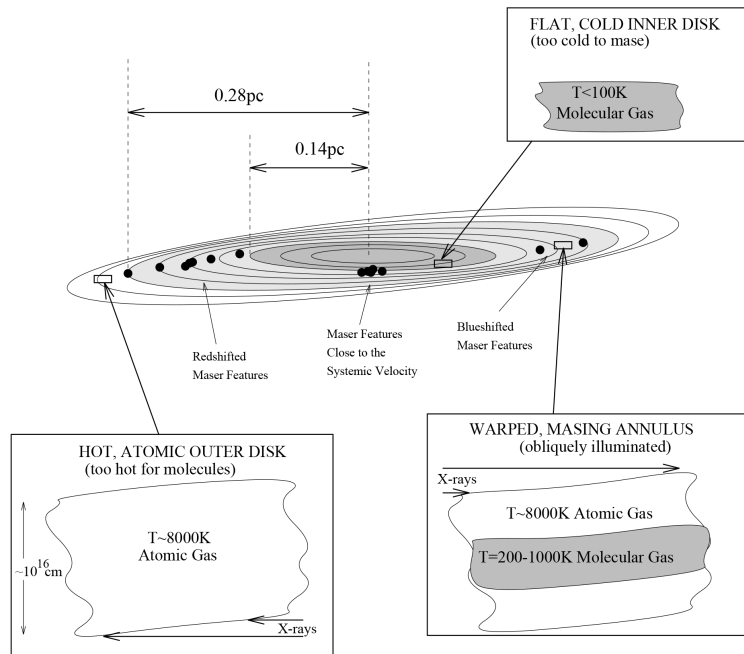


**Fig. 1.7:** Schematic of the sub-pc warped accretion disk in NGC 4258, inferred from H<sub>2</sub>O masers (dots). It is often thought that the disk is multi-layered (bottom right). The conditions for masing (a gas kinetic temperature of 300 K to 1000 K, hydrogen densities of  $n_{\text{H}_2} \sim 10^7 - 10^{11} \text{ cm}^{-3}$ ) are reached in the dense inner molecular layer of the disk near the atomic–molecular transition region via a combination of disk midplane pressure and X-ray heating by the central engine. A warp is crucial for oblique X-ray illumination and heating of the disk. Flat regions and regions self-shadowed by a warp are too cold to mase (top right). Conversely, X-ray ionization increases with larger radii (bottom left) and near the surface of the disk, with temperatures too high for water molecules. Masers trace the disk over about  $10^5$  to  $10^7$  gravitational radii. Image adopted from Neufeld & Maloney (1995).

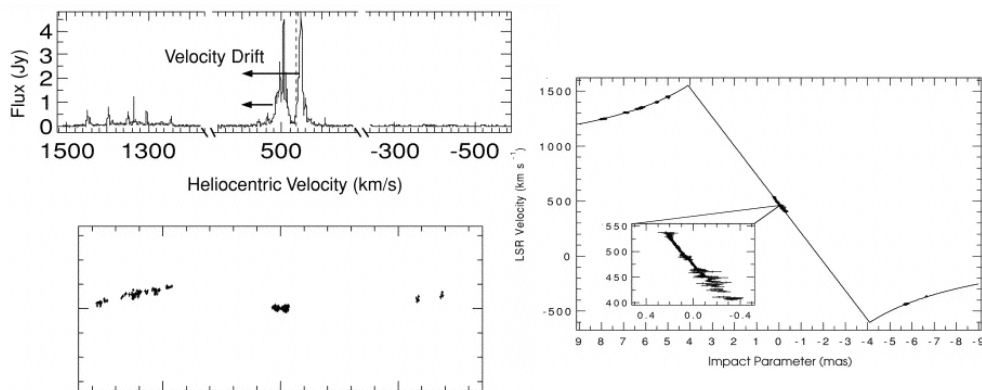


**Fig. 1.8:** The maser single-dish spectrum (top left), the interferometric map of the maser distribution (bottom left), and the Keplerian rotation curve (right) of the water masers in the prototypical disk maser galaxy NGC 4258. Image adopted from Bragg et al. (2000).

## 1.5 Water Masers in AGN Accretion Disks

The disk masers in over 15 known active galaxies of Seyfert 2 and LINER types appear to trace the accretion disk around the SMBH at sub-parsec scales.

The prototypical example of a disk maser galaxy is NGC 4258. As indicated in the previously mentioned Figs. 1.7 and 1.8, the spatial maser distribution and the maser kinematics (reflected by the position–velocity diagram) appear to be consistent with a well-defined edge-on thin Keplerian disk that is slightly warped and has a diameter of about 0.3 pc. For another disk maser galaxy, IC 2560, X-ray observations by Tilak et al. (2008) further suggest a possible relation between the obscuring torus and the disk with different accretion disk geometries, shown in Fig. 1.10: in some geometries, the warped masing accretion disk may itself provide the obscuration of the central engine, taking the function of an obscuring “torus”.

In general, AGN disk water masers can also provide very accurate “gold standard” mass measurements for SMBHs (Kuo et al. 2011). These masses are inferred from the disk kinematics in the sub-parsec inner region of an AGN, close to the gravitational sphere of influence of the SMBH. They reflect the SMBH mass more reliably than the virial masses that are determined from the H I rotation curve at kiloparsec scales or from the stellar velocity dispersion in the galactic bulge (if the galaxy has a bulge rather than pseudo-bulge).

The maser-based SMBH mass estimates are important for constraining the empirical  $M_{\text{BH}}-\sigma_{\star}$  relation between black hole mass and stellar velocity dispersion in the bulge – current findings suggest the  $M_{\text{BH}}-\sigma_{\star}$  relation is not universal, but depends on the type of galaxy (see Fig. 1.9). The black hole mass in early type galaxies and maser galaxies may follow a different relation than in late type galaxies (McConnell et al. 2011), which in turn suggests a different black hole feeding and accretion history in these galaxies (Greene et al. 2010).

In addition to SMBH masses, the disk masers around a SMBH can provide extremely accurate geometric distance determinations without the need for indirect assumptions about the cosmology and the geometry (curvature) of the universe (Braatz et al. 2009; Reid et al. 2013).

The maser distance and a redshift determined for the spectral emission lines of the AGN allow measuring the Hubble constant,  $H_0$ . With several disk maser galaxies at a distance between

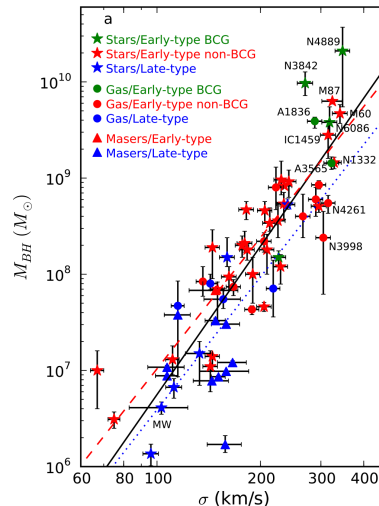


**Fig. 1.9:** The  $M_{\text{BH}}-\sigma_{\star}$  relations for different types of galaxies. Image adopted from McConnell et al. (2011).

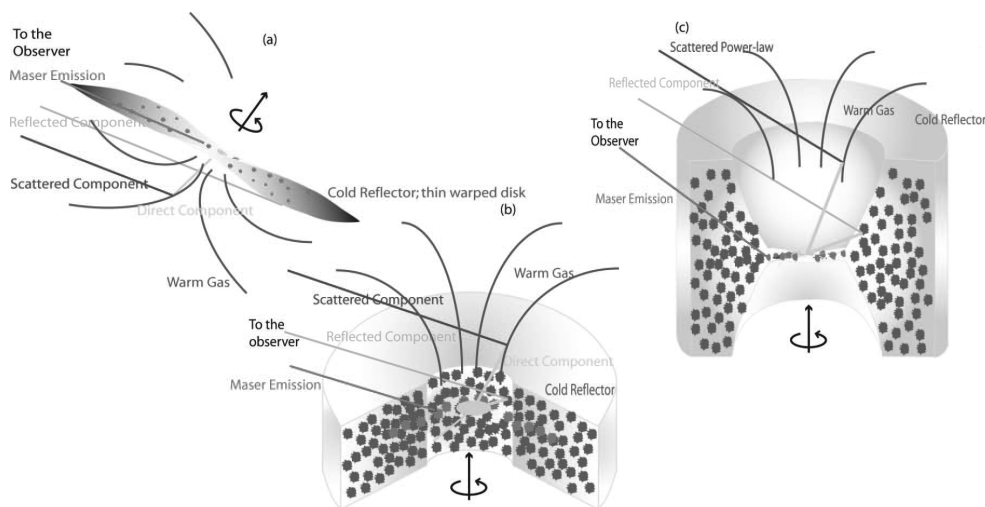


**Fig. 1.10:** Schematic illustration of three possible accretion disk geometries. X-ray observations in water megamaser galaxy IC 2560 find a cold reflecting medium (interpreted as the disk detected in water maser emission) and a warm scattered component. Image adopted from Tilak et al. (2008).

about 20 Mpc to 250 Mpc,  $H_0$  could be ultimately determined to better than 3% precision, the goal of the Megamaser Cosmology Project (MCP) by Braatz et al. (2009).

A maser-based  $H_0$  determined to 3% with nearby galaxies at low redshifts is able to place tighter constraints on Dark Energy -like models (models that explain the current expansion of the Universe) than measurements at higher redshifts, such as baryon acoustic oscillation and cosmic microwave background observations. The main practical obstacle of the MCP project are sensitivity and resolution; the disk water masers are faint with a very low flux density (typically between 0.01 Jy and 1 Jy) compared to galactic water masers (typically  $\gg 1$  Jy), and masers are distributed over a small region of only a few milliarcseconds. Due to these factors, not many of the currently known disk maser galaxies are suitable for a low-uncertainty  $H_0$  measurement. The MCP project thus also conducts surveys to find new disk maser galaxies.

Water disk megamaser observations related to the MCP project, i.e., a short survey, one “jet” maser galaxy (NGC 23), a disk maser galaxy (UGC 3193) yielding a new maser-based black hole mass, and a disk maser galaxy (IC 2560) yielding a measurement of the Hubble constant that updates a previously published  $H_0$  for this galaxy by a different group and that is based on new data and an improved technique, will be presented in a later Chapter of this thesis.

Before proceeding with the above maser galaxies, however, the following two Chapters will first introduce the radio interferometric technique that was used in these observations, and will also cover two radio frequency interference (RFI) mitigation techniques pertaining to future interferometric observations.

## 2 Radio Interferometry

Astrophysics has a continuous demand for observational astronomy to observe ever fainter or distant sources and resolve them down to ever smaller scales. Increases in both sensitivity and resolution are crucial to this. Compared to optical telescopes, however, radio astronomical telescopes have a notably lower resolution. This is due to the physical resolution limit,  $\propto \lambda/D$ , set by diffraction in a circular telescope aperture of diameter  $D$  at a wavelength  $\lambda$  (e.g., Airy 1835), and due to the factor of  $\gtrsim 10^4$  difference in the typical radio ( $\sim 1$  cm) and optical ( $\sim 500$  nm) wavelengths. The observing wavelength is often fixed due to, e.g., the need to observe a certain spectral line. Higher resolution would require a larger telescope. Unfortunately, with the exception of stationary dishes like the 305 m Arecibo Observatory and soon the 500 m Aperture Spherical Telescope, the limits of support structure and surface stability and financial feasibility have already been reached with the largest steerable telescope, the 110 m Green Bank Telescope.

*Optical interferometers*, on the other hand, are relatively small and very sensitive to propagation delays and signal phase differences. The latter allow a high angular resolution, as shown later. In 1655 Grimaldi detected the first optical interference patterns, diffraction *fringes*. This sparked a search for a theory of light that eventually led to modern quantum mechanics and quantum field theory, and also produced a series of inventions that led to the first highly phase-sensitive optical interferometers. Examples include the optical stellar interferometer by Fizeau and Stéphan in 1879, the 1887 Michelson–Morley interferometric experiment with its non-detection of an æther wind, the Fabry–Pérot interferometer and filter used in optical astron-

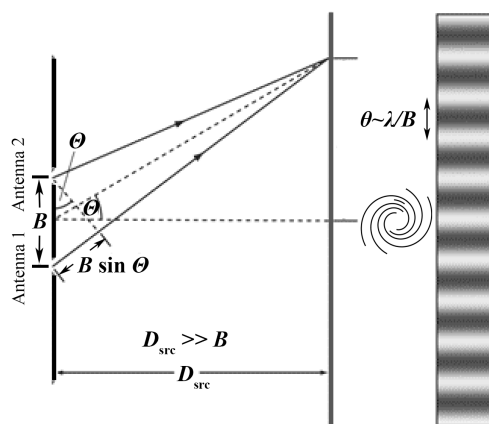


**Fig. 2.1:** The interferometric fringe pattern of a two-antenna baseline. The baseline has maximum sensitivity towards source regions that coincide with the constructive interference peaks of the fringe pattern.

omy today, the modern Mach–Zehnder interferometers used in quantum-optical “which-way” experiments, and optical interferometric telescopes, most recently the VLT Interferometer.

During the 1950s, high angular resolution *radio interferometry* was pioneered by the Nobel laureates Ryle and Hewish, and others such as Neville and Pawsey (see, e.g., Ryle 1955, 1957, 1962, and Ryle & Hewish 1960). In radio interferometry the radiation incident from the astronomical source is simultaneously received at widely separated antennas and their signals are combined to produce a fringe (Fig. 2.1). The angular resolution  $\theta \propto \lambda/B$  improves as one increases the observing frequency or the projected distance between antenna-pairs as seen from the source, also called the *baseline length*  $B$ . This is illustrated in Fig. 2.2. Widely separated antenna pairs very easily yield a resolution that is unattainable with a single telescope. Due to the higher resolution for example *source positions* can be measured to much greater precision than with a single telescope.

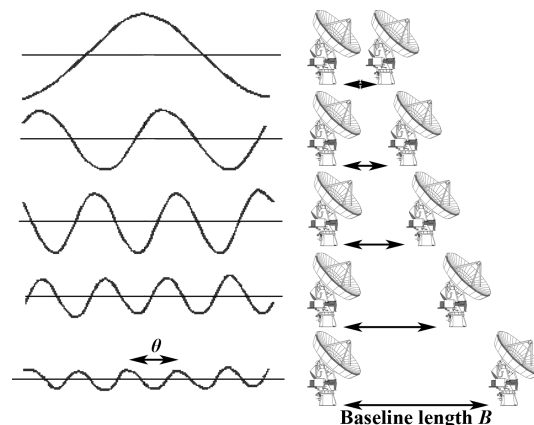


**Fig. 2.2:** The effect of longer baselines on fringe spacing: an increase in resolution.

Also note that baselines have their highest sensitivity towards the directions of peaks of the fringe pattern (constructive interference) and are insensitive to source emission from the null regions of the fringe pattern (destructive interference). In addition, to detect a fringe at a given resolution the source must also be spatially coherent over the respective angular spacing. This can be used to measure the *source diameter* of a compact object, e.g., a quasar: one simply narrows the fringe spacing (via longer baselines) until it eventually becomes comparable to the source diameter. Beyond this spacing the source is *resolved out* and the spatial coherence is lost. The non-detection of the fringe below a certain fringe spacing reveals the source diameter.

Other important techniques are *radio interferometric imaging* and the non-imaging technique of *modelfitting*. The average amplitude and the difference in the phase of the incident signal can be measured between many antenna pairs. This samples structural information of the astronomical target over a large number of spatial frequencies. With sufficient data and certain algorithms it is possible to reconstruct an *image* of the source brightness distribution. With fewer data, the spatial frequency representations of simple superposed Gaussian-shaped image components may be fit to derive the most likely image of the source. A technique called *Earth rotation aperture synthesis* is also often used to improve the data; Earth rotation increases the effective number of the spatial measurements. A glimpse of this can be seen in Fig. 2.7 discussed later.

Among the first notable radio interferometric observations were the sunspot measurement

by Ryle & Vonberg (1946), the stellar observation by Scott et al. (1961), and a survey of the North Polar region by Ryle & Neville (1962), and a series of galactic 1665 MHz hydroxyl and 22 GHz water maser mapping observations by, e.g., Rogers et al. (1967) and Moran et al. (1973). More about the history and observations can be found in the reviews by Kellermann & Cohen (1988) and Kellermann & Moran (2001). See also Alef (2004) for a terse technical review of VLBI instrumentation.

## 2.1 Modern Arrays

Turning to current times, radio astronomical instrumentation often places small antenna arrays in the telescope primary focus. These *multi-beam* or *multi-pixel receivers*, *focal-plane arrays* (FPAs), and *phased array feeds* (PAFs) allow a larger sky area to be observed in a shorter time and dramatically increase the speed of, e.g., 21 cm H $\alpha$  mapping and spectral line surveys, continuum surveys, cosmological surveys, and pulsar and radio transient searches.

For better resolution and sensitivity one may also use a traditional *local array* of several antennas, such as the Low-Frequency Array (LOFAR), the Long Wavelength Array (LWA), the Karl G. Jansky Very Large Array (VLA), the Atacama Large Millimeter/submillimeter Array (ALMA), and the Square Kilometre Array (SKA). Modern arrays cover different frequency bands from about 40 MHz (LOFAR) up to 1.6 THz (ALMA), with an angular resolution of arc minutes to some ten milliarcseconds depending on the array, and are highly suitable for a broad range of galactic and extragalactic astrophysics, including cosmology.

Even higher resolution observations became routine thanks to many innovations over the past decades, such as specialized image reconstruction techniques, calibration algorithms like the “closure phase”-based array self-calibration by Jennison in the 1950s, and digital recording and signal processing advances towards increasingly wider-bandwidth signals. These paved the path to *very long baseline interferometry* (VLBI) with antennas on most continents. VLBI provides baselines of 100 km to 12,000 km, or, with space VLBI, up to some 100,000 km, with sometimes

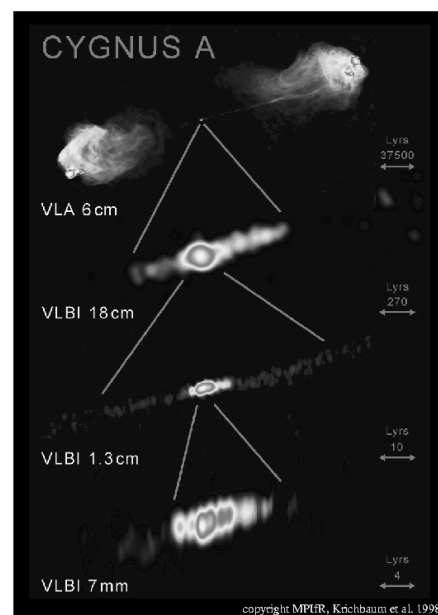


**Fig. 2.3:** The large scale jet and the core region of the active radio galaxy Cygnus A seen by a local array (VLA) and by a VLBI array (GMVA).





**Fig. 2.4:** Common radio interferometric antenna arrays and their various scales: a focal-plane array (left), a high sensitivity connected local interferometer (middle), and a network of antennas for very long baseline interferometry (right). (Images courtesy of Verheijen et al., ALMA (ESO/NAOJ/NRAO) and T.-H. Jung.)

spectacular resolution. Many VLBI arrays are in operation today, such as the European VLBI Network (EVN), the Very Long Baseline Array (VLBA), the new East Asia VLBI Network (EAVN), the Global mm-VLBI Array (GMVA), and the Event Horizon Telescope (EHT). At the time of writing, VLBI reaches arcsecond resolution at 1.4 GHz and 30 microarcseconds at 230 GHz, surpassing the milliarcsecond best optical resolution of e.g. the VLT Interferometer optical telescope. Note, however, that large scale source structure is resolved out by VLBI. It can be imaged at the given frequency using a local array owing to its lower resolution, as illustrated by images of Cygnus A (Fig. 2.3) and its compact radio core region and famous large scale jet. The science goals of the observation thus dictate the choice between VLBI or an array.

All arrays can in principle operate in two modes: in *phased array mode* and *interferometric mode*. Both are fundamentally identical and differ mainly in the final output of the antenna array signal processing. A phased array *coherently sums* all antenna signals and produces a single high-sensitivity time domain output signal. (Antenna signal phases are adjusted so that geometric propagation delay differences from each antenna towards a chosen position on the sky have been removed. The array is then phase-coherent towards that direction, quite related to *beam forming* and tracking of the target position under Earth rotation). Conversely, in *interferometric mode* the antenna phases are also adjusted as described, but the final output is the 3-D spatial coherence of the source radiation incident on the array and can be used for imaging.

To show the scale of the three types of arrays introduced in this Section, representative examples and the locations of some VLBI antennas are shown in Fig. 2.4. For more details, a useful review of modern arrays is given by Garrett & Greenwood (2012) and other articles of the online proceedings of the RTS 2012<sup>1</sup> conference.

<sup>1</sup>Resolving The Sky - Radio Interferometry: Past, Present and Future (<http://pos.sissa.it/cgi-bin/reader/conf.cgi?confid=163>)

Finally, a deeper background knowledge of VLBI and radio interferometry, though arguably exotic, may be useful to a perhaps unfamiliar reader to follow the radio interference mitigation algorithms in this thesis, the imaging of the observed sources, and the model fitting. The essential background relevant to later Chapters is thus reviewed in the following Sections. Many details can by necessity not be presented here. Instead, for a thorough introduction to radio interferometry the books by Zensus et al. (1995), Taylor et al. (1999), and Thompson et al. (2001) may serve as excellent references, in addition to the Ph.D. thesis by McLintock (1980).

## 2.2 The Principle of Synthesis Imaging

To set the context, a terse summary is provided here. Source structure can be inferred from the interference pattern of a radio interferometer. By the van Cittert–Zernike theorem (e.g., van Cittert 1934 and later), the spatial brightness distribution  $I(l, m, k)$  (image) of an incoherent source (different points of the source radiate independently) is related to the spatial coherence  $\Gamma(u, v, w)$  through a Fourier-like transform

$$I(l, m, k) = \iiint \Gamma(u, v, w) e^{-j2\pi(ul+vm+wk)} du dv dw$$

where the spatial coherence of the source, or the spatial mutual coherence as seen by the array,

$$\Gamma(u, v, w, \tau) = \langle E(x, y, z, t) E^*(x + u, y + v, z + w, t + \tau) \rangle \quad \text{at } \tau = 0$$

can be measured directly and would allow a perfect image to be reconstructed if the spatial coherence were measured over the infinite range of  $u, v, w$  coordinates.

Due to the finite size of the antenna array, however,  $\Gamma$  is sampled only inside the synthetic aperture of the array. The maximum  $u, v, w$  coordinate range covered by an array is set by its longest and shortest baselines, i.e. pairwise antenna separations as seen from the source. The longest baseline also corresponds to the outer diameter of the synthetic aperture. In addition, due to the limited number of antennas, the finite-sized synthetic aperture is only partially filled and the coherence  $\Gamma$  is sampled incompletely even within this aperture. The effect on image reconstruction is perhaps most clearly demonstrated on a non-astronomical image, see Fig. 2.5. For comparison, a typical synthetic aperture in VLBI is shown in Fig. 2.7. In effect, special deconvolution techniques are required to reconstruct a source image



**Fig. 2.5:** Imaging with a completely (top) or incompletely (others) filled synthetic aperture. (Image courtesy of unknown author, and was modified).

with minimum artifacts from sparsely sampled spatial coherence data (see, e.g., Högbom 1974).

Note the type of image is unrestricted, e.g., the cross-polarization spatial coherence of a polarimetric observation allows polarization maps to be produced (see, e.g., Zensus et al. 1995).

### 2.3 The Coherence Function

For imaging a source at high resolution, radio astronomical interferometers first measure the coherence of the radiation emitted by the source, a quantity that is related to the fringe pattern. The *coherence function* for an electric field  $E$  emitted by the source is given by

$$\Gamma(u, v, w, \tau) = \langle E(x, y, z, t) E^*(x+u, y+v, z+w, t+\tau) \rangle \quad (2.1)$$

where the angle brackets denote the expectation value and  $E^*$  is the complex conjugate of  $E$ .

The coherence describes the “similarity” of the emitted field at two positions in space with respect to time, given by the mean correlation of the field over a location offset, at the antenna locations  $(x, y, z)$  and  $(x+u, y+v, z+w)$ , and over a time offset, at times  $t$  and at  $t+\tau$ . See Fig. 2.6 for examples. In an antenna array the location offset corresponds to the pairwise antenna separation i.e. the baseline length.

There are two limit cases of the general coherence function: for  $u, v, w = 0$  the coherence function is equal to the *temporal coherence* or the *autocorrelation* of  $E$ , and conversely, at  $\tau=0$  the function measures the (*mutual*) *spatial coherence* of  $E$ , also called the *cross-correlation* of the field detected at the two locations.

Incidentally, the relation between the fringe pattern (a superposition or “sum” of  $E$ ) and spatial coherence (a product of  $E$ ) is that the contrast between the intensities of the light and dark stripes in the interference pattern (e.g. Fig 2.1) is proportional to  $\|\Gamma\|$ .

### 2.4 The Intensity Distribution

Two special cases of *Bochner’s theorem* – the *Wiener-Khinchin theorem* (1933) and the *van Cittert–Zernike theorem* (1934) – state that under certain assumptions the intensity distribution

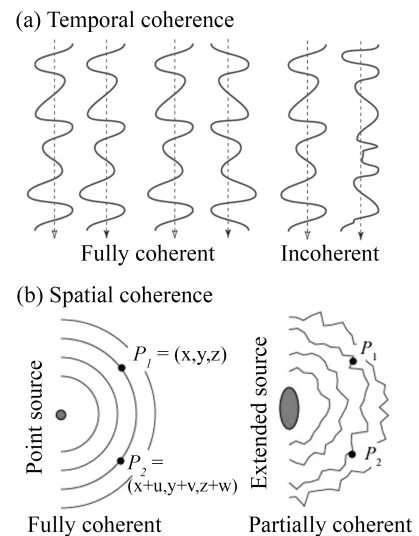


**Fig. 2.6:** Examples of temporal and spatial coherence. (Adopted from unknown author.)

of the field  $E$  emitted by the source may be obtained through the Fourier transform of the source coherence function. The Fourier relations for the temporal and spatial coherences are

$$\Gamma(0, 0, 0, \tau) = \int S(\nu) e^{-j2\pi(\tau\nu)} d\nu \quad (2.2)$$

$$\Gamma(u, v, w, 0) = \iiint I(l, m, k) e^{-j2\pi(ul+vm+wk)} dl dm dk \quad (2.3)$$

where  $S(\nu)$  is the intensity distribution over frequencies  $2\pi\nu$ , and  $I(l, m, k)$  is the intensity distribution over spatial angular frequencies  $2\pi l$ ,  $2\pi m$ , and  $2\pi k$ . Simply put,  $S(\nu)$  is the radio *spectrum* of the source and  $I(l, m, k)$  is the *brightness distribution* or *image* of the source. It is somewhat remarkable that these can be recovered through the products of mutually offset copies of field  $E$ .

The assumptions mentioned above are that the emitted field  $E$  is overall incoherent, meaning that: 1) the radiation is noise-like and well-approximated by many monochromatic emitters that radiate statistically independently, and 2) the source structure is well-approximated by many point-source components that radiate independently.

The above implies that for two electric fields  $E_a$  and  $E_b$  the mutual coherence must be zero

$$\Gamma = \langle E_a E_b^* \rangle = 0 \quad \text{when } a \neq b \quad (2.4)$$

unless the fields both originated from the same point-source and frequency.

For completeness, note that in Eqs. 2.2 and 2.3 the left hand sides are usually normalized by the *zero spacing* coherence  $|\Gamma(0)|$  and the right hand sides are normalized by  $\int S d\nu$  and  $\iiint I dl dm dk$ , respectively. For details, see, e.g., Thompson et al. (2001).

## 2.5 The Complex Visibility

To produce an image from coherence data using the Fourier transform, or specialized methods such as CLEAN (Högbom 1974), the spatial coherence function must first be measured over many  $(u, v, w)$  locations. Certain assumptions are usually made that simplify the array geometry and the Fourier relation of Eq. 2.3 (Thompson et al. 2001) so that two coordinates suffice, and

$$V(u, v) = \Gamma(u, v, 0, 0) \simeq \iint I'(l, m) e^{-j2\pi(ul+vm)} dl dm \quad (2.5)$$

where the complex *visibility function*,  $V$ , is just a special case of the spatial coherence function. Certain corrections must be applied to  $I'(l, m)$  during post-processing to yield the final image.

The individual measurements that sample  $V(u, v)$  are called *visibilities* and are obtained by cross-correlating the voltage signals (related to the electric field  $E$  reaching the aperture) of every

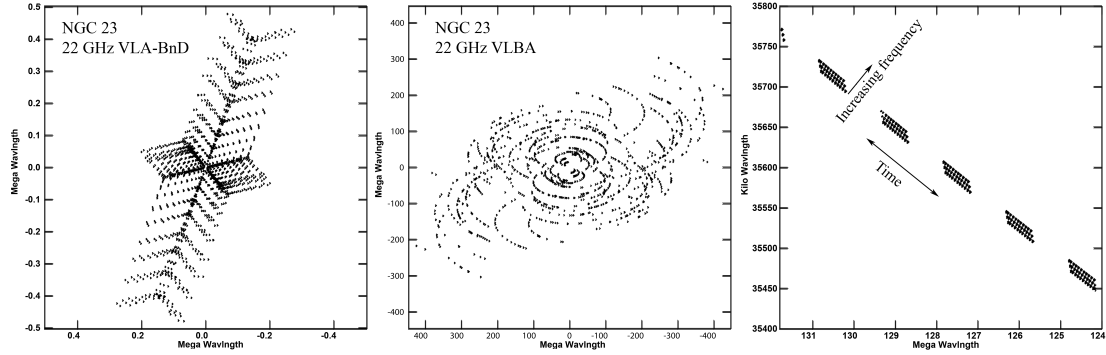


**Fig. 2.7:** The  $uv$  plane coverage at 22 GHz ( $\lambda = 1.3$  cm) towards water maser galaxy NGC 23. Axes are the projected baseline lengths in wavelengths, e.g.,  $0.5 M\lambda = 6.5$  km. NGC 23 was observed for 40 minutes with the 27-antenna VLA array with  $\leq 36$  km baselines (left), and for 7 hours with the 10-antenna VLBA network with  $\leq 8611$  km baselines (middle). As a consequence of Earth rotation the individual baseline trace elliptical  $uv$  tracks. The coverage is further improved by observing at several wavelengths (right).

antenna pair inside the synthetic aperture. Their  $uv$  plane coordinates of a visibility sample correspond to the baseline length, or the projected antenna-pair separation in a plane as seen from the target source, usually normalized by the observing wavelength such that

$$(u, v) = (B_u/\lambda, B_v/\lambda) \simeq (1/\theta_{f,u}, 1/\theta_{f,v}) \quad (2.6)$$

where the baseline resolution or fringe spacing is  $\theta_f = \sin^{-1}(\lambda/B) \sim \lambda/B$ .

For example, in observations at  $\lambda = 1.3$  cm a baseline of  $(B_u, B_v) = (130, 26)$  km would correspond to a  $uv$  location of  $(u, v) = (10, 2) M\lambda$  and a fringe spacing of  $(21, 103)$  mas. This is about the angular diameter of Pluto that is at a distance of around  $6 \times 10^9$  km (Kuiper 1950).

As already mentioned in § 2.2 the visibility data obtained during an actual observation are sparse, presenting a problem for imaging. As the Earth rotates under the source, however, the projected baselines follow elliptical  $uv$  tracks (e.g., Fig. 2.7) and allow visibilities to be sampled from a larger number of  $uv$  locations. In addition, due to the dependence on  $\lambda$ , a better  $uv$  coverage may be possible by using several relatively close wavelengths (Fig. 2.7 right), provided that source structure does not change significantly (e.g., continuum emission, but not spectral lines).

## 2.6 Derived Observables

An interferometer has several observables related to the phase of the complex visibility,

$$\phi_f(t) = \arg(V(u, v)(t)) \quad (2.7)$$

The time dependency denotes that the  $uv$  location of the baseline seen by a moving source changes with time, due to either Earth rotation or actual source motion relative to the array. Continuing the example of § 2.5 a source component at a sky position  $(l, m)$  of  $(7, 0)$  mas would produce a phase  $\phi_f$  equal to  $2\pi l/\theta_{f,u} + 0$  or  $2\pi/3$ .

The derived observables of  $\phi_f$  at a sky frequency,  $\nu$ , are the phase delay,  $\tau_\phi$  (time delay of the phase of a single frequency component), group delay,  $\tau_g$  (time delay of the fringe amplitude envelope), and the phase delay rate or *fringe frequency*,  $\nu_f$ , given by (Thompson et al. 2001)

$$\tau_\phi = \phi_f / 2\pi\nu \quad \sigma_{\tau_\phi} = 1/(2\pi\nu \cdot \text{SNR}) \quad (2.8)$$

$$\tau_g = \frac{1}{2\pi} \partial\phi_f / \partial\nu \quad \sigma_{\tau_g} = 1/(2\pi\Delta\nu \cdot \text{SNR}) \quad (2.9)$$

$$\nu_f = \nu \partial\tau_\phi / \partial t = \frac{1}{2\pi} \partial\phi_f / \partial t \quad \sigma_{\dot{\tau}_\phi} = 1/(2\pi\nu \cdot \Delta t \cdot \text{SNR}) \quad (2.10)$$

where  $\nu_f$  is alternatively defined as an angular frequency,  $2\pi\nu \partial\tau_\phi / \partial t$ , in the literature. Uncertainties on the right are for discrete estimates of the observables, formed across a time interval,  $\Delta t$ , or over individual bands separated by  $\Delta\nu$ , at some signal-to-noise ratio (SNR) of the fringe.

The time interval,  $\Delta t$ , also reflects the fact that interferometric visibilities are usually time averaged to improve fringe SNR and reduce data storage requirements (post-processing is done on stored data). To avoid coherence loss (a reduction in fringe SNR) the averaging period (AP) must be a small fraction of the anticipated array coherence time, typically some seconds, depending on the fast atmospheric phase fluctuations and, rarely for VLBI, sometimes also on the stability of the local frequency reference at each antenna (e.g., Rioja et al. 2012).

In practice the observed fringe phase,  $\phi_{\text{obs}}$ , and its derived quantities are contaminated by non-source contributions. Expressed as delays (e.g.,  $\tau_{\text{obs}} = \phi_{\text{obs}}/2\pi\nu$ ), one may write

$$\tau_{\text{obs}} = \tau_s + \tau_{\text{geo}} + \tau_{\text{atm}} + \tau_{\text{inst}} + \tau_{\text{resid}} \quad (2.11)$$

where two geometric propagation delays,  $\tau_s$  and  $\tau_{\text{geo}}$ , reflect source structure and array geometry under Earth rotation, respectively. Other delays are due to the atmosphere and instrumentation, and other non-source delays due to e.g. position errors. Most non-source delay (phase) contaminations can be compensated by calibration (e.g., Taylor et al. 1999, § 5).

The Earth rotation produces a *natural fringe frequency* (e.g., Thompson et al. 2001),

$$\nu_{\text{geo}} = \nu \partial \tau_{\text{geo}} / \partial t \simeq \omega_e \cdot \cos(\delta) \cdot \cos(HA) \cdot (\|B_{\text{E-W}}\| / \lambda) \quad (2.12)$$

where the mean angular velocity of the Earth,  $\omega_e$ , is  $\sim 7.292115 \cdot 10^{-5} \text{ rad s}^{-1}$  (Groten 2004),  $\delta$  and  $HA$  are the declination and hour angle (position) of the source, and the last term is the baseline length in the East-West direction (see also McIntock 1980; Offringa et al. 2012).

Some radio frequency interference mitigation methods, presented in the next Chapter, can be applied to the visibility data prior to the averaging mentioned above, while yet other methods can be applied to the pre-averaged data.

### 3 Radio Frequency Interference and Interference Mitigation

Radio frequency interference (RFI) can disturb both interferometric and single-dish observations. It is defined as any unwanted signal of non-astronomical origin and typically has a notably higher power level than the cosmic source.

The amount of RFI, both externally and internally generated, is a growing problem for radio astronomical observations due to the need for wider astronomical bands contrasted with the increasing number of other users that compete for the radio spectrum.

The telescopes are intrinsically highly sensitive to RFI for obvious reasons. The consequences of RFI are dependent on the RFI power, variability, and type of observation; RFI may cause an elevated system temperature and poorer delay precision in geodetic very long baseline interferometry (VLBI), may cause a possibly unnoticed level of corruption to the observation, a partial loss of non-critical subbands and sensitivity, an intermittent loss of the astronomical signal, or a complete loss of the observation, including the destruction of the receiver.

RFI mitigation involves attempts at reducing interference in the protected bands to, e.g., an equivalent of at most 10 % of the receiver system noise, and also recover parts of the spectrum outside protected bands. The reader may consult the ITU-R RA.769-2 for a rough estimate of

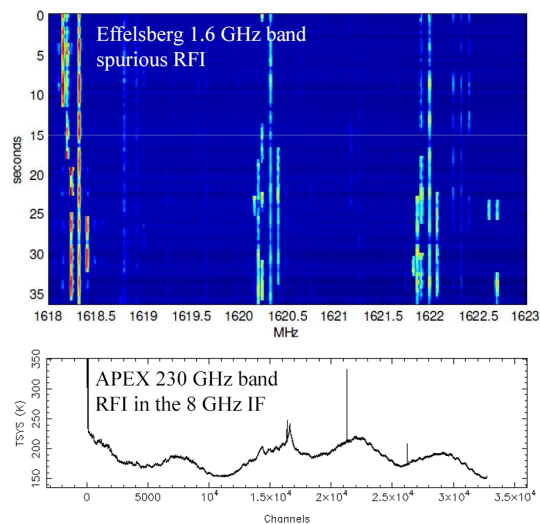


**Fig. 3.1:** Internally generated narrow RFI at Effelsberg at 1.6 GHz in a 5 MHz bandwidth (top; image courtesy of K. Grypstra), and in the APEX IF frequency in a 2.5 GHz bandwidth (bottom).





tion, and others. The amount of interference is pronounced at longer wavelengths ( $\geq \lambda 3.75\text{cm}$ ) as these bands are crowded with short- and long-range radio traffic. However, even the higher frequencies up 300 GHz are increasingly over-allocated (Fig. 3.2). Even if RFI is attenuated by several 10 dB as it enters through the most common route, via sidelobes of the primary beam or reflections off telescope support structure, RFI may still corrupt an observation.

Enforcing “clean” bands with only natural RFI, due to, e.g., space weather, would be the ideal solution for maintaining a non-degraded sensitivity. Unfortunately the non-profit astronomical users are in conflict with the exploding growth in commercial utilization of the spectrum and are set against user that may have a more direct impact on the national economy. Many users further want to operate modern radio services that are as bandwidth hungry as radio astronomy.

Often RFI is also self-generated and originates from, e.g., poorly shielded digital equipment that is operated at a radio observatory (e.g., Fig. 3.1 shows RFI from various equipment), or leakage in the receiver chain or back-end (e.g., local oscillator leakage in a VLBI downconverter, Fig. 3.1). With direct access and ownership of the equipment mitigation is relatively straightforward. Examples of countermeasures can be found in Manners (2007).

RFI outside the control of an observatory is more problematic. It is a challenge for international spectrum management and national regulators to resolve interference violations, find a compromise between astronomy and other current and future spectrum users, arrange radio-quiet zones around radio telescopes, and mediate agreements on the level of RFI “permitted” to leak from commercial adjacent bands, or shared-use bands, into an astronomical observation.

### 3.1.1 Proactive Interference Mitigation

Apart from telescope site selection, the best proactive mitigation approach is political and regulatory. For example, ETSI<sup>1</sup>, CEPT<sup>2</sup>, and ITU<sup>3</sup> receive astronomers’ input from the CRAF<sup>4</sup> committee of the European Science Foundation and similar committees. These authorities then coordinate spectrum management and compatibility by forming standards with special care of radio astronomy, and by releasing recommendations, rules of procedures, and radio regulations to the governments and the industry. It is the task of the observatory to monitor its local RFI situation. When another spectrum user is detected in violation of the emission or interference limits, astronomers can contact the operator of the interferer and ask the regulatory authority to enforce the limits. The approach is generally successful. It is, however, a slow process.

---

<sup>1</sup>European Telecommunications Standards Institute

<sup>2</sup>European Conference of Postal and Telecommunications Administrations

<sup>3</sup>International Telecommunication Union

<sup>4</sup>Committee on Radio Astronomy Frequencies, <http://www.craf.eu/>

### 3.1.2 ITU Interference Limits

Several ITU recommendations can be found under the ITU-R RA series<sup>1</sup>. The recommendation RA.314-10 maintains a list of preferred continuum and spectral line bands. The radial velocity window protected around a spectral line is  $\pm 300 \text{ km s}^{-1}$  (galactic) but certain molecules such as OH, H<sub>2</sub>O, and NH<sub>3</sub> are given an extended window of  $\pm 1000 \text{ km s}^{-1}$  (nearby galaxies).

The toleration of RFI is usually specified as some fraction (1 % to 10 %) of the ratio of the received interferer power and the system noise power of the telescope (ITU-R RA.769-2),

$$\sigma_{\text{RFI}}^2 / \sigma_{\text{sys}}^2 \equiv \frac{F_{\text{RFI}} \lambda^2 / 4\pi}{k_{\text{b}} T_{\text{sys}} \Delta\nu} \cdot \frac{1}{\sqrt{t \Delta\nu}} \quad (3.1)$$

where  $F_{\text{RFI}}$  is due to RFI, the observing bandwidth is  $\Delta\nu$ , and the last term with integration time  $t$  reflects the reduction in the noise floor (most astronomical signals are below the noise floor and time integration is required for a detection). The assumed  $T_{\text{sys}}$  depends on the frequency but is about 50 K on average. In addition, the RFI is received not via the primary beam but through the *sidelobes* approximated by an isotropic (0 dBi) antenna with a collecting area of  $\lambda^2/4\pi$ ,

ITU-R RA.769-2 provides upper limits on the RFI flux densities that are considered “detrimental”. For spectral line observations it states RFI thresholds of between  $-240 \text{ dBW m}^{-2} \text{ Hz}^{-1}$  (100 Jy) and  $-200 \text{ dBW m}^{-2} \text{ Hz}^{-1}$  ( $10^6$  Jy), thought to reflect 10 % of the noise floor after a time integration of 2000 s and a bandwidth of a few 100 kHz. Continuum observations are given similar limits, while for VLBI  $\sim 40$  dB less strict limits are allowed as ITU assumes VLBI to have better immunity towards uncorrelated RFI.

A third ITU-R recommendation (RA.1513) considers a 2 % data loss due to RFI to be acceptable. Lastly, the ITU recommendations only consider RFI that enters through the sidelobes. For reference, if RFI were to enter the primary beam with a typical gain of 50 dBi rather than 0 dBi, the RFI limit given by the ITU for spectral line observations would already be exceeded for an RFI source that has a flux density of  $\gtrsim 10$  Jy.

### 3.1.3 Dynamic Range

Dynamic range is critical to RFI mitigation. Low-noise amplifiers (LNAs) are used to pre-amplify the sky frequency signal and must have a high dynamic range to ensure linearity in amplification of the astronomical signal and the received RFI. Linearity avoids spectral distortion and loss of signal-to-noise ratio (SNR). A typical good LNA has a dynamic range of about 30 dB to 120 dB (Petrachenko 2010; Beaudoin et al. 2013). For the 2-bit sampling common in VLBI the total dynamic range of raw station data is much lower, around 15 dB. It can be improved

<sup>1</sup>ITU-R RA Recommendation series, <http://www.itu.int/rec/R-REC-RA>

by time averaging according to the radiometer equation. Time averaging increases the dynamic range by  $\sim 3$  dB for every doubling in the amount of averaged data.

Nevertheless, if the combined dynamic range of the LNA and the entire signal chain that follows is exceeded the system saturates and the RFI spreads across the system bandwidth. In this case RFI mitigation is generally not possible. All RFI mitigation techniques thus implicitly assume that the RFI is not strong enough to saturate the LNA and the rest of the signal chain.

### 3.1.4 Active Interference Mitigation

It is clear that many galaxies fall outside the relatively narrow local volume protected by the ITU recommendation, and that the flux density of most nearby extragalactic masers and many other types of astrophysical sources of radiation is far below the  $100 \text{ Jy}$  to  $10^6 \text{ Jy}$  RFI limit.

It is often necessary to observe outside the RA.314-10 protected bands and proactive mitigation is not possible. Strong RFI may occur even in protected bands if the interferer (e.g., a satellite or aircraft) passes the primary beam, or the antenna sidelobe contribution is significant as is usually the case when the RFI source is within about  $10^\circ$  of the antenna pointing.

Various active RFI mitigation techniques exist that may make additional spectrum available to astronomy. The methods work at various stages, from the receiver and real-time analog or digital data up to the post-processing of averaged data. For example, *real-time cancellation* with a regenerated/synthesized and then subtracted GLONASS satellite signal has been successful in 1.6 GHz OH line observations (Poulsen et al. 2005). Cancellation preserves most of the spectral and time domain data. On the other hand, when RFI is not easily modeled it may also be spectrally *excised* or temporally *blanked* in real-time data. The future geodetic VLBI2010 Global Observing System (VGOS) for example will span the complete range of frequencies from 2 GHz to 14 GHz (Petrachenko et al. 2010). RFI-affected times and subbands are excised in the digital backend and only RFI-free subbands are used for correlation. The excision technique requires statistical methods to classify a signal as RFI (e.g., Tarongi & Camps 2009; Thompson et al. 2011). Many are not effective at classifying noise-like RFI produced by modern modulation techniques. Pulsar observations are especially sensitive to modulated or (quasi-)stationary RFI that may mimic a pulsar, e.g., RFI with a 1 ms to 10 s period, that may lead to a false detection. For five RFI detection techniques and blanking and excision the reader may refer to Hogden et al. (2012). Each technique has strengths and weaknesses relative to different types of RFI.

“Mitigation” through excision has limitations, as observations often require wider bandwidths and higher sensitivities. Excising corrupted frequency bands that may contain valuable scientific information leads to a loss of bandwidth, while temporal blanking leads to a loss in sensitivity relative to the target sensitivity of the observation. However, there are methods that can preserve some of the scientific information. These methods are applicable in antenna arrays.

## 3.2 Interference Mitigation for Arrays

Some methods to mitigate RFI are known to be very effective but are not yet implemented at many radio observatories. Sophisticated approaches for arrays like the Square Kilometer Array and focal-plane arrays are still to be fully explored.

Under this thesis two types of RFI mitigation were implemented. The initial goal was to apply certain RFI mitigation methods to HI, OH, and H<sub>2</sub>O spectral line observations and surveys. The instrumentation considered to benefit from the RFI mitigation methods were the Effelsberg  $\lambda$ 21 cm 7-beam receiver used in the Effelsberg HI survey (1260 MHz to 1510 MHz, 7 antenna elements or “beams”; e.g., Ruiz et al. 2005) or a future APERTIF-like focal-plane array in Effelsberg for spectral line and pulsar surveys (1 GHz to 1.7 GHz), possibly also the Robert C. Byrd Green Bank Telescope (GBT) K-band focal-plane array used in H<sub>2</sub>O surveys and ammonia mapping, and the existing 1.4 GHz to 22 GHz VLBI with the European VLBI Network (EVN) and the International VLBI Service (IVS) when the antenna array data are correlated at an RFI mitigation -augmented software correlator at the Bonn MPIfR.

First, a RFI mitigation approach for VLBI by Roshi & Perley (2003) was implemented in the software correlator used by the Bonn MPIfR. It works during correlation, at the time averaging stage. Details are provided in the following sections. Second, an RFI mitigation method for focal-plane arrays and local arrays was implemented and improved. It makes use of one or more RFI reference antennas to form a subtractable “template” of the RF interferer. The subtraction is done post-correlation and one is not committed to the correction.

Both types of RFI mitigation above are applicable to antenna arrays. They attenuate correlated and uncorrelated RFI, or subtract correlated RFI from the antenna array data.

### 3.2.1 Correlated and Uncorrelated RFI

An interferer seen simultaneously at two or several antennas is said to be *correlated RFI*. Correlated RFI is most likely to affect focal-plane arrays and local arrays. In VLBI correlated RFI from satellites typically appears on short baselines. At distances greater than a few 100 km the interferer is not visible to both antennas. Long baselines experience uncorrelated RFI.

Uncorrelated RFI on the other hand is interference local to a single antenna. RFI will also appear uncorrelated when the time delay difference from the interferer to different antennas in the array exceeds the coherence time of the RFI signal, seen in Eq. 2.1 for  $\tau = 0$ .

For an array operating in interferometric mode, uncorrelated RFI is indistinguishable from an elevation of the noise floor. Even correlated and mitigated RFI elevates the noise floor. To see this, we can expand the coherence function (Eq. 2.1) in terms of a field  $E$  represented by the

actually measured antenna signals  $S_1$  and  $S_2$  at the ends of a baseline. The expansion yields

$$\begin{aligned}\Gamma_{12} &= \langle S_1 S_2^* \rangle = \langle (A + N_1 + I)(A + N_2 + I)^* \rangle \\ &= \langle AA^* \rangle + \langle AN_2^* + A^* N_1 \rangle + \langle AI^* + A^* I \rangle + \langle N_1 N_2^* \rangle + \langle IN_2^* + \alpha I^* N_1 \rangle + \alpha \langle II^* \rangle \\ &= \langle AA^* \rangle + \langle \text{noise-like cross-terms} \rangle + \langle II^* \rangle\end{aligned}\quad (3.2)$$

where the common astronomical signal,  $A$ , is usually below the noise floor determined by the independent antenna noise signals,  $N_1$  and  $N_2$ , which in turn are weaker than the RFI signal,  $I$ . Antenna gain differences have been omitted for brevity. A parameter  $\alpha$  of 0 corresponds to uncorrelated RFI, typical on a long baselines, and a value of 1 models correlated RFI.

In the expression the expectation values of the noise-like cross-terms are zero because noise and RFI are mutually uncorrelated. However, if the expectation values are approximated by time averaging over a finite time interval,  $T_{\text{int}}$ , as is done in practice, the cross-terms introduce nonzero residual errors. The residuals approach zero at a rate proportional to  $1/\sqrt{T_{\text{int}}}$  and eventually the estimated coherence  $\Gamma_{12}$  is dominated by the astronomical signal.

Even if RFI is successfully mitigated, such that  $\langle II^* \rangle$  vanishes, we can see from Eq. 3.2 that the degradation in sensitivity relative to the sensitivity in an RFI-free environment,  $\Delta S$ , is

$$\Delta S' / \Delta S = \sqrt{1 + (I/N)^2 + \alpha(I/N)^2} \quad (3.3)$$

where for simplicity we assume the noise signals in both antennas have equal power. To provide some context: in protected bands, ITU limits interference to 10% of the system noise. The decrease in sensitivity is then about 1%. Conversely, outside protected bands an  $I/N$  ratio of 10 is plausible. This would degrade sensitivity by 1400%. As the noise in RFI-contaminated subbands is higher than in adjacent clean subbands, there is also an increased probability of measuring a large coherence. This was also seen in VLBI test data. The effect can be particularly detrimental to spectral line observations.

In summary, even if RFI mitigation succeeds, noise in previously RFI-contaminated subbands remains elevated. The cross-power spectrum of the multi-frequency visibility data of a baseline can then contain additional features that are not spectral lines but RFI/noise artifacts.

Nevertheless, with the above limitation in mind, RFI can still be removed or suppressed in array visibility data. The first method (Roshi & Perley 2003) was implemented here and enhances the natural rejection of RFI fringe frequency components after fringe stopping.

### 3.2.2 Array Phasing and Fringe Stopping

As mentioned in § 2.6 the Earth rotates beneath the radio source in the sky at a mean angular rate,  $\omega_e$ , of roughly  $7.3 \cdot 10^{-5}$  rad/s. This causes the phase center of baselines in a ground-based

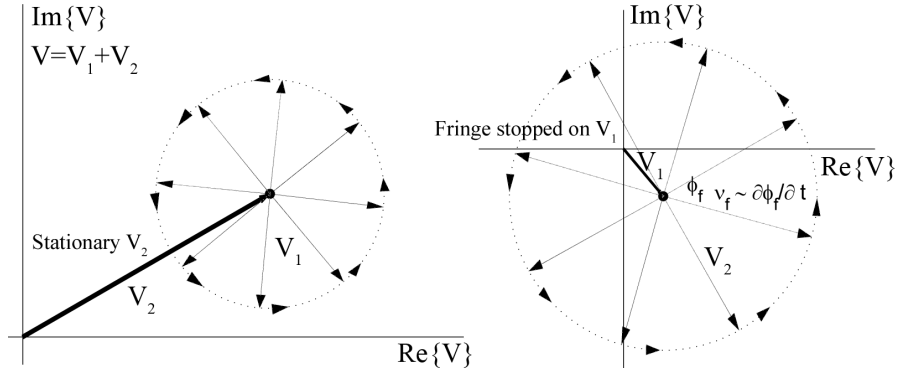


**Fig. 3.3:** “Fringe stopping” shown as a phasor diagram of the sum of a source visibility,  $V_1$ , and an RFI visibility,  $V_2$ . Left: The RFI is stationary with respect to the array so its visibility is constant, whereas  $V_1$  has a non-zero fringe frequency as it drifts off the array phase center due to Earth rotation. Right: After fringe stopping, the phase center tracks the source and the situation is reversed, with RFI visibility  $V_2$  imparted with a non-zero fringe frequency.

array to drift off source. As the array tilts the source moves through the interferometric fringe pattern and produces a time-variable phase and non-zero fringe frequency,  $\nu_f$  (Eq. 2.12). This leads to a rotation of the phase of the complex visibility with time,

$$V(t) = \|V\| e^{j\phi(t)} \quad \text{where} \quad \phi(t) = \phi_f + 2\pi\nu_f t \quad (3.4)$$

where  $\phi_f$  is the phase due to actual source structure. To track the moving source with the array phase center, array signal processing compensates for the changes in geometric delay and phase. This *array (re-)phasing* towards the source direction is performed in, e.g., VLBI correlators such as *DiFX* (Deller et al. 2011)<sup>1</sup>. It numerically realigns the array  $uv$  plane to the orientation of the plane waves impinging from the source direction.

The continuous phasing also restores the source fringe frequency to zero (*fringe stopping*). The effect is demonstrated in the phasor diagrams of Fig. 3.3 where the phase winding of a source component  $V_1$  (left panel) due to Earth rotation is compensated by fringe stopping to yield a constant phase (right panel) that again reflects source structure rather than motion.

The RFI sources are not expected to move synchronously with the target source. In any case, such a coincidental situation is extremely unlikely. Thus fringe stopping usually shifts initially stationary RFI components ( $V_2$  in Fig. 3.3) towards a higher fringe frequency.

Incidentally, the array re-phasing to stop the fringe is also equivalent to *beamforming*, i.e., forming a high-resolution beam (the fringe spacing is narrower than the beam of a single antenna) that has a peak sensitivity towards the target source. Phasing ensures that all antenna sig-

<sup>1</sup><http://cira.ivec.org/dokuwiki/doku.php/di:fx/start>

nals could be coherently summed in a phased-array configuration to produce a high-sensitivity time-domain signal received from the target direction.

### 3.2.3 Attenuation of the RFI Fringe

The size of the antenna array and the available observing time are finite and a limited number of visibilities are measured at discrete points of the uv plane, e.g.  $V(u[n],v[n])$ . The expectation value for  $V$  in Eq. 2.1 is replaced by the instantaneous  $V$  averaged over some time duration  $T_{\text{int}}$ . After fringe stopping, any RFI that is not co-moving with the source will have a non-zero fringe frequency relative to the source. Due to the winding phase (Eq. 3.4) time averaging attenuates the rotating RFI fringe. This makes interferometers naturally less susceptible to RFI.

The visibility phase winding and the attenuation of an off-source interferer is demonstrated in Fig. 3.4. It shows raw visibilities computed from the antenna signals of the data set provided by Bell et al. (2001), a public data set of antenna signals made available by Bell et al. for testing new RFI mitigation algorithms. Their data contain a 1.6 GHz observation of the IRAS 1731-33 OH maser with the 6-antenna ATCA array<sup>1</sup>. The observation was affected by interference from GLONASS satellites. On the longest baseline of 6 km we find the fringe frequency of the interferer to be 2.8 Hz. The time evolution and natural attenuation of this RFI component, 18 dB after time-integrating 610 visibilities of 16.4 ms, is shown in Fig. 3.4.

### 3.2.4 Filtering out RFI Fringe Components

If the fringe frequency of the RF interferer is low (i.e.  $T_{\text{int}} \cdot \nu_f \ll 100$ ) and the interference is relatively strong compared to the source, the natural attenuation may not be sufficient.

In this case, significant RFI ringing can leak into the averaged visibilities. This is a spectral aliasing effect. The raw cross-antenna products have an input bandwidth of, say, 62.5 kHz per subband. Time averaging to 2 s is identical to filtering and down-sampling the visibility data to an output bandwidth of 0.5 Hz. All poorly filtered input frequency components above 0.5 Hz will then fold onto the output spectrum (cf. Mitra 2000).

Aliasing adds source-like contributions to the visibility. This leads to errors in *closure phase* (the argument of the product of complex coherences of three baselines), and causes errors in *fringe fitting* (the removal of sub-Hz fringe rate residuals on the source, stemming from, e.g., uncertainties in the Earth rotation model).

At post-correlation, strong ringing along the uv visibility time series can be fit to a single sinusoid model that is subtracted using the *RfiX* technique by Athreya (2009), successful in GMRT observations below 400 MHz, provided that the ringing has a period of several  $T_{\text{int}}$ .

---

<sup>1</sup>Australia Telescope Compact Array (<http://www.narrabri.atnf.csiro.au/>)



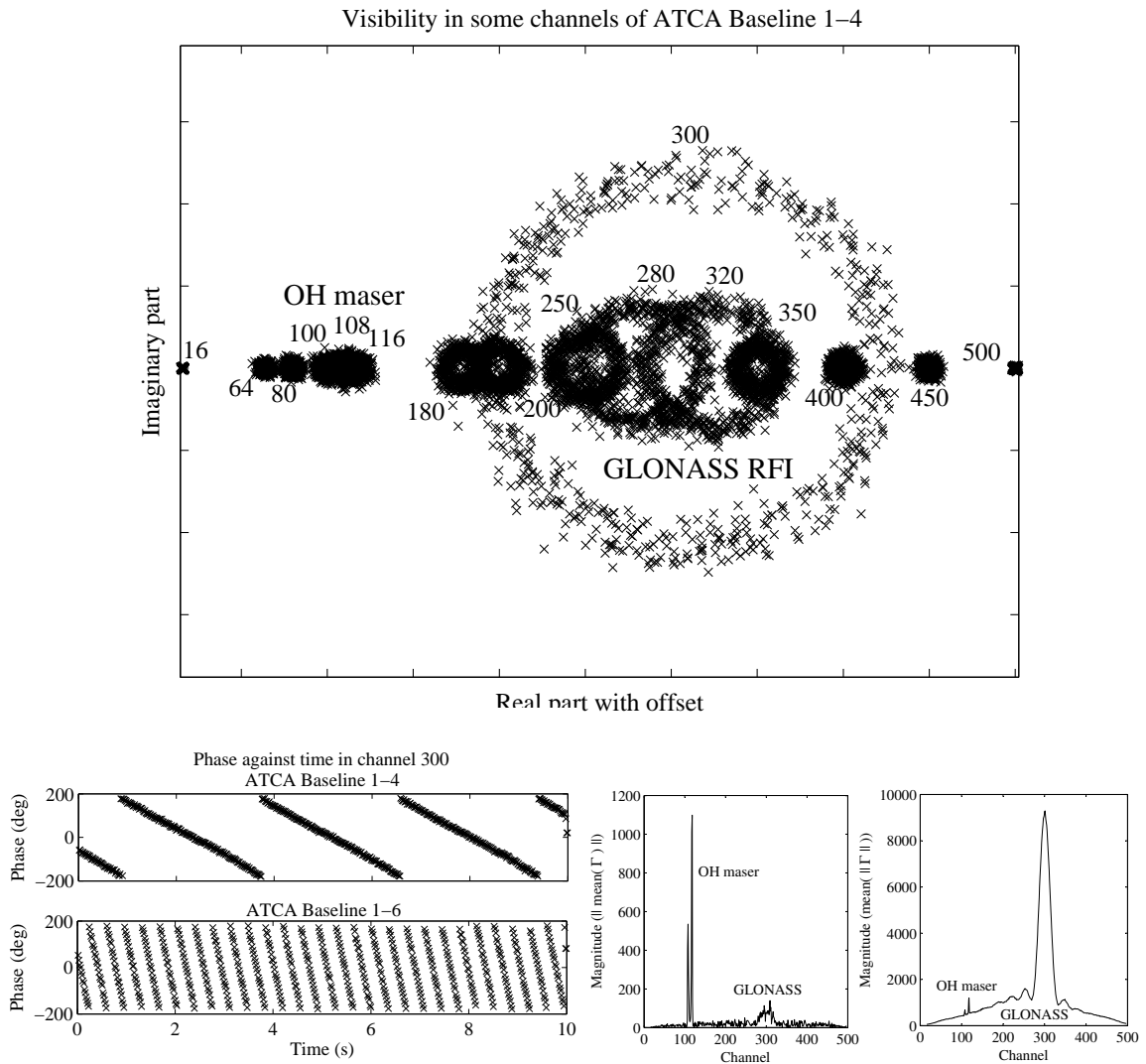


**Fig. 3.4:** Evolution in fringe phases over 10 s and natural attenuation of the RFI fringes. Visibilities were derived from baseband recordings of a 1612 MHz spectral-line and RFI test data set (for the raw data, see Bell et al. 2001). A bandwidth of 8 MHz and 512 channels cover the redshifted OH maser emission (IRAS 1731-33; channels 106 to 116) and satellite interference (GLONASS; channels 150 to 450, carrier in channel 300). Top: A complex plane diagram of the visibilities of some frequency channels (channel numbers are indicated). A horizontal offset was added for clarity. Bottom left: The phase of the RFI fringe in 16 ms intervals in channel 300. The fringe frequency on baseline 1–4 was 0.4 Hz, and 2.8 Hz on the longer baseline 1–6. Bottom right: The natural attenuation of the RFI fringe by 18 dB in a 10 s vector average of complex visibilities, shown next to an unattenuated reference given by the scalar average of visibility magnitudes.

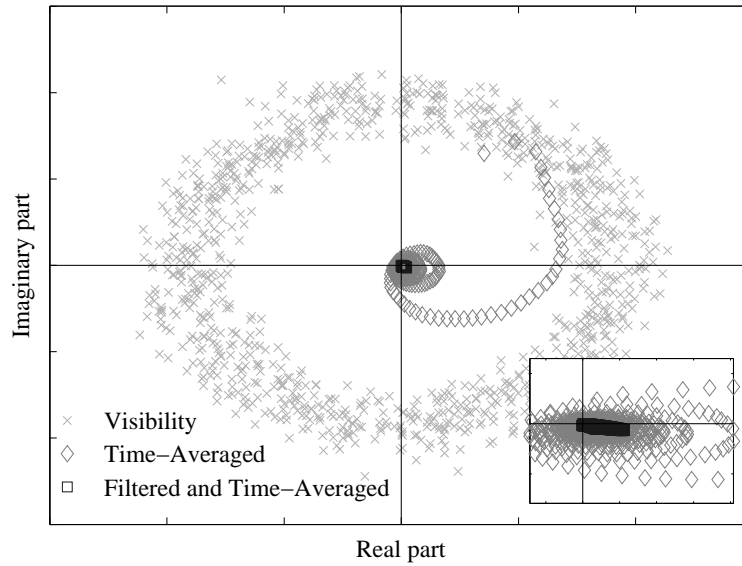


**Fig. 3.5:** Fringe rate filtering and the time trajectories of complex visibility data over 10 seconds. The raw input visibilities (crosses) were either time averaged (diamonds), or low-pass filtered and averaged (squares). The filter was a 1 Hz, 4<sup>th</sup> order IIR elliptic low-pass. Raw data are from channel 300 of the ATCA baseline 1-6 and are contaminated by the carrier signal of a GLONASS satellite, see also Fig. 3.4. Each point represents the latest raw or processed visibility sample at the output of the continuous averaging or filtering process, and was smoothed to a 16 ms resolution for clarity.

Rather than subtracting a model, it is also possible to filter the uv plane with a 2-D low-pass filter, a technique introduced by Offringa et al. (2012) for the WSRT below 200 MHz.

To enhance the natural attenuation of the RFI fringe at a pre-correlation stage, Roshi & Perley (2003) suggest replacing coherence data time averaging with a steeper low-pass filter. The effect in the fringe frequency domain is to change what was a sinc-squared drop-off with increasing fringe rate (which has an -13 dB first sidelobe level) to a designer-selectable function (typically a  $\leq -60$  dB floor and no sidelobes).

Filtering is computationally more expensive than averaging, but can achieve better than 20 dB improvement over the natural suppression of the RFI fringe. An example of fringe rate filtering of a GLONASS interferer is shown in Fig. 3.5, where visibility data shown in 66 ms increments have either been time averaged, or 1 Hz low-pass filtered and time averaged. Both visibilities convergence in 0.7 s to within 95 % of the final value. The low-pass filtered data converges faster, while time averaging has more ringing due to its sinc-squared drop-off.

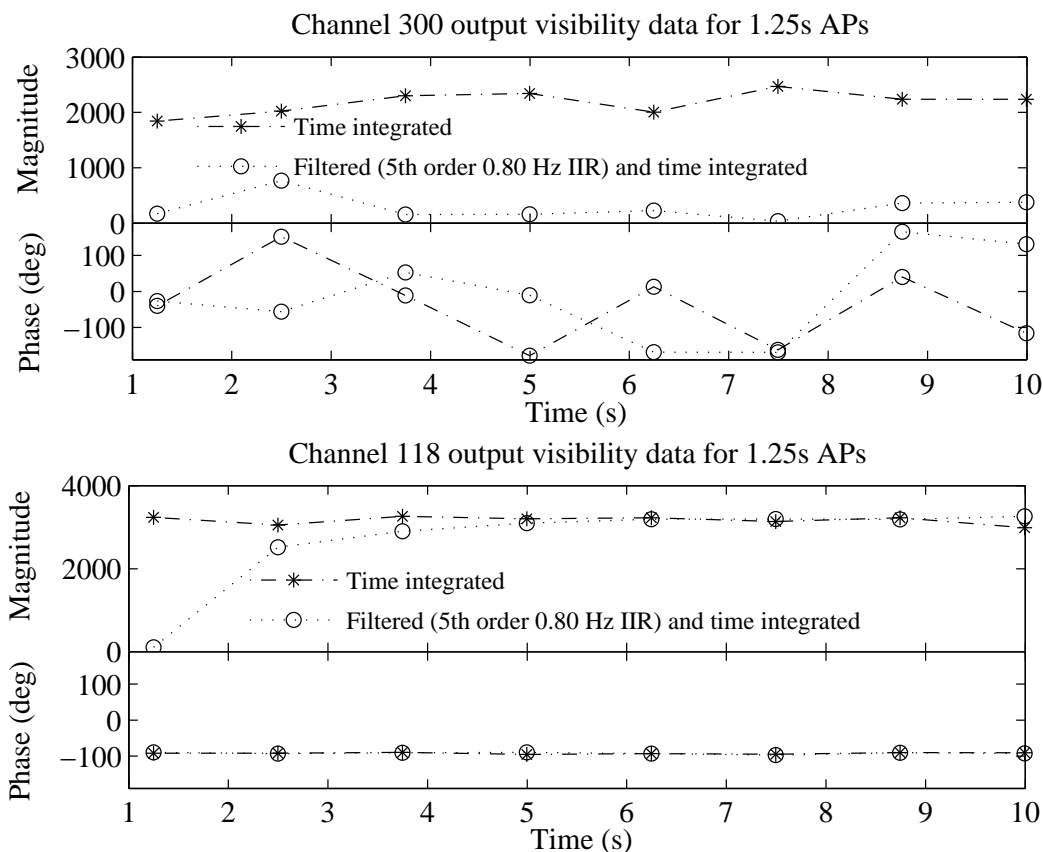


**Fig. 3.6:** The correlator output for ATCA baseline 1–6 data and an averaging period (AP) of 1.25 s, either after filtering with a 0.8 Hz low-pass and averaging the continuous filter output into non-overlapping APs of 1.25 s (circles), or after traditional time averaging to 1.25 s APs (asterisks). **Top:** The GLONASS carrier channel. The RFI amplitude is much reduced by the filter. **Bottom:** The OH maser channel. The amplitude and phase are unaffected by the filter. Note that the unavoidable additional group delay of the low-pass filter, here about 1.2 s, has not been compensated for.

### 3.3 A Fringe Rate Filter Implementation for DiFX-2

The DiFX-2 correlator is an open-source software correlator that runs on a distributed cluster computing architecture (Deller et al. 2011). It supports astronomical VLBI, geodetic VLBI, and pulsar observations, and offers a large number of features. These include the detection (but not mitigation) of transients and RFI-like signals via a Jarque-Bera test of time domain Gaussianity (Thompson et al. 2011). DiFX also includes a basic implementation of phased array processing. DiFX can be relatively easily extended to test new RFI mitigation algorithms (Deller 2010).

We implemented the array mitigation methods described in this thesis, and the filtering approach of § 3.2.4, see also Sachdev & Udaya Shankar (1995) and Roshi & Perley (2003). The

### 3.3 A Fringe Rate Filter Implementation for DiFX-2

---

software is in form of a library that includes a reference implementation with synthetic RFI data generation and algorithm testing code in Matlab® (2010), and a C/C++ library that implements both the array and VLBI RFI mitigation algorithms. The library, documentation and a modified version of the DiFX correlator that invokes the library are available via the DiFX-2 source code repository<sup>1</sup> and are found under source code branch that is labelled “rfi”. Documentation is also available on the RadioNet EU FP7 pages of the ALBiUS project (Wagner 2011)<sup>2</sup>.

The modifications that were necessary for interfacing DiFX to the larger filter library had a relatively small footprint ( $\approx 50$  source code lines). It was verified that the DiFX correlator output visibility data produced by standard time averaging and by time averaging via the interfaced library were identical. The operation of the other filters was verified by comparing filtered test data to the output of the Matlab filter reference designs. Certain common filter types are implemented, and additional filters may be added relatively easily. For general information on filters, see, e.g., Mitra (2000), or the EU FP7 ALBiUS project page (Wagner 2011). For the design of filters and the calculation of filter coefficients the reader may consult the vast literature on the topic. A good starting point is the already mentioned book by Mitra (2000).

To correlate a VLBI experiment in DiFX with RFI fringe rate filtering, one entry in the correlation setup file and a custom filter coefficients file are sufficient. The coefficients file is used to configure a serial interconnection, or *cascade*, of one or more filters of identical or different types. A brief summary of the files is given in Appendix A.1.

#### 3.3.1 Filter Details

DiFX splits the input bandwidth of the antenna signals into several frequency subbands (channels). Signals in these channels are fringe-stopped and cross-correlated with the signals from the matching channels of the other antennas. Time averaging or fringe rate filtering operates on data in these channels. That is, the effective sampling rate in each channel,  $f_s$ , is twice the bandwidth of the original antenna data divided by the number of channels.

For example, when 512 channels are used, VLBI data that have an input bandwidth of 16 MHz would yield a sampling rate of 62.5 kHz in each channel. The low-pass filters operate at the channel sampling rate. This allows the use of less steep filters.

As in traditional time averaging, the same consistent filter configuration is applied to baseline cross-correlation i.e. visibility data and antenna autocorrelation data. This keeps the filter gain and phase response characteristics identical to all data and avoids introducing non-closing baseline phase errors. It also maintains a consistent relation between the cross-correlation and autocorrelation magnitudes. Note that the gain and phase calibration steps commonly applied

---

<sup>1</sup>The “rfi” branch in the current (2014) DiFX source code repository at <https://svn.atnf.csiro.au/di fx/>

<sup>2</sup>RadioNet <http://www.radionet-eu.org/fp7/albius.html>

### 3.3 A Fringe Rate Filter Implementation for DiFX-2

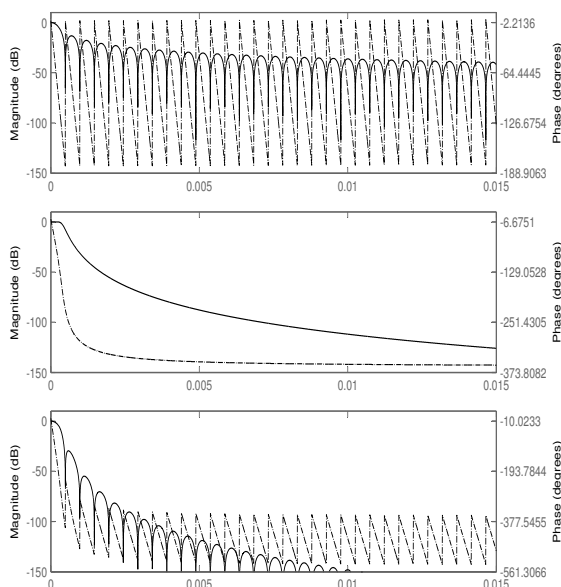


**Fig. 3.7:** The overlaid magnitude (solid) and phase (dashed) response shown against normalized frequency (e.g., the lower 300 Hz of a 62.5 kHz bandwidth) for two fringe rate filters, compared to standard time integration without additional filtering. **Top:** VLBI time integration of 4096 samples, equivalent to a 4096 point moving average. It has group delay of 2047.5 samples (not shown). **Mid:** 25 Hz Butterworth low-pass as a 4<sup>th</sup> order IIR in single precision arithmetic. The group delay is 2000 to 3000 samples in the passband. **Bottom:** The cascade of both filters, with a group delay that is the sum of the above delays.

during the post-processing of visibility data in, e.g., AIPS (Bridle & Greisen 1994), automatically remove the instrumental gain and phase errors due to time averaging, or due to filtering.

Lastly, all filters implemented in DiFX use single precision (32-bit floating point) arithmetic to match the precision of the DiFX visibility data.

#### Filters Implemented for DiFX Fringe Rate Filtering

In the filter descriptions below we follow the usual notation where the next filter output sample,  $y[n]$ , is given in terms of past outputs,  $y[n - p]$ , the present input,  $x[n]$ , and the past inputs,  $x[n - p]$ . The low-pass corner frequency,  $f_c$ , also written as a normalized angular frequency,  $\omega_c = 2\pi f_c / f_s$ , is the frequency at which the filter attenuation reaches 3 dB. The filter transfer function  $H(\omega)$  is the ratio of the output to the input. For fundamentals, see, e.g., Mitra 2000.

**Decimator** The decimator described by  $y[m] = x[nR]$  has an adjustable integer decimation factor  $R$  that is the ratio between the input and the output sampling rates. A multi-rate filter design can be realized with lower demands on the numerical precision of filter coefficients for a given low-pass corner frequency.

**Integrator** The integrator is a finite impulse response (FIR) filter described by

$$y[n] = y[n - 1] + x[n]$$

and it outputs the sum of all earlier samples. It is equivalent to the VLBI time averaging

of visibilities if the filter is reset back to zero at the end of an averaging period. A closer equivalent to VLBI time averaging without the reset is the moving average filter.

**Moving average** The  $M$ -point moving average filter,

$$y[n] = 1/M \sum_{k=0}^{M-1} x[n-k]$$

integrates visibility data over a window of length  $M$  where sample weights are assigned to  $1/M$  and weights outside the window are zero. The zero truncation causes pronounced sinc-like ringing, evident also from the transfer function of the moving average of

$$H[\omega] = \frac{\sin(M \omega/2)}{M \sin(\omega/2)}$$

The low-frequency response is shown in the top of Fig. 3.7. The moving average is an exceptionally good smoothing filter, but an exceptionally bad low-pass filter.

**IIR biquad** This is an infinite impulse response (IIR) filter of order  $2N$ , implemented as a cascade of  $N$  second order sections (IIR SOS, IIR biquad), each given by

$$y[n] = + b_0x[n] + b_1x[n-1] + b_2x[n-1] \\ - a_1y[n-1] - a_2y[n-2]$$

A nearly arbitrary filter response can be implemented, up to floating point precision limits. An example of a 4<sup>th</sup> order IIR low-pass (two biquad sections) is show in the middle panel of Fig. 3.7. The same IIR cascaded with an integrator is shown in the bottom panel of Fig. 3.7. In single precision arithmetic as used by DiFX a single IIR SOS section is stable to a cut-off of about  $\omega_c = 10^{-6}$  but at this narrow passband width does not allow a very strong attenuation. The single precision attenuation can be about 15 dB at  $\omega_c = 10^{-6}$  for a single SOS section. Filter stability and steepness depend on the type of filter design. Common designs are, e.g., Chebyshev, Butterworth, elliptic, and maximally flat filters.

DiFX implements the canonical Direct Form II realization of the IIR SOS filter. It has the lowest memory and arithmetic cost.

The filter coefficients for any desired filter characteristic can be readily obtained using the filter design utilities in Matlab<sup>®</sup>, GNU Octave, and other software.

**Digital State Variable Filter** The Digital State Variable Filter (DSVF) is a 2<sup>nd</sup> order filter and it may have the best low-frequency response of the above filters (Chamberlin 1985; Dattorro



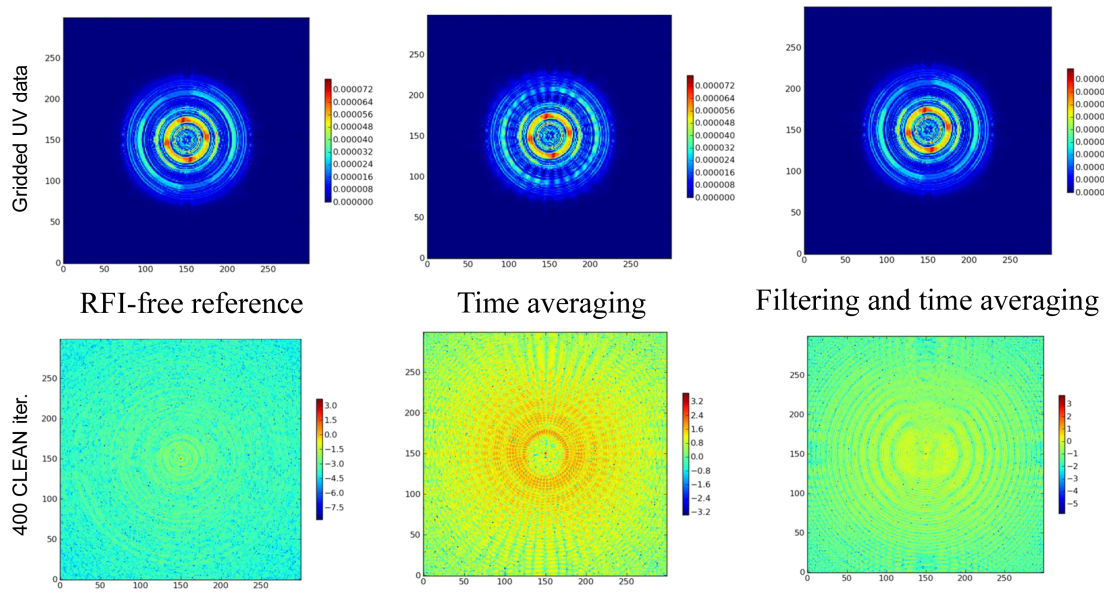


**Fig. 3.9:** The simulated PAPER array visibility data in the uv plane (top) and the respective source images after deconvolving and restoring with a Gaussian beam (bottom). The data have a 5 kJy point source at the celestial South Pole (the central pixel in the images). The simulation shows, subjectively, the image corruption due to aliasing of RFI fringe components into VLBI visibility data during time integration. Left: The visibility data and image without RFI. Middle: Artifacts due to RFI at 1 % of the source flux density, with RFI leaked via aliasing. Right: Reduction in artifacts after an additional 20 dB of RFI fringe attenuation by low-pass filtering before time integration.

and have a non-constant delay against fringe frequency. The delay at the zero fringe frequency adds a (deterministic and calculable) time offset until the final visibility of an averaging period is available. This is evident for example in the filtered ATCA visibility data of Fig. 3.6. Note also that for cascaded filters the total group delay is the sum of the delays of the individual filters.

The additional group delay can cause a slight rotation in the uv plane data, and thereby the image. This is an issue similar to that solved by Garn et al. (2007) and their AIPS task UVFXT.

## 3.4 Fringe Rate Filter Tests and Results

### 3.4.1 Aliasing of RFI into Visibility Data

The VLBI fringe stopping changes the fringe frequency of any sources (e.g., RFI) that are not co-moving with the astronomical source, shown earlier in Fig. 3.3. When the RFI fringe frequency is relatively low, additional attenuation with a fringe rate filter may avoid a leak of RFI into



output visibility data through the aliasing effect. Aliasing occurs when the times series of the raw baseline visibility data is resampled at, e.g., 2 second intervals and when filtering such as time integration has not yet sufficiently attenuated the fringe frequency components above 0.5 Hz in this example. The aliased RFI would then cause ringing in the visibility data and ringing would follow the uv track (§ 3.2.4).

To test how leaked RFI subjectively affects images produced from RFI-contaminated visibility data, synthetic visibility data were generated with the AIPY interferometry package (see Parsons & PAPER Team 2009). AIPY was modified to enable an addition of aliased, constant fringe frequency RFI on all baselines towards a certain antenna. Three sets of synthetic visibility data for a 150 MHz observation with the PAPER<sup>1</sup> array of a 5 kJy point source at the celestial South Pole were generated. The visibility data had time spacing of 2 seconds. The first data set was free of RFI. The second included residual RFI at a level of 1 % of the source flux density that leaked through the 2 s time integration process via aliasing, with a resulting aliased RFI fringe period of 200 s. Such a fringe period would be produced by RFI with a fringe frequency that is any integer multiple of 0.005 Hz prior to the 2 second time integration. In the third data set, the RFI was attenuated by the amount expected from fringe rate filtering, or about 20 dB.

The results of the AIPY simulation are shown in Fig. 3.2.4. They suggest that relatively low levels of RFI can corrupt source structure, and that a modest (~20 dB) attenuation of RFI fringe components in the visibility data may be able to subjectively improve the source image.

#### 3.4.2 Synthetic VLBI Data

To test the performance of the fringe rate filter a new set of synthetic VLBI data were correlated in the modified DiFX software correlator. The new test data were generated by a new program that is now included in the DiFX utilities (`datagen5b.py`; listed with other programs in Appendix A.2). The program generates recordings for several VLBI antennas with four identical 16 MHz wide frequency bands. Uncorrelated and correlated noise with a signal power of 1.0 are added to each station and a GPS satellite carrier signal with an amplitude of 1.0 is placed at 6 MHz of the 16 MHz wide bands.

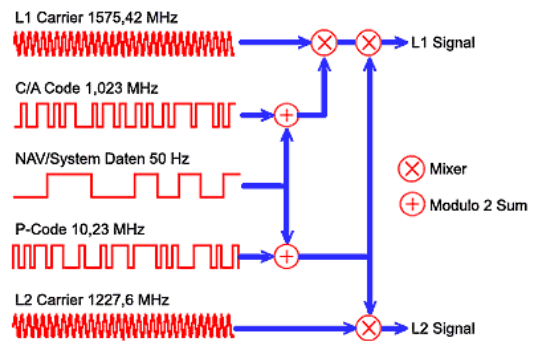


**Fig. 3.10:** Modulation of GPS Coarse Acquisition and Y Code chip sequences onto the L1 and L2 carriers. Image courtesy of P.H. Dana (1998).

<sup>1</sup>Precision Array for Probing the Epoch of Reionization (PAPER), see, e.g., Parsons et al. (2010).

The synthetic GPS L1 carrier can be optionally modulated with the GPS Coarse Acquisition (C/A) and P Code (or Y Code) pseudo-random chip sequences (Fig. 3.10). This allows to test the effect of modulation on the spectral spread-out of the RFI in the fringe frequency domain and test the fringe rate filter performance for complex modulated RFI. The `datagen5b.py` program modulated the chip sequence onto the carrier using the standard binary phase-shift keying modulation scheme. The program does not apply Doppler shifts or geometric delays; the GPS satellite is effectively at the baseline zenith and co-rotates with the Earth. Lastly, before output the generated synthetic antenna signals are quantized to four voltage levels (2 bits). The quantized data are then written to Mark5B files<sup>1</sup>.

#### DiFX Correlation

The synthetic 1.6 GHz L-band VLBI data with GPS L1 RFI were correlated in DiFX with a virtual array that included Effelsberg (Ef), Jodrell Bank (Jb), and Westerbork (Wb). The shortest baseline was 266 km (Ef–Wb). A source at a declination of  $\delta = 45^\circ$  was specified in the correlation setup and it had a starting elevation of about  $80^\circ$ . The correlation in DiFX was configured to 128 channels and had an empty phase center without any actual astronomical source signal. A 10 Hz Chebyshev low-pass filter was provided to DiFX via a filter coefficients file.

#### DiFX Filter Verification

For validation purposes the raw antenna data after DiFX fringe stopping, just before time averaging and cross-correlation, were written to external “dump” files. The new filter infrastructure in DiFX was verified by loading the dump data of one DiFX averaging period into Matlab. A filter with the same coefficients as supplied to DiFX was used to filter the fringe-stopped data in Matlab. The output at the end of the averaging period of the reference filter design was consistent with the visibility sample produced by the DiFX implementation.

#### Attenuation of the GPS RFI Fringe Component

The “dump” data DiFX produced for the synthetic 1.6 GHz VLBI experiment were inspected. The cross-power spectrogram and fringe frequency spectrum of the first 0.1 seconds of Ef–Wb baseline data are shown in Fig. 3.11. They indicate that although the synthetic GPS satellite itself had a fringe frequency of 22 Hz after fringe stopping, the GPS C/A modulation spreads the interference across a wide fringe frequency range.

The fringe frequency spectrum of Fig. 3.11 further suggests that a fraction of the signal power of the modulated RFI may overlap the near-zero fringe frequency range. This range

---

<sup>1</sup>The Mark 5B file format is described in the MIT Haystack Mark 5 Memo Series, Memo #017, <http://www.haystack.edu/tech/vlbi/mark5/memo.html>

### 3.4 Fringe Rate Filter Tests and Results

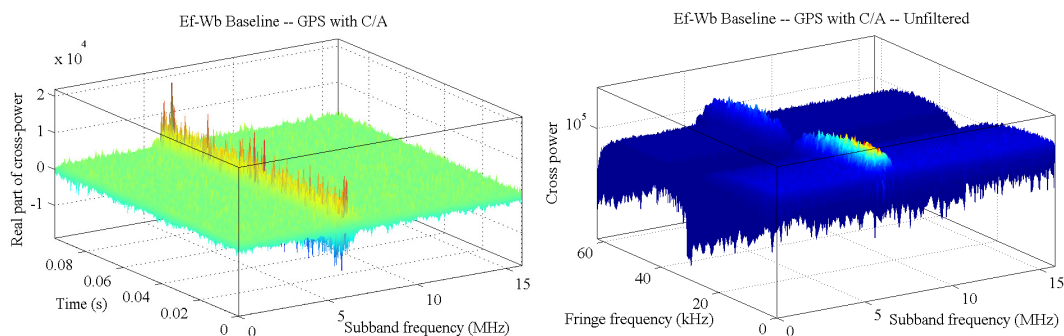


**Fig. 3.11:** Synthetic 1.6 GHz VLBI data on the Effelsberg(Ef)–Westerbork(Wb) 266 km (1.4 M $\lambda$ ) baseline after fringe stopping in DiFX. An GPS L1 interferer with C/A modulation is centered on 6 MHz and has a peak fringe frequency of 22 Hz. Left: the cross-power spectrogram of the first 0.1 seconds of fringe stopped data. Right: the fringe frequency spectrum in logarithmic scale. The GPS C/A modulation spreads out the interference in the frequency and fringe frequency domains.

also carries the spatial coherence information of the astronomical source, which would then be degraded to some degree depending on the RFI carrier power, carrier modulation scheme and modulation bandwidth, and the carrier location in fringe frequency. In general, a fraction of the RFI contamination due to a modulated interferer can most likely not be mitigated by the fringe rate filter in actual observations.

The filter responses near the zero fringe frequency range were practically identical (Figs. 3.12 and 3.13), indicating that both filtering processes, that is, low-pass with time integration, or only standard VLBI time integration, do not have any negative impact on the astronomical signal.

The reduction in peak RFI after fringe rate filtering (with a 10 Hz Chebyshev IIR low-pass filter) compared to time integration is shown in Fig. 3.12. A close-up of the lower < 50 Hz fringe frequency range is shown in Fig. 3.13. Compared to the standard VLBI time integration fringe rate filtering with time integration achieved an additional reduction of the GPS carrier of 30 dB.

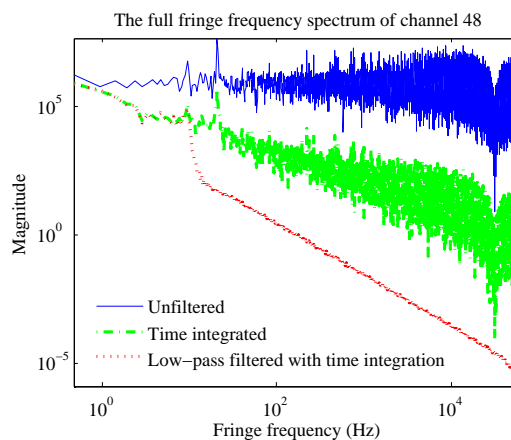


**Fig. 3.12:** The fringe frequency spectrum of the GPS L1 carrier channel in the synthetic 1.6 GHz VLBI data set. Filtering strongly reduces the RFI peak. The low fringe frequency range is shown in greater detail in Fig. 3.13.

The absolute difference between the normalized time integrated and low-pass filtered and time integrated data are shown in the frequency–fringe frequency domain in Fig. 3.14. Some

of the RFI power along fringe frequency that is seen in Fig. 3.13 appears not to have been fully attenuated by time integration but has been suppressed by the 30 dB of additional filtering.

The output visibility data at the end of an AP is shown at the right of Fig. 3.14. It reveals that relative to neighbouring frequency channels that contain mostly attenuated noise there is still significant RFI leak into the  $\sim 0$  Hz fringe frequency in channels around the GPS carrier. The leak is attenuated by about 26 dB relative to merely time integration, but stands out because the neighbouring noise channels undergo a similar attenuation. This RFI leak is partly due to GPS modulation that spreads (un-)correlated RFI in fringe frequency, but it is also due to the cross-terms of RFI and noise. This effect was described in § 3.2.1, see Eqs. 3.2, 3.3.

The RFI suppression by VLBI fringe rate filtering is thus not quite as effective as one might assume from the 30 dB suppression of the main, high fringe rate RFI component. The modulation spread and the RFI–noise cross-terms degrade the effectiveness of this mitigation method.

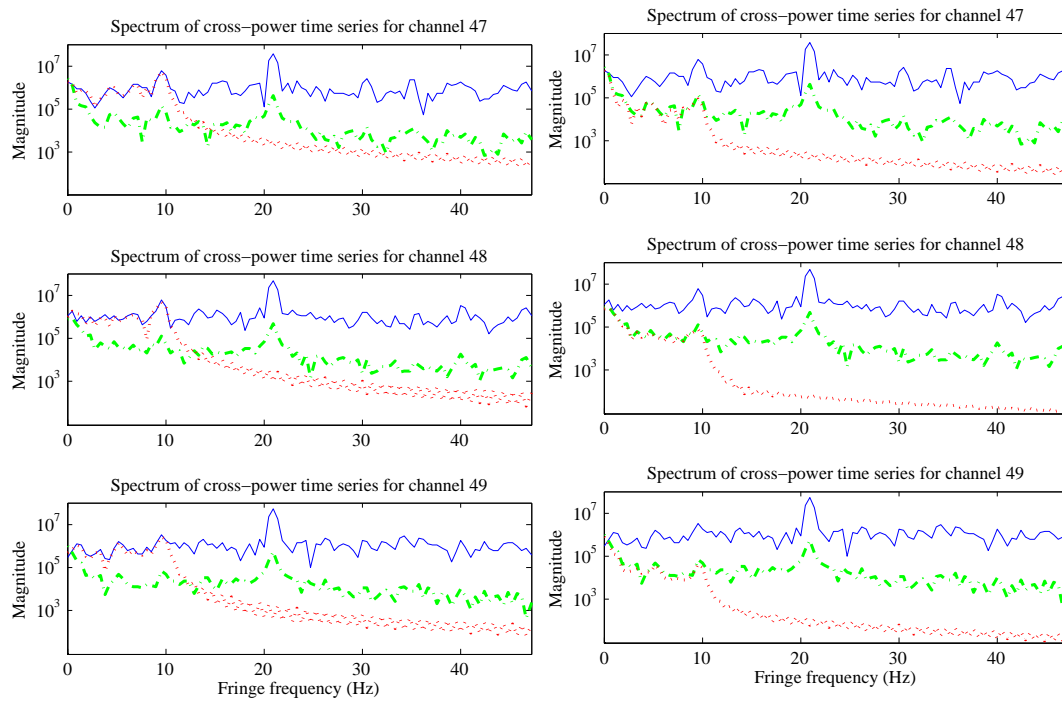


**Fig. 3.13:** The fringe frequency spectrum of the GPS L1 interferer in channels 47 to 49 out of 128 in the DiFX fringe stopped synthetic data (see Fig. 3.11). The GPS carrier is in channel 48 and the satellite has a fringe frequency of 22 Hz. The GPS signal spreads out in frequency and fringe frequency due to the C/A modulation. Channels 47 (top), 48 (middle), and 49 (bottom) are shown. The three panels on the left show the RFI fringe without processing (solid), after VLBI time integration (dash-dot), and after fringe rate filtering with a single precision 10 Hz Chebyshev IIR low-pass filter (dotted, left). The three panels on the right are otherwise identical, but the 10 Hz low-pass is followed by time integration of the filter output (dotted, right) and this attenuates the RFI fringe peak by an additional 30 dB compared to only VLBI time integration.

### 3.4 Fringe Rate Filter Tests and Results

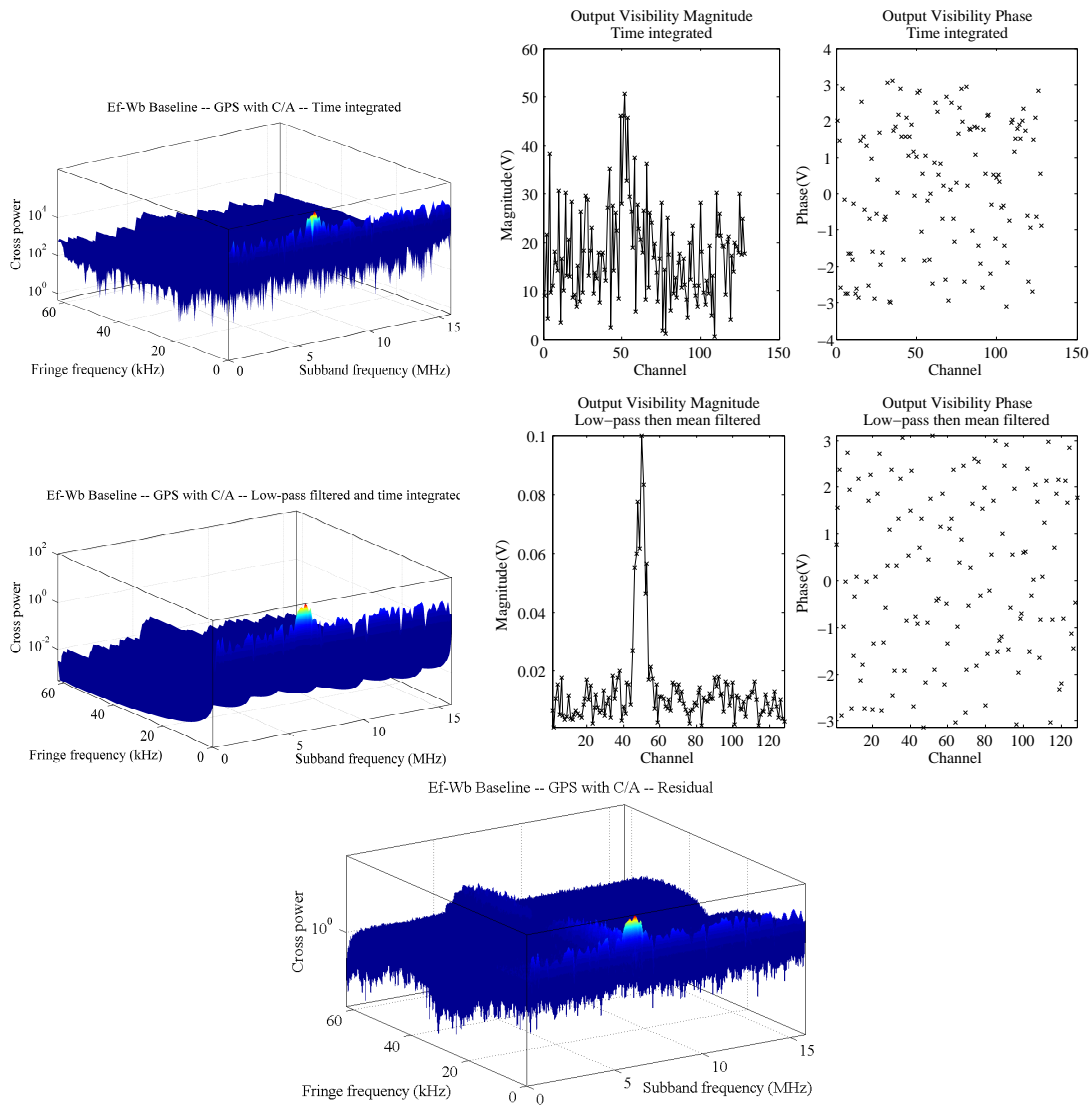


**Fig. 3.14:** The subband frequency–fringe frequency spectra and the output visibility data at the end of an AP for the synthetic 1.6 GHz VLBI experiment. The data are fringe-stopped in DiFX and were time-integrated (top), or filtered and time-integrated (middle) outside of DiFX. Modulated GPS RFI is centered on channel 48 out of 128 channels. The RFI is strongly attenuated by filtering (see Fig. 3.13). However, relative to the neighbouring channels with mostly noise, RFI leak into the  $\sim 0$  Hz range is still significant around channel 48. The leak is due to RFI modulation that spreads (un-)correlated RFI in fringe frequency, and is also due to the  $\text{RFI} \times \text{noise}$  terms, as described in § 3.2.1 (see Eqs. 3.2, 3.3). Top left: The fringe frequency spectrum after time integration i.e. mean filtering. Top right: The magnitude (in cross-power units) and phase (in radians) of the output integrated visibility data at the end of the AP. Middle left: The spectrum after 10 Hz low-pass filtering followed by time integration. Middle right: The magnitude and phase of the output filtered visibility data at the end of the AP. Bottom: The residual between the two spectra above after first normalizing each spectrum, showing that filtering does indeed suppress a wide range of RFI fringe frequencies above 10 Hz.

## 3.5 EVN VLBI Test Observation for RFI Mitigation

The practical performance of the VLBI RFI mitigation implemented in DiFX was also tested on data of a VLBI search for 1.6 GHz OH spectral lines, conducted under this thesis with the European VLBI Network (EVN). Two galaxies, Cygnus A and NGC 1068, were searched for OH in emission and absorption at the two main OH lines (with rest frequencies of 1665.4018 MHz and 1667.3590 MHz) and the two OH satellite lines (1612.2310 MHz and 1720.5299 MHz). The science goal was to find evidence of a parsec-scale obscuring torus at the center of these galaxies. The existence of a circumnuclear obscuring torus, key to the Seyfert unification scheme, has been suggested through molecular line detections in other active galaxies. For example, Sawada-Satoh et al. (2008) speculate that in NGC 1052 the torus may be traced out by the H<sub>2</sub>O maser emission detected close to a synchrotron self-absorbed nuclear region, while in Mrk 348 Simpson et al. (1996) and Peck et al. (2003) find that a torus might have been detected in OH and optical spectral lines. Molecular tori may have also been detected by Impellizzeri (2008) in the several single-dish OH detections towards NGC 4261 and other galaxies, some also detected in methanol lines. In our VLBI search for circumnuclear molecular tori, we expect OH to be seen in absorption against a strong radio core.

### 3.5.1 Source Selection

Three sources were proposed for the EVN VLBI search for OH molecules. The galaxy Cygnus A was a leading candidate in the search due to its edge-on orientation, Type 2 optical spectrum, large X-ray absorption, and the tentative detection of excited OH in absorption (Impellizzeri 2008). Hydra A was an equally good candidate that had not been observed due to the risk of encountering strong RFI – the GLONASS satellite band is within 3 MHz of the expected OH lines in Hydra A. The third source, NGC 1068, is a known OH kilomaser detected with the VLA (Gallimore et al. 1996). The OH detection has not yet been followed up with VLBI.

### 3.5.2 Sources

Out of the three proposed sources two were observed, namely Cygnus A and NGC 1068. The two sources are introduced below.

#### Cygnus A

The edge-on FR-II radio galaxy Cygnus A (3C 405) launches a twin-jet and shows strong X-ray absorption towards the nucleus (e.g., Young et al. 2002) with a type II optical spectrum indicating that the direct line of sight to the nucleus is blocked, possibly by a obscuring torus

### 3.5 EVN VLBI Test Observation for RFI Mitigation

posited by the Seyfert unification scheme. The redshift of  $z = 0.056075$  (Owen et al. 1997) translates to a recessional velocity of about  $16829 \text{ km s}^{-1}$  (LSR) and a distance of about 230 Mpc (Kerr & Lynden-Bell 1986) in the fiducial cosmology used by the the NASA/IPAC Extragalactic Database (NED). The scale on Cygnus A is about  $1132 \text{ pc}''$ . Even for a radio galaxy Cygnus A has very high flux densities at radio frequencies, e.g., about  $1300 \text{ Jy}$  at  $1.7 \text{ GHz}$  (Yaji et al. 2010).

The galaxy has a strong radio core against which OH absorption might readily be seen. In fact, in a 2 cm VLBI observation with the Very Long Baseline Array (VLBA) Impellizzeri (2008) tentatively detects absorption of OH in the excited state at  $13.424 \text{ GHz}$ . Impellizzeri finds a line width of  $90 \text{ km s}^{-1}$  full width at half maximum (FWHM) with a peak absorption of about  $-20 \text{ mJy beam}^{-1}$ , and a line profile suggestive of a diffuse OH distribution around the source, with OH most prevalent within 4 pc towards the central region. Perhaps surprisingly, however, an earlier  $1.6 \text{ GHz}$  Karl G. Jansky Very Large Array (VLA) A-array search for OH by Conway & Blanco (1995) did not detect OH in absorption nor in emission. Their VLA observation was affected by RFI and had a sensitivity of 12 to  $18 \text{ mJy beam}^{-1}$  in  $8.3 \text{ km s}^{-1}$  wide channels and had a  $1.3''$  synthesized beam. To provide a reference for the structure in the inner  $\sim 150 \text{ mas}$  of Cygnus A, three EVN VLBI images by Bach et al. (2002) are shown in Fig. 3.15. Bach et al. find the size of the brightest  $1.6 \text{ GHz}$  component to be less than  $10 \text{ mas FWHM}$ .

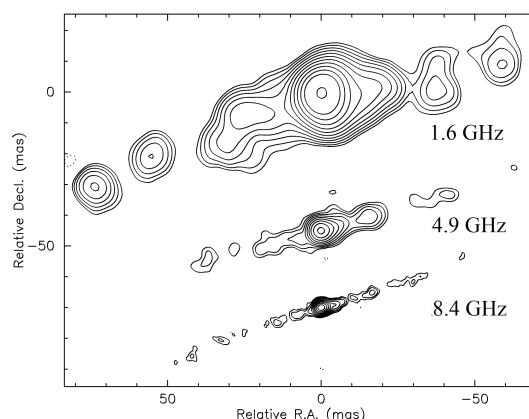


**Fig. 3.15:** The inner  $\sim 150 \text{ mas}$  of Cygnus A. The EVN VLBI images are adopted from Bach et al. (2002), see the Proc. 6th EVN Symposium 2002.

#### NC 1068

The nearby galaxy NGC 1068 is an archetypical Seyfert 2 galaxy. The redshift of NGC 1068 of  $z = 0.003793$  (Huchra et al. 1999) translates to a recessional velocity of about  $1126 \text{ km s}^{-1}$  LSR and a distance of about 12.5 Mpc (NED; Kerr & Lynden-Bell 1986). The scale is about  $70 \text{ pc}''$ . The galaxy has a more moderate L-band flux density, with a total flux density at  $1.4 \text{ GHz}$  of about  $4.9 \text{ Jy}$  (Condon et al. 2002). Gallimore et al. (1996) detect  $\text{H}_2\text{O}$  masers and find main-line OH kilomaser emission in a VLA A-array map taken in year 1994 (also see Gallimore et al. 2004, 1996). The OH maser spectrum has two spectral features, the first blueshifted by about  $-310 \text{ km s}^{-1}$ , the other redshifted by about  $+200 \text{ km s}^{-1}$ . The two features have equivalent isotropic luminosities of  $0.32 L_\odot$  and  $0.51 L_\odot$ , and peak flux densities of about  $5 \text{ mJy}$  and  $3 \text{ mJy}$



### 3.5 EVN VLBI Test Observation for RFI Mitigation

**Table 3.1:** Overview of the 1.6 GHz EVN VLBI experiment conducted on 2011 Feb 26.

Source	Time (UT)	Array	IF 1 (MHz)	IF 2 (MHz)	IF 3 (MHz)	IF 4 (MHz)
Cygnus A	02:00–15:20	EB, JB, (TR <sup>f</sup> ),	1527	1577 <sup>a</sup>	1629	1609 <sup>b</sup>
		ON, WB <sup>c</sup>	OH sat.	OH main	OH sat.	GLONASS
NGC 1068	15:20–19:00	EB, JB, (TR <sup>f</sup> ),	1606	1659	1714	1688 <sup>d</sup>
		(ON <sup>e</sup> ), WB, MC	OH sat.	OH main	OH sat.	Radiosonde

**Notes.** Col. 3: The telescopes are Effelsberg (EB), Jodrell Bank (JB/JB1), Torun (TR), Onsala (ON), the phased Westerbork telescope (WB), and Medicina (MC). Cols. 4–7: The IF center frequency. The expected signal in each IF is shown below, either an OH satellite line (OH sat.), or the OH main lines, or continuum with a potential RFI contamination. **Footnotes:** <sup>(a)</sup> Close to the GPS L1 carrier at 1575.42 MHz. <sup>(b)</sup> Covers the GLONASS satellite band of 1602 MHz to 1616 MHz. <sup>(c)</sup> WB joined at UT 03:10. <sup>(d)</sup> Covers the radiosonde band used by, e.g., weather balloons. <sup>(e)</sup> ON produced no fringes in the NGC 1068 part of the experiment. <sup>(f)</sup> Due to time stamp and recording issues about 50 % of TR data were corrupt.

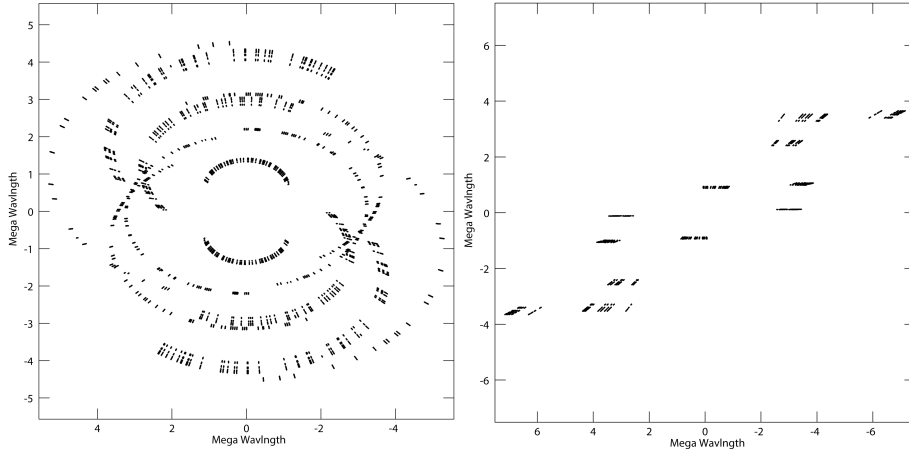


**Fig. 3.16:** The uv coverage on Cygnus A (left) and NGC 1068 (right) in the EVN VLBI experiment.

(see Table 1 and Fig. 2 in Gallimore et al. 1996). The VLA detection had a sensitivity of  $0.5 \text{ mJy beam}^{-1} \text{ rms}$  in  $35.5 \text{ km s}^{-1}$  wide channels with a  $1.4''$  beam. The two OH features were spatially unresolved by the VLA. Gallimore et al. associate both 1.6 GHz OH features with a single southern 22 GHz continuum component that is also detected in  $\text{H}_2\text{O}$  maser emission and in H $\alpha$  absorption, with similar Doppler velocity ranges. To date, there has been no high resolution VLBI follow-up on the OH emission region.

### 3.5.3 EVN VLBI Observation

The two sources were observed on 2011 Feb 26 at UT 02:00–19:00 in the EVN experiment EW014. The radio galaxy Cygnus A was observed with five EVN telescopes in the first part of the experiment (UT 02:00 to UT 15:20) and NGC 1068 was observed in the second part (UT 15:20 to UT 19:00), now with six stations included in the array. The frequency setup specified four frequency bands (IFs), dual polarization, and a 16 MHz IF bandwidth. The total data rate was 512 Mbps. Three of the IFs covered the redshifted OH lines. The fourth IF was centered on a potential RFI frequency, e.g., the GLONASS satellite band or the radiosonde band. The participating EVN telescopes and the IF frequency setups are provided in Table 3.1.

As NGC 1068 is an equatorial source with a zero declination the EVN uv coverage, shown in Fig. 3.16 for both sources, is a challenge. The poor uv coverage did not allow “proper” imaging of NGC 1068. In addition, both sources have significant extended structure. To calibrate the fluctuations in the atmospheric phase, the experiment was thus phase-referenced against compact and bright phase reference sources (quasars) located within  $3^\circ$  to  $10^\circ$  of each target source. At 1.6 GHz the atmospheric changes are relatively slow. A source-switching time interval of about 15 minutes was selected of which about 12 minutes were spent on the target and 3 minutes were spent on the reference quasar.

### 3.5.4 Correlation and Data Reduction

After an antenna clock offset and fringe search, the raw dual-polarization antenna data were correlated in half-Stokes on the MPIfR Bonn computing cluster. Antenna data were correlated with the standard DiFX version (“trunk DiFX”) and the new “RFI DiFX” version with an averaging period (AP) of 2.048 seconds, and 1024 channels for a resolution of  $\sim 2.8 \text{ km s}^{-1} \text{ channel}^{-1}$ . Different RFI filter configurations were tested. The final RFI DiFX run split the 2.048 s AP into the smallest possible number of sub-integrations, i.e. the longest possible sub-integration time (limited by the DiFX architecture and computer memory) with 4 sub-integrations of 0.512 s each, matched by a 2 Hz fourth-order elliptic IIR low-pass filter followed by time integration.

There were some issues with the experiment and effectively only four EVN telescopes provided reasonably good data. First, the high flux density of Cygnus A of about 1.3 kJy was problematic for the sensitive Effelsberg 100 m radio telescope (EB) L-band receiver. The system temperature,  $T_{\text{sys}}$ , was typically above 3000 K when EB was pointed towards Cygnus A (the nominal Effelsberg L-band gain is 1.4 K/Jy). Second, the Torun (TR) recordings had time stamp issues resulting in about 50 % data corruption. Third, Onsala (ON) produced no fringes in the second part of the experiment. Fourth, Westerbork (WB) joined an hour into the experiment and had a swapped polarization. The latter issue was minor and was corrected in the AIPS post-processing software (Bridle & Greisen 1994) with the AIPS task SWPOL before calibration.

The visibility data output by the trunk DiFX version were calibrated in AIPS following the approach in Diamond (1995). The first steps corrected antenna gains via  $T_{\text{sys}}$  and weather data. Instrumental delays and atmospheric phases were calibrated on the reference sources and were applied to the targets. This was followed by iterations between imaging the targets and phase self-calibrating the residual atmospheric phase using the latest image as the source model.

Because the station  $T_{\text{sys}}$  values on Cygnus A were generally quite high (JB:  $\gtrsim 1500$  K, EB:  $\gtrsim 3000$  K, WB:  $\gtrsim 700$  K, TR:  $\gtrsim 200$  K, ON:  $\gtrsim 170$  K), and also due to essentially a loss of TR (and later ON, too), the angular resolution was poorer and the achieved sensitivity was over a factor 100 worse than estimated. To recover some sensitivity the 1024-channel IF data on Cygnus A were averaged to 128 channels.

Most of the IFs contained broad or narrow RFI. Some RFI appeared to be local to the telescopes and was detected towards all sources, both the main and calibrator sources. The AIPS calibration tables were copied over from the trunk visibility data set to the RFI DiFX visibility data set for a comparison between the visibilities produced by trunk and RFI DiFX.

#### 3.5.5 Results and Conclusions

##### Performance of the Fringe Rate Filter in DiFX

The same effect as for synthetic data (e.g., Fig. 3.14 on page 45) was also found here – strong suppression of high fringe frequencies, yet in RFI-affected channels also a leak and elevated power relative to the neighbouring noise channels, due to reasons described in § 3.2.1, § 3.4.2.

A second effect was seen in DiFX: the filter did not have enough time to settle within the short sub-integration time interval. This is because of the data time-discontinuity in DiFX. DiFX segments a say 60 second raw recording into separate 1 s averaging periods that are processed in parallel on the computing cluster nodes. Raw data of the individual APs are further subdivided to allow an even higher degree of parallelism and faster processing. This is diametrically opposed to filtering that requires time-continuous input data.

The issue could not be worked around by extending the length of each sub-integration beyond 0.5 seconds as DiFX ran out of memory even on computing cluster nodes with a large main memory capacity. A representative comparison of trunk DiFX and RFI DiFX output data on NGC 1068 with interference in the IF 1 is shown in Fig. 3.17.

Compared to the good theoretical performance shown in the earlier sections, filtering in DiFX appears to be ineffective in practice – a completely different software correlator architecture would be needed to benefit from this RFI mitigation technique for VLBI.

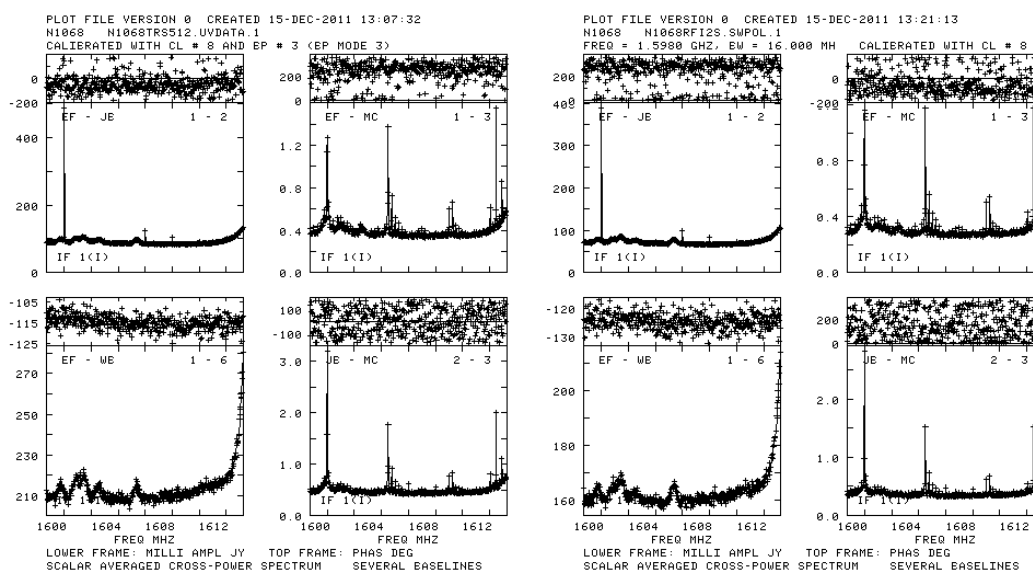


**Fig. 3.17:** Example of EVN visibility data on NGC 1068 produced by trunk and RFI DiFX. The full 2.5-hour scalar averaged cross-power spectra of IF 1 on some baselines are shown for trunk DiFX with time integration (four left-hand panels), and RFI DiFX with a 2 Hz 4th order IIR low-pass filter followed by time integration (four right-hand panels), with  $4 \times 0.512$  s sub-integrations. The AIPS calibration was copied from the trunk to the RFI DiFX data set, and a fixed phase offset due to the inserted IIR filter is seen. Amplitude ratios show that RFI filtering in DiFX appears to be ineffective for these data. Reasons are the DiFX architecture, sub-integrations too short for filter settling (i.e. changes in amplitudes due to filter group delay and filter amplitude peaking), and the lack of time continuity in data during correlation (as outlined in, e.g., § 3.3.2) which prevents efficient filtering.

### Cygnus A

The 1.6 GHz EVN continuum image of Cygnus A is shown in Fig. 3.18. It reached a sensitivity of  $3.0 \text{ mJy beam}^{-1}$  rms in Stokes I over the 64 MHz total bandwidth. The synthetic beam size was  $44.1 \times 26.7$  mas and the beam had a PA of  $-67^\circ$ . Several continuum components of sub-10 mas size are seen in the 1.6 GHz image of Bach et al. (Fig. 3.15) observed with the full EVN. In contrast in our observation with effectively four stations the central region was unresolved. A single  $231 \text{ mJy beam}^{-1}$  peak continuum component with a FWHM size of  $\sim 75$  mas was detected with an equivalent brightness temperature of about  $3 \times 10^7$  K. However, the flux density scale has a high uncertainty, estimated to be at least 20%, because the  $T_{\text{sys}}$  measurements used for gain (amplitude) calibration were contaminated by the dominant radio lobes of Cygnus A that are in the primary beam of the WB, ON and TR antennas.

To improve the single-channel sensitivity the visibility data were averaged to 64 output channels for roughly  $\sim 40 \text{ mJy beam}^{-1}$  rms in  $45 \text{ km s}^{-1}$  wide channels. This was not much better than the VLA A-array sensitivity in Conway & Blanco (1995) – their OH search achieved a sensitivity of  $\sim 15 \text{ mJy beam}^{-1}$  over  $8.3 \text{ km s}^{-1}$ , or about  $35 \text{ mJy beam}^{-1}$  over  $45 \text{ km s}^{-1}$ .

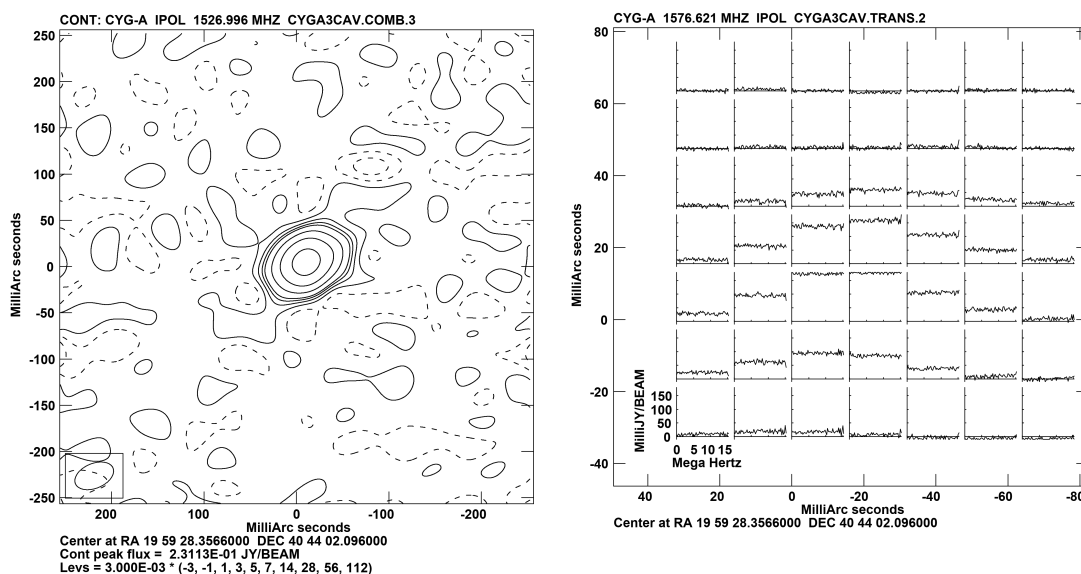


**Fig. 3.18:** The 1.6 GHz Stokes I image of Cygnus A (top left) averaged over the 4 IFs in Table 3.1. The beam size is  $44.1 \times 26.7$  mas with a  $-67^\circ$  PA. The peak flux density was  $231 \text{ mJy beam}^{-1}$  in Stokes I. The sensitivity was  $3.0 \text{ mJy beam}^{-1}$  rms over 64 MHz with 8.8 hours spent on-source. An example spectral line cube over regions of the continuum component illustrates the non-detection of OH main-line absorption and emission (top right). Other regions and smaller sky patches also produced a non-detection of the OH main and satellite lines at a  $3\sigma$  upper limit of about  $120 \text{ mJy beam}^{-1}$  rms in  $45 \text{ km s}^{-1}$  wide channels.

A search for OH in patches of the EVN VLBI spectral line data cube produced OH non-detections for all four OH lines. This sets loose  $3\sigma$  upper limits of  $120 \text{ mJy beam}^{-1}$  over  $45 \text{ km s}^{-1}$  for any OH emission and absorption in the inner 200 mas of Cygnus A.

The most robust finding here is that the EVN non-detection confirms the Conway & Blanco VLA A-array non-detection of OH, now with a factor of 30 higher spatial resolution.

## NGC 1068

The EVN data on the less radio-luminous galaxy NGC 1068 reached a comparably better sensitivity of  $0.15 \text{ mJy beam}^{-1}$  rms over the full 64 MHz bandwidth with a  $200 \text{ mas} \times 32 \text{ mas}$  beam. However, with practically four instead of six stations with usable data, the uv coverage problem (Fig. 3.16) was exacerbated in NGC 1068, as already indicated by the beam size. The continuum image, shown in Fig. 3.19, detected two out of the four components of the VLA A-array continuum image in Gallimore et al. (1996). By their absolute position we presume the two detected continuum components are associated with C and S1 of Gallimore et al. The OH main-line kilomaser emission detected by Gallimore et al. towards component S1 and the EVN spectrum over the same region are shown at the right of Fig. 3.19.

### 3.5 EVN VLBI Test Observation for RFI Mitigation

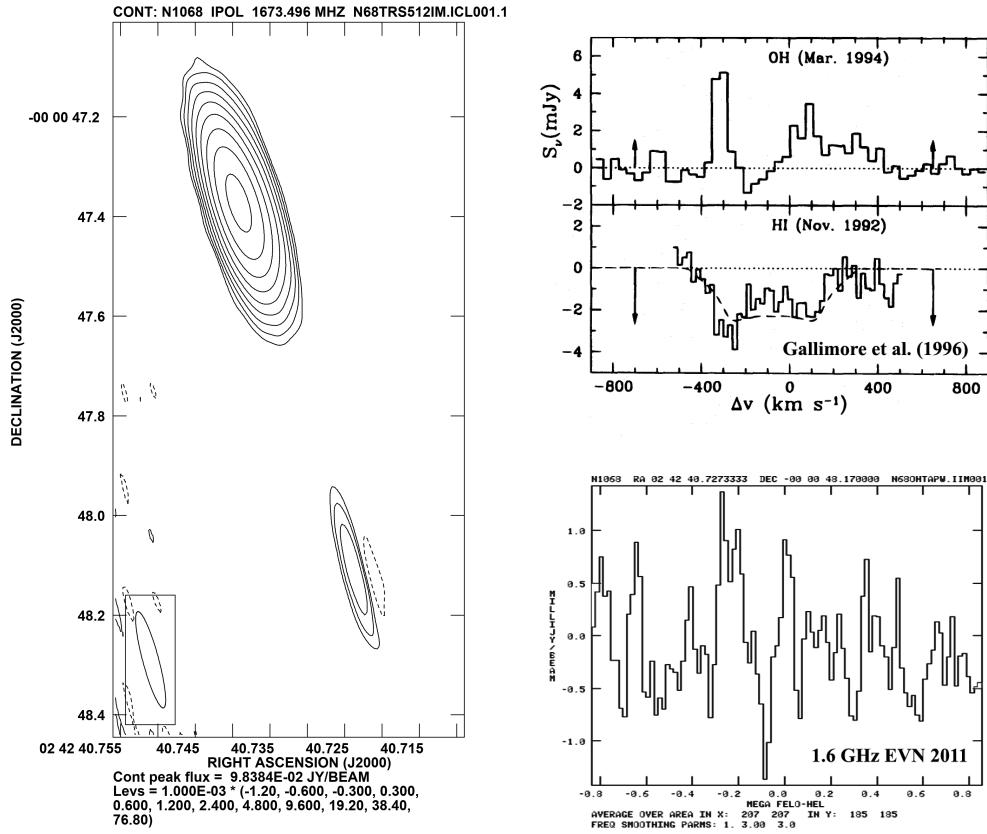


**Fig. 3.19:** The EVN 1.6 GHz VLBI continuum image of NGC 1068 (left), the VLA A-array spectrum towards the southern component showing the Gallimore et al. (1996) detection of main line OH emission with a 1.4'' beam, and their HI absorption (top right), and the 1.6 GHz EVN non-detection over the same component (bottom right). The EVN continuum image sensitivity is 0.15 mJy beam<sup>-1</sup> rms over 64 MHz and the smoothed EVN spectrum covers about 32 MHz with a sensitivity of about 1 mJy beam<sup>-1</sup> rms. The beam size is 200 mas × 32 mas with a 15° PA, or 14 × 2 pc given the scale on NGC 1068 of about 70 pc''.

The EVN observation produced a non-detection at about 1 mJy beam<sup>-1</sup> rms in ~13 km s<sup>-1</sup> wide channels. Although the EVN spectrum in Fig. 3.19 hints at possible emission and absorption lines with counterparts in the VLA spectrum, though blueshifted by about +50 km s<sup>-1</sup>, the respective flux densities are below the 3 $\sigma$  detection limit of 3 mJy beam<sup>-1</sup>. The EVN beam corresponds to 14 × 2 pc and it is unlikely that the OH maser regions were resolved out, as OH masing cloudlets in general may be <0.7 pc in size (Diamond et al. 1999). This leaves variability as the most plausible explanation of the non-detection, especially as the VLA-detected OH line peak flux densities were  $\leq$  5 mJy beam<sup>-1</sup>, comparable to the 3 $\sigma$  detection limit above.

## 3.6 Conclusions for VLBI RFI Mitigation in DiFX

The search for 1.6 GHz OH in Cygnus A and NGC 1068 produced non-detections in both galaxies, discussed above. A more detailed analysis of the continuum components is omitted here due to the low novel science output. The reader is instead referred to Wagner et al., in preparation.

The EVN experiment allowed to assess the performance of the VLBI RFI mitigation method as implemented in DiFX. Compared to the good theoretical performance demonstrated in earlier sections, filtering in DiFX turned out to be ineffective in practice – a completely different software correlator architecture would be needed to fully benefit from this RFI mitigation technique.

The architecture of a more “RFI filter -friendly” software correlator would be such that it processes individual antenna recordings (scans) in a time-continuous fashion. Parallel computation could be achieved not via time division, as currently in DiFX, but via processing entire scans in parallel, combined with parallel processing by frequency division (into IF’s and sub-bands) rather than splitting scans into averaging periods and sub-integrations.

The suggested architecture would help in two issues related to fundamental filter properties:

**Filter peaking:** Any filter started from a blank internal state (e.g., with zero initial values for the past inputs and outputs, see § 3.3.1) may peak after a certain time delay, manifested as a transient amplification of the near zero fringe frequency components, before the internal filter state settles to the characteristics of the input visibility data. Since DiFX processes antenna-pair data in chunks of sub-integrations, in parallel and in no specific time order, input visibility data may change radically between sub-integrations. The filter state must be reset to zero at the start of a sub-integration to avoid the past states from contaminating the output visibility data produced from the entirely new input visibility data. Due to this reset the filter output may then peak again. For continuous rather than time division processing the reset would not be necessary and there would be no (re-)peaking in the filter output visibility data.

**Filter group delay:** Any filter will introduce an additional group delay over the usual group delay of the time integrating filter (§ 3.3.3). In DiFX, the information contained in visibility data still “to appear” at the filter and time integration output, delayed and after the end of a sub-integration, would be lost as DiFX does not feed new data to the filter input after the sub-integration time ends. Several attempts at compensating the extra group delay did not produce good results. Such attempts, e.g. feeding the filter beyond the end of a sub-integration with samples from its own output, or with zero-valued samples, or with Gaussian noise samples, all added output amplitude offsets relative to the proper output visibility expected for continuous time processing. Without time division the above would be no problem, the filter and time integration would pass smoothly over the full scan, and no information would be lost. Compensating for the additional group delay in terms of uv plane coordinate shifts is relatively trivial and may be performed in, e.g., the AIPS task UVFXT by Garn et al. (2007).

### **3.6 Conclusions for VLBI RFI Mitigation in DiFX**

---

In conclusion, the VLBI RFI mitigation technique would be notably more effective and not toxic to the observation if the DiFX architecture were completely revised to perform scan-based division, frequency band division, and subband division, rather than time division, to achieve fast parallel processing.

Given the relatively good simulated performance, it may be worth to re-evaluate the RFI fringe rate low-pass filtering approach in other software correlators, or a future version of DiFX if the architecture is updated to allow time-continuous parallel data processing.



## 3.7 RFI Mitigation for Arrays

### 3.7.1 Array Coherence Matrix

How are spatial coherences  $V(u[n], v[n])$  measured in practice? The answer combines the expectation value in Eq. 2.1 and the digitized source signal recorded at each antenna.

The fringe-stopped digital signal stream  $x_i[t]$  of each antenna  $i$  is a sum of the source signal, noise, and RFI interference,

$$x_i[t] = s_i[t] + n_i[t] + i_i[t] \quad (3.6)$$

with respective signal powers,  $\sigma_{S,i}^2$ , and  $\sigma_{N,i}^2$ ,  $\sigma_{I,i}^2$ , that can vary between antennas (e.g., RFI reference antennas).

The signals  $x_i$  may be antenna voltage samples, or Fourier voltage samples taken from one bin (subband) of a time series of Fast Fourier Transforms (FFTs). A snapshot at time  $t$  of the samples of all  $N_{\text{ant}}$  antennas,

$$\vec{x}(t) = [x_1[t], \dots, x_{N_{\text{ant}}}[t]] \quad (3.7)$$

yields a complex covariance matrix that is an estimate of Eq. 2.1,

$$\mathbf{C}[t] \equiv \langle \vec{x}^H \vec{x} \rangle - \langle \vec{x} \rangle^H \langle \vec{x} \rangle \simeq \langle \vec{x}^H \vec{x} \rangle \simeq V(u[n], v[n]) \quad (3.8)$$

The complex conjugate transpose is denoted by  $\vec{x}^H$ . By its definition,  $\mathbf{C}$  is symmetric and Hermitian ( $\mathbf{C} = \mathbf{C}^H$ ). The samples  $\vec{x}$  are measured at the antenna locations and thus  $\mathbf{C}$  is also known as the spatial *array coherence matrix*. The expectation is that the source, noise, and interference signals are mutually temporal-spatially uncorrelated (as in Eq. 2.4) so that their cross-products vanish, yielding

$$\mathbf{C} = \mathbf{C}_S + \mathbf{C}_N + \mathbf{C}_{\text{RFI}} \simeq \mathbf{C}_S + \sigma_N^2 \mathbf{I} + \mathbf{C}_{\text{RFI}} \quad (3.9)$$

The observing time is limited before the  $(u[n], v[n])$  location of the baseline moves significantly due to Earth rotation or target motion. To retain a high coherence towards the target, matrix  $\mathbf{C}$  is estimated within a relatively short time interval,  $T_{\text{int}}$ , of a few 10 ms,

$$\mathbf{C}[t] = \frac{1}{M} \sum_m^M \vec{x}[t + m/f_s]^H \vec{x}[t + m/f_s] ; M = T_{\text{int}} f_s \quad (3.10)$$

The number of samples  $M$  in an averaging interval depends on the sampling rate  $f_s$ . Averaging

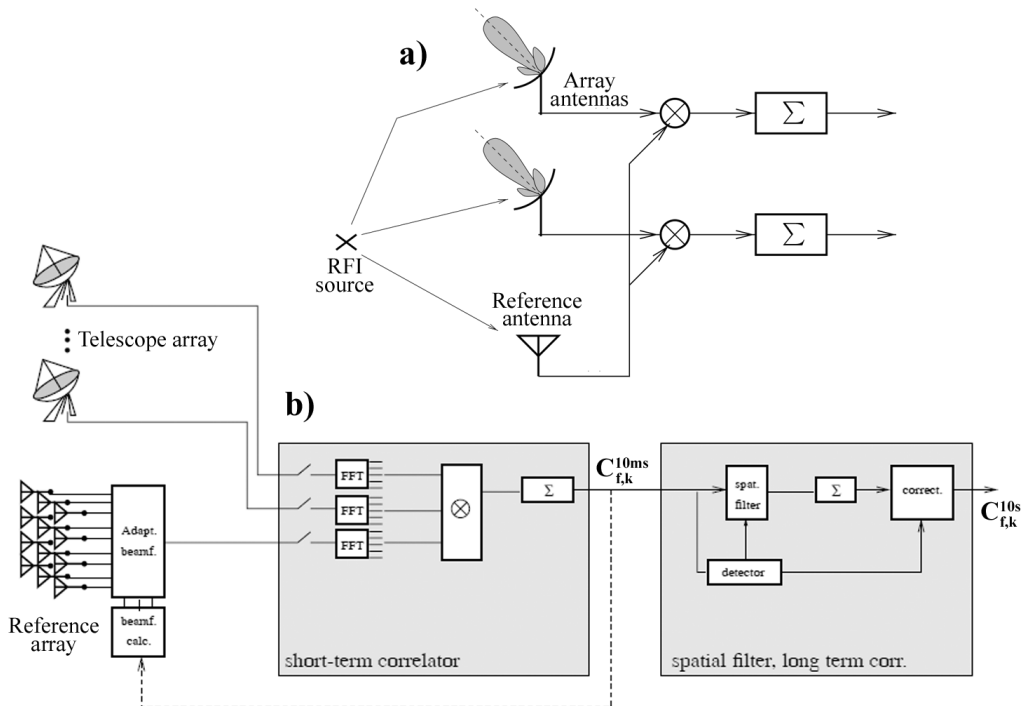


**Fig. 3.20:** A diagram of the antenna signals contributing to the array coherence matrix. Top: RFI enters the astronomical antennas through sidelobes and an RFI reference signal is received with one or more omnidirectional reference antennas. Bottom: The signals from all antennas (e.g., focal plane array, telescopes, reference antennas) are split into frequency subbands (FFT). Short-term integrated array coherence matrices,  $C_{f,k}^{10ms}$ , are formed for each subband via cross-correlation and averaging. Post-correlation RFI mitigation methods work on  $C_{f,k}^{10ms}$ . Figures adopted from Leshem et al. (2000).

can also be improved with the low-pass filter approach by Roshi & Perley (2003).

Array RFI mitigation uses the inverse  $C^{-1}$ , thus  $C$  needs to be invertible, or equivalently,  $C$  needs to have a full rank of  $N_{\text{ant}}$  (the rank of a matrix is defined as the number of linearly independent rows or columns of the matrix). To achieve a full rank at least  $M \geq N_{\text{ant}}$  samples must be included in the coherence matrix. Usually there is noise in the  $\vec{x}$  voltage data. Each sample is thus slightly different from earlier samples and increases the rank of a rank-deficient  $C$  by one. For example, an array of 64 antennas would require at least 64 samples for  $C$  to have full rank. Assuming 15.6 kHz subbands (an  $f_s$  of 31.2 kHz), this would correspond to an integration time of 2 milliseconds.

### 3.7.2 Mitigation of RFI Based on the Coherence Matrix

Similarly to source structure that is captured in the phases of the coherence matrix, any RFI signal impinging on the array inserts its own spatial (phase) footprint into  $\mathbf{C}$ , too.

An interferer can be mitigated if its footprint in  $\mathbf{C}$  can be removed. Several techniques exist that make use of the short-term ( $\lesssim 50$  ms) time-averaged coherence matrices  $\mathbf{C}[t]$ . An introduction can be found in, e.g., Section 6 of Briggs & Kocz (2005b).

The advantage of these methods is a typically good performance and that the RFI mitigation (nulling or subtraction) is done post-correlation, so one is not committed to the correction.

We implemented a common, simple yet powerful mitigation method in the DiFX RFI library, interferer nulling (e.g., Leshem et al. 2000; Briggs & Kocz 2005b; Kocz et al. 2010). When the spatial direction of the interferer is known, a null can be inserted into the array beam pattern, equivalent to a linear projection,  $\mathbf{P}^\perp$ , that projects out the subspace of  $\mathbf{C}$  that responds to the RFI footprint (e.g., Leshem et al. 2000; Switzer et al. 2013),

$$\mathbf{C}_{\text{clean}} = \mathbf{P}^\perp \mathbf{C} \mathbf{P}^\perp \quad \text{where} \quad \mathbf{P}^\perp = \mathbf{I} - \mathbf{A}(\mathbf{A}^H \mathbf{A})^{-1} \mathbf{A}^H \quad (3.11)$$

with  $\mathbf{A} : N_{\text{ant}} \times q$  being the expected signals (Eq. 3.7) and their phase differences that different antennas would see for signals arriving from the known directions of each of the  $q$  interferers.

If the RFI direction is unknown, one may assume RFI is the highest-power signal and locate it via a common factoring, e.g.,

$$\text{EVD} : \mathbf{C} = \mathbf{W} \mathbf{\Lambda} \mathbf{W}^H \quad (3.12)$$

$$\text{SVD} : \mathbf{C} = \mathbf{U} \mathbf{\Sigma} \mathbf{V}^H \quad (3.13)$$

where diagonal matrix  $\mathbf{\Lambda}$  (or  $\mathbf{\Sigma}$ ) contains the (real-valued) eigenvalues  $\lambda$ , and  $\mathbf{W}$  (or  $\mathbf{U}$  and  $\mathbf{V}$ ) contains the orthogonal eigenvectors that define the subspaces (or left and right subspaces) of  $\mathbf{C}$  in its eigenvalue decomposition (EVD), or singular value decomposition (SVD), respectively. For details see, e.g., Trefethen & Bau 1997, or § 6 of the overview given by Briggs & Kocz (2005b). The SVD tends to be numerically more stable in practice. For simplicity, we use the EVD here, and note the SVD approach is identical. A clean  $\mathbf{C}$  can be reconstructed from

$$\begin{aligned} \mathbf{C}_{\text{clean}} &= \mathbf{C} - \hat{\mathbf{C}}_{\text{RFI}} = \mathbf{W} \begin{bmatrix} \mathbf{\Lambda}_{11} & 0 \\ 0 & \mathbf{\Lambda}_{22} \end{bmatrix} \mathbf{W}^H - \hat{\mathbf{C}}_{\text{RFI}} \\ &= \mathbf{W} [(\mathbf{\Lambda}_S + \mathbf{\Lambda}_N + \mathbf{\Lambda}_{\text{RFI}}) - \hat{\mathbf{\Lambda}}_{\text{RFI}}] \mathbf{W}^H \end{aligned} \quad (3.14)$$

where the partitioning into  $\mathbf{\Lambda}_{11}$  and  $\mathbf{\Lambda}_{22}$  separates RFI and signal subspaces, respectively. The

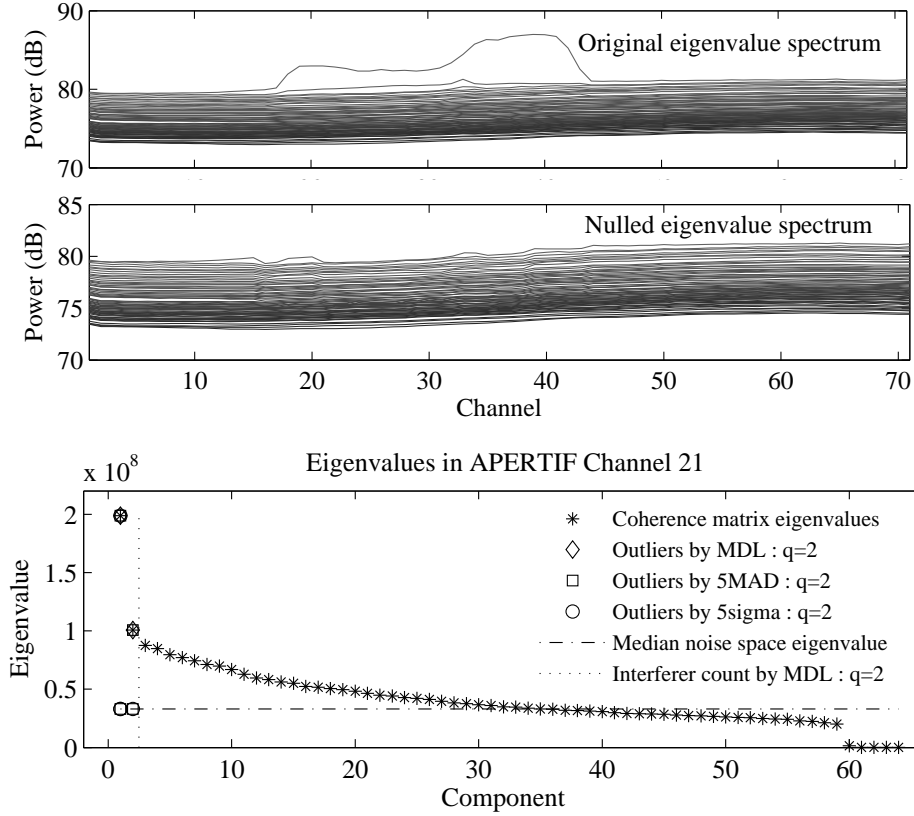


**Fig. 3.21:** The coherence matrix eigenvalue spectrum and RFI “nulling” of the 1.49 GHz 64-element APERTIF PAF data on Virgo A. Top: The eigenvalue spectrum (1.4830-1.4967 GHz) with 64 eigenvalues per channel, before nulling of the AfriStar interference. Middle: The eigenvalue spectrum after nulling. Bottom: The RFI eigenvalue detection in channel 21 out of 71. The trailing zero eigenvalues are due to inactive PAF antenna elements. The three methods for estimating interferer count  $q$  detected 2 interferers. The RFI eigenvalues are replaced with the median (circles) of non-RFI eigenvalues for later reconstruction of a clean coherence matrix, see also Fig. 3.22.

estimated RFI coherence matrix  $\hat{\mathbf{C}}_{\text{RFI}}$  has eigenvalues  $\hat{\Lambda}_{\text{RFI}}$ . For  $q$  interferers the submatrices are

$$\mathbf{\Lambda}_{11} : (q \times q) \approx \text{diag}(\sigma_{I,1}^2 + \sigma_{N,1}^2, \dots, \sigma_{I,q}^2 + \sigma_{N,q}^2) \quad (3.15)$$

$$\mathbf{\Lambda}_{22} : (N_{\text{ant}} - q) \times (N_{\text{ant}} - q) \approx \text{diag}(\sigma_{N,N_{\text{ant}}-q}^2, \dots, \sigma_{N,N_{\text{ant}}}^2) \quad (3.16)$$

where the source signal is assumed to be comparable to the instrumental noise power and weaker than the RFI and is thus omitted. The  $q$  RFI eigenvectors in  $\mathbf{W}$  contain the phase shifts (or geometric delays) at which the RFI was detected at the array antennas (similar to  $\mathbf{A}$  in Eq. 3.11). Using the known antenna positions, the unknown spatial directions of the  $q$  interferers can be estimated (see, e.g., Schmidt 1986; Chellappa & Theodoridis 2013).

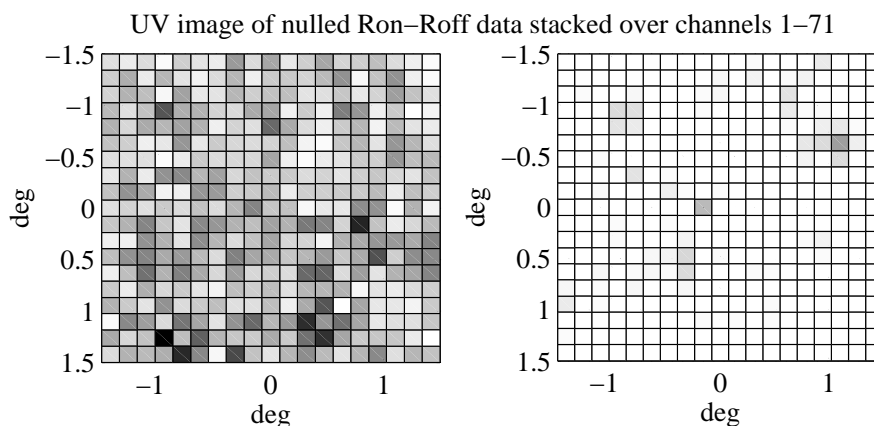


**Fig. 3.22:** The result of “nulling” RFI in 1.49 GHz APERTIF PAF data of Virgo A. The difference of the coherence matrices measured towards Virgo A and the blank sky was uv gridded, averaged over all 71 frequency channels, and imaged. Left: The original coherence matrix data after uv gridding and imaging, with an image rms  $\sigma = 3.99$ . Right: An image of the “nulled” coherence matrix,  $\sigma = 1.11$ , with Virgo A at  $\sim(0^\circ, 0^\circ)$ . The field of view is  $\pm 1.5^\circ$ . The WSRT main dish  $f/D = 0.35$ ,  $D = 25$  m, subtends  $\pm 55^\circ$  and the point source at  $(1.1^\circ, -0.7^\circ)$  is likely wide-band RFI in WSRT spill-over. After nulling the SNR on Virgo A increased by a factor 1.12 and the spill-over RFI INR by a factor 2.25.

When the power of the astronomical signal is comparable to or below the noise power of the instrumental noise floor, and when the interference to noise power ratio (INR), defined as (e.g., Kesteven 2003)

$$INR = \sigma_{I,i}^2 / \sigma_{N,1}^2 \quad (3.17)$$

is relatively high ( $INR \gtrsim 5$ ), it becomes possible to detect the number eigenvalues,  $q$ , that are significantly above the noise floor and likely represent RFI. One robust statistic estimator for the interferer count  $q$  is the Minimum Description Length (MDL; Rissanen et al. 1978),

$$q = \arg \min_{k \in [0, N_{\text{ant}} - 1]} L(\Lambda|k) \quad (3.18)$$

where the likelihood

$$L(\Lambda|k) = -M(N_{\text{ant}} - k) \cdot \ln \frac{(\prod_{i=k}^{N_{\text{ant}}-1} \lambda_i)^{\frac{1}{N_{\text{ant}}-k}}}{\frac{1}{N_{\text{ant}}-k} (\sum_{i=k}^{N_{\text{ant}}-1} \lambda_i)} + \frac{1}{2}k(2N_{\text{ant}} - k + 1) \cdot \ln M \quad (3.19)$$

is expressed as a ratio of the geometric and arithmetic means of the  $k$  largest eigenvalues, cor-

rected by the number of averaged samples,  $M$ , used in Eq. 3.10. The above likelihood determines the number of signals in Gaussian noise (e.g., Wax & Kailath 1985). Other statistical methods include the Akaike information criterion (AIC) or the Bayesian information criterion (BIC), also see Wax & Kailath (1985), and eigenvalue outlier detection using a limit of five standard deviations ( $5\sigma$ ), or a more robust limit of five median absolute deviations ( $5\text{MAD}$ ).

In all of the above methods (implemented also in the source code library), the number of interferers must be less than half the number of antennas ( $q < N_{\text{ant}}/2$ ).

An RFI-cleaned coherence matrix can be constructed by replacing the detected  $q$  outliers in the original eigenvalue matrix with zero, or with the median of  $\Lambda_{22}$  (Leshem et al. 2000). We found median replacement performs better, as it attenuates RFI to the noise floor, and retains some of the noise and source information that is mixed in on the “RFI” eigenvectors (i.e.,  $N_{\text{ant}}$  eigenvectors are insufficient to separate the full  $2N_{\text{ant}} + q$  noise, source, and RFI terms, hence the “RFI” eigenvectors contain a mix of these other signals).

An example of nulling in APERTIF phased array feed (PAF; Oosterloo et al. 2010) data is shown for 1.4 GHz test data that were provided by van Cappellen (private comm.). The PAF was located in the focus of one WSRT dish, and was tracking Virgo A in a  $3^\circ \times 3^\circ$  field of view. The observed band of 1.4830 GHz to 1.4967 GHz contained wide-band interference by the AfriStar digital radio satellite (ETSI EN 302 550-1-3). The detection of the interferer count  $q$  in one of the 71 subbands is shown in the bottom panel of Fig. 3.21 and the eigenvalue spectra of the 71 subbands before and after nulling are shown in the top panels. The respective gridded, frequency averaged and imaged array coherence data are shown in Fig. 3.22.

The simple nulling method that we implemented in the DiFX RFI library was successful at removing the strongest RFI contamination and recovered the source in the image center (Fig. 3.22). However, probable low-level interference from spill-over, with a flux density similar to the 140 Jy of the Virgo A target (Dunn et al. 2010), could not be removed. Residual RFI in the nulled image is seen in the form of additional faint sources that have no sky counterpart. The point source near  $(1.1^\circ, -0.7^\circ)$  is found in AfriStar-free channels of the original and nulled data. This low-level RFI signal probably enters the PAF elements from outside the main dish and through the sidelobes.

#### 3.7.3 Reference Antenna Method

Low-level interference can be mitigated if the array includes RFI reference antennas, e.g. omnidirectional antennas, that are not sensitive to the astronomical source. With reference and array

antennas we may partition the coherence matrix as follows:

$$\begin{aligned} \mathbf{C} &= \begin{bmatrix} \mathbf{C}_{rr} & \mathbf{C}_{ra} \\ \mathbf{C}_{ar} & \mathbf{C}_{aa} \end{bmatrix} \quad \text{where} \quad \mathbf{C}_{aa} = \mathbf{C}_S + \mathbf{C}_N + \mathbf{C}_{\text{RFI}} \\ &= \begin{bmatrix} \mathbf{A}_{\text{ref}} \mathbf{A}_{\text{ref}}^H + \sigma_{N,\text{ref}}^2 \mathbf{I} & \mathbf{A}_{\text{ref}} \mathbf{A}_{\text{arr}}^H \\ \mathbf{A}_{\text{arr}} \mathbf{A}_{\text{ref}}^H & \mathbf{C}_S + \sigma_{N,\text{arr}}^2 \mathbf{I} + \mathbf{A}_{\text{arr}} \mathbf{A}_{\text{arr}}^H \end{bmatrix} \end{aligned} \quad (3.20)$$

where the coherence between the  $n$  reference antennas is  $\mathbf{C}_{rr} : n \times n$ , between the reference and array is  $\mathbf{C}_{ar} : (N_{\text{ant}} - n) \times n$ , and between array antennas is  $\mathbf{C}_{aa} : (N_{\text{ant}} - n) \times (N_{\text{ant}} - n)$  as before. The signal snapshots for the array,  $\mathbf{A}_{\text{arr}} : (N_{\text{ant}} - n) \times q$ , and reference antennas,  $\mathbf{A}_{\text{ref}} : q \times (N_{\text{ant}} - n)$ , contain only the  $q$  interferer signals (i.e, matrix  $\mathbf{A}$  contains, side by side,  $q$  different signal vectors  $\vec{x}$ , and each  $\vec{x}$  is as in Eq. 3.7). Internal noise powers are initially assumed to be uniform, with  $\sigma_{N,\text{ref}}^2 \cong \sigma_{N,\text{arr}}^2$ .

For RFI mitigation, an estimate of the interference term  $\mathbf{C}_{\text{RFI}} = \mathbf{A}_{\text{arr}} \mathbf{A}_{\text{arr}}^H$  is needed. This ‘‘RFI template’’ can be subtracted from the coherence data of the main antenna array.

$$\mathbf{C}_{\text{clean}} = \mathbf{C}_S + \sigma_{N,\text{arr}}^2 \mathbf{I} = \mathbf{C}_{aa} - \mathbf{A}_{\text{arr}} \mathbf{A}_{\text{arr}}^H \quad (3.21)$$

The template can be expressed through the other submatrices,

$$\begin{aligned} \mathbf{A}_{\text{arr}} \mathbf{A}_{\text{arr}}^H &= \mathbf{A}_{\text{arr}} \left( (\mathbf{A}_{\text{ref}}^H \mathbf{A}_{\text{ref}}^H)^{-1} (\mathbf{A}_{\text{ref}}^{-1} \mathbf{A}_{\text{ref}}) \right) \mathbf{A}_{\text{arr}}^H \\ &= \mathbf{A}_{\text{arr}} \mathbf{A}_{\text{ref}}^H (\mathbf{A}_{\text{ref}} \mathbf{A}_{\text{ref}}^H)^{-1} \mathbf{A}_{\text{ref}} \mathbf{A}_{\text{arr}}^H \\ &= \mathbf{C}_{ar} (\mathbf{A}_{\text{ref}} \mathbf{A}_{\text{ref}}^H)^{-1} \mathbf{C}_{ra} \end{aligned} \quad (3.22)$$

$$\cong \mathbf{C}_{ar} (\mathbf{A}_{\text{ref}} \mathbf{A}_{\text{ref}}^H + \sigma_{N,\text{ref}}^2 \mathbf{I})^{-1} \mathbf{C}_{ra} = \mathbf{C}_{ar} \mathbf{C}_{rr}^{-1} \mathbf{C}_{ra} \quad (3.23)$$

The approximation for Eq. 3.22 holds if the interference to noise ratio (INR) in the reference antennas is high. The noise  $\sigma_{N,\text{ref}}^2 \mathbf{I}$  in  $\mathbf{C}_{rr}$  guarantees that it is always invertible, even for  $q < n$ , including the interference-free case. Thus the pseudo-inverse  $\mathbf{C}_{rr}^\dagger$  given by van der Veen & Boonstra (2004) for Eq. 3.23 can be replaced by  $\mathbf{C}_{rr}^{-1}$ . The final cleaned coherence estimate is

$$\text{‘‘VB04’’} : \quad \mathbf{C}_{\text{clean}} = \mathbf{C}_{aa} - \mathbf{C}_{ar} \mathbf{C}_{rr}^{-1} \mathbf{C}_{ra} \quad (3.24)$$

Noise on the diagonal of  $\mathbf{C}_{rr}^{-1}$  decreases the accuracy of the ‘‘template’’. When reference antennas are increasingly noisy, the performance of the van der Veen & Boonstra (2004) template (Eq. 3.23) degrades. It fails completely at an INR below about 10.

A special case with  $q \leq 1$  interferers and  $n = 2$  reference antennas is covered by Briggs et al.

(2000) using phase closure,

$$\text{“BK00” : } C_{\text{clean},i,j} = C_{i,j} - \frac{C_{i,1}^* C_{1,2} C_{j,2}}{C_{1,2}^* C_{1,2} + \sigma_{N,i,j}^4} \quad (3.25)$$

where the indices of the reference antennas are 1 and 2, and  $\sigma_{N,i,j}^4$  is some small number, e.g. the squared estimate of the uncertainty in cross-powers due to finite time averaging. The method by Briggs et al. provides better cancellation than Eq. 3.24 and is less sensitive to noise.

An improvement presented here for the general method is to replace  $C_{\text{rr}}^{-1}$  of Eq. 3.24 with an estimate derived from  $C_{\text{ra}}$  so the template is less affected by array-unrelated noise.

$$\text{“W14A” : } C_{\text{clean}} = C_{\text{aa}} - C_{\text{ar}}(C_{\text{ra}}C_{\text{aa}}^{-1}C_{\text{ar}})^{\dagger}C_{\text{ra}} \quad (3.26)$$

and after some algebraic manipulation,

$$\text{“W14B” : } C_{\text{clean}} = C_{\text{aa}} - (C_{\text{ar}}C_{\text{ar}}^{\dagger})C_{\text{aa}}(C_{\text{ar}}C_{\text{ar}}^{\dagger})^{\text{H}} \quad (3.27)$$

$$= C_{\text{aa}} - PC_{\text{aa}}P^{\text{H}} \quad (3.28)$$

where  $C_{\text{ar}}^{\dagger}$  is the left pseudoinverse of  $C_{\text{ar}}$ . The large inverse  $C_{\text{aa}}^{-1}$  is avoided in “W14B”, improving the numerical accuracy. The two methods allow for low INR interferers to be removed.

In principle, both the “nulling” and reference antenna methods can be applied to local array and VLBI array coherence data (and this has in fact already been suggested by Kesteven 2003). Both techniques are post-correlation steps and thus the technique that provides the best mitigation outcome may be selected by manual trial and without significant computational effort.



## 3.8 Array RFI Mitigation Tests and Results

### 3.8.1 Actual Array Data: APERTIF Phased Array Feed

The first test data set, APERTIF PAF 1.4 GHz test data on Virgo A, was obtained from W. van Cappellen (private comm.) in the form of time averaged array coherence matrices produced by the LOFAR backend<sup>1</sup> that was attached to the APERTIF tile. The test data set was processed with the eigenspace interferer detection and traditional “nulling” techniques of § 3.7.2 that are implemented in the Matlab mitigation scripts listed in Appendix A.2. The results from Matlab were consistent with the results produced by the DiFX C++ library.

As already mentioned in the details given on page 61, nulling of the AfriStar satellite interference that contaminated the APERTIF snapshot was successful (Figs. 3.21 and 3.22). Unfortunately there was no RFI reference antenna available to test the advanced RFI template subtraction. Instead, an attempt was made to designate any of the 64 antenna elements within APERTIF itself as the RFI reference antenna and then apply the two existing methods (Eqs. 3.24 and 3.25) and the two improved methods (Eqs. 3.26 and 3.27) to identify and subtract the RFI signature from the array coherence matrix.

Accounting for the fact that all of the APERTIF antenna elements were sensitive to the astronomical signal, and the explicit assumption of the subtraction methods that the RFI reference antenna(s) must not be sensitive to the astronomical source, it was not surprising that all four subtraction methods produced subjectively extremely poor results in comparison to “nulling”.

This suggests that at least for APERTIF-like focal plane arrays an external RFI reference antenna is necessary, and array-internal elements are not suitable. Traditional “nulling” was successful. However, in the time frame of this thesis no APERTIF-like focal plane array nor suitable backend were available at Effelsberg to carry out additional test observations.

### 3.8.2 Actual Array Data: Effelsberg $\lambda 21$ cm 7-beam Receiver

The dual-polarization  $\lambda 21$  cm 7-beam receiver at the Effelsberg radio telescope (e.g., Ruiz et al. 2005) is used in HI and pulsar surveys and in radar tracking of space debris. The astronomical observations are regularly affected by narrow- and broad-band RFI, and the current approach to interference mitigation is temporal blanking and subband excision which discard all contaminated data (Flöer et al. 2010; Kerp et al. 2011).

A test data set was obtained from B. Winkel and R. Karuppusamy (private comm.) to judge whether future observations with this receiver could benefit from advanced RFI mitigation. The data were a 10 minute observation of the radio pulsar PSR B0355+54. This pulsar has a period of 0.1563 seconds and a dispersion measure of  $57.1420 \text{ pc cm}^{-3}$  (Taylor et al. 1993). Spectrograms

<sup>1</sup>A polyphase filterbank backend used by the Low Frequency Array (LOFAR)

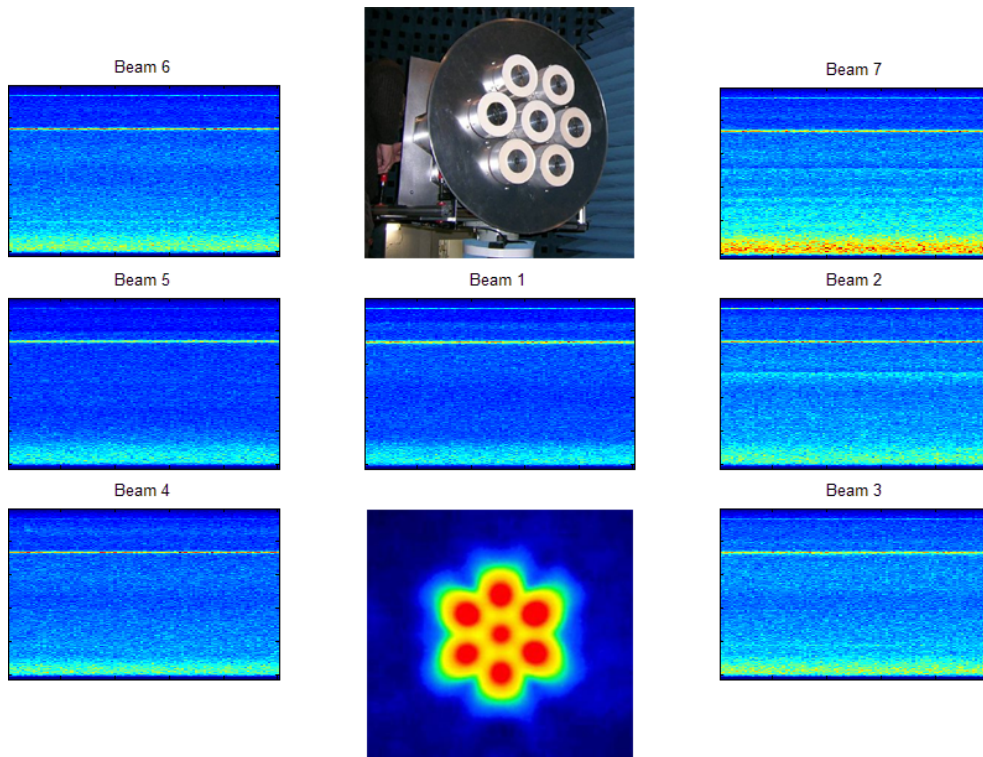


**Fig. 3.23:** The Effelsberg  $\lambda 21$  cm 7-beam dual-polarization receiver (top middle), the combined beam pattern (bottom middle), and 300 MHz wide spectrograms from individual beams. The bandwidth of the receiver is 240 MHz but is oversampled to 300 MHz by the backend.

from the beams are shown in Fig. 3.23. They demonstrate narrow-band RFI in all of the beams with no immediately visible spectral signature of the pulsar. The pulsar was detected strongly even without dedispersion after temporal folding of 64 pulsar periods.

Detailed inspection of the test data revealed that the Effelsberg 7-beam receiver system is not suitable for RFI mitigation (in the sense of recovering some rather than discarding all data). The 7-beam setup and the issue for interference mitigation are as follows. First, each individual beam signal with a bandwidth of 240 MHz is oversampled to 300 MHz and this is then split into 512 spectral channels in the FFTS spectrometer backend (Stanko et al. 2005). The spectrometer backend works in Stokes I total power mode and discards all signal phase information. The fastest spectrometer dump cycle is  $54 \mu\text{s}$ , equal to the rate of the test data, and it corresponds to 32 input spectra averaged to one output spectrum. Further, each segment of the FFTS operates only on its own beam. FFTS thus produces seven independent Stokes I spectra, without any cross-beam data, and outputs a new set of spectra every  $54 \mu\text{s}$ .

The FFTS hardware architecture was reviewed and was found not to be flexible enough

to calculate the cross-beam coherence matrices required for RFI mitigation. While work is in progress in the MPIfR pulsar group to have a more versatile 7-beam backend, and even a new focal plane array, these projects did not complete in the time frame of this thesis.

An attempt was nevertheless made to recover some phase information from the FFTS data. Beam cross-power matrices were formed in each FFTS channel by taking a 1-D Fourier transform along the time direction and cross-multiplying these Fourier data between beams. This produced a  $7 \times 7$  cross-beam “coherence matrix” for each of the 512 spectral subbands. However, the approach did not succeed at recovering sufficient spatial phase information and consequently the RFI mitigation algorithms were not able to separate RFI from the astronomical signal. The main issue appeared to be the loss of phase coherence between the 7 beams, stemming from the total power time integration in the FFTS spectrometer. Phase information is only retained if the cross-beam stage precedes time integration, and not vice versa.

In conclusion, neither “nulling” nor reference antenna -based mitigation of interference in Effelsberg  $\lambda 21$  cm 7-beam data was possible. Incidentally, the same was also true for the K-Band Focal Plane Array and the GBT Spectrometer installed at the Green Bank Telescope that are technically quite similar to the Effelsberg 7-beam receiver and FFTS spectrometer.

After Effelsberg hardware upgrades the advanced RFI mitigation techniques can also be applied in practice in the future.

### 3.8.3 Simulations with Synthetic Array Data

In anticipation of more versatile backends in Effelsberg in the future, the performance of the four reference antenna -based interference mitigation approaches (Eqs. 3.24 to 3.27) was assessed in simulations with synthetic 1.48 GHz array coherence data.

#### Geometric Model for Synthetic Data

An array geometry identical to the APERTIF PAF was selected. The 64 antenna elements were laid out as an uniform  $8 \times 8$  grid (Fig. 3.24) and two or more RFI reference antennas were placed near the array. The positions of the reference antennas were not critical.

The coherence data were derived for a point source model that approximates the astronomical source and the interferer by several point sources. The point sources are defined by their position on the sky,  $\theta_i$  and  $\phi_i$ , in angular co-

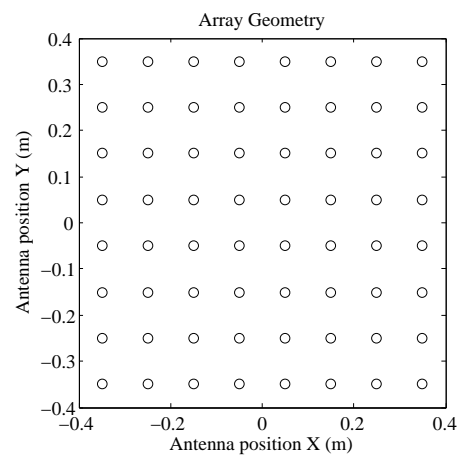


**Fig. 3.24:** The geometry of the simulated uniform 64-antenna array.

ordinates off the antenna array zenith. The coordinates of each point source are equal to the direction of propagation, relative to the array, of the plane wave emitted by the point source. The plane wave is characterized by its wave vector,

$$\vec{k}_i = \frac{2\pi}{\lambda} [\sin(\theta_i) \cos(\phi_i) \quad \sin(\theta_i) \sin(\phi_i) \quad \cos(\theta_i)] \quad (3.29)$$

The positions of the antenna elements in the uniform grid are  $\vec{r}_1$  to  $\vec{r}_{N_{\text{ant}}}$ , expressed in wavelengths. The orientation of the impinging plane wave relative to the array plane produces different geometric propagation delays to different array elements. Assuming the plane wave has an amplitude,  $A_i$ , in some convenient units, the signal picked up at the antenna locations is

$$\vec{x}_i = A_i \cdot \left[ e^{-j\vec{k}_i \cdot \vec{r}_1} \quad e^{-j\vec{k}_i \cdot \vec{r}_1} \quad \dots \quad e^{-j\vec{k}_i \cdot \vec{r}_{N_{\text{ant}}}} \right] \quad (3.30)$$

and when all point sources in the model are considered, their sum at the antenna locations is

$$\vec{x} = \sum \vec{x}_i \quad (3.31)$$

The array coherence matrix,  $\mathbf{C}$ , was computed for this multiple point source model using Eq. 3.10. Two types of noise were added to the coherence matrix: uncorrelated antenna-based noise, and residual noise that mimics the effects of finite integration time and sensitivity. In addition, as the array and reference antennas have different characteristics in practice, the synthetic model allowed different levels of array antenna noise and reference antenna noise. The strength of the interfering signal was also adjustable, such that the interferer amplitude was allowed to be lower or higher in the array antennas compared to the reference antennas, with different INR ratios in the array and reference antennas.

The model parameters are:

$N_{\text{ant}}$  The total number of array and reference antennas.

$\sigma_{S,i}^2, \theta_i, \phi_i$  The signal power and direction of the astronomical point source(s) as seen by the array antenna elements. The power level corresponds to  $A_i$  above.

$\sigma_{\text{RFI,arr},i}^2, \theta_i, \phi_i$  The signal power and direction of the point source interferer(s) as seen by the array antenna elements. The power level corresponds to  $A_i$  above.

$\sigma_{\text{RFI,ref},i}^2, \theta_i, \phi_i$  The signal power and direction of the point source interferer(s) as seen by the reference antennas.

$\sigma_{N,\text{arr}}^2$  The receiver noise power level of the array antenna element receivers.

$\sigma_{N,\text{ref}}^2$  The receiver noise power level of the reference antenna receivers.

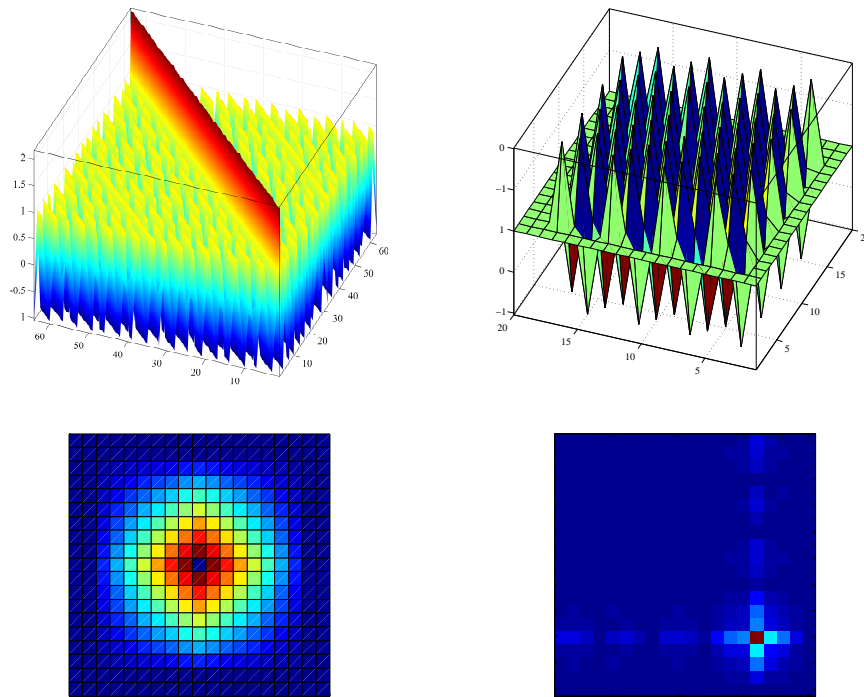


**Fig. 3.25:** An example synthetic array coherence matrix showing the response of a 64-antenna array to a point source. Top left: The real part of the complex-valued array coherence matrix. Top right: The real part of the uv plane data after uv gridding. Bottom left: The synthesized beam. Bottom right: The imaged uv plane data showing the full sky over the synthetic array. The sinc-type ringing around the point source is due to the Fourier transform and the geometric boxcar shape of the array.

$\sigma_C^2$  The residual Gaussian zero-mean complex-valued noise added to the array coherence matrix to mimic the effects of a finite time integration and finite sensitivity.

The coherence matrix produced by the model and the geometry of the array can be used to image the spatial distribution of the source and interferer point sources. The matrix elements, i.e. baseline visibilities, are first placed onto a uv plane grid at the respective uv location,  $(u, v)$ , of each baseline. The complex conjugates of the visibilities are placed at the opposing uv locations,  $(-u, -v)$ . The gridded uv data are Fourier transformed to yield an image. An example of the array coherence matrix, the gridded uv data, and the resulting beam and image is shown in Fig. 3.25.

#### Simulations

To be able to measure the performance of the RFI mitigation methods two coherence matrices are required. The first,  $C_1$ , is an RFI-free array coherence with noise terms and the astronomical source contribution, seen only by the array but not the reference antennas. The second coherence

matrix,  $\mathbf{C}_2$ , is a copy of the first to which the RFI contribution was added. This RFI-contaminated coherence matrix  $\mathbf{C}_2$  was processed by the four reference antenna -based methods (Eqs. 3.24 to 3.27) to yield “mitigated” coherence matrices  $\mathbf{C}'_2$ .

For robust statistics the entire process was repeated over 100 iterations, with identical parameters, but each time starting from a new  $\mathbf{C}_1$  with new random noise terms.

The quality of the mitigation is quantified by the residual error,  $\varepsilon$ , expressed in terms of the noise floor. The residual error is defined as the mean absolute deviation of values in the “mitigated” coherence matrix from the RFI-free matrix, divided by the standard deviation of all the values in the RFI-free coherence matrix,  $\sigma_{C_1}$ . The residual error is

$$\varepsilon = \overline{\|\mathbf{C}'_2 - \mathbf{C}_1\|} / \sigma_{C_1} \quad (3.32)$$

For successful mitigation the residual error should be comparable to or below the noise floor of the original RFI-free reference data. The residual errors of the four methods, Eqs. 3.24 to 3.27, are denoted by  $\varepsilon(\text{BK00})$ ,  $\varepsilon(\text{VB04})$ ,  $\varepsilon(\text{W14A})$ , and  $\varepsilon(\text{W14B})$ , respectively.

A simple simulation was run with various parameter settings, including a varying number of RFI reference antennas, interferers and their position, and different noise and INR levels.

In addition, a more extensive simulation was run to probe the range of array and reference antenna interference to noise ratios that are expected to be encountered during normal array operation. In this detailed simulation the noise floors were held constant. The antenna array noise power,  $\sigma_{N,\text{arr}}^2$ , was set to  $10^{-3}$  (in arbitrary units), and the reference antenna noise power,  $\sigma_{N,\text{ref}}^2$ , was set to  $50 \cdot 10^{-3}$ . The estimation noise of the array coherence matrix,  $\sigma_{C'}^2$ , was set to  $10^{-3}$ . The astronomical source was given a constant signal amplitude of  $10^{-3}$ , also in arbitrary units, and was still detectable in the antenna-pair cross-correlation data despite the noise level. The amplitude of the RFI in the array and in the reference antennas was derived from the INR ratios probed by the simulation (0.05, 0.1, 0.25, 0.5, 1, 2, 4, 8, 16, 32, 64, 128, 256, 512, 1024, 2048, and 4096). The array antennas and reference antennas had independent INR parameters, and in the simulations the INR of one antenna type was allowed to vary while the INR of the other was held constant at 10 or 200, corresponding to low or high INR scenarios, respectively.

#### Results

A subjective comparison of the performance of the four mitigation methods can be found in Fig. 3.26. The figure shows images of different RFI-free and RFI-contaminated array coherence data with a varying number of interferers next to images after interference mitigation by each of the four methods (BK00, VB04, W14A, and W14B). In most cases, the astronomical point source is successfully recovered from underneath the RFI contamination, with only a small or negligible amount of residual RFI visible.

The images in Fig. 3.26 are related to a subset of RFI test cases listed in Table 3.2 on page 73. As the number of model parameters is relatively large, Table 3.2 lists only a few example settings, i.e. test cases, together with the residual errors of each mitigation method. Subjectively, all four mitigation methods performed overall well.

In the scenario without any RFI the four methods did not introduce any detectable artifacts. All four methods thus appear to be subjectively *non-toxic* to the astronomical signal.

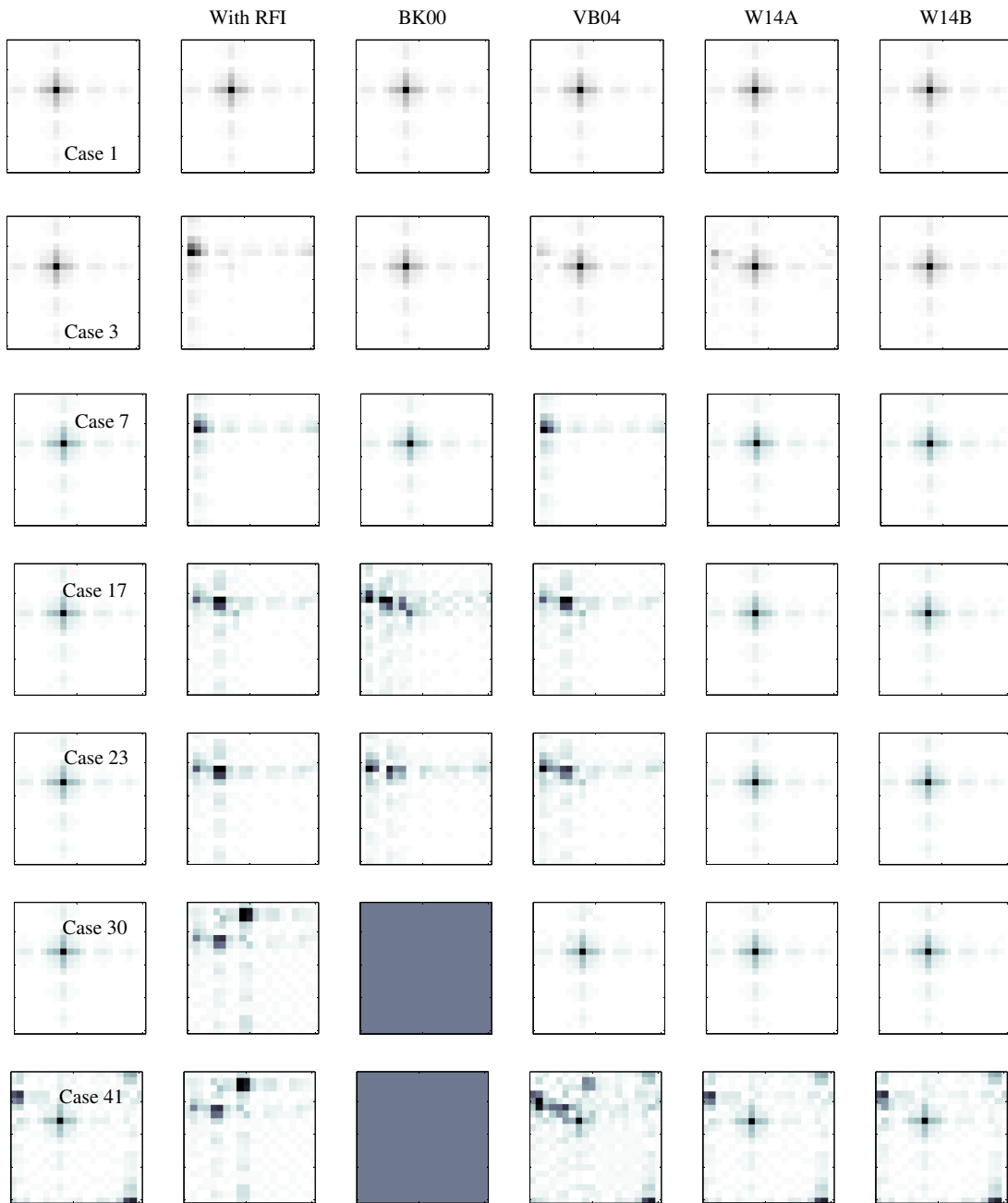


**Fig. 3.26:** Images of simulated array coherence data with the four RFI subtraction methods applied. The images were derived by uv gridding and a Fourier transforming the array coherence data. Column 1: The RFI-free image of the point source model, with a reference to a test case in Table 3.2 on page 73. Column 2: The image contaminated by simulated RFI impinging on the antenna array. Columns 3–6: The images after RFI template subtraction using the BK00, VB04, W14A, and W14B approaches. The first row, Case 1, is completely RFI-free and mitigation produced no artifacts, thus the methods appear to be *non-toxic* to astronomical data. The other test cases show RFI with INRs between 10 and 700. A single interferer is present in Cases 3 and 7. Cases 17 and 23 are affected by two interferers. Cases 30 and 41 have three interferers. The BK00 closure phase method works extremely well for single RFI but fails in other RFI environments. See Table 3.2 on page 73 for the parameter values that were used in each test case.



### 3.8 Array RFI Mitigation Tests and Results

---

The results of the detailed simulation are given in Figs. 3.27 to 3.30. The simulation included four RFI scenarios: two reference antennas and a single interferer detected in the same frequency subband (Fig. 3.27), two reference antennas and two interferers in the same subband (Fig. 3.28), three reference antennas and two interferers (Fig. 3.29), and finally, three reference antennas and three interferers (Fig. 3.30). Each figure has four panels that show the residual error against INR, the first pair of panels showing the results for a constant array INR of 10 and 200, and the second pair of panels showing the results for a constant reference antenna INR of 10 and 200.

When the residual errors were below  $2\sigma_C$  the interference mitigated array coherence data typically produced subjectively good images with only a small amount of visible residual RFI. For a more objective assessment one may adopt a  $0.1\sigma_C$  threshold (10% of the noise floor) as the criterium for successful RFI mitigation and *non-toxicity*.

We note that when the RFI seen by the array is below the noise floor, which corresponds to low INRs of  $\lesssim 1.0$  in the two lower panels in the series of Figs. 3.27 to 3.30, none of the four mitigation methods introduced any large residual error. The residual error in these essentially RFI-free cases was generally below  $0.1\sigma_C$ , i.e., below the noise floor. This level of residual error would be undetectable in practice. This suggests that all four methods are objectively *non-toxic* to the astronomical signal in an RFI-free environment.

The performance of the methods was varied. The BK00 closure phase method stood out as the overall best approach for mitigating a single interferer as it exhibited the overall lowest residual error (Fig. 3.27). On the other hand, the VB04 method performed relatively well in comparison to W14A and W14B, on the condition that the INRs in the array and in the reference antennas is quite high ( $\gtrsim 20$ ). At lower INR ratios VB04 performed poorly, however, and it also appeared to be less suitable for mitigating RFI in a three-interferer environment.

In comparison, W14A and W14B of this thesis performed exceptionally well down to low INR. Both also had very low residual errors in the three-interferer case. In general W14A and W14B had quite similar residual error levels, but W14B appeared to be generally slightly better. On the other hand, at very high INR the VB04 method outperformed W14A/B in single- and dual-interferer but not in three-interferer environments.

When the INR in the reference antennas is below 1, i.e., when the RFI signal is below the noise floor of the reference antennas, it is not surprising that mitigation results are poor. The reference antenna receivers should thus be designed to have a low system temperature. Interestingly, the W14A and W14B methods work extremely well even if the INR in the reference antennas is lower than in the array. That is, when the array has stronger interference than the detection in the reference antennas, W14A/B still lead to an accurate subtraction of RFI from the array data.

ID	$N_{\text{ant}}$	$\sigma_S^2$	$\sigma_{\text{RFI,arr}}^2$	$\sigma_{\text{RFI,ref}}^2$	$\sigma_{N,\text{arr}}^2$	$\sigma_{N,\text{ref}}^2$	$\sigma_C^2$	INR	$\varepsilon'(\text{BK00})$	$\varepsilon'(\text{VB04})$	$\varepsilon'(\text{W14A})$	$\varepsilon'(\text{W14B})$
1	2+64	1e-3	0	0	10 <sup>-3</sup>	10 <sup>-3</sup>	10 <sup>-6</sup>	0	1.5e-26	3.1e-19	1.9e-5	3.7e-5
3	2+64	1e-3	10e-3	20e-3	1e-3	1e-3	1e-6	20,10	2.5e-7	2.4e-4	4.3e-4	3.0e-5
4	2+64	1e-3	0.1e-3	0.1	1e-3	1e-3	1e-6	100,0.1	1.0e-10	1.5e-6	1.6e-5	3.2e-5
7	2+64	1e-3	2	30	1e-3	3	1e-3	10,2e3	5.3e-6	9.5e-2	2.3e-5	3.3e-5
10	2+64	1e-3	1e-3	15e-3	1e-3	1e-3	1e-3	15,1	5.3e-6	3.6e-6	2.3e-5	3.5e-5
11	2+64	1e-3	1e-3	15e-3	1e-3	1e-3	1e-6	15,1	4.4e-8	3.2e-5	7.4e-5	3.0e-5
12	2+64	0.1	1e-3	15e-3	1e-3	1e-3	1e-6	15,1	4.4e-8	3.2e-5	6.8e-5	1.2e-3
13	2+64	1e-3	2e-1, 5e-1	3.0, 7.5	1e-3	1e-3	1e-3	>3e3,>200	-	5.4e-5	2.2e-5	2.3e-5
21	2+64	1e-3	2, 5	30, 75	1e-6	3	1e-9	>10,>2e6	-	0.2	6.8e-8	2.7e-7
23	2+64	1e-3	20e-3,50e-3	0.3, 0.75	1e-4	3e-2	1e-9	>10,>200	-	2.4e-3	2.0e-7	2.7e-7
14	2+64	1e-3	2e-3, 5e-3	30e-3, 75e-3	1e-3	1e-3	1e-3	30	-	1.9e-4	2.3e-5	2.5e-5
15	2+64	1e-3	2e-3, 5e-3	30e-3, 75e-3	1e-3	1e-3	1e-6	>30	-	5.3e-5	2.0e-5	2.0e-5
16	2+64	1e-3	2e-3, 5e-3	2e-3, 5e-3	1e-3	1e-3	1e-6	>2	-	7.6e-4	2.0e-5	2.0e-5
17	2+64	1e-3	2e-3, 5e-3	2e-3, 5e-3	1e-3	3	1e-6	<1	-	5.3e-3	2.5e-5	3.0e-5
19	3+64	1e-3	2e-3, 5e-3	30e-3, 75e-3	1e-3	1e-3	1e-3	>30	-	4.8e-5	2.8e-5	3.8e-5
20	4+64	1e-3	2e-3, 5e-3	30e-3, 75e-3	1e-3	1e-3	1e-3	>30	-	4.3e-5	3.3e-5	5.1e-5
21	3+64	1e-3	0.02, 0.05, 0.07	0.2, 0.5, 0.7	1e-3	1e-3	1e-6	>200,>20	-	2.8e-4	2.5e-5	2.6e-5
30	3+64	1e-3	0.02, 0.05, 0.07	0.02, 0.05, 0.07	1e-3	1e-3	1e-6	>20,>20	-	1.1e-3	2.5e-5	2.6e-5
41	3+64	3x 1e-3	0.02, 0.05, 0.07	0.02, 0.05, 0.07	1e-3	1e-3	1e-3	>20,>20	-	1.6e-3	3.7e-5	2.5e-4

**Table 3.2:** Performance comparison of the four RFI subtraction methods, based on simulations of a 64-element antenna array. The parameters are described in more detail in § 3.8.3 on page 66. Col. 1: a cross-reference ID number to Fig. 3.26. Col. 2: the number of reference and array antennas. Col. 3: source signal power (arbitrary units). Col. 4: RFI signal power in array antennas. Col. 5: RFI signal power in reference antennas. Col. 6: noise power in array antennas. Col. 7: noise power in reference antennas. Col. 8: the power of Gaussian noise added to the coherence matrix. Col. 9: the INR in the reference and array antennas, respectively. Cols. 10–13: post-mitigation residuals. The residuals are mean absolute deviation of the RFI-mitigated coherence matrix elements from the elements of an RFI-free reference matrix, and are shown here without a normalization by  $\sigma_{N,\text{arr}}$ .

### 3.8 Array RFI Mitigation Tests and Results

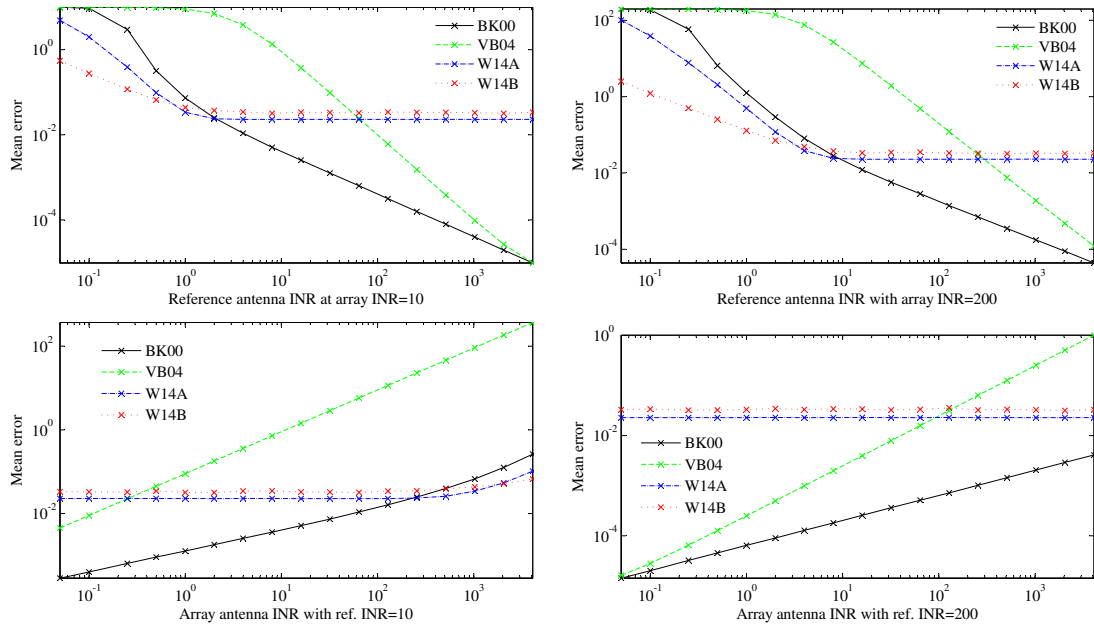


**Fig. 3.27:** A comparison of the residual errors (Eq. 3.32) of the four RFI subtraction methods for arrays (Eqs. 3.24 to 3.27). A lower residual error is better. The simulation included one interferer and two reference antennas. The residual errors are given in units of the standard deviation in the original RFI-free covariance matrix. The residual errors are shown against the interference to noise ratio (INR) in the reference antennas (top) and against the INR ratio in the array antennas (bottom).

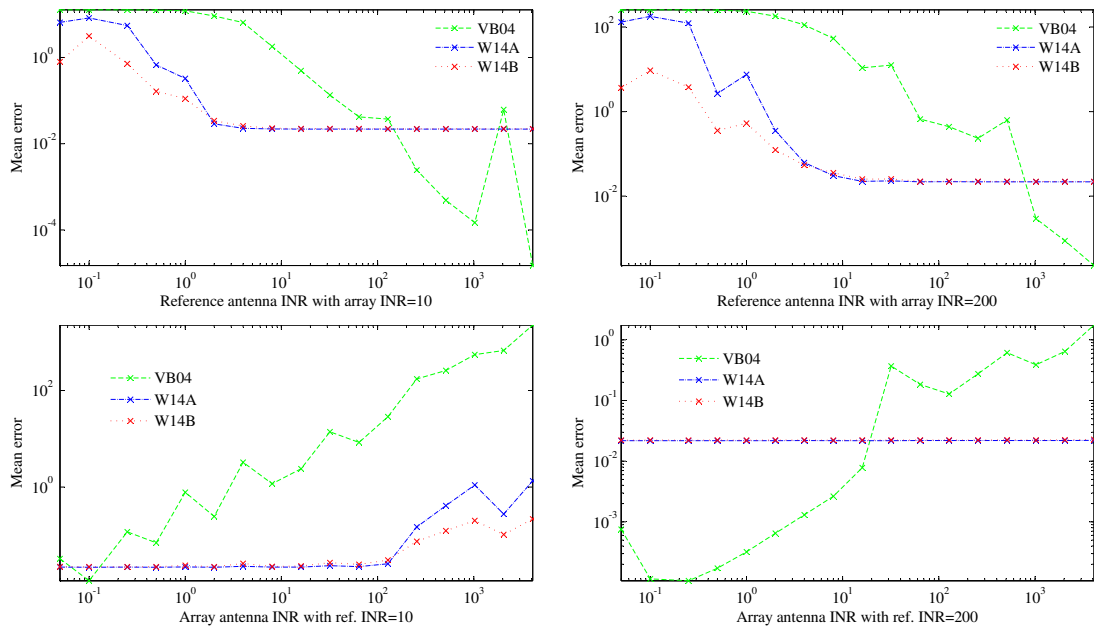


**Fig. 3.28:** As in Fig. 3.27 but for 2 interferers and 2 reference antennas. The BK00 method is specific to a single-interferer scenario and for this reason BK00 has been omitted from the plots.

### 3.8 Array RFI Mitigation Tests and Results

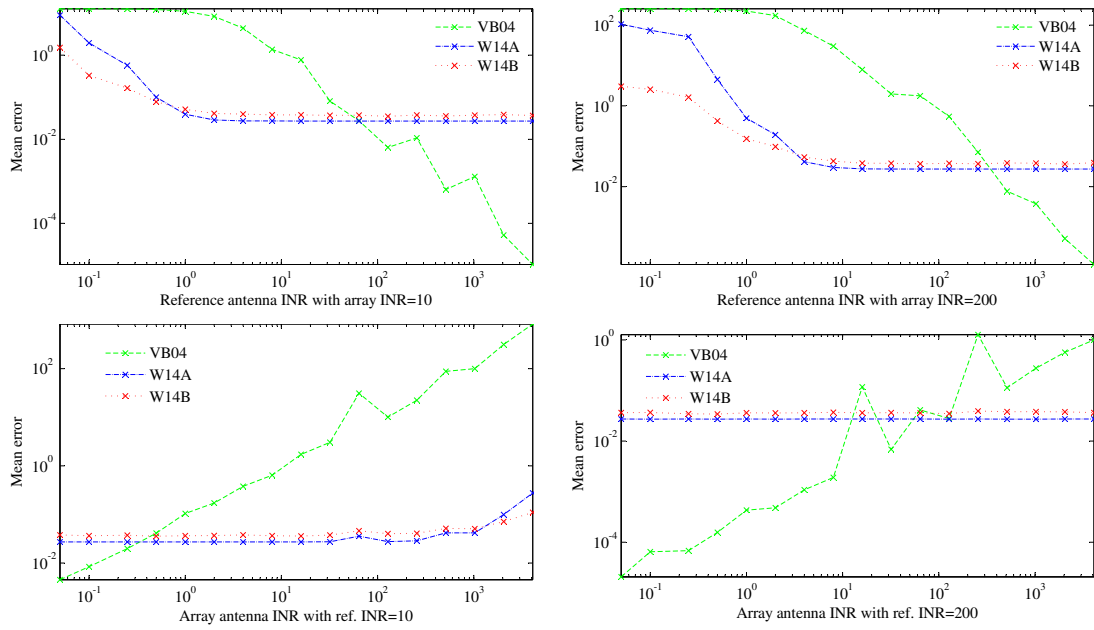


**Fig. 3.29:** As in Fig. 3.28 but for 2 interferers and 3 reference antennas.

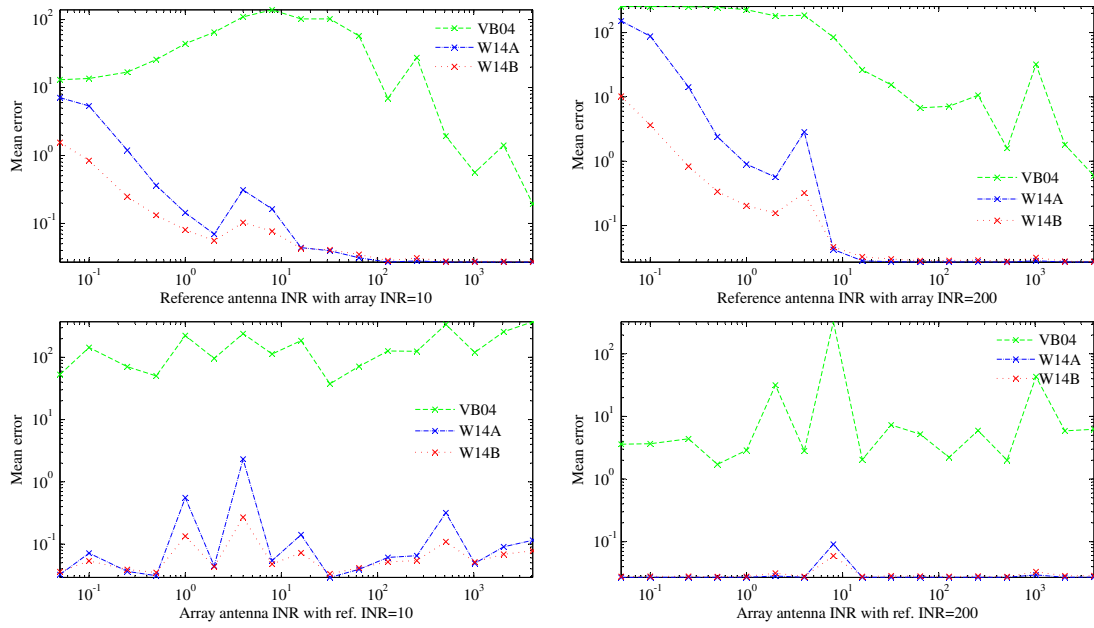


**Fig. 3.30:** As in Fig. 3.29 but for 3 interferers and 3 reference antennas.

## 3.9 Summary and Conclusions for Array RFI Mitigation

The promising results of the simulations presented in the previous sections suggest that all four reference antenna -based mitigation methods (VK00, VB04, W14A, and W14B) are *non-toxic* when no RFI is present, i.e., the residuals of the correction are several orders of magnitude below the noise floor of the RFI-free reference environment. Each method was found to have a certain range of interference to noise ratios at which it produced better results compared to the other methods and had lower residual errors with a more complete RFI subtraction. The residuals of the interference mitigated array coherence matrix relative to its RFI-free reference counterpart were generally proportional to or below the noise floor of the antenna array, indicating very good to excellent removal of RFI from the data and no significant remaining or introduced artifacts.

As the four methods are applied during post-processing to already averaged array data, one is not critically committed to any specific method. This allows the user to experiment and select the method that for a given data set produces the overall best outcome in terms of the most plausible array coherence or visibility data and the most plausible image of the source.

Incidentally, we note that the mitigation methods could be applied just as well to VLBI array data. The mitigation methods can subtract “uncorrelated” antenna-based RFI or correlated short baseline RFI (e.g., satellite interference) from the visibility data. The main obstacle perhaps is the amount of stored station data. Because VLBI experiments are often correlated several days after the observation, both the raw telescope baseband recordings and the recordings from two RFI reference antennas would have to be stored until correlation (i.e., until the time averaged array coherence data are computed). This would triple the required storage capacity. For spectral line observations that have a narrow bandwidth this may not be a problem, however.

Finally, due to the current receiver and backend status at Effelsberg the practical evaluation of the above RFI mitigation methods had to be postponed. In the future, when new capable backends become available in Effelsberg (or elsewhere), and when two or more RFI reference antennas can be installed and included in the antenna array signal processing pipeline, these mitigation methods can find a direct application in radio astronomical observations.

## 4 Water Megamaser Survey

Water masers ( $\text{H}_2\text{O}$ ) and hydroxyl masers (OH) in the megamaser luminosity class have equivalent isotropic luminosities that far exceed their Galactic counterparts. They are best known as probes into some extreme environments, such as merging galaxies, nuclear starbursts in molecular tori at 100 pc scales in the case of OH, active galactic nucleus (AGN) accretion disks at sub-pc scales, outflows, and the vicinity of jets in the case of  $\text{H}_2\text{O}$ . Additionally,  $\text{H}_2\text{O}$  disk masers as in UGC 3789 allow a direct measurement of the angular diameter distance to the galaxy and also can determine the value of the Hubble constant (Reid et al. 2013).

To date, over 4030 galaxies have been searched for  $\text{H}_2\text{O}$  masers, resulting in about 150 detections that include about 20 disk maser galaxies (see, e.g., Nakai et al. 1995; Braatz et al. 1997; Henkel et al. 2005; Kondratko et al. 2006; Braatz & Gugliucci 2008; Bennert et al. 2009; and the project web sites Water Maser Cosmology Project (WMCP)<sup>1</sup> and Megamaser Cosmology Project (MCP)<sup>2</sup>. In comparison, about 500 galaxies have been searched for OH masers, 120 were detected (at up to  $z = 0.265$ ), and about 10 exhibit OH in absorption (see, e.g., Impellizzeri 2008; Klöckner 2004).

Sources that maser in both molecules are extremely rare. This may be expected since extragalactic OH and  $\text{H}_2\text{O}$  maser species have a quite different pumping mechanism. While OH is radiatively pumped in regions of enhanced density by AGN or star-formation photons reprocessed via  $\geq 45$  K dust to  $35\ \mu\text{m}$  to  $53\ \mu\text{m}$  infrared (IR), gas phase  $\text{H}_2\text{O}$  is collisionally pumped at  $\geq 400$  K. Nevertheless, five objects that maser in both species are known: OH and  $\text{H}_2\text{O}$  kilomasers (OH KM,  $\text{H}_2\text{O}$  KM;  $L_{\text{OH}}, L_{\text{H}_2\text{O}} < 10 L_{\odot}$ ) coexist in the starbursts NGC 253 (Frayer et al. 1998; Henkel et al. 2004) and M 82 (Baudry & Brouillet 1996; Argo et al. 2007), an OH KM and an  $\text{H}_2\text{O}$  megamaser (OH MM,  $\text{H}_2\text{O}$  MM;  $L_{\text{OH}}, L_{\text{H}_2\text{O}} > 10 L_{\odot}$ ) are found in the Sy 2 NGC 1068 (Gallimore et al. 1996) and radio-quiet Sy 2 AGN NGC 3079 (Baan & Irwin 1995), whereas Arp 299 is the only OH MM and  $\text{H}_2\text{O}$  MM object (Tarchi et al. 2007). No source with an OH MM and an  $\text{H}_2\text{O}$  KM has yet been found. This is likely because  $\text{H}_2\text{O}$  KM tend to occur in nearby objects, whereas OH MM are found up to high redshifts, where  $\text{H}_2\text{O}$  KM emission falls

---

<sup>1</sup><https://www.cfa.harvard.edu/~lincoln/demo/HoME/>

<sup>2</sup><https://safe.nrao.edu/wiki/bin/view/Main/MegamaserCosmologyProject>

below sensitivity limits (see Tarchi et al. 2011).

There is no clear general link between OH and H<sub>2</sub>O maser species in such “dual-species” objects. However, OH maser emission (and OH seen in absorption) may point towards sources that contain denser molecular regions and a generally larger reservoir of H<sub>2</sub>O; OH is formed from the evaporation and dissociation of grain-bound H<sub>2</sub>O (Lo 2005; Hollenbach et al. 2009). A larger H<sub>2</sub>O abundance may favor an H<sub>2</sub>O maser detection. Furthermore, both H<sub>2</sub>O KM, OH KM and OH MM have a similar association with, among others, star-forming regions and nuclear regions with bursts of intense star formation (Lo 2005). We consider that an earlier OH detection could be one of the selection criteria that might increase the H<sub>2</sub>O maser detection rate.

The search presented here attempts to identify new water maser galaxies, new dual maser species objects, and in particular any H<sub>2</sub>O KM in an OH MM galaxy, as well as new AGN disk maser galaxies suitable for constraining the Hubble constant.

## 4.1 Source Sample

We considered only sources within 250 Mpc ( $< 16\,000\text{ km s}^{-1}$ ). We first assembled a database of initially over 8000 known water maser detections and nondetections published in the literature, including WMCP and MCP project web site catalogs of published and unpublished maser search results. We then used an automated the NASA/IPAC Extragalactic Database (NED) lookup of source coordinates and name aliases to merge duplicates. This produced a final catalog of 4038 unique objects already observed for H<sub>2</sub>O.

Next we identified 126 galaxies in the catalog with a low sensitivity H<sub>2</sub>O nondetection (40 mJy to 200 mJy rms) that could be re-observed with a factor 10 higher sensitivity. To identify new sources not yet observed at 22 GHz, we reviewed recent X-ray and AGN data and literature, including recent extragalactic hydroxyl searches (e.g., Impellizzeri 2008; Klöckner 2004). We chose objects with 2–10 keV X-ray data, high X-ray luminosities ( $L_X > 10^{40}\text{ W}$ ), and large absorbing column densities ( $N_H \gtrsim 10^{22}\text{ cm}^{-2}$ ), as found in over 90 % of water maser galaxies (e.g., Kondratko et al. 2006; Zhang et al. 2006; Greenhill et al. 2008). We also chose objects with a nucleus classified as NLS1, Sy 1.5 to Sy 2.0, LINER, or HII region. Some of the sources are Infrared Astronomical Satellite (IRAS) survey objects with OH masers or OH seen in absorption.

The final selection of 40 nearby galaxies, mergers, binary AGN and triple AGN systems is shown at the end of this Chapter in Table 4.2 on page 89ff. The selection consists of 17 previous nondetections at  $\geq 40\text{ mJy rms}$ , 10 objects with OH seen in emission at 1.6 GHz (3 being previous H<sub>2</sub>O nondetections), 1 source with strong OH absorption at 6 GHz (a previous H<sub>2</sub>O nondetection), and 16 other sources not yet observed for 22 GHz water masers. Out of this sample, the OH maser galaxy ESO 320-G030 had the highest IRAS 100  $\mu\text{m}$  flux density (46 Jy).

## 4.2 Observations

To uncover kilomasers among the source sample a 4 mJy rms target sensitivity over 24.4 kHz (about  $0.31 \text{ km s}^{-1}$ ) was chosen, equivalent to between  $0.1 L_{\odot}$  rms and  $1.0 L_{\odot}$  rms in isotropic luminosity. Observations were carried out in four runs during February and March 2013 under project AGBT13A-172 using the National Radio Astronomy Observatory (NRAO<sup>1</sup>) Robert C. Byrd Green Bank Telescope (GBT). Sessions were scheduled in late winter under good 22 GHz weather conditions. The UTC date and time and zenith opacity  $\tau_0$  are listed in Table 4.1. Excellent weather conditions (zenith  $\tau_0 = 0.033$  to  $0.047$ ) and low  $T_{\text{sys}}$  (35 K to 75 K) allowed us to observe most of the 40 sources in 16 hours. We spent between 12 and 20 minutes on each source and the remainder on calibration.

We used the GBT spectrometer backend and GBT K-band Focal Plane Array (KFPA) receiver, and selected two KFPA elements near the cryo cooler with the lowest  $T_{\text{rx}}$  ( $< 25$  K over 75% of the band). Beams were  $33''$  FWHM with an aperture efficiency  $\eta_{ap}$  of 0.66 at 21 GHz and had a  $94.9''$  beam separation. Observations were in dual-circular polarization and had a 30-second dual-beam nod cycle. Both 200 MHz frequency windows of each polarization (i.e. four windows in total) were centered on the systemic velocity. The 8192 spectrometer channels were 24.4 kHz wide and covered  $V_{\text{sys}} \pm 1250 \text{ km s}^{-1}$ .

Pointing and focusing were corrected using strong standard calibrators ( $> 0.8$  Jy). The GBT dynamic corrections compensated for gravitational and thermal surface deformations and remained stable. The full setup was occasionally verified using brief pointings at megamaser galaxies NGC 1068, NGC 3079, and NGC 5793. Pointing and focusing were repeated every 1.5 to 2 hours and after sunrise, with only small adjustments ( $< 2.5''$  and  $< 8$  mm). Wind speeds were low with little to no cloud cover. Zenith opacity measurements  $\tau_0$  at 21 GHz were supplied by nearby weather stations and remained stable during the observing runs.

## 4.3 Data Reduction

The flux density scale was calibrated via noise injection ( $T_{\text{cal}}$ ), and accounting for pointing uncertainties (3-8'' relative to the GBT beamwidth of  $36''$  at 22 GHz) was accurate to about 15%. The initial aperture efficiency  $\eta_{ap0}$  calculated by the GBTIDL toolbox was corrected for elevation via the GBT 22.236 GHz gain-elevation curve<sup>2</sup> of April 8, 2008, which is based on the current Zernike model (*FEM plus 2005WinterV2*) for the GBT adaptive surface. The correction curve is  $\eta_{ap} = \eta_{ap0} * (0.910 + 0.00434 * ZD - 5.22 \times 10^{-5} * ZD * ZD)$ , where  $ZD =$

<sup>1</sup>The National Radio Astronomy Observatory is a facility of the National Science Foundation operated under cooperative agreement by Associated Universities, Inc.

<sup>2</sup><https://safe.nrao.edu/wiki/bin/view/GB/Observing/GainPerformance>



**Table 4.1:** Observing dates of the GBT survey.

Epoch	Start time (UT)	Hours	$\tau_0$
1	2013-02-21 20:30	3:15	0.036–0.037
2	2013-03-02 03:45	3:45	0.047
	2013-03-02 07:30	1:30	0.043
	2013-03-02 09:00	1:30	0.041
3	2013-03-03 18:30	2:15	0.036
	2013-03-03 20:45	1:15	0.033
4	2013-03-09 11:15	2:15	0.036–0.035

**Notes.** Columns list the UTC start time, session duration in hours, and the zenith opacity,  $\tau_0$ , at 21 GHz of the four K-band observing runs in project GBT13A-172.

$90^\circ$  – elevation is the angle off zenith.

Nod scans were processed in GBTIDL. The  $\tau_0$  and  $\eta_{ap}$  gain corrections were applied first. Next, subspectra affected by internal radio frequency interference (RFI) or spectrometer faults were flagged. To improve the signal to noise ratio (SNR), the blank sky reference subspectra (for subtracting the standing wave across the band) were smoothed with a short 4- to 32-channel boxcar function. Care was taken to avoid introducing artifacts. Third-order baselines were removed from individual subspectra. All subspectra and both polarizations were time averaged into a Stokes I spectrum, and a final third-order baseline fit was removed. Sensitivity was calculated over line-free channels without smoothing.

For each detection, Gaussian models  $S(\nu) = a * e^{-(\nu-\mu)^2/2\sigma_\nu^2}$  were fit to the calibrated non-smoothed spectra to estimate line peak  $a$  (Jy), center  $\mu$  ( $\text{km s}^{-1}$ ) and FWHM width  $w$  ( $\text{km s}^{-1}$ ). The integrated line profile  $S_{\text{int}} = \int_{-\infty}^{+\infty} S(\nu) d\nu$  (Jy  $\text{km s}^{-1}$ ) for a single Gaussian  $S(\nu)$  equals  $a \sigma_\nu \sqrt{2\pi}$ . Noting that  $\sigma_\nu = w/2.35482$  and using the luminosity distance  $D_L$  and redshift  $z$  of the source, the equivalent isotropic luminosity (see, e.g., Bennert et al. 2009) given by

$$\frac{L_{\text{iso}}}{L_\odot} = 0.023 \times \frac{S_{\text{int}}}{[\text{Jy km s}^{-1}]} \times \frac{1}{1+z} \times \left( \frac{D_L}{[\text{Mpc}]} \right)^2 \quad (4.1)$$

can be written for the Gaussian model in form of a sum over all Gaussian components,

$$\frac{L_{\text{iso}}}{L_\odot} = \frac{0.023 \sqrt{2\pi}}{2.35482} \times \frac{\sum_i a_i \cdot w_i}{[\text{Jy km s}^{-1}]} \times \frac{1}{1+z} \times \left( \frac{D_L}{[\text{Mpc}]} \right)^2 \quad (4.2)$$

The factor 0.023 contains unit conversions and the water maser rest frequency. For 1.6 GHz OH masers the factor is 0.0017. Upper luminosity limits for water maser nondetections are given for single wide Gaussian  $\text{H}_2\text{O}$  line with  $2.0 \text{ km s}^{-1}$  FWHM and a  $3\sigma$  peak. The luminosities for detections are based on Eq. 4.1, with  $S_{\text{int}}$  evaluated directly over the line regions of the spectrum

using Simpson’s Rule. Spectra of the detections presented here were smoothed with a third-order, nine-point ( $2.79 \text{ km s}^{-1}$ ) Savitzky-Golay shape-preserving filter to reduce the noise floor by 70 % while maintaining the shape and height of the maser features.

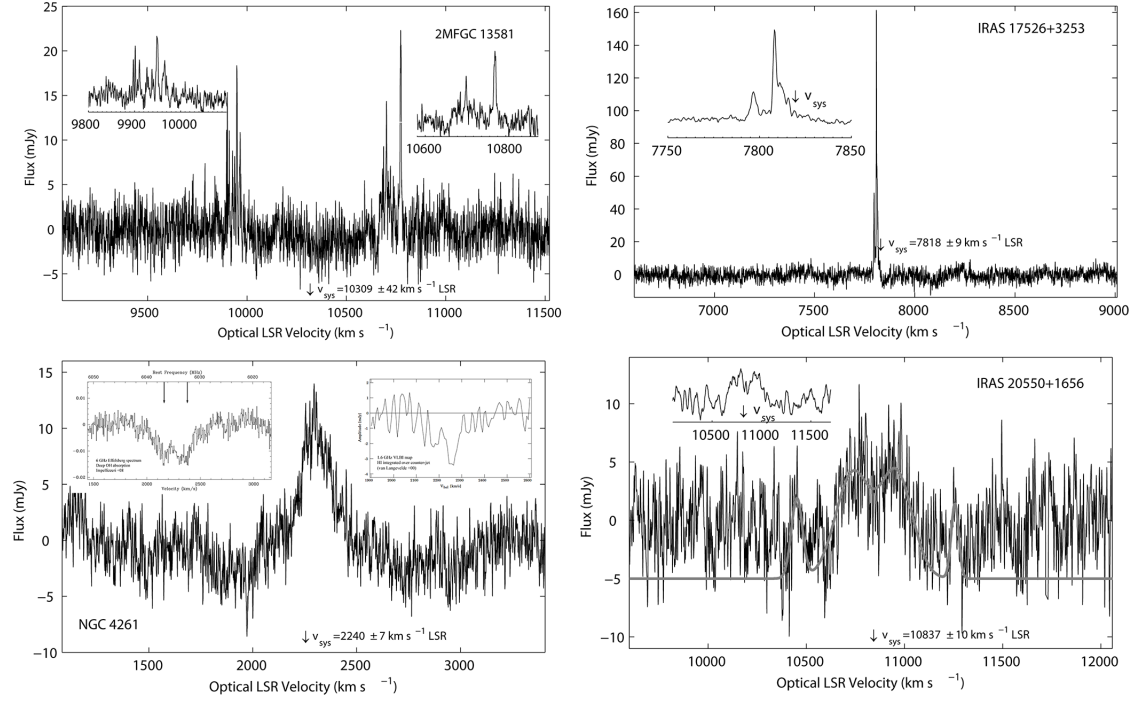


**Fig. 4.1:** Spectra of the four 22 GHz water megamasers detections. Recession velocities,  $V_{\text{sys}}$ , are adopted from NED. The channel spacing is  $0.3 \text{ km s}^{-1}$ . The uncertainty of the flux density scale is  $\leq 15 \%$ . *Top left:* Maser features towards possible Sy 2 galaxy 2MFGC 13581 are typical of masing sub-parsec accretion disks around AGN. *Top right:* IRAS 17526+3253 (UGC 11035) is an OH KM galaxy and has narrow  $360 L_{\odot}$  water masers. *Bottom left:* NGC 4261 (3C 270; twin-jet, torus) shows deep H I absorption at  $2260 \text{ km s}^{-1}$  (right inset) and deep 6 GHz OH absorption at  $2100\text{--}2400 \text{ km s}^{-1}$  (left inset) against the counter-jet (insets adopted from van Langevelde et al. 2000; Impellizzeri 2008). The broad  $\text{H}_2\text{O}$  MM feature is slightly redshifted with respect to the systemic velocity. *Bottom right:* IRAS 20550+1656 (II Zw 96) is an OH MM object and has a tentative  $\text{H}_2\text{O}$  MM detection at  $5\sigma$  after 16-channel Gaussian smoothing (inset). Fits for two main features that are symmetric around  $V_{\text{sys}}$  are overlaid, together with two narrower “suggestive” features that are also symmetric but otherwise similar to the noise peaks even after stronger smoothing.

## 4.4 Detections and Discussion

Of the 40 sources listed in Table 4.2, 37 were observed for H<sub>2</sub>O masers with a detection rate of 11 %. Three sources have a strong maser detection, and one has a tentative detection. The spectra are shown in Fig. 4.1. Interestingly, three detections are in the set of 11 sources that are also detected in hydroxyl in emission or in deep absorption. No spectra were captured for three sources (NGC 3341, NGC 7130, and ESO 323-G077). Spectra of the water maser nondetections are shown in Fig. A.3.1 in Appendix A.3 on page 207. The spectra for the three known water maser galaxies observed to verify the GBT spectrometer setup are shown in Fig. A.3.2 of the same Appendix. A list of the 37 observed sources, the achieved sensitivities, isotropic luminosities (H<sub>2</sub>O and OH), and X-ray absorbing column densities is given in Table 4.2. The luminosity distances, source redshifts, and recessional velocities,  $v_{\text{LSR}}$ , were adopted from NED. The listed recessional velocities are in the optical definition and are in the kinematic local standard of rest (LSR) reference frame.

The source selection by X-ray data did not appear to enhance the H<sub>2</sub>O maser detection rate. In our sample, 14 active galaxies have a published X-ray absorbing column density. Two of these yielded a H<sub>2</sub>O MM detection. One source hosts a heavily obscured AGN ( $N_{\text{H}} > 10^{23} \text{ cm}^{-2}$ ) and the other a Compton-thick AGN ( $N_{\text{H}} \geq 10^{24} \text{ cm}^{-2}$ ). This is consistent with Castangia et al. (2013), who find 96 % (45/47) of H<sub>2</sub>O MM sources have  $N_{\text{H}} > 10^{23} \text{ cm}^{-2}$ . However, the same two sources were also selected by OH, resulting in an apparent better detection rate given by the OH selection (3/11) than by the X-ray selection (2/14). To see whether the difference in detection rates is significant, a dual population two-tailed Z-test<sup>1</sup> with a significance level of  $p < 0.05$  was applied. The p-value for both rates being equal was 0.42. Thus the X-ray and OH selection produced identical detection rates. Below we discuss the four new detections.

### 2MFGC 13581

A new H<sub>2</sub>O disk MM is found in the optically edge-on galaxy 2MFGC 13581 ( $v_{\text{LSR}} = 10309 \pm 42 \text{ km s}^{-1}$  (Hopp et al. 2000),  $D_{\text{L}} = 145 \text{ Mpc}$ ,  $z = 0.034$ ). It is the second-closest of six Seyfert candidates in the Hamburg/SAO survey for emission-line galaxies and is a probable Sy 2 (Hopp et al. 2000). Masers are detected in two high-velocity groups, which are symmetrically offset from the systemic velocity by about  $\pm 390 \text{ km s}^{-1}$ . No systemic emission is detected, giving a  $3\sigma$  upper limit of 6.3 mJy. The red group peaks at 25 mJy and forms a forest of  $\approx 3 \text{ km s}^{-1}$  FWHM lines, similar to the blue group that peaks at 20 mJy. Each group can be approximated by a wide profile, with the blue one centered at  $9940 \text{ km s}^{-1}$  (5.3 mJy peak,  $61.5 \text{ km s}^{-1}$  FWHM) and the red one at  $10724 \text{ km s}^{-1}$  (4.4 mJy peak,  $114.4 \text{ km s}^{-1}$  FWHM). Their mean,  $10332 \text{ km s}^{-1}$ ,

<sup>1</sup>The Z-test tests the hypothesis that between two populations, A and B, some parameter,  $\mu_{\text{A}}$  and  $\mu_{\text{B}}$  respectively, is greater ( $H_1 : \mu_{\text{A}} > \mu_{\text{B}}$ ), smaller ( $H_1 : \mu_{\text{A}} < \mu_{\text{B}}$ ), or different ( $H_1 : \mu_{\text{A}} \neq \mu_{\text{B}}$ ). The latter is the “two-tailed” Z-test.

lies within  $1\sigma$  of the systemic recession velocity. The blue and red groups have luminosities of  $120 L_{\odot}$  and  $170 L_{\odot}$ , respectively.

The symmetric spectrum suggests that emission most likely originates from a circumnuclear masing disk. The absence of systemic emission may be explained by a warp in the disk that shadows parts of the disk from X-ray emission by the central engine which is thought to support maser emission (Neufeld et al. 1994). The undetected systemic masers may also have a quite low flux density. Alternatively, they may be highly variable like the systemic (disk-)maser emission in Circinus and thus not always detected (Greenhill et al. 2003; McCallum et al. 2009).

We can estimate the radius of the masing disk annulus in 2MFGC 13581 if we assume Keplerian rotation, a black hole mass of  $10^7 M_{\odot}$  typical of other disk maser galaxies (e.g., Kuo et al. 2011), and a fully edge-on disk. The observed orbital velocity of  $\pm 390 \text{ km s}^{-1}$  then translates into a 0.4 parsec (0.8 mas) average disk diameter. Unfortunately, given the low maser flux, prospects for a successful VLBI map, and a single-dish determination of variability and the secular acceleration of possibly existing weak systemic maser components are poor.

### IRAS 17526+3253

Water megamasers in this IR galaxy (UGC 11035;  $v_{\text{LSR}} = 7818 \pm 9 \text{ km s}^{-1}$  (de Vaucouleurs et al. 1991),  $D_{\text{L}} = 108 \text{ Mpc}$ ,  $z = 0.026$  (NED),  $L_{\text{IR}} \approx 7 \times 10^{11} L_{\odot}$  estimated from IRAS fluxes using the method by Wouterloot & Walmsley 1986a) have a relatively high peak flux of  $\approx 170 \text{ mJy}$ . Emission appears in a narrow, slightly blueshifted  $40 \text{ km s}^{-1}$  window around the systemic velocity. It has three features: two wider profiles at  $7797 \text{ km s}^{-1}$  (47 mJy peak,  $4.0 \text{ km s}^{-1}$  FWHM,  $50 L_{\odot}$ ) and  $7810 \text{ km s}^{-1}$  (65 mJy peak,  $10.9 \text{ km s}^{-1}$  FWHM,  $210 L_{\odot}$ ) and a narrow emission line at  $7808 \text{ km s}^{-1}$  (170 mJy peak,  $2.2 \text{ km s}^{-1}$  FWHM,  $100 L_{\odot}$ ).

Literature lists UGC 11035 as an OH KM galaxy. An early nondetection ( $L_{\text{OH}} < 4 L_{\odot}$  at 1.0 mJy rms) by Garwood et al. (1987) was followed by a broad blueshifted feature (3.7 mJy peak,  $L_{\text{OH}} = 6.46 L_{\odot}$ ) detected near  $7450 \text{ km s}^{-1}$  by Martin et al. 1989, but no spectrum was published. A recent observation suffered from RFI and had insufficient sensitivity to confirm the kilomaser (McBride & Heiles 2013).

The 2MASS image shows two near-infrared components separated by  $60''$  (about 30 kpc) with an angular size ratio of  $\approx 5$ . The image suggests UGC 11035 could be a major merger system. The hard X-ray luminosity would then be expected to exceed  $10^{43} \text{ erg s}^{-1}$ . This would contribute to enhanced IR luminosity through core emission reprocessed in the dense concentration of gas accumulated during the merger event. Using  $60 \mu\text{m}$ ,  $100 \mu\text{m}$ , and  $S_{1.4\text{GHz}}$  flux points from NED, the  $q$  parameter (see, e.g., Yun et al. 2001) of this galaxy is 4.74, indicating an IR excess. The  $q$  is notably higher than  $2.34 \pm 0.01$  of the IRAS 2 Jy sample (Yun et al. 2001) and exceeds  $2.57 \pm 0.36$  of typical OH MM galaxies (Klöckner 2004), indicating a buried AGN or

enhanced star formation. UGC 11035 also has a curiously flat velocity field of  $210 \text{ km s}^{-1}$  at 9 kpc from the center, suggesting either a giant irregular galaxy or interaction of two face-on objects. The inner 18 kpc have a kinematic mass of  $\approx 10^{11} M_{\odot}$  (Andreasian 1992; Andreasian & Alloin 1994).

Given limited data on the object, we speculate that  $\text{H}_2\text{O}$  emission might originate from a small shocked region in an ongoing merger similar to Arp 299. The maser features lack the high velocities associated with jet and nuclear outflow masers (e.g., Greenhill et al. 2003). Their velocity span of  $40 \text{ km s}^{-1}$  is narrow but still typical of star formation masers. Assuming that a buried AGN gives rise to the IR excess, the systemic masers may also be associated with a slightly inclined, not fully edge-on warped accretion disk. A warp along the line of sight towards the nucleus can compensate for the disk inclination and produce the velocity coherent path lengths along the line of sight that are necessary for luminous systemic maser emission. Monitoring of the possible drift in line velocities (the accelerations of maser orbits in a disk) or a VLBI observation would be required to rule out a nuclear association.

### NGC 4261

The WMAP project lists the giant elliptical galaxy NGC 4261 ( $v_{\text{LSR}} = 2240 \pm 7 \text{ km s}^{-1}$  (Trager et al. 2000),  $D_{\text{L}} = 35.6 \text{ Mpc}$ ,  $z = 0.0075$ ) as a 109 mJy rms nondetection observed in 2002. We reached 3.1 mJy rms and detect broad emission that was best fit by a single Gaussian of 10.3 mJy,  $154 \text{ km s}^{-1}$  FWHM centered on  $2302 \text{ km s}^{-1}$ . Peak emission is redshifted by about  $+60 \text{ km s}^{-1}$  relative to the systemic velocity and has a total isotropic luminosity of  $50 L_{\odot}$ .

NGC 4261 is a LINER galaxy associated with the low-luminosity FR-I radio source 3C 270 that launches a highly symmetric kpc-scale twin jet. The galaxy is known for its 240 pc nuclear torus/disk found by the Hubble Space Telescope. The nucleus hosts a  $4.9 \times 10^8 M_{\odot}$  SMBH and has an X-ray absorbing column density  $N_{\text{H}}$  of  $> 5 \times 10^{22} \text{ cm}^{-2}$  (Gliozzi et al. 2003). Recent hard X-ray data show a slightly higher obscuring column density of  $16.4_{13.25}^{21.64} \times 10^{22} \text{ cm}^{-2}$  (González-Martín et al. 2009).

The VLBI shows neutral HI absorption against the counter-jet, with deepest absorption at  $2260 \text{ km s}^{-1}$ , redwards with respect to the systemic velocity. It has been modeled by atomic gas in a thin disk with an absorbing column density of  $N_{\text{H}} \approx 10^{21} \text{ cm}^{-2}$  (van Langevelde et al. 2000). There is also deep OH absorption at 6 GHz against a 1.3 Jy continuum with a  $400 \text{ km s}^{-1}$  FWHM around the systemic velocity (Impellizzeri 2008).

With its low-luminosity core, an optical dusty torus, molecular absorption, and a twin radio jet, NGC 4261 is remarkably similar to the twin jet LINER NGC 1052. The spectrum of NGC 1052 has a single, broad, and slightly redshifted luminous 150 mJy maser feature. The VLBI observations of NGC 1052 found water masers in two regions along the jet axis. Emis-

sion has been associated with continuum seed emission from jet blobs being amplified in an X-ray dissociation region located on the inner surface of a torus at a typical (for a J-type shock) temperature of 400 K (Sawada-Satoh et al. 2008). Given the evidence for abundant HI and OH molecules and a high X-ray absorbing  $N_{\text{H}}$  column density towards NGC 4261, combined with the radio jet and the maser profile, a masing torus region with gas infalling at  $+60 \text{ km s}^{-1}$  seems plausible. Existing VLBI datasets map only NGC 4261 continuum emission and do not cover the maser frequency range. A VLBI follow-up is required to determine a masing torus association.

### IRAS 20550+1656

We tentatively find broad megamasers in the LIRG/ULIRG irregular galaxy IRAS 20550+1656 (II Zw 96;  $v_{\text{LSR}} = 10837 \pm 10 \text{ km s}^{-1}$  (Giovanelli & Haynes 1993),  $D_{\text{L}} = 148 \text{ Mpc}$ ,  $z = 0.036$ ). With Arp 299, IRAS 20550+1656 may be the second galaxy that hosts megamasers of both the OH and  $\text{H}_2\text{O}$  species. The sensitivity was 5.8 mJy per  $0.3 \text{ km s}^{-1}$  channel and 1.5 mJy after 16-channel Gaussian smoothing. Two 9 mJy features are seen at  $\pm 110 \text{ km s}^{-1}$  around the recessional velocity. The combined isotropic luminosity of the blue  $10737 \text{ km s}^{-1}$  feature (9.0 mJy peak,  $102.8 \text{ km s}^{-1}$  FWHM) and the red  $10957 \text{ km s}^{-1}$  feature (9.1 mJy peak,  $96.4 \text{ km s}^{-1}$  FWHM) is relatively high with  $600 L_{\odot}$ . Narrower features seem to be symmetrically distributed around the systemic velocity, such as two offset by  $-380 \text{ km s}^{-1}$  and  $+420 \text{ km s}^{-1}$ . However, this could also be explained as a particularly pronounced baseline ripple. These and the broad features are, however, persistent over different smoothing settings for the nod reference spectra, and different baseline fits prior to averaging all subspectra. The broad masers have a post-fit confidence of somewhat better than  $5\sigma$ . The GBT integration time was 12 minutes, and additional time would be needed for a more robust detection, especially of the narrower features.

The object is an ongoing merger or close binary system with a peculiar rotation curve that is known to host an OH MM with 26 mJy peak and  $83.2 L_{\odot}$  luminosity (Andreasian 1992; Klöckner 2004). HI is seen in emission with an FWHM of about  $200 \text{ km s}^{-1}$  (van Driel et al. 2001). XMM-Newton observations found a single X-ray source and a high abundance of alpha process elements suggestive of starburst activity, but they could not rule out an AGN or AGN-starburst composite. The X-ray core is either very faint or has an  $N_{\text{H}} > 10^{24} \text{ cm}^{-2}$  (Inami et al. 2010; Mudd et al. 2012). Starburst activity would be consistent with earlier optical and IR spectroscopy (Goldader et al. 1997). The VLBI observations of the OH MM emission have placed it off-center in a merging system. The OH masers trace a 300 pc region around the second nucleus with a mass of  $10^9 M_{\odot}$  that has some probability of being a heavily obscured AGN (Migenes et al. 2011). Spitzer observations found starburst activity similar to extranuclear starbursts in NGC 4038/9 and Arp 299. In the latter, three maser regions are associated with both nuclear regions of Arp 299 and an overlap region (Tarchi et al. 2011). The spectrum of the

IRAS 20550+1656 water masers is also strongly reminiscent of that of NGC 2146 with its massive star formation kilomasers. The data are quite suggestive that IRAS 20550+1656 masers can be related to starburst and star-formation activity. The maser flux is unfortunately rather low for a VLBI follow-up.

## 4.5 Dual Maser Species

In the literature, there are five known sources (or six, if including uncertain OH masers in UGC 5101) that are known to host both OH and H<sub>2</sub>O maser species. These dual-species objects typically have a complex morphology and the masers are located in unrelated regions. Our two detections in ten searched OH maser objects increase the number of known dual-species objects to eight.

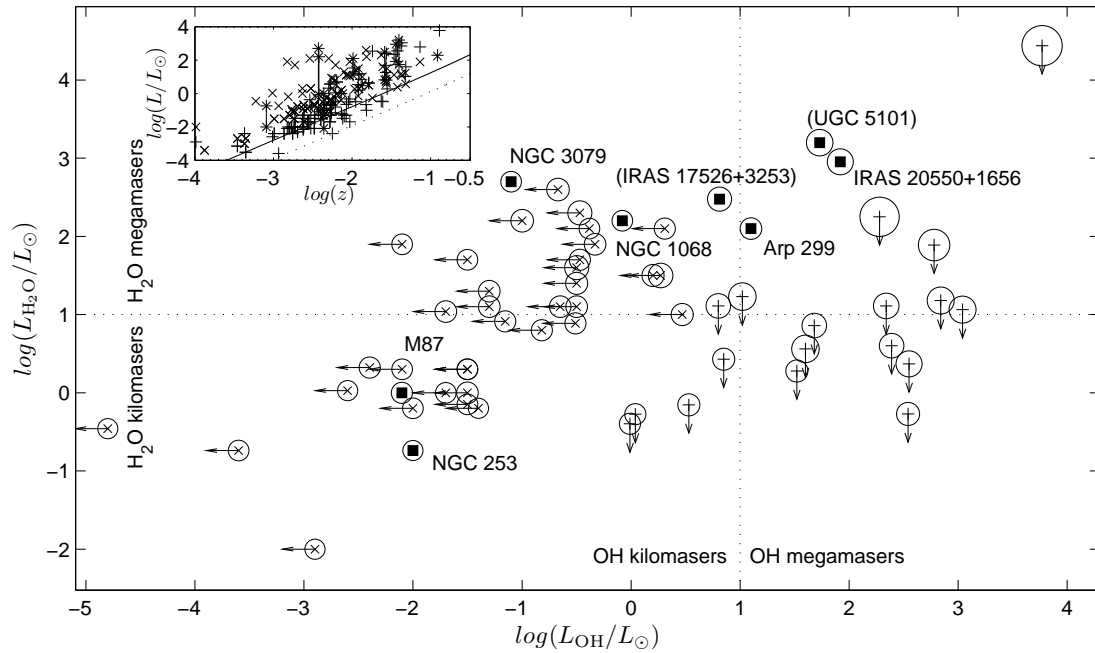


**Fig. 4.2:** Equivalent isotropic luminosities and  $3\sigma$  upper limits (arrows) for all 61 sources detected in one or both of the 1.6 GHz OH and 22 GHz H<sub>2</sub>O maser species, with 35 detected in H<sub>2</sub>O only (x) and 18 in OH only (+). The circle diameters are proportional to the source redshift. The OH MM sources tend to have a higher redshift. Masers of both species may be found in up to 8 sources (solid squares; source names given), with the caveat that the OH KM in UGC 5101 and IRAS 17526+3253 reported by Martin et al. (1989) were not detected in later (or earlier) observations. The inset shows OH and H<sub>2</sub>O luminosities or  $3\sigma$  upper limits against redshift for the 61 detected sources and for 34 sources undetected in either species. The H<sub>2</sub>O and OH detection thresholds (solid and dashed lines) assume 1.0 mJy rms and a 2.0 km s<sup>-1</sup> FWHM.

Tarchi et al. (2011) report 57 sources searched for both 1.6 GHz OH and 22 GHz H<sub>2</sub>O maser species. Six are detected in neither species, 45 in only one, and six in both species. Tarchi et al. also note a curious lack of H<sub>2</sub>O kilomasers in OH megamaser objects. Adding our sources and sources common to the 4038-entry H<sub>2</sub>O database and recent OH searches (Staveley-Smith et al. 1992; Klöckner 2004; Impellizzeri 2008; Willett et al. 2011), we find a total of 95 sources searched for both transitions, 34 detected in neither, 35 detected in H<sub>2</sub>O only, 18 in OH only, and about 8 detected in both species (if the two uncertain OH masers in UGC 5101 and IRAS 17526+3253 are included). This gives a total of 61 sources detected in at least one of the two maser species. Luminosities,  $3\sigma$  limits, and redshifts of these 61 detected sources are presented in Fig. 4.2. Luminosities against source redshifts for all 95 sources are shown in the inset. The upper limits of the nondetections have a median of  $0.04 L_{\odot}$  for OH and  $0.4 L_{\odot}$  for H<sub>2</sub>O. This demonstrates that a large fraction of H<sub>2</sub>O kilomasers ( $L < 10 L_{\odot}$ ) may go undetected. The difference in the two medians is partly due to the frequency proportionality of the isotropic luminosity in Eq. 4.1. An at least factor 13 higher sensitivity (lower mJy rms) is required for detecting H<sub>2</sub>O kilomasers at 22 GHz in a 1.6 GHz OH MM object. The probability of detecting a H<sub>2</sub>O KM in OH MM objects is further reduced by the higher average redshift of OH MM galaxies, with currently known H<sub>2</sub>O KM galaxies found at redshifts up to 0.014 and OH MM galaxies at redshifts between 0.010 and 0.264.

We can address the lack of H<sub>2</sub>O kilomasers in OH megamaser objects noted by Tarchi et al. with the now larger sample. In the two groups of OH maser galaxies, consisting of 10 OH KMs and 16 OH MMs, there are respectively 2 and no H<sub>2</sub>O KM detections (see Fig. 4.2). We treat upper limits as nondetections, and use the two-tailed Z-test for the null hypothesis that the H<sub>2</sub>O KM detection rate is identical in both OH KM and OH MM galaxies. The p-value of the Z-test is 0.063 and does not reach a significance level of  $p < 0.05$ . Consequently, H<sub>2</sub>O kilomasers are statistically just as frequent in OH MM objects as they are in OH KM objects.

The six reliable dual-species detections correspond to a conditional water maser detection rate of  $P(\text{H}_2\text{O}|\text{OH}) = 25\%$  in the 24 OH galaxies and to a detection rate of  $P(\text{OH} \cap \text{H}_2\text{O}|s_1) = 6\%$  for all  $N = 95$  targets selected for an OH search by some criteria  $s_1$ , such as a high infrared flux density. Over current searches, the average detection rate for OH is about  $P(\text{OH}|s_1) = 25\%$  (120 in 500) and about  $P(\text{H}_2\text{O}|s_2) = 4\%$  for H<sub>2</sub>O (150 in 4030), where the selection criteria  $s_2$  typically include starburst or AGN activity, X-ray luminosity, or a high absorbing column density  $N_{\text{H}}$ . Accounting for apparently mutually exclusive pumping mechanisms of the OH and H<sub>2</sub>O species and assuming selections  $s_1$  and  $s_2$  are independent (although Tarchi et al. 2004 find a significantly increased H<sub>2</sub>O maser detection rate in FIR-luminous sources), the lower bound for the expected probability of two species independently coinciding would be  $P(\text{OH} \cap \text{H}_2\text{O}|s_1, s_2) \geq 1\%$ . This is on the order of 6% of the  $N = 95$  dataset. However, an accurate estimate of the coincidence rate would require a detailed comparison of the potentially



different selection criteria of each of the 95 sources, and this is left as a subject of future work.

## 4.6 Conclusions and Summary

We detected water megamasers in four galaxies: three in OH galaxies, and one in a Sy 2 galaxy with no previous OH search. The OH MM galaxy IRAS 20550+1656 has a tentative starburst-like H<sub>2</sub>O MM detection, the presumed OH KM galaxy IRAS 17526+3253 has narrow 0.17 Jy systemic masers, and the 6 GHz OH absorber NGC 4261 (3C 270) with a twin jet hosts a likely jet maser. Disk masers were found towards the probable Sy 2 AGN in 2MFGC 13581. The black hole mass is unknown, but assuming a mass of  $10^7 M_{\odot}$  typical of AGN disk maser galaxies, the masing disk may be around 0.4 pc in diameter.

The lack of systemic features in 2MFGC 13581 makes this source unsuitable for angular diameter distance and Hubble constant measurements. However, a precise SMBH mass measurement for the  $M_{\text{BH}}-\sigma_{\star}$  relation may still be possible. The maser flux densities are very low for VLBI and a high-sensitivity VLBI array would be needed.

Masers in NGC 4261 are particularly interesting because the host galaxy is famous for its optical dusty torus. The maser profile, the morphology of the host galaxy, and the AGN classification is remarkably similar to the H<sub>2</sub>O galaxy NGC 1052. We would thus expect a VLBI map of NGC 4261 to produce masers in or near the molecular torus, pumped by the background twin-jet continuum, similar to the findings in NGC 1052 by Sawada-Satoh et al. (2008). A dual-frequency VLBA follow-up to map the NGC 4261 water masers and the previous detection of 6031/6035 MHz excited OH by Impellizzeri (2008) has already been proposed. However, the results of the observation will be subject of a future paper and are not a part of this thesis.

Finally, our detection of water masers in two OH maser galaxies updates the current count of six dual-species objects to eight. The conditional H<sub>2</sub>O detection rate in OH maser galaxies,  $P(\text{H}_2\text{O}|\text{OH}) = 25\%$ , is higher than the average 4% rate achieved in H<sub>2</sub>O maser searches. We could speculate that OH masers point towards systems with an overall larger molecular reservoir or a larger number of over-densities and shocked regions with more favorable conditions for also producing detectable luminous H<sub>2</sub>O maser emission.

The dual-species detections in a sample of 95 objects may also be explained by a statistically expected coincidence, rather than any causal connection, of two regions with suitable maser conditions in a single system. A more detailed analysis that inspects actual source selection criteria of each of the 95 sources is necessary. Such an analysis, not included in this thesis, is required to determine if the dual-species detections are indeed a coincidence, and whether the enhanced detection rate of H<sub>2</sub>O masers in extragalactic objects selected by the presence of OH masers is a result of the small dataset.

Table 4.2: Source sample of the 22 GHz H<sub>2</sub>O maser search

Source	Epoch	Position ( $\alpha_{2000}$ $\delta_{2000}$ )	$V_{\text{sys}}$ ( $\text{km s}^{-1}$ )	$1\sigma S_{22}$ (mJy)	$S_{22}$ (mJy)	$L_{22}$ ( $L_{\odot}$ )	$L_{1.6}$ ( $L_{\odot}$ )	$N_{\text{H}}$ ( $\text{cm}^{-2}$ )	Notes
01 IRAS 00160-0719 <sup>(a)</sup>	3	00:18:35.9 -07:02:56.0	5396	2.9	< 8.7	< 2.06			Sy2+HII
02 ESO 350-IG038 <sup>(a)</sup>	3	00:36:52.7 -33:33:17.0	6175	4.6	< 13.8	< 4.48			pair, LIRG, HII/SB
03 IRAS 00494-3056 <sup>(a)</sup>	3	00:51:51.8 -30:40:00.0	15529	5.3	< 15.9	< 34.86			SB, ULIRG
04 NGC 0315 <sup>(a)</sup>	3	00:57:48.9 +30:21:09.0	4942	3.0	< 9.0	< 1.54		$5.0 \times 10^{22}$	LINER(?), jet
05 NGC 0526A	1	01:23:54.4 -35:03:56.0	5725	4.3	< 12.9	< 3.62		$2.0 \times 10^{22}$	Sy1.9
06 IRAS 01418+1651	3	01:44:30.5 +17:06:05.0	8225	2.9	< 8.7	< 5.11	245.0		Sy2, LIRG
07 NGC 0833	1	02:09:20.8 -10:08:59.0	3864	2.9	< 8.7	< 1.05		$2.7 \times 10^{23}$	Sy2/LINER
08 NGC 0925 <sup>(a)</sup>	3	02:27:16.9 +33:34:45.0	553	2.7	< 8.1	< 0.03			LLAGN
09 IC 1858 <sup>(a)</sup>	1	02:49:08.4 -31:17:22.0	6070	3.5	< 10.5	< 3.41			LINER(?)
10 IRAS 02580-1136	1	03:00:30.6 -11:24:57.0	8962	3.5	< 10.5	< 8.37		$5.6 \times 10^{23}$	Sy2+HII, merger
11 NGC 1167 <sup>(a)</sup>	1	03:01:42.4 +35:12:21.0	4945	2.7	< 8.1	< 1.70		$3.0 \times 10^{21}$	Sy2/LINER, jet
12 NGC 1275 <sup>(a,b)</sup>	3	03:19:48.1 +41:30:42.0	5264	26.4	< 79.2	< 17.73		$1.5 \times 10^{22}$	Sy1.5
13 IRAS F04023-1638 <sup>(a)</sup>	1	04:04:40.6 -16:30:14.0	8643	3.1	< 9.3	< 6.37			n/a
14 IRAS 04332+0209	1	04:35:48.4 +02:15:29.0	3590	2.7	< 8.1	< 0.93	1.9		HII
15 MCG+02-21-013	2	08:04:46.4 +10:46:36.0	10323	4.1	< 12.3	< 12.93			pair, Sy2+Sy1
16 NGC 2974	2	09:42:33.3 -03:41:57.0	1919	3.0	< 9.0	< 0.27			Sy2, SF
17 ESO 374-IG032 <sup>(a)</sup>	2	10:06:05.1 -33:53:17.0	10223	5.3	< 15.9	< 16.49	724.0		LIRG, merger, pair
18 NGC 3341	-	10:42:31.5 +05:02:38.0	8196	-	-	-			Sy2+LINER+comp
19 UGC 05881	2	10:46:42.5 +25:55:54.0	6173	2.9	< 8.7	< 3.40		$2.5 \times 10^{24}$	LINER
20 NGC 3563B <sup>(a)</sup>	2	11:11:25.2 +26:57:48.9	10774	3.0	< 9.0	< 10.35			jet, FSRs
21 NGC 3655 <sup>(a)</sup>	2	11:22:54.6 +16:35:24.1	1473	2.8	< 8.4	< 0.39			HII
22 ESO320-G030 <sup>(a)</sup>	2	11:53:11.7 -39:07:49.0	3232	6.9	< 20.7	< 2.41	33.0		LIRG, SB, AGN
23 NGC 4261 <sup>(a,c)</sup>	2	<b>12:19:23.2 +05:49:31.0</b>	2238	3.1	<b>10.3</b>	<b>50</b>	abs.		LINER, twin-jet
24 NGC 4939 <sup>(a)</sup>	4	13:04:14.4 -10:20:23.0	3110	12.8	< 38.4	< 2.83		$1.6 \times 10^{23}$	Sy2
25 ESO 323-G077	-	13:06:26.1 -40:24:53.0	4501	-	-	-		$> 1.0 \times 10^{25}$	Sy2
26 UGC 8327	2	13:15:15.6 +44:24:26.0	11002	2.7	< 8.1	< 9.55		$5.5 \times 10^{23}$	Sy1.2/LINER
27 IC 4374 <sup>(a)</sup>	2	14:07:29.8 -27:01:04.3	6535	4.0	< 12.0	< 5.16		$5.2 \times 10^{22}$	Sy2+Sy2
28 NGC 5806	2	15:00:00.4 +01:53:29.0	1359	3.4	< 10.2	< 0.32		$> 8.0 \times 10^{21}$	FSRS, FRII
29 IRAS 15065-1107 <sup>(a)</sup>	2	15:08:49.1 -11:12:28.0	2105	3.6	< 10.8	< 0.53	1.1		Sy2
30 IRAS 15179+3956	4	15:19:47.1 +39:45:38.0	14261	2.9	< 8.7	< 16.92	10.5		pair
									2core, HII

Table 4.2: continued.

Source	Epoch	Position ( $\alpha_{2000}$ $\delta_{2000}$ )	$V_{\text{sys}}$ ( $\text{km s}^{-1}$ )	$1\sigma S_{22}$ (mJy)	$S_{22}$ (mJy)	$L_{22}$ ( $L_{\odot}$ )	$L_{1.6}$ ( $L_{\odot}$ )	$N_{\text{H}}$ ( $\text{cm}^{-2}$ )	Notes
31 Ark 481 <sup>(a)</sup>	2	15:39:05.2 +05:34:16.6	7781	3.3	< 9.9	< 5.82			n/a
32 IRAS 16399-0937	2	16:42:40.2 -09:43:14.0	8098	3.9	< 11.7	< 7.25	47.0		Sy2+HII/LINER
33 2MFGC13581	2+4	<b>16:58:15.5 +39:23:29.0</b>	10290	2.1	<b>25.5</b>	<b>290</b>			Sy2
34 IRAS 17208-0014	2+4	17:23:21.9 -00:17:01.0	12834	2.5	< 7.5	< 11.54	1090.0	$5.2 \times 10^{21}$	HII, LINER, SB
35 IRAS 17526+3253	4	<b>17:54:29.4 +32:53:14.0</b>	7798	5.3	<b>170</b>	<b>360</b>	6.5		ULIRG, LINER(?) Sy2+Sy2
36 UGC 11185NED01	2	18:16:09.4 +42:39:23.0	12426	3.0	< 9.0	< 12.81		$> 1.0 \times 10^{24}$	LIRG, HII, pair
37 IRAS 20550+1656	4	<b>20:57:23.9 +17:07:39.0</b>	10822	$5.8^{(d)}$	<b>9.1</b>	<b>600</b>		$> 6.0 \times 10^{23}$	Sy2/LINER/HII
38 NGC 7130	–	21:48:19.5 -34:57:04.0	4842	–	–	–		$1.9 \times 10^{23}$	Sy2/SB, SNIa
39 UGC 12237	3	22:54:19.7 +11:46:57.0	8476	3.1	< 9.3	< 7.01			Sy2/LINER,SB,HII
40 NGC 7742	3	23:44:15.8 +10:46:01.0	1663	1.8	< 5.4	< 0.13			

**Notes.** Epochs refer to observing dates (see Table 4.1). The three sources without epochs were not observed. Optical heliocentric recession velocities ( $V_{\text{sys}}$ ) are adopted from NED. The maser search covered  $V_{\text{sys}} \pm 1250 \text{ km s}^{-1}$ . The flux scale is accurate to better than 15%. Sensitivity ( $1\sigma S_{22}$ ) is the rms over the line-free 75% of the 200 MHz band and is derived from 24.4 kHz channels without smoothing. The peak flux ( $S_{22}$ ) and total equivalent isotropic luminosity ( $L_{22}$ ) are stated for detections (sources in bold; 23, 33, 35, 37). For non-detections,  $3\sigma$  upper limits on  $S_{22}$  and  $L_{22}$  are given, with  $L_{22}$  based on  $3 \cdot 1\sigma S_{22}$  and a  $2.0 \text{ km s}^{-1}$  FWHM Gaussian. Sources with hydroxyl (OH) masers are indicated in italic and the OH maser luminosities ( $L_{1.6}$ ) are adopted from Staveley-Smith et al. (1992); Impellizzeri (2008); Klöckner (2004); Willett et al. (2011). The 2–10 keV X-ray absorbing column densities ( $N_{\text{H}}$ ) are adopted from literature (Risaliti et al. 1999; González-Martín et al. 2009; Noguchi et al. 2009; Tan et al. 2012; Vasudevan et al. 2013). The last column shows the object classification adopted from NED and literature. Remarks: (a) Source has a previous published or unpublished  $\text{H}_2\text{O}$  non-detection (20 mJy to 200 mJy rms), with references on the WMCP or MCP project pages. (b) The velocity coverage on NGC 1275 was 3000 to 14000  $\text{km s}^{-1}$  (800 MHz) to include the infalling object at +3000  $\text{km s}^{-1}$ . (c) NGC 4261 exhibits HI in absorption at 1.4 GHz and OH in deep absorption at 6 GHz, but has not been searched for OH at 1.6 GHz (Impellizzeri 2008; van Lagenvelde et al. 2000). (d) Sensitivity on IRAS 20550+1656 was 5.8 mJy without smoothing and 1.5 mJy rms after 16-channel Gaussian smoothing.

## 5 Jet Water Masers in NGC 23

This Chapter presents results of a follow-up under the Megamaser Cosmology project on the NGC 23 (Mrk 545) water megamasers first detected in a 2005–2008 survey by Braatz & Gugliucci (2008). The Chapter partially follows a short paper to be submitted to the ApJ.

### 5.1 Abstract

The masers in NGC 23 have a spectral profile similar to the NGC 1052 or Mrk 348 “jet masers”. In single-dish monitoring with the Robert C. Byrd Green Bank Telescope (GBT) we detected two broad blueshifted features with a 10–45 km s<sup>-1</sup> full width at half maximum (FWHM) and also detect the possible emergence of a third narrower feature. The total equivalent isotropic luminosity of the detected maser emission was about 110  $L_{\odot}$ .

The bluemoost broad feature is unusual in that its central velocity appears to drift by  $+9.1 \pm 0.3$  km s<sup>-1</sup> yr<sup>-1</sup> towards the systemic velocity. In the first spectrum, observed in 2005 December, it had a central velocity of 4499 km s<sup>-1</sup>, blueshifted by about 70 km s<sup>-1</sup> from the recessional velocity. In the last spectrum, observed in 2009 November, it blended with a second maser feature. The second broad feature is blueshifted by about 25 km s<sup>-1</sup> from the recessional velocity. It appeared “stationary” with practically no drift, but narrowed in FWHM and increased in peak flux density with a timescale,  $\Delta t$ , of  $\sim 3 \cdot 10^8$  s, corresponding to an upper limit on  $c\Delta t$  of  $\lesssim 3$  pc.

Interferometric imaging with the Very Long Baseline Array (VLBA) and Karl G. Jansky Very Large Array (VLA) identified a single compact  $< 0.11$  mas maser distribution. The maser distribution exhibited a steep velocity gradient of 13720 km s<sup>-1</sup> mas<sup>-1</sup>, or about  $0.046c$  mas<sup>-1</sup>, which might be explained by a low viewing angle if the maser distribution is spatially extended in the direction of the line of sight. The masers appear located within  $44 \pm 33$  pc of a compact component in 1.6 GHz and 4.8 GHz VLA continuum images that has a brightness temperature of  $1.6 \times 10^3$  K, typical of a starburst. It is the only component detected at 4.8 GHz and is not detected at 14.8 GHz. For the 22 GHz continuum we find a conservative upper limit of 1 mJy beam<sup>-1</sup>. This non-detection above 4.8 GHz suggests that the radio-quiet NGC 23 may be dominated by compact, steep-spectrum emission. We find no direct evidence of a jet. If the megamasers are

of star formation origin, they have an exceptionally high equivalent isotropic luminosity. Alternatively, the blueshift and the fast drift of the bluest feature may indicate material entrained in an approaching low luminosity (undetected) jet that is mass-loaded and truncated at parsec scales off a heavily obscured AGN core, with the “stationary” spectral feature closest to the observer and past the jet. Simultaneous 22 GHz maser monitoring and multi-wavelength light curves may be required to determine the nature of the NGC 23 megamaser emission.

## 5.2 Introduction

Extragalactic water vapor megamasers ( $\nu_0 = 22.23508$  GHz;  $L_{\text{H}_2\text{O}} > 10 L_\odot$ ) are generally associated with jets, outflows or sub-parsec accretion disks surrounding the nuclear engine of active galaxies. In the galaxies NGC 1068, NGC 1052, and Mrk 348, very long baseline interferometry (VLBI) imaging has revealed some H<sub>2</sub>O masers (“jet masers”) to be located along the radio jet (Gallimore et al. 1996; Claussen et al. 1998; Peck et al. 2003). Generally jet masers are thought to reside in post-shock regions of jet-cloud interactions, but Sawada-Satoh et al. (2008) suggest that jet masers in NGC 1052 are related to the torus of the Seyfert Unification scheme (see, e.g., Bianchi et al. 2012; Antonucci 1993), with dense molecular clouds in the torus amplifying the seed radio continuum emission by the background jet components. In either case, the spectral signature of most jet associated 22 GHz H<sub>2</sub>O masers appears to be a redshifted broad  $\sim 100$  km s<sup>-1</sup> emission profile, with a high luminosity that sets it apart from the sometimes broad emission of star formation kilomasers ( $\lesssim 1 L_\odot$ ) as in, e.g., NGC 253 (Hofner et al. 2006) and Cen A (Ott et al. 2013).

The water megamaser galaxy NGC 23 (Mrk 545, IRAS 00073+2538) is classified as a luminous infrared galaxy (LIRG) with a luminosity of  $L_{\text{IR}} = 10^{11.05} L_\odot$  (Sanders et al. 2003) and a 100  $\mu\text{m}$  flux density of 15 Jy (Moshir et al. 1990). Its optical redshift,  $z=0.015231$  (Huchra et al. 1999), corresponds to a recessional velocity,  $V_{\text{LSR}}$ , of  $4570 \pm 2$  km s<sup>-1</sup> in the kinematic local standard of rest reference frame (LSR) in the optical velocity definition ( $V_{\text{LSR}} \equiv cz$ ). Given the redshift determined by Huchra et al. (1999) the NASA/IPAC Extragalactic Database (NED) estimates a luminosity distance of  $\approx 58.5$  Mpc. This gives a scale of 0.28 pc/mas. The adopted recessional velocity of  $4570 \pm 2$  km s<sup>-1</sup> is based on the optical redshift of NGC 23 (Huchra et al. 1999). Other redshifts found in the recent literature also include  $\lambda 21$  cm H I line based redshifts (Haynes et al. 2011; Springob et al. 2005). They are consistent with the above optical recessional velocity within  $\pm 3$  km s<sup>-1</sup>. Regarding the nature of NGC 23, the literature suggests that NGC 23 is a likely AGN/nuclear starburst composite, but that it is starburst-dominated with the bulk of IR luminosity due to star formation, both in the nucleus as well as in a starforming ring  $\sim 7''$  from the core with a younger stellar population (Alonso-Herrero et al. 2009, 2012).

Braatz & Gugliucci (2008) detected broad  $\sim 30$  km s<sup>-1</sup> FWHM water megamaser emission

towards NGC 23 in 2003 July. The emission is blueshifted relative to the systemic recession velocity. The spectrum of 2006 November published in Braatz & Gugliucci (2008), averaged with three previously unpublished epochs and one new epoch, is shown in Fig. 5.1. The slightly asymmetric and overall broad  $\sim 50$  kms FWHM maser spectral profile resembles that of “jet masers” and the maser emission is over a factor of 10 too luminous for star formation kilomasers. With AGN activity but no jet, NGC 23 appears to present an enigmatic case of “jet-like” masers in absence of any known kiloparsec-scale radio jet. Braatz & Gugliucci (2008) suggest that high-resolution imaging might resolve the issue whether masers in NGC 23 are associated with an AGN or with star formation.

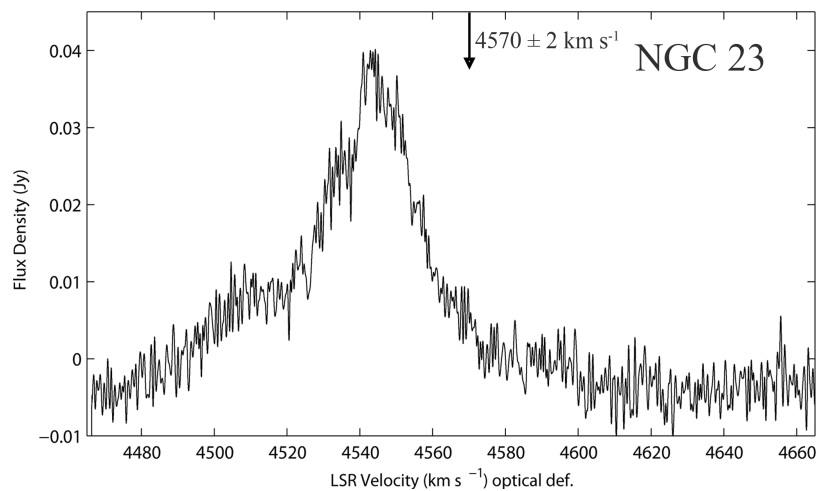


**Fig. 5.1:** The rms-weighted integrated spectrum of five GBT epochs (see Table 5.1) peaks at  $\sim 40$  mJy. The channel spacing is  $0.34 \text{ km s}^{-1}$  and the noise is  $2.8 \text{ mJy rms}$  in  $0.34 \text{ km s}^{-1}$  wide channels.

### 5.3 Observations and Data Reduction

We conducted 22 GHz single-dish monitoring with the National Radio Astronomy Observatory (NRAO<sup>1</sup>) Robert C. Byrd Green Bank Telescope (GBT), and carried out radio interferometric observations with the Karl G. Jansky Very Large Array (VLA), and with the NRAO Very Long Baseline Array (VLBA). The VLA observations were conducted during the construction phase of the Expanded Very Large Array (EVLA).

The Braatz & Gugliucci (2008) detection was followed up with one new GBT epoch and we include three previously unpublished GBT epochs in the analysis. The absolute position of

<sup>1</sup>The National Radio Astronomy Observatory is a facility of the National Science Foundation operated under cooperative agreement by Associated Universities, Inc.

### 5.3 Observations and Data Reduction

the maser region was estimated in a VLA K band observation. To provide a large-scale context we further reduced a multi-wavelength L, C, and U band VLA continuum observation found in NRAO archival data. The archival data are part of the Parra et al. (2010) survey of compact objects in low-power AGN (COLA) that inspects the starburst–AGN connection, e.g., whether Eddington-limited circumnuclear starbursts can feed the central black hole in the AGN with gas from the galactic disk (Corbett et al. 2003; Parra et al. 2010). The VLA array included new EVLA antennas during the K-band observation, while the multi-wavelength observations had a more consistent array configuration with only VLA antennas. Lastly, the VLBA was used to image the K band maser distribution at high resolution.

The single-dish and radio interferometric observations of NGC 23 are listed in Table 5.1. The interferometric observations were phase-referenced. The phase reference quasars and their position uncertainties are also provided in Table 5.1.

**GBT** The single-dish observations followed the setup and data reduction described in Braatz et al. (2010). We used the GBT K band Focal Plane Array in a dual beam switched mode. The GBT spectrometer had a  $0.34 \text{ km s}^{-1}$  velocity resolution with 8192 channels over 200 MHz. The flux density scale was calibrated via noise injection ( $T_{\text{cal}}$ ), and accounting for pointing uncertainties (3-8'' relative to the GBT beamwidth of 36'' at 22 GHz) was accurate to about 15%. The spectra were calibrated in GBTIDL. We fit Gaussian components to the maser spectral features to estimate their central velocity, peak flux density, and line width.

Table 5.1. Single-Dish and Radio Interferometric Epochs on NGC 23.

Date	Instrument	Band	Project Code	Phase reference quasar <sup>c</sup> ( $\Delta\text{RA mas} \times \Delta\text{DEC mas}$ )	Beam size and PA (arcsec; deg)	RMS (mJy beam <sup>-1</sup> )
2003 Jul 20 <sup>a</sup>	VLA-A	L	AC0685	J0019+2021 ( $\pm 0.11, \pm 0.10$ )	$1.65 \times 1.54; -25.1^\circ$	0.78 <sup>d</sup>
2003 Jul 20 <sup>a</sup>	VLA-A	C	AC0685	J0019+2021 ( $\pm 0.11, \pm 0.10$ )	$0.47 \times 0.43; -29.0^\circ$	0.10
2003 Jul 20 <sup>a</sup>	VLA-A	U	AC0685	J0019+2021 ( $\pm 0.11, \pm 0.10$ )	$0.16 \times 0.15; -44.0^\circ$	0.18
2005 Dec 14	GBT	K	AGBT05C-051-11	...	34	12.1 <sup>e</sup>
2005 Dec 18	GBT	K	AGBT05C-051-12	...	34	5.4
2006 Oct 03	GBT	K	AGBT06A-014-07	...	34	5.7
2006 Nov 26 <sup>b</sup>	GBT	K	AGBT05C-051-26	...	34	5.0
2008 Feb 22	(E)VLA-CnB	K	BG187	J0019+2602 ( $\pm 0.20, \pm 0.38$ )	$1.13 \times 0.43; 69.8^\circ$	5.15
2009 Nov 28	GBT	K	AGBT08C-035-25	...	34	5.1
2010 Apr 04	VLBA	K	BG187A	JVAS J0010+2619 (n/a)	$0.77 \times 0.40 \cdot 10^{-3}; 19.7^\circ$	1.05 (0.08) <sup>f</sup>

Note. — <sup>a</sup>NRAO archival data. <sup>b</sup>The detection published in Braatz & Gugliucci (2008). <sup>c</sup>The phase reference source name in the IVS or JVAS catalogues. The position uncertainties (J2000) are from L. Petrov, rfc.2014a. <sup>d</sup>Over the whole IF for VLA continuum data. <sup>e</sup>The K-band spectral line sensitivity in 24.4 kHz channels for GBT data, and 391 kHz for the (E)VLA data. <sup>f</sup>The VLBA K band sensitivity is for 250 kHz channels, and the sensitivity after averaging all 64 channels/subband over 4 subbands is given in parentheses.

**VLA** The archival multi-wavelength VLA snapshot observation was phase-referenced. It had two 50 MHz continuum bands. The data reduction in NRAO AIPS (Bridle & Greisen 1994)

included flagging and phase calibration against a reference quasar. The flux density scale was calibrated on 3C 48 using the source models included in AIPS that gave a 3C 48 total flux density of 15.9 Jy at L-band, 5.34 Jy at C-band, and 1.76 Jy at U-band. The calibration was followed by several passes of imaging and phase self-calibration of the visibility data using the clean components of the latest image as the source model (e.g., Cornwell & Fomalont 1989).

The phase-referenced VLA K band spectral line observation had a bandwidth of 12.1 MHz. We followed the standard high-frequency reduction method described in the VLA Calibrator Manual<sup>1</sup>. The high-frequency reduction yielded a sensitivity of 5.2 mJy beam<sup>-1</sup> in 391 kHz wide channels. However, the compact phase reference quasar and the amplitude calibration source produced a large number of closure phase errors on all baselines, including baselines between the old VLA antennas, and between the new EVLA antennas. This indicated a potential issue with the VLA spectral line hardware setup. Nevertheless the data yielded an acceptable point source image of the quasar reference. The phase solutions were then applied to NGC 23.

**VLBA** The phase-referenced VLBA observation was scheduled with geodetic blocks for atmospheric corrections (e.g., Brunthaler et al. 2005) and recorded four 16 MHz bands in dual polarization. One band was centered on the broad maser feature and the other bands were placed on the presumed detectable continuum. The visibility data were calibrated and reduced in AIPS generally as described in Paper I of the Megamaser Cosmology Project Reid et al. (2009). Phase referencing failed as the reference quasar had a K band flux density of  $\sim 40$  mJy (Davies et al. 2013), and the atmospheric phase solutions produced an image of the quasar but not of NGC 23. However, self-calibration against a  $\sim 15$  km s<sup>-1</sup> window around the 40 mJy peak maser emission succeeded, albeit phase solutions had signal-to-noise ratios (SNRs) not larger than 3 to 5. We transferred the phase solutions to the continuum bands, velocity averaged the calibrated data to  $\sim 3.2$  km s<sup>-1</sup> channels using a sliding boxcar with 50 % overlap, and produced a final Stokes I image cube with a resolution of  $0.03 \times 0.03 \times 3.2$  mas<sup>2</sup> km s<sup>-1</sup>.

## 5.4 Results

The sensitivities achieved in the epochs are listed in Table 5.1. A rms-weighted average of the GBT spectra is shown in Fig. 5.1. The individual spectra and their best-fit Gaussian components are shown in Fig. 5.2 and the components are also listed in Table 5.2. We detect two broad spectral features of about 35 km s<sup>-1</sup> FWHM at a  $10\sigma$  to  $70\sigma$  confidence. Both appear blueshifted relative to the recessional velocity.

<sup>1</sup><http://www.vla.nrao.edu/astro/calib/manual/>



### 5.4.1 Single-Dish Results

The more prominent maser feature near  $4545 \text{ km s}^{-1}$  had a central velocity that remained quite stable and changed over time (“drifted”) by only  $-0.3 \pm 0.1 \text{ km s}^{-1} \text{ yr}^{-1}$  ( $1\sigma$ ). It narrowed in FWHM by  $-7.1 \pm 0.2 \text{ km s}^{-1} \text{ yr}^{-1}$  while brightening in flux density,  $S$ , by about  $+4.7 \pm 0.4 \text{ mJy yr}^{-1}$ , with a near-constant (except for the 2009 epoch) equivalent isotropic luminosity. This could point towards a slow increase in the optical depth; in unsaturated masers a larger optical depth causes the spectral width to narrow, with a simultaneous increase in intensity (Dopita & Sutherland 2003). The variability time scale of the changes in the flux density was about  $\Delta t \sim S/\dot{S} \sim 3 \cdot 10^8 \text{ s}$ , or  $\sim 9$  years. This constrains the size of the emission region (the background seed photon source, or the masing region if variability is intrinsic) to  $c\Delta t \lesssim 3 \text{ pc}$ , or  $< 11 \text{ mas}$ . The flux density increase and a  $< 11 \text{ mas}$  region correspond to a brightness temperature,  $T_b$ , increasing by  $\Delta T_b > 10^5 \text{ K}$ . It would be indicative of an AGN if this increase were correlated with the continuum flux, alas, no 22 GHz continuum emission was detected and no flux monitoring data are available.

Conversely, the bluemost feature in the GBT spectrum shows a relatively stable peak flux density, with a possible slight increase by  $2.1 \pm 0.5 \text{ mJy yr}^{-1}$ . The feature appears to broaden in width by  $+6.8 \pm 1.1 \text{ km s}^{-1} \text{ yr}^{-1}$  FWHM, corresponding to an increase in the equivalent isotropic luminosity. We also find an unusual high velocity drift of  $+9.1 \pm 0.3 \text{ km s}^{-1} \text{ yr}^{-1}$ . This apparent drift rate in the line is similar to that of the systemic masers in the disk maser galaxy NGC 4258 that drift at a rate of 7.7 to  $8.9 \text{ km s}^{-1} \text{ yr}^{-1}$  (Humphreys et al. 2008). Also the sign of the drift (i.e. redward) is consistent with centripetal acceleration.

In the (latest) 2009 epoch the above “bluemost” feature blended with the more prominent blueshifted feature, and a possible third feature newly emerged (Table 5.2 and Fig. 5.2).

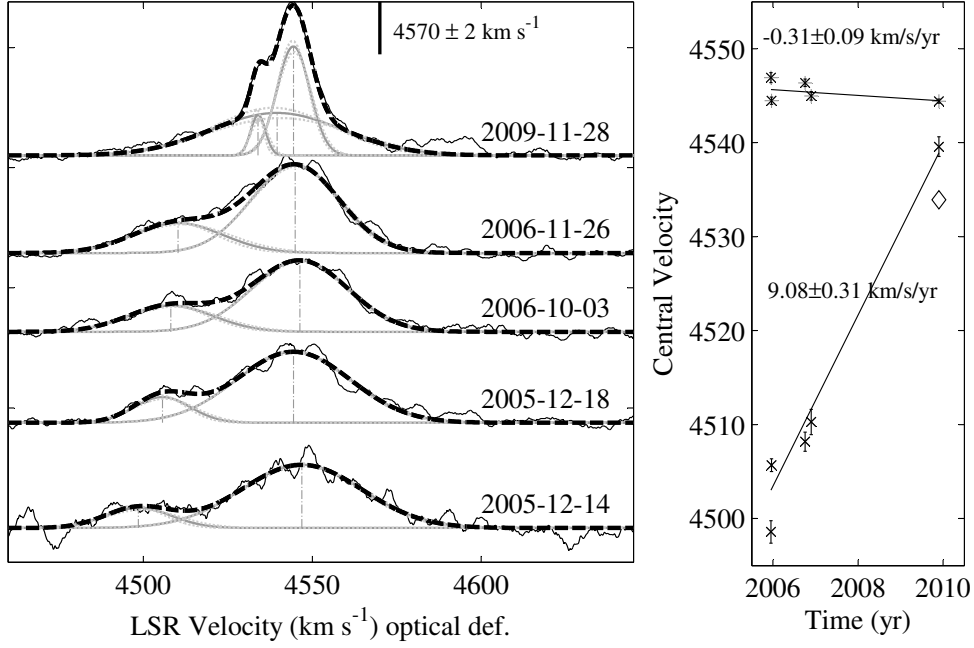


**Fig. 5.2:** The GBT epochs, smoothed with a  $10 \text{ km s}^{-1}$  Savitzky-Golay shape-preserving filter, together with Gaussian components fit to the original data (left). The recession velocity is indicated above. The component central velocities, shown with formal  $1\sigma$  uncertainties, appear to change with time (right). The empty diamond in the upper right indicates the third component that is new to the 2009 epoch. The flux densities of all components are provided in Table 5.2.

Table 5.2. Spectral Features in GBT Epochs.

Date	$S \pm \sigma_S$ (mJy)	$v \pm \sigma_v^{(a)}$ ( $\text{km s}^{-1}$ )	$w \pm \sigma_w^{(b)}$ ( $\text{km s}^{-1}$ )	$L \pm \sigma_L$ ( $L_\odot$ )
2005-12-14	$26.3 \pm 0.6$	$4546.93 \pm 0.53$	$42.13 \pm 1.45$	$92 \pm 4$
	$8.4 \pm 0.8$	$4498.58 \pm 1.20$	$23.08 \pm 2.95$	$16 \pm 3$
2005-12-18	$29.6 \pm 0.4$	$4544.48 \pm 0.38$	$39.62 \pm 0.98$	$97 \pm 3$
	$10.7 \pm 0.7$	$4505.68 \pm 0.69$	$19.65 \pm 1.80$	$17 \pm 2$
2006-10-03	$29.7 \pm 0.4$	$4546.37 \pm 0.40$	$33.45 \pm 0.89$	$82 \pm 2$
	$10.9 \pm 0.4$	$4508.18 \pm 1.01$	$29.52 \pm 2.11$	$26 \pm 2$
2006-11-26 <sup>(c)</sup>	$36.5 \pm 0.5$	$4544.98 \pm 0.46$	$30.77 \pm 0.85$	$93 \pm 3$
	$12.5 \pm 0.5$	$4510.28 \pm 1.35$	$31.28 \pm 2.68$	$32 \pm 3$
2009-11-28	$45.4 \pm 2.3$	$4544.42 \pm 0.21$	$11.42 \pm 0.67$	$43 \pm 3$
	$17.7 \pm 2.1$	$4539.58 \pm 1.06$	$45.71 \pm 4.22$	$67 \pm 10$
	$16.8 \pm 2.3$	$4533.98 \pm 0.37$	$5.19 \pm 0.37$	$7 \pm 2$

Note. — <sup>a</sup>The line central velocity in the LSR reference frame. <sup>b</sup>The width  $w$  is FWHM ( $2.355\sigma$ ). The mean equivalent isotropic luminosity is shown for reference and is based on the peak flux density,  $S$ , and the FWHM width,  $w$  (see Eq. 4.2). <sup>c</sup>A new fit of the epoch published in Braatz & Gugliucci (2008).

### 5.4.2 VLA Results

Does NGC 23 launch a radio jet? It appears unlikely, at least a jet is not directly evident in the VLA images (Fig. 5.3). Although the 1.4 GHz (L band) continuum image shows diffuse structure and a center region with bright components, the strongest with a  $5.5 \text{ mJy beam}^{-1}$  peak flux density, at 4.8 GHz (C band) only a single unresolved component was detected. The C band component has a diameter of  $\sim 0.50 \pm 0.01 \text{ asec}$  ( $\sim 140 \text{ pc}$ ) and a peak flux density of  $5.2 \text{ mJy beam}^{-1}$ . Its location coincides with the L band image peak. The C band component has a  $T_b$  of  $\sim 1.6 \times 10^3 \text{ K}$ , well below that of an AGN or jet. Starbursts on the other hand typically reveal  $T_b < 10^5 \text{ K}$  (Condon et al. 1991). The component has a flattish spectrum between 1.4 GHz and 4.8 GHz. No emission was detected at 14.9 GHz (U band) at a  $5\sigma$  level of  $0.9 \text{ mJy beam}^{-1}$  rms, suggesting the component has a steep turnover between 4.8 GHz and 14.9 GHz with a spectral index of  $\alpha \lesssim -1.5$  (for a  $S \propto \nu^\alpha$  power law).

The NGC 23 water maser region is shown overlaid on the C band continuum in Fig. 5.4 (inset in left panel). The masers appear to be located close to the strong L and C band component, with a small RA offset of  $0.16 \pm 0.12''$  ( $44 \pm 33 \text{ pc}$ ).

By combining the position of the VLA 22 GHz (C band) component with the K band maser detection we find a new tentative position for NGC 23. The new position, with conservatively inflated uncertainties, is  $0^{\text{h}}09'53.43'' \pm 0.04''$   $25^{\circ}55'25.90 \pm 0.01''$  (J2000;  $3\sigma$ ). This estimated position is within 430 mas of the latest position given by the 2MASS  $2 \mu\text{m}$  survey (Skrutskie et al. 2006) that has an uncertainty of  $1.25''$ .

### 5.4.3 VLBA Results

The VLBA image of the maser and continuum bands (Fig. 5.4 left) reached an image noise of  $0.08 \text{ mJy beam}^{-1}$  rms. No continuum components were detected. In individual  $\sim 3.2 \text{ km s}^{-1}$  velocity channels the stronger masers ( $\text{SNR} > 5$ ) appeared to occupy a compact  $0.11 \times 0.08 \text{ mas}$  ( $< 0.03 \text{ pc}$ ) region (Fig. 5.4, middle). The diameter of the region is comparable in size to the nominal  $3\sigma$  uncertainty of the position fit of  $0.09 \text{ mas}$ . The peak integral maser flux density over this compact region was  $17.6 \pm 0.2 \text{ mJy}$ , corresponding to a  $T_b$  of  $> 7 \times 10^9 \text{ K}$ , in agreement with the apparent brightness temperature of  $\sim 10^{10} \text{ K}$  typical of 22 GHz water masers.

The maser positions are given in Table A.6.1, see Appendix A.6. The maser positions along the best-fit position angle of  $48.1 \pm 7.7^\circ$  are shown against velocity in the Fig. 5.4 PV diagram (right). The PV diagram shows a steep slope of  $13720 \text{ km s}^{-1} \text{ mas}^{-1}$  or  $0.046c \text{ mas}^{-1}$ . The maser distribution in the PV diagram is consistent to  $1.5\sigma$  with a single maser group, rather than clearly distinct maser groups. The two features in the GBT epoch closest to the VLBA observation (Fig. 5.2) would thus appear to originate from the same region. This may be explained by

masers spatially arranged along a radial direction, with two groups at different radial distances that are moving at different velocities towards the observer at a low viewing angle. Although the steep PV slope is peculiar, similar steep slopes in position against velocity are also seen for the presumed “jet masers” (or “obscuring torus masers”) of the twin-jet galaxy NGC 1052, see Figs. 4 and 5 in Sawada-Satoh et al. (2008).

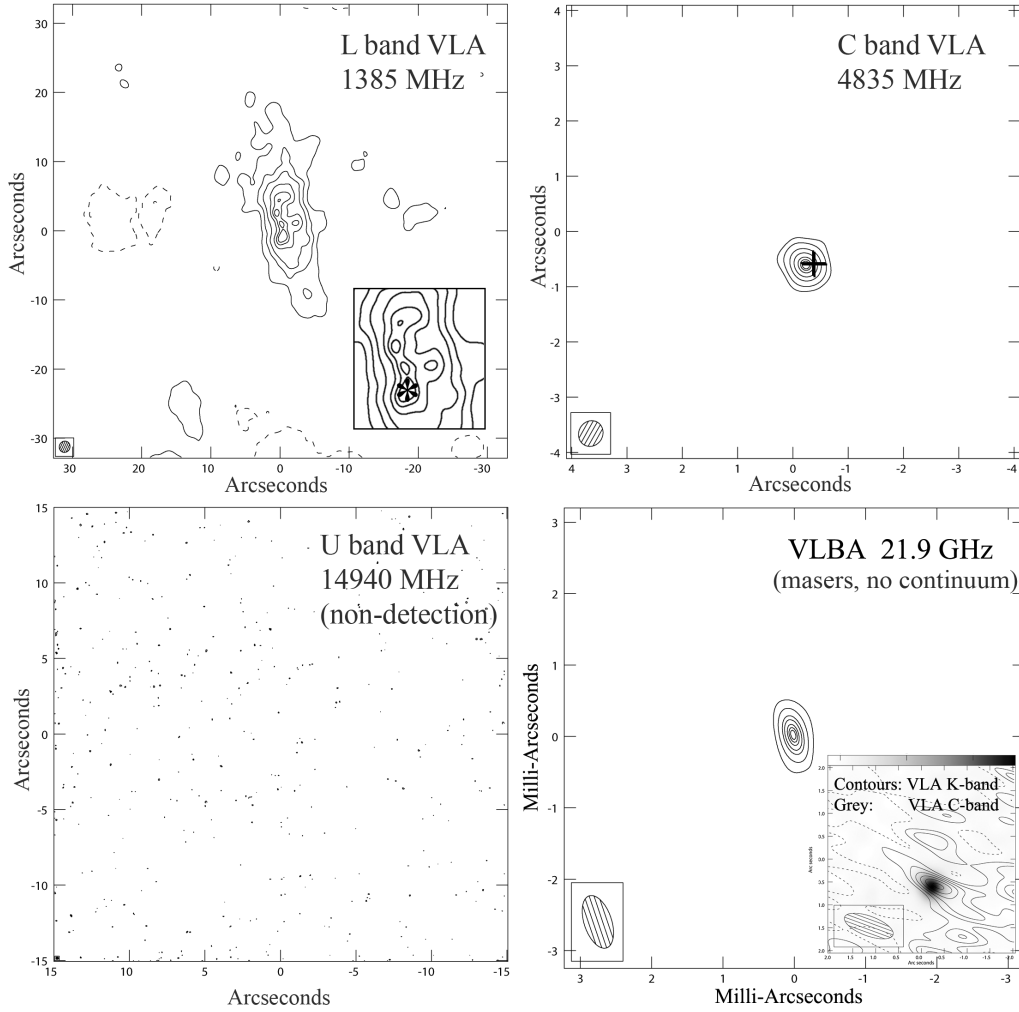


**Fig. 5.3:** The multi-wavelength VLA images of NGC 23 showing the L band continuum (top left), C band continuum (top right), the U band continuum non-detection (bottom left), and the K band VLBA maser map (bottom right), and the K band VLA maser map (inset, bottom right). The L band emission peak (asterisk in inset, top left) coincides with the location of the compact C band component. Conversely, the K band VLA H<sub>2</sub>O maser detection closely coincides with the C band component, indicated by a cross (top right). The masers appears offset by  $0.16 \pm 0.12''$   $0.0 \pm 0.07''$  from the C band component. All coordinates are relative to  $00^{\text{h}}09^{\text{m}}53.45^{\text{s}}$   $25^{\circ}55'26.50''$  (J2000) and the axes span  $\pm 30''$ ,  $\pm 4''$ , and  $\pm 15''$  for the three respective VLA images,  $\pm 2.0''$  in the K band VLA (inset, bottom right), and about  $\pm 3$  mas in the K band VLBA image.

The L band VLA contours are at -10, 10, 20, 40, 80, 90, 95, and 98 % of the peak. The C band VLA contours are at -10, 10, 50, 75, 85, 90, 95, 98, and 100 % of the peak. The U band VLA image (a non-detection) contours are at -60, 60, 80, 90, 95, 98 % of the peak to reduce the noise. The K band VLBA contours (showing only the maser detection) are at -15, 15, 50, 75, 90, 95, and 98 % of the peak and the contours of the poorer K band VLA maser detection are at -30, 30, 50, 70, 80, 90, 95, and 98 % of the peak.

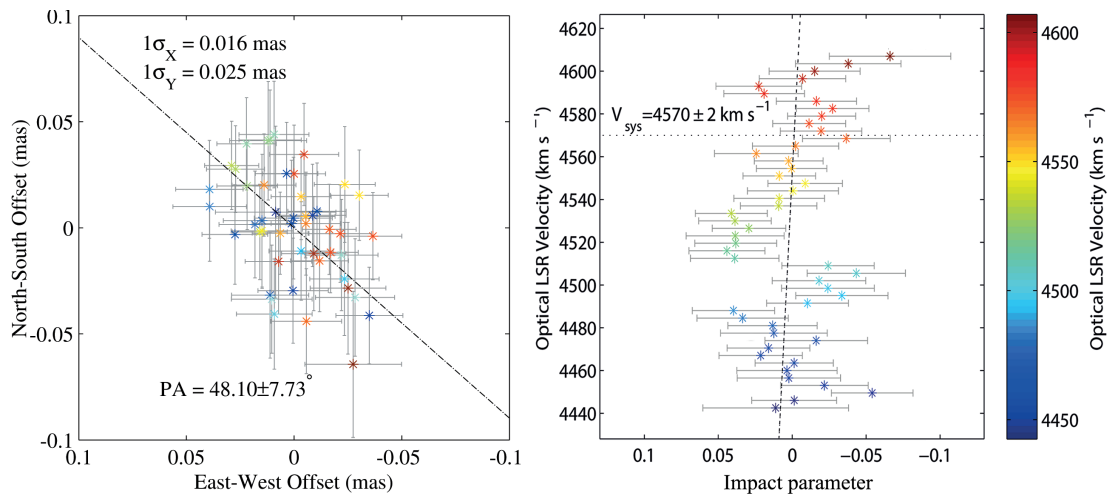


**Fig. 5.4:** Water masers in NGC 23. Masers but no continuum are detected in the VLBA image (left). Coordinates are relative to the  $\sim 4545 \text{ km s}^{-1}$  maser peak. The VLA K band maser emission, a low quality detection, is overlaid on the C band continuum (left inset). The strong VLBA maser features with  $\text{SNR} \geq 5$  (middle) have a steep gradient in position against velocity (right). Error bars indicate  $1\sigma$  uncertainties.

## 5.5 Discussion

As the optical spectroscopy by Alonso-Herrero et al. (2009) suggests, the IR luminosity of NGC 23 is starburst-dominated and NGC 23 may be an AGN/starburst composite. The X-ray observation by Walther (2012) provides an upper limit on the  $L_{20-100 \text{ keV}}$  luminosity of  $1.2 \times 10^{42} \text{ erg s}^{-1}$ , consistent with either an AGN that is of the low-luminosity type (a LLAGN), or an LLAGN/starburst composite. If we assume NGC 23 hosts an (LL)AGN, the  $L_{2-10 \text{ keV}}$  luminosity may be estimated from the  $[\text{O III}]_{\lambda 5007}$  luminosity (see § 5.2 in Panessa et al. 2006). The  $[\text{O III}]_{\lambda 5007}$  flux density of  $1.2 \times 10^{-14} \text{ erg s}^{-1} \text{ cm}^{-2}$  measured by Zhu et al. (2011) corresponds to a luminosity of  $4.9 \times 10^{39} \text{ erg s}^{-1}$ , which according to the relation given by Panessa et al. produces an estimated  $L_{2-10 \text{ keV}}$  luminosity of  $\sim 10^{40.8} \text{ erg s}^{-1}$ . This is also consistent with the  $L_{20-100 \text{ keV}}$  upper luminosity limit by Walther. This would support the assumption that NGC 23 indeed hosts a LLAGN.

Spectral data in the NED database further suggest that NGC 23 is radio quiet. In addition, the low continuum level of  $74.3 \pm 2.7 \text{ mJy}$  at 1.4 GHz (total VLA flux, Condon et al. 1998), and  $8.0 \pm 1.8 \text{ mJy}$  at 23.1 GHz (single-dish, Bica et al. 1995), does not suggest the presence of a strong radio core nor a radio jet. If NGC 23 contains an AGN, it is indeed radio-quiet and low luminosity, or dust-enshrouded and “hidden”, and the jet is either absent or very weak.

It is unclear whether the detected velocity drift of one of the blueshifted maser features reflects actual gas motion, or whether it is a pattern velocity. A pattern velocity might result from, e.g., an X-ray flare after episodic feeding of the central black hole in the galaxy. The blueshifted maser features may arise as the flare propagates through a rotating clumpy medium and heats molecular clouds in the medium to sufficiently high temperatures ( $\sim 400$  K) for collisional  $\text{H}_2\text{O}$  maser excitation. A propagating flare appears inconsistent, however, with the slow increase in isotropic luminosity while the blueshifted maser feature drifts towards the recessional velocity during the 4 years of GBT epochs, and would require a radially increasing density and clumpiness of the medium.

On the other hand, the VLBA image constrains masers to a  $< 0.03$  pc region that, according to the K band and C band VLA data, is within  $44 \pm 33$  pc of the single compact C band component. The component detected in C band has a starburst-like brightness temperature, and due to the relatively high positional uncertainty a spatial association of masers with an intense starburst region is not entirely ruled out. In contrast, even a (LL)AGN association is plausible, if the putative C band starburst region traces a nuclear starburst near a radio-undetected AGN core. In disk maser galaxies, for example, the AGN core is generally undetected by VLBI. In fact, the compact sub-0.03 pc maser distribution in NGC 23 and the fast velocity drift of one of the two blueshifted features would be typical of systemic masers in a masing AGN accretion disk such as in NGC 4258 (Humphreys et al. 2008). Yet the broadness of the drifting NGC 23 maser feature and its initial high blueshift of  $70 \text{ km s}^{-1}$  would be relatively atypical of the sub-pc disk masers seen in other active galaxies (e.g., Braatz et al. 2010; Impellizzeri et al. 2012; Kuo et al. 2013). NGC 23 also lacks the narrow (typically  $< 10 \text{ km s}^{-1}$  FWHM) high-velocity ( $\gtrsim 200 \text{ km s}^{-1}$ ) maser features seen in masing accretion disks. It thus appears unlikely that the NGC 23 masers are (LL)AGN disk masers.

The galaxy NGC 23 is thus not suitable for a maser-based black hole mass measurement, nor for a maser-based angular diameter distance and Hubble constant measurement.

Speculatively, the high-drift feature in the GBT spectra and the overall maser blueshift might be related to matter in an LLAGN outflow or a shell expanding towards the observer that interacts with the interstellar medium (ISM) near a core and slows down via ISM pile up, with the “stationary” broad blueshifted masers at the dense end of the pile up. Similarly, as low-luminosity jets launched by  $\lesssim 10^4 M_\odot$  central engines can be significantly decelerated at pc scales by small obstacles like stellar winds and stars (see, e.g., Huarte-Espinosa et al. 2013; Hubbard & Blackman 2006), the feature might also be related to material (clouds, disrupted stars) entrained in an approaching, truncated low luminosity jet ( $\ll 10^{42} \text{ erg s}^{-1}$ ). A low-luminosity jet launched by the LLAGN may be heavily mass loaded, and effectively terminate spatially close to the location of the “non-drifting” maser component. A low-luminosity truncated jet would also be consistent with the relatively low maser velocity offsets from the systemic velocity, as would also a low-

velocity outflow under inefficient jet launching. A low-luminosity jet (or outflow) association, with two maser groups nearly along the line of sight towards the core, would agree best with the compact VLBI maser distribution, the distinct maser groups in the GBT spectra, and the high maser luminosity.

Lastly, if a jet is absent and if masers are not associated with a disk, jet, or outflow of an LLAGN, the high maser luminosity of  $110 L_{\odot}$  may also be the result of cumulative emission by star formation kilomasers associated with LIRGs, and the masers might be associated with nuclear or extranuclear star formation. Both activities have been detected in NGC 23 (e.g., Alonso-Herrero et al. 2009, 2012). Fridman et al. (2005) find possible evidence in H $\alpha$  line observations of a radial, or rather, anomalous “non-circular”, gas motion at blueshifts of -170 to -200 km s $^{-1}$  and at redshifts of 130 to 200 km s $^{-1}$ . They estimate a non-circular motion projected along the line of sight of higher than 100 km s $^{-1}$ , in some agreement with the blueshifted GBT maser velocities. Fridman et al. consider that the anomalous motion may be the result of nuclear activity or an active star formation in the nucleus. They further detect HII-region -like emission line intensity ratios that are not consistent with a Sy 2 AGN or LINER, which again would not support a disk maser association (all AGN disk masers to date have been detected in Sy 2 and LINER galaxies). While the gas traced by H $\alpha$  lines may itself be unrelated to the H $_2$ O maser regions, the star formation activity that may drive this gas at larger scales is generally thought to pump 22 GHz maser emission via producing shocked regions (e.g., Ott et al. 2013). The blueshifted maser velocities may thus be indirectly related to the anomalous gas motion observed by Fridman et al. If the NGC 23 masers are indeed the result of cumulative emission by several star formation regions, these masers would be the most luminous star formation water masers to date.

## 5.6 Summary and Conclusions

The nature of the megamaser emission in NGC 23 remains elusive. For an association with a low-luminosity jet or outflow in a (LL)AGN, the maser distribution that was detected in VLBI would require a relatively peculiar geometry. The outflow or jet traced by maser emission would have to be directed towards the observer. There is some evidence of star formation and star-burst activity, and the maser distribution does not rule out a star formation association. For star formation masers the maser luminosity would however be exceptionally high.

Further observations may be required to determine the nature of the NGC 23 megamaser emission. Such observations should include simultaneous 22 GHz maser monitoring and multi-wavelength light curves to search for radio flaring and correlation between maser and continuum flux densities.



# 6 A Black Hole Mass Measurement for Megamaser Galaxy UGC 3193

This Chapter partially follows a paper to be submitted to the ApJ, and similar to Chapter 5, it presents the results of single-dish and interferometric follow-ups under the Megamaser Cosmology Project (MCP) of the 22 GHz water megamasers in the galaxy UGC 3193.

The megamaser emission towards UGC 3193 was first detected in a 2005–2008 survey by Braatz & Gugliucci (2008), the same survey that led to the maser detection towards NGC 23. Unlike the “jet maser” or star formation maser galaxy NGC 23, however, UGC 3193 masers have clear evidence of an accretion disk association. The spatial distribution and kinematics of the UGC 3193 maser emission are highly suggestive of a (near-)Keplerian sub-parsec accretion disk around the nuclear engine. The disk masers allow a high-precision measurement of the mass,  $M_{\text{BH}}$ , of the central supermassive black hole (SMBH).

The mass determined in this Chapter of  $0.61 \pm 0.17 \times 10^6 M_{\odot}$  for a Keplerian model fit with relativistic corrections (or  $0.8 \pm 0.5 \times 10^6 M_{\odot}$  for a direct fit without corrections and with a fixed SMBH position) may be combined with a measurement of the stellar velocity dispersion,  $\sigma_{\star}$ , in the galactic bulge. While currently still the subject of a future optical observation, a stellar velocity dispersion measurement will provide a new  $M_{\text{BH}}-\sigma_{\star}$  sample for the diverse  $M_{\text{BH}}-\sigma_{\star}$  relations (see, e.g., Greene et al. 2010; McConnell et al. 2011). This will allow further insight to the currently debated AGN feeding and feedback models with SMBHs at the low-mass end.

**Conventions:** As in Chapter 5 the velocities are in the kinematic local standard of rest reference frame (LSR) and are given in the optical velocity definition,  $v_{\text{opt}} \equiv cz \equiv c(\nu_0/\nu_{\text{obs}} - 1)$ , where  $\nu_0$  is the rest frequency of the 22 GHz water maser line,  $\nu_0 = 22.23508$  GHz.

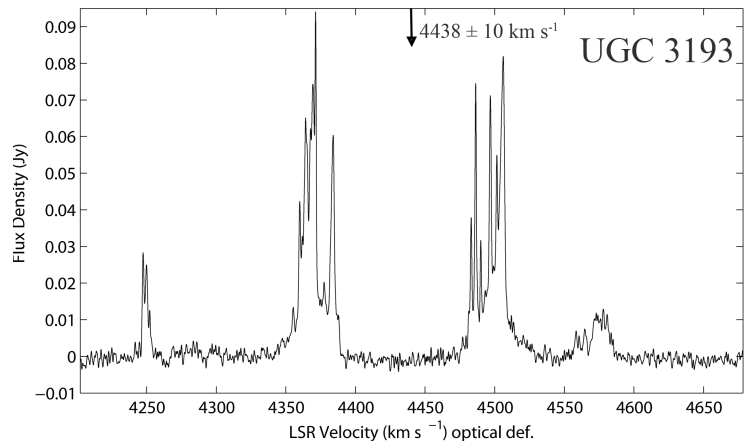


**Fig. 6.1:** The 22 GHz GBT water maser detection towards UGC 3193. The spectrum is an rms-weighted average of all 8 epochs (see Table 6.1) with a sensitivity of 1.2 mJy rms in  $0.33 \text{ km s}^{-1}$  wide channels. The recessional velocity is indicated at the top of the figure.

## 6.1 The Megamaser Galaxy UGC 3193

The barred spiral galaxy UGC 3193 ( $z=0.01486$ ; de Vaucouleurs et al. 1991) has a redshift-based recessional velocity of  $4438 \pm 10 \text{ km s}^{-1}$ . We adopt an angular diameter distance,  $D_A$ , of  $59.5 \pm 0.1 \text{ Mpc}$  that is based on the de Vaucouleurs et al. redshift and a fiducial cosmology with a Hubble constant,  $H_0$ , of  $73 \text{ km s}^{-1} \text{ Mpc}^{-1}$ , and density parameters,  $\Omega_\Lambda = 0.73$  and  $\Omega_m = 0.27$ , for dark energy and for mass (both baryonic and dark), respectively, as is also used by the NASA/IPAC Extragalactic Database (NED) at the time of writing. The currently only redshift-independent distance for UGC 3193 is that of Theureau et al. (2007) who find a Tully-Fisher luminosity distance of  $64.1 \pm 11.8 \text{ Mpc}$ , corresponding to an angular diameter distance of  $62.2 \pm 11.5 \text{ Mpc}$ . The galaxy UGC 3193 lacks an optical spectral type classification. Some indication of the nature of activity in UGC 3193 may be given by the total infrared (IR) luminosity. The galaxy has the mid to far infrared flux densities of 0.14 Jy, 0.28 Jy, 2.64 Jy, and 5.67 Jy, at  $12 \mu\text{m}$ ,  $25 \mu\text{m}$ ,  $60 \mu\text{m}$ , and  $100 \mu\text{m}$ , respectively (Moshir et al. 1990). These translate into a total IR luminosity of about  $10^{10.58} L_\odot$  using the method by Wouterloot & Walmsley (1986b). The IR luminosity is below the  $10^{11} - 10^{12} L_\odot$  range of luminous IR galaxies (LIRGs), but well above that of the Milky Way ( $10^{10.08} L_\odot$ ) and similar to those of local starburst galaxies like NGC 253 ( $10^{10.5} L_\odot$ ) and M 82 ( $10^{10.8} L_\odot$ ).

Water megamasers towards UGC 3193 were first detected by the Braatz & Gugliucci (2008) water maser survey. The single-dish maser spectrum towards UGC 3193 is shown in Fig. 6.1, and is an rms-weighted average of the Braatz & Gugliucci epoch and eight other epochs. The spectrum exhibits four high-velocity (HV) maser groups that span a total of  $\sim 350 \text{ km s}^{-1}$  sym-

metrically around the systemic recession velocity. Braatz & Gugliucci estimate a total equivalent isotropic luminosity of  $\sim 270 L_{\odot}$  for the HV features, but detect no maser emission at the systemic recessional velocity. They speculate that discrete rings or a spiral density pattern in an accretion disk could produce the four HV spectral groups, and that the systemic features may be undetected due to an unsuitable disk inclination, a disk warp, or a lack of background continuum emission that would seed the systemic maser emission.

Apart from the maser detection there are no 22 GHz flux density data on UGC 3193. Two 1.4 GHz observations with the Karl G. Jansky Very Large Array (VLA) find a 1.4 GHz flux density of about 18 mJy (Condon et al. 2002, 1998).

As already indicated by the radio continuum data, UGC 3193 is not known to contain an AGN. The typical AGN signature in the IR spectrum, a 25–60  $\mu\text{m}$  color index that is “warm” ( $-1.5 \leq \alpha_{25,60} \leq 0$ ;  $F \propto \nu^{\alpha}$ ), is absent in UGC 3193. Instead, UGC 3193 appears IR “cold” with an  $\alpha_{25,60}$  color index of -2.56. The IRAS flux density ratios, another AGN criteria (e.g., Desert & Dennefeld 1988), do not show any strong AGN-like signature. These limited IR data suggest that UGC 3193 might be energetically dominated by star formation processes. However, the spectral symmetry and the high luminosity of the water masers is more typical of an AGN accretion disk rather than the less luminous ( $\lesssim 1 L_{\odot}$ ) star formation kilomasers. An upper X-ray luminosity limit of  $L_{20-100\text{keV}} < 10^{42} \text{ erg s}^{-1}$ , but no absorbing column density, is given in Walther (2012) who list a *Swift*/BAT X-ray satellite observation of UGC 3193 under alias MASER 045252.7+0303. The upper luminosity limit allows for a low luminosity AGN (LLAGN;  $L_X \sim 10^{42} \text{ erg s}^{-1}$ ) or an obscured Compton-thick nucleus.

## 6.2 Single Dish Observations

Single dish monitoring at 22 GHz was conducted with the National Radio Astronomy Observatory (NRAO<sup>1</sup>) Robert C. Byrd Green Bank Telescope (GBT). The GBT epochs and one additional Effelsberg radio telescope (EB) epoch are listed in Table 6.1.

For the GBT observations the same setup and data reduction as in Braatz et al. (2010) and as in § 5.3 was followed. The galaxy UGC 3193 was observed with the K-band Focal Plane Array (KFPA) in dual polarization and in a dual beam-switched mode. The flux density scale was calibrated using noise injection ( $T_{\text{cal}}$ ) and accounting for pointing errors was accurate to about 15%. The GBT spectrometer backend was configured for 8192 channels and a bandwidth of 200 MHz with two identical frequency windows overlaid to increase the sensitivity in Stokes I.

The GBT spectra were calibrated in GBTIDL and the EB epoch was reduced in CLASS. Bad sub-integrations and bad channels containing local radio frequency interference were flagged.

---

<sup>1</sup>The National Radio Astronomy Observatory is a facility of the National Science Foundation operated under cooperative agreement by Associated Universities, Inc.

Table 6.1. Single Dish and Interferometric Epochs on UGC 3193.

Date	Project	Sensitivity (mJy rms)	Date	Project	Sensitivity (mJy rms)
2005 Nov 03	AGBT05C-051-05	4.2	2010 Feb 25	AGBT09C-051-05	3.6
2005 Nov 20	AGBT05C-051-08 <sup>a</sup>	2.7	2010 Jun 11	(BG187B VLBA)	–
2006 Apr 11	AGBT06A-022-02	5.2	2010 Nov 28	AGBT10A-014-04	11.2
2008 Feb 23	(BG187 VLA-CnB)	2.8 <sup>b</sup>	2012 Jul 09	Effelsberg <sup>c</sup>	21.0
2008 Nov 11	AGBT07A-066-52	2.0	2012 Sep 26	GBT technical time	11.8
2009 Nov 16	AGBT08C-035-24	3.4	2012 Oct 17	(BB313Z HSA)	0.13 <sup>d</sup>

Note. — The sensitivities are in  $0.33 \text{ km s}^{-1}$  wide spectral channels. Interferometric epochs are in parentheses. <sup>a</sup>The GBT epoch published in Braatz & Gugliucci (2008). <sup>b</sup>The image noise in  $\text{mJy beam}^{-1}$  rms in  $\sim 1 \text{ km s}^{-1}$  wide channels and a beam size of  $1.07 \times 0.51 \text{ asec}$ . <sup>c</sup>The Effelsberg epoch was provided by B. Winkel (private comm.). <sup>d</sup>The image noise in  $\text{mJy beam}^{-1}$  rms in Stokes I over the full bandwidth of  $4 \times 16 \text{ MHz}$  with a  $1.6 \times 0.4 \text{ mas}$  beam.

Smoothed blank-sky reference spectra were subtracted to remove standing waves and ripple, and third order baseline fits were subtracted from the individual sub-integrations prior to averaging the data into a final spectrum for each epoch with a resolution of  $0.33 \text{ km s}^{-1}$  per channel. The EB epoch was observed with a setup largely identical to the GBT configuration. The EB observation primarily verified the maser flux density before a second interferometric follow-up. The single-dish sensitivities are listed in Table 6.1.

An rms-weighted integrated spectrum of water masers towards UGC 3193 is shown in Fig. 6.1 and the nine epochs are shown separately in Fig 6.2. The sensitivity after an effective integration time of about 5.5 hours was  $1.2 \text{ mJy rms}$  in  $0.33 \text{ km s}^{-1}$  wide channels. The integrated line profile was  $3.25 \text{ Jy km s}^{-1}$  with a respective total isotropic maser luminosity of  $\sim 270 L_{\odot}$  (Eq. 4.1). Four distinct HV groups were detected. The masers had relatively narrow line widths ( $\lesssim 10 \text{ km s}^{-1}$  FWHM), and the individual maser features were discernible despite some minor blending of the lines. Interestingly, as in Braatz & Gugliucci (2008), no maser emission was detected at the recessional velocity, despite an over a factor of 4 times higher sensitivity.

### 6.3 Fitting of Maser Accelerations

The single dish monitoring data were used in spectral line fitting and to determine the drift in the maser central velocities, i.e., the maser line accelerations,  $a_i$ , in units of  $\text{km s}^{-1} \text{ yr}^{-1}$ .

Assuming that the masers trace orbits at different radii in a Keplerian disk, as is suggested by the symmetry of the UGC 3193 maser emission, the acceleration and velocity data may be

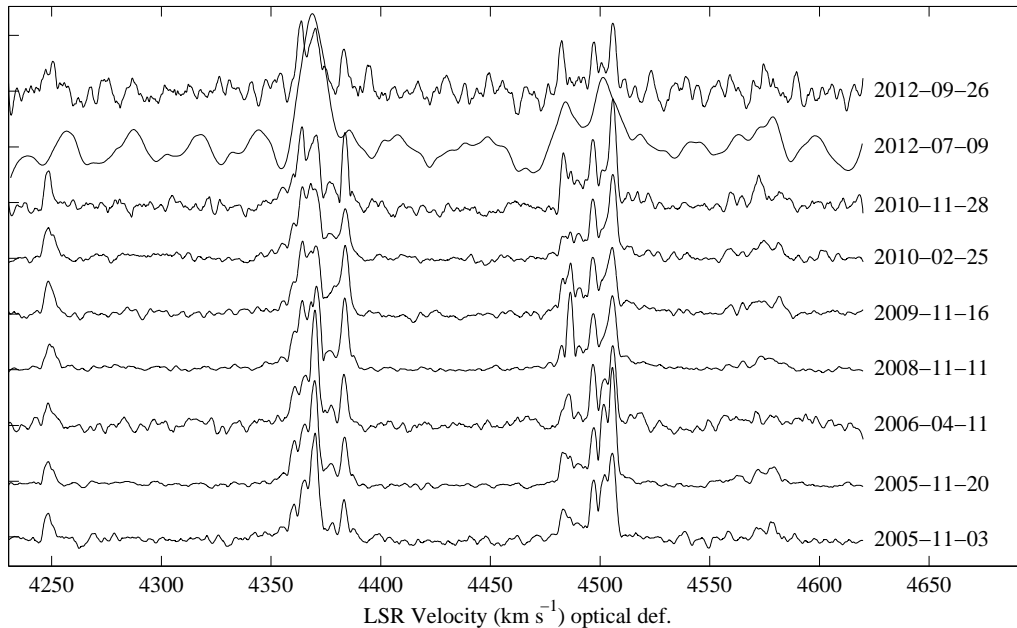


**Fig. 6.2:** Spectra of the eight 22 GHz GBT epochs on UGC 3193. For clarity the noise has been reduced by smoothing with a Savitzky–Golay filter with a  $5.2 \text{ km s}^{-1}$  wide window.

used in fitting a Keplerian disk model (see Appendix A.4). For the high-velocity maser features that are located along the midline of a circumnuclear accretion disk, the line of sight (LOS) projection of the orbit acceleration (see Eq. A.15 in Appendix A.4) is expected to be zero ( $a_i \simeq 0$ ). Conversely, systemic masers located on the near side of the disk, along the LOS towards the core, would show the full range of non-zero radial accelerations, typically between  $1 \text{ km s}^{-1} \text{ yr}^{-1}$  to  $10 \text{ km s}^{-1} \text{ yr}^{-1}$  (see, e.g., Bragg et al. 2000; Humphreys et al. 2008; Braatz et al. 2010; Yamauchi et al. 2012). Usually no emission is seen from other regions of the disk. This is generally attributed to the viewing angle, with the longest velocity coherent paths along the LOS, and thus the strongest maser amplification, are achieved only in the aforementioned regions.

The velocity drifts were determined for individual maser lines, or groups of lines, that were detected across several epochs. Below we summarize the four fitting methods. The first two methods produced estimates for the maser accelerations that were adopted as highly approximate a priori starting values for an acceleration fit with the other two methods.

**Accel I** – Manual fits in GBTIDL employed an IDL script by C. Y. Kuo (private comm.). Also a new Matlab<sup>®</sup> (2010) script was used. Both scripts allow to manually select peaks in the spectra, cross-identify the maser peaks between epochs, and perform a linear least squares (LLSQ) fit to

determine the approximate velocity drift.

**Accel II** (cross-correlation) – The spectra were first interpolated by a factor 32. A spline interpolant was selected to avoid Runge’s phenomenon, i.e., oscillation. Spectral cross-correlations were then formed between epoch-pairs to locate the peak in velocity offset. A linear velocity drift was fit to these offsets using LLSQ and weights proportional to the time separation of the epoch pairs. For single lines and non-blended groups the accelerations agreed reasonably well with those of the Accel I method. Variability in flux density was problematic in fitting groups with blended lines. Discarding the absolute amplitude information via taking the signum of the discrete first derivative of the spectra as input to Accel II did, however, not improve the performance. For blended groups the least squares Accel IIIa/b fit below performed better.

**Accel IIIa and IIIb** (iterative least squares) – The approximate expected range of the maser accelerations was estimated with the methods above. The final accelerations were derived with the two approaches outlined in Reid et al. (2013) and they used the accelerations determined above as loose a priori starting values. The first fitting method (IIIa), or Method-1 in Reid et al., has a parameter set consisting of the number of Gaussians, their amplitudes, full width at half maximum (FWHM) line widths, accelerations, and initial velocities in a freely specified reference epoch, chosen to be the date of the closest interferometric epoch(s). The second method (IIIb), or Method-2 in Reid et al., replaces the independent maser accelerations with two parameters, an average acceleration,  $a_0$ , and a acceleration-velocity gradient,  $da/dv$ . Both fitting methods perform a weighted non-linear least squares fit to find the parameters that produce the lowest reduced  $\chi^2$ . To reduce the impact of local minima and to be less sensitive to the initial parameter selection, the fit is repeated several times, typically 100 times, with randomized different initial values. The accelerations given by the overall best fits, if they were consistent, were selected as the final values for the maser accelerations.

## 6.4 Maser Accelerations in UGC 3193

The best acceleration fits in terms of reduced  $\chi^2$  were produced by Accel IIIa and are given in Table 6.2. The weighted arithmetic mean accelerations,  $\hat{a}_w$ , were calculated for the accelerations of all masers in a group and are given at the end of Table 6.2 in the form  $\hat{a}_w \pm \sigma_{\hat{a}} \pm \sigma_w$ , where  $\sigma_{\hat{a}}$  is the unbiased standard deviation of the weighted mean, and  $\sigma_w$  is the weighted standard deviation of the data. The accelerations are shown against velocity in Fig. 6.3.

Some epoch pairs processed with Accel I and Accel II had possibly associated HV features that exhibited sign reversals in their acceleration (although accelerations were small, with  $|a| < 0.1 \text{ km s}^{-1} \text{ yr}^{-1}$ ). The reversal in drift may occur if masers cross the disk midline at the periapsis

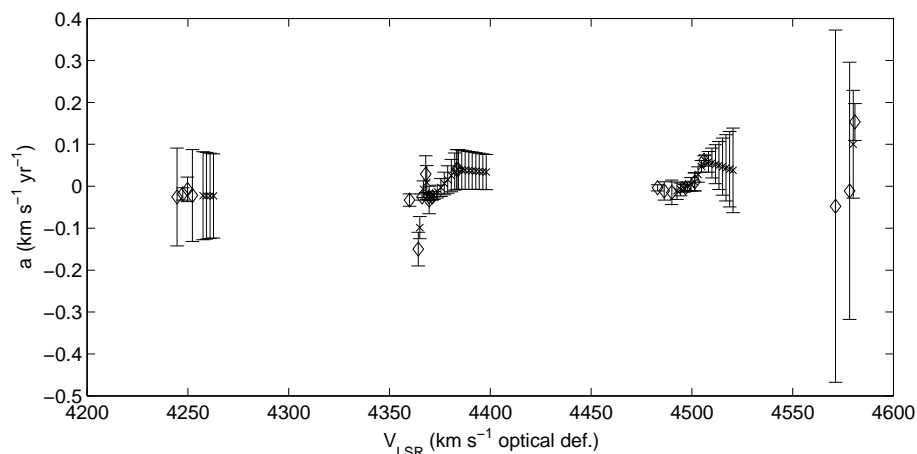


**Fig. 6.3:** The Accel IIIa best-fit UGC 3193 maser accelerations and  $1\sigma$  uncertainties.

of a highly eccentric orbit. However, the separation of epoch pairs of up to 2 years (Table 6.1) precludes a robust cross-identification of these features. The final accelerations in Table 6.2 are thus based on Accel IIIa with an a priori acceleration of zero and a velocity that drifts over time at a constant rate rather than at a changing rate.

While the blueshifted HV groups show a slightly negative and the redshifted HV groups a slightly positive mean acceleration, no high trust is placed into these fits. The mean accelerations are possible artefacts of the long epoch separation, noise, and a possible slight variability in flux density. In general, most of the distinctive maser features in Fig. 6.2 were remarkably stable in peak flux density and in central velocity over nearly 7 years. This is similar to the HV features in other disk maser galaxies such as NGC 4258, UGC 3789, IC 2560 and NGC 6264 that have been typically monitored for 5 years or less (Humphreys et al. 2008; Braatz et al. 2010; Yamauchi et al. 2012; Kuo et al. 2013). In these galaxies very long baseline interferometry (VLBI) has been able to spatially associated the HV features with the midline of a slowly rotating thin Keplerian accretion disk. It appears plausible that the UGC 3193 masers have a similar disk midline association.

Table 6.2. The best-fit accelerations of the maser features in UGC 3193.

Bluemost group		Blue group		Red group		Redmost group	
$v_{\text{LSR}}$ ( $\text{km s}^{-1}$ )	$a \pm \sigma_a$ ( $\text{km s}^{-1} \text{yr}^{-1}$ )	$v_{\text{LSR}}$ ( $\text{km s}^{-1}$ )	$a \pm \sigma_a$ ( $\text{km s}^{-1} \text{yr}^{-1}$ )	$v_{\text{LSR}}$ ( $\text{km s}^{-1}$ )	$a \pm \sigma_a$ ( $\text{km s}^{-1} \text{yr}^{-1}$ )	$v_{\text{LSR}}$ ( $\text{km s}^{-1}$ )	$a \pm \sigma_a$ ( $\text{km s}^{-1} \text{yr}^{-1}$ )
4244.68	$-0.0256 \pm 0.1169$	4360.02	$-0.0329 \pm 0.0146$	4483.05	$-0.0037 \pm 0.0073$	4571.32	$-0.0475 \pm 0.4200$
4247.57	$-0.0183 \pm 0.0146$	4364.29	$-0.1497 \pm 0.0402$	4486.36	$-0.0110 \pm 0.0219$	4578.29	$-0.0110 \pm 0.3068$
4249.80	$-0.0073 \pm 0.0292$	4366.20	$-0.0256 \pm 0.0073$	4490.07	$-0.0146 \pm 0.0292$	4580.91	$+0.1534 \pm 0.0438$
4252.24	$-0.0219 \pm 0.1096$	4368.00	$+0.0292 \pm 0.0438$	4496.84	$-0.0037 \pm 0.0073$	...	...
...	...	4369.69	$-0.0329 \pm 0.0329$	4501.55	$+0.0110 \pm 0.0219$	...	...
...	...	4369.70	$-0.0256 \pm 0.0073$	4506.12	$+0.0621 \pm 0.0110$	...	...
...	...	4371.36	$-0.0256 \pm 0.0073$	...	...	...	...
...	...	4383.35	$+0.0402 \pm 0.0475$	...	...	...	...
...	...	4384.12	$+0.0402 \pm 0.0475$	...	...	...	...
$\hat{a}_w: -0.016 \pm 0.003 \pm 0.008$		$-0.026 \pm 0.005 \pm 0.018$		$+0.007 \pm 0.011 \pm 0.029$		$+0.148 \pm 0.022 \pm 0.125$	

Note. — Weighted mean accelerations,  $\hat{a}_w$ , are shown below each respective group, with the two  $1\sigma$  uncertainties corresponding to the unbiased standard deviation of the weighted mean,  $\sigma_{\hat{a}}$ , and the weighted sample variance,  $\sigma_w$ , respectively.

## 6.5 Interferometric Observations

The maser distribution in UGC 3193 was mapped in K-band VLBI observations conducted with the Very Long Baseline Array (VLBA) and with the High Sensitivity Array (HSA). The HSA consists of the VLBA and the large GBT and EB telescopes. In addition, a K-band VLA track was scheduled to improve the coordinates of the maser galaxy.

### 6.5.1 A New VLA Position for UGC 3193

The current coordinates for UGC 3193 are given by the 2MASS near-infrared  $2 \mu\text{m}$  survey and have an uncertainty of  $1.25''$  (Skrutskie et al. 2006). The VLA K-band observations were conducted by N. Gugliucci under the MCP project in 2008 February with the VLA in CnB configuration. The data were reduced in NRAO AIPS (Bridle & Greisen 1994) using the standard low-frequency and high-frequency approaches (see the VLA Calibrator Manual<sup>1</sup>). The high-frequency reduction achieved a sensitivity of  $2.8 \text{ mJy beam}^{-1}$  in  $\sim 1 \text{ km s}^{-1}$  wide channels. The water maser emission but no continuum was detected. The non-detection provides a conservative upper limit of  $20 \text{ mJy}$  ( $7\sigma$ ) on the  $22 \text{ GHz}$  continuum emission in UGC 3193 at scales smaller than the VLA beam size of  $1.07'' \times 0.51''$ .

The new UGC 3193 coordinates were determined using the two data reduction approaches above were in good agreement. They also agreed with the 2MASS position. The updated position is that of the HV maser group at  $4575 \text{ km s}^{-1}$ , the only group covered by the VLA setup, and is tied to the quasar PKS J0459+0229 of the International Celestial Reference Frame 2 (ICRF2)

<sup>1</sup><http://www.vla.nrao.edu/astro/calib/manual/>



catalog. The quasar has a 0.05 mas position uncertainty and is within  $1.8^\circ$  of UGC 3193. The formal uncertainty given by the VLA high-frequency reduction was 31 mas, which is wider than the masing disk found in the VLBA observation (further below) that has a diameter smaller than 10 mas. Propagating these position and fit uncertainties, and accounting for a 10 mas uncertainty in the black hole position (though presumably located at the center of the masing disk), produced a new UGC 3193 position of  $4^h52^m52^s.557 \pm 0^s.004$ ,  $3^\circ03'25''.73 \pm 0''.05$  (J2000). The position has an uncertainty of 50 mas ( $1\sigma$ ) and is offset by about 300 mas relative to the 2MASS position.

### 6.5.2 VLBI Observations

The masers in UGC 3193 were observed under the MCP project using the VLBA and the HSA. The VLBI epochs are listed in Table 6.1. The raw telescope data were correlated at the VLBA correlator in half-Stokes with dual polarization, with a 1.024 s integration time and a frequency (velocity) resolution of between 256 channels (BG187B) and 1024 channels (BB313Z) across each of the four dual-polarization 16 MHz wide frequency windows (IFs). For the correlation at NRAO of the BB313Z experiment the new UGC 3193 VLA coordinates of § 6.5.1 were adopted.

The two VLBI experiments (BG187B, BB313Z) were scheduled with two types of blocks: a maser block in dual circular polarization, and two or more geodetic-like blocks (see, e.g., Brunthaler et al. 2005) in a single polarization. The maser blocks were laid out for phase referencing against a bright quasar reference in the BG187B VLBA track. Under the HSA track BB313Z the main observing time was spent in self-calibration mode, with short phase-referenced sections inserted for a fallback in case of a loss of the GBT or the EB telescope.

In general, self-calibration is possible when the continuum emission of the core or the flux density of a single  $\text{H}_2\text{O}$  maser feature is large compared to the VLBI sensitivity. The source must be sufficiently strong such that the fringe is detectable within the short atmospheric coherence time of  $< 150$  s at 22 GHz. The atmospheric phase changes can be calibrated in this case.

Phase referencing has to be used if the source flux density is too low for the array (e.g., when the GBT or EB telescopes that provide the main HSA sensitivity are lost due to some fault). Geodetic blocks can help to map the delays through the troposphere and improve the transfer of phase solutions from the phase reference onto the maser target. The geodetic blocks measure the actual tropospheric delays towards 20 or more quasars. The quasars are typically selected from the catalog of sources that define the ICRF2 reference frame and that have positions accurate to better than 1 mas.

The atmospheric delays measured in the geodetic blocks can improve upon the basic, seasonally averaged tropospheric zenith delay model applied by the VLBA correlator. These model delays tend to be accurate to a few cm at K-band, and measuring the actual delays to sub-cm precision using geodetic blocks can notably improve phase referencing accuracy (Brunthaler

et al. 2005). Geodetic blocks were placed at the beginning and at the end of the phase referenced maser block. The geodetic blocks were about one hour in duration and had 16 frequency bands uniformly distributed over a total bandwidth of 512 MHz.

## 6.6 VLBI Data Reduction

The AIPS calibration followed the steps common to the MCP project (cf. Reid et al. 2009). There are two main challenges: 1) the low flux density of the relatively narrow maser features in different velocity channels, and 2) the small angular scale of the maser distribution relative to the size of the synthetic beam. As masers are at different positions that are unknown a priori, the standard approach in VLBI continuum data reduction, averaging over frequency i.e. over velocity, does not help to improve the signal-to-noise ratio (SNR) of the maser detection (and does rather the contrary). Careful calibration and flagging is required to achieve the highest sensitivity and detect most of the maser features. For the full data reduction details the reader is referred to Reid et al. (2009) and in particular to the “MCP Cookbook” by C. Y. Kuo that may be found on the MCP project page<sup>1</sup>. The general calibration and data reduction steps are described below.

Calibration and flagging were performed automatically using the AIPS Python interface (ParseITongue) developed by Kettenis et al. (2006) and a custom data reduction pipeline written in Python. The pipeline calibrations were inspected manually, and calibrations were occasionally iterated to find better settings that improved the data. The manually determined settings were then adopted for a final pipeline re-run.

The early, a priori calibrations included a correction of cross-correlation amplitudes due to errors in sampler thresholds (Kogan 1995), amplitude calibration using recorded system temperature data, corrections for the telescope elevation dependent gains, and corrections for atmospheric opacity. Delays and phases were corrected for dispersive ionospheric delay and Faraday rotation via total electron content maps measured with GPS and provided by the NASA CDDIS (Walter & Chatterjee 1999). We also applied negligible corrections due to the final Earth orientation parameter (EOP) solutions provided by the USNO. Typically the EOPs did not differ from those already applied by the VLBA software correlator. Finally, phases of the single or dual polarizations were corrected for the rotation of the parallactic angle. During all steps, the calibration data were inspected and bad data were flagged. The early calibrations employed automatic flagging of outliers (e.g., corrupt system temperature measurements). Automatic flagging was based on the tests by Grubbs and Hampel with robust statistics (cf. Pearson 2005).

Complex baseline band-passes on a strong ( $> 1$  Jy) fringe finder source were subtracted from the visibility data. Instrumental delays were calibrated by fringe fitting one scan on a bright com-

<sup>1</sup><https://safe.nrao.edu/wiki/bin/view/Main/MegamaserCosmologyProjec>

compact delay monitor source. For geodetic blocks, the multi-band delays towards each quasar were determined via fringe fitting. The multi-band delays were converted into a tropospheric zenith delay and clock rate local to each telescope. These solutions were applied to the maser blocks as part of the atmospheric corrections. We then performed phase calibration. The residual independent delay, rate and phase errors, mainly due to changes in the atmosphere, were determined for each frequency band using a typical solution interval of 5 s to 30 s. These residuals were determined either towards the phase reference quasar (in BG187B), or a single strong and compact maser feature in the target source (in BB313Z). The phase solutions were then transferred to all frequency bands of the target source. Time ranges with erratic phase or delay solutions during phase referencing or self-calibration were flagged manually.

All VLBI tracks produced good geodetic solutions for most stations, with occasional exceptions due to poor local weather. The first VLBA track (BG187B) produced a non-detection due to phase referencing under highly variable atmospheric conditions. The sensitivity of the VLBA was insufficient for self-calibration against single maser features that had a  $> 100$  mJy peak flux density (masers are at different image locations and represent complex source structure that can not be easily used for self-calibration, unless the maser positions are known a priori).

The second track with the HSA (BB313Z), however, produced a strong detection both in self-calibration and in phase referencing modes. Due to an error during correlation at NRAO, data of the large GBT and EB telescopes that remained on-source during the short VLBA phase referencing blocks were not correlated with the rest of the array. To avoid maser position shift artifacts only from the self-calibration blocks were used to determine the maser positions.

The BB313Z track on UGC 3193 reached an average sensitivity of about  $0.4 \text{ mJy beam}^{-1}$  in Stokes I over each 16 MHz wide band. The four 16 MHz wide frequency bands had an original channel spacing of  $0.86 \text{ km s}^{-1}$ . The visibility data were imaged in Stokes I with a cell size of 0.03 mas. The convolving beam size was  $1.6 \times 0.4 \text{ mas}$  with a  $-6.7^\circ$  position angle (PA). The channels were averaged in velocity using a 50% overlapped sliding boxcar and the channel width after averaging was about  $1.7 \text{ km s}^{-1}$ . The sensitivity in the  $1.7 \text{ km s}^{-1}$  wide channels of the four image cubes was typically  $3 \text{ mJy beam}^{-1}$  and at worst  $4.5 \text{ mJy beam}^{-1}$ .

The best-fit maser positions were derived from the image cube via the standard Gaussian component fitting tools in AIPS. The positions are listed in Table A.6.2, see Appendix A.6. In addition, the line-free image cube slices of each of the four frequency bands were collapsed into a plane and the bands were averaged to search for continuum emission at a Stokes I sensitivity of  $125 \mu\text{Jy beam}^{-1}$  in the full averaged  $4 \times 16 \text{ MHz}$  bandwidth.

## 6.7 VLBI Results

### 6.7.1 The Maser Distribution in UGC 3193

Each velocity slice of the image cube was fit in AIPS by Gaussians to estimate the diameter, integrated flux density, SNR, position, and position uncertainty of the compact unresolved maser features. The maser positions and velocities of the maser features with a  $\text{SNR} \geq 5$  were analyzed with existing and new tools of the MCP project. The VLBI images and P–V diagrams are shown in Fig. 6.4.

No continuum components and no systemic masers were detected. This sets a  $3\sigma$  limit on the continuum emission of  $0.4 \text{ mJy beam}^{-1}$ . In total, 54 high velocity maser spots were detected that had SNRs of  $\geq 5$ . The mean maser position uncertainties were  $0.041 \text{ mas}$  ( $1\sigma_X$ ) and  $0.132 \text{ mas}$  ( $1\sigma_Y$ ). The masers are shown in Fig. 6.4 and trace an elongated disk-like structure that agrees with a large-diameter rotating disk with a PA of  $-29.96^\circ \pm 0.03^\circ$ , an outer diameter of  $7.35 \text{ mas}$  (or  $2.12 \text{ pc}$ ), and an inner diameter of  $0.57 \text{ mas}$  ( $0.16 \text{ pc}$ ). The “emission gaps” between the two blue and the two red HV groups are  $1.3 \text{ mas}$  ( $0.4 \text{ pc}$ ) and  $1.8 \text{ mas}$  ( $0.5 \text{ pc}$ ), respectively. As noted earlier, the linear scale assumes a distance of  $59.5 \text{ Mpc}$  adopted from NED.

As suggested by the maser map in Fig. 6.4 the detected masing disk may consist of two slowly rotating concentric rings: an outer ring traced by the two “slower” HV maser groups located at the velocity offsets  $V_{\text{sys}} \pm 70 \text{ km s}^{-1}$ , and an inner ring traced by the two “faster” HV maser groups with central velocities near  $V_{\text{sys}} \pm 150 \text{ km s}^{-1}$ . The outer ring has a PA of  $-30.01^\circ \pm 0.03^\circ$  with masers along orbital diameters of  $4.10 \text{ mas}$  to  $7.35 \text{ mas}$  ( $1.18 \text{ pc}$  to  $2.12 \text{ pc}$ ). The inner ring has a best-fit PA of  $-64.42^\circ \pm 1.68^\circ$  and is tilted in PA relative to the outer ring. The inner ring is traced over maser orbital diameters of  $0.76 \text{ mas}$  to  $1.03 \text{ mas}$  ( $0.22 \text{ pc}$  to  $0.30 \text{ pc}$ ). Assuming the observed maser velocities are peak (orbital/circular) velocities, the respective approximate full rotation periods,  $T = 2\pi r/v_{\text{circ}}$ , for Keplerian maser orbits in the outer and inner rings are between  $52 \times 10^3 \text{ yr}$  and  $4500 \text{ yr}$ , and this indicates that both rings are slowly rotating.

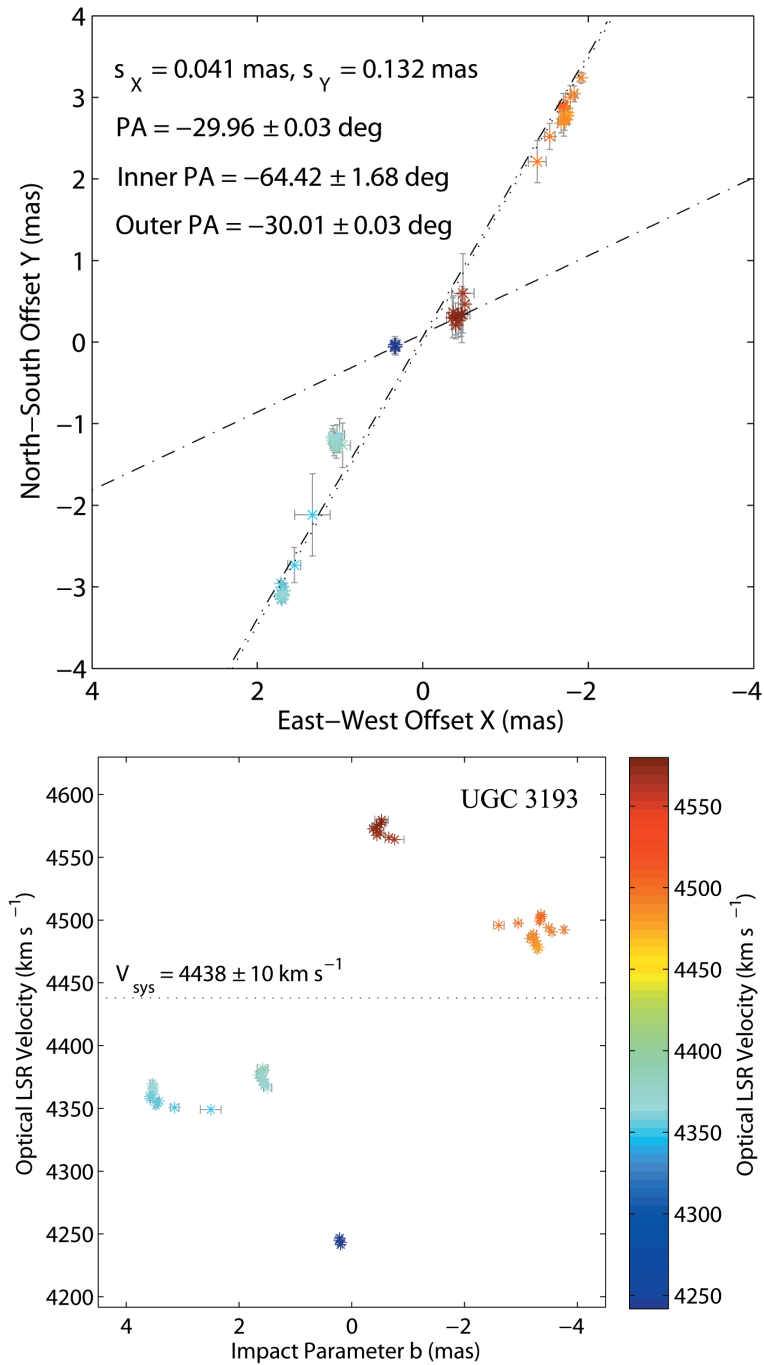


**Fig. 6.4:** The VLBA/HSA maser map (top) and position–velocity diagram (bottom) of the disk water masers in UGC 3193. The maser features strongly detected with a  $\text{SNR} \geq 5$  are shown. The error bars indicate  $1\sigma$  uncertainties. The coordinates of the maser map are relative to the mean of the maser distribution. The PA fit through all maser features (dotted), fit through the inner maser features (dash-dot) and the outer maser features (dashed) are overlaid on the top panel. The dotted line in the bottom panel indicates the recessional velocity.

There are several warped or disrupted thin disk geometries that can produce the observed ring-like pattern and emission gap. The first explanation may be an exceptionally heavily warped disk. It is thought that masing is supported by X-ray heating by the central engine, and that AGN disk masers occur preferentially in the inward-facing layer of disk warps illuminated obliquely by the central engine (e.g., Neufeld et al. 1994; Neufeld & Maloney 1995). Both a radial warp and a suitable inclination are required to detect the usually strongly beamed maser emission along the LOS. Assuming a disk with no rings, the two red and blue HV groups are at opposite sides of the disk, and reside on the disk midline as suggested by the zero GBT accelerations. The inner masers then trace a radial warp that partially self-shadows the outer disk regions. Inclination and tilt of the warped disk can account for the undetected LOS systemic masers and the misalignment of the inner masers relative to the overall PA seen in Fig. 6.4. On the other hand, assuming the disk is broken into two rings, distinct rings can be produced through a break in viscous accretion near the inner edge of the accretion disk, with the break then propagating outwards (cf. Nixon & King 2012). Nixon et al. (2013) also consider tearing of the disk near a binary black hole due to a combination of disk plane–spin equatorial plane misalignment (e.g., Bardeen–Petterson effect, one of the explanations for the disk warp in maser galaxy NGC 4258; Wu et al. 2013) as well as binary plane–disk plane misalignment. In an older hypothesis by Pringle (1996, 1997) a self-induced and growing warp is produced by radiation pressure, and is one of the possible explanations for the disk warp in NGC 4258 (Maloney et al. 1996). Once the self-reinforcing warp grows excessive a viscous disconnect in the warped disk region in UGC 3193 can result in two rings.

Alternatively, “systemic” masers at the near and far ends of a disk with a strong point-symmetric warp both along and transverse to the LOS can give rise to the “slower” HV masers. Albeit not seen in any other disk maser galaxy, this would allow systemic masers at the far end to be detected. Assuming the latter scenario, and assuming both rings have similar outer diameters, the observed difference in the outer diameter of the outer ring (2.12 pc) and the inner ring (0.30 pc) would be due to viewing angle effects, with the then heavily warped disk seen at an inclination of about  $82^\circ$ . However, large velocity drifts of the “slower” HV masers would be expected in the latter scenario. The wide temporal spacing of the current GBT epochs does not allow us to support a scenario with large maser accelerations. Assuming instead a heavy warp and  $90^\circ$  inclination, we can estimate the disk “obliquity”,  $\mu$ , the angle between the disk normal and the radius vector. A 3rd order polynomial fit to the VLBI data indicates a peak  $\mu \sim 11^\circ$  along the inner blueshifted HV masers, and reflects the peak projected warp of the disk.

## 6.8 Geometric Keplerian Disk and Plummer Cluster Models

The central mass enclosed by a masing accretion disk in an AGN is often thought to be a central SMBH point-mass. As an alternative to SMBHs, as put forth by Maoz (1995, 1998) and Kuo et al. (2011), it is worth to verify whether a compact cluster of stars or stellar remnants can provide an equally valid description of the observed near-Keplerian rotation curve. The closest to a Keplerian disk model in terms of complexity is the Plummer toy model for N-body systems such as clusters (Plummer 1915; Dejonghe 1987; Binney & Tremaine 2008). The Plummer model fit determines the cluster total mass, core radius, and density. The lifetime of the cluster is constrained by the evaporation and collision timescales, dependent on e.g. the cluster density. A dense cluster rather than a SMBH is plausible when the cluster lifetime is similar to or greater than the age of the host galaxy ( $\sim 10$  Gyr). Conversely, following the argument applied by Kuo et al. (2011) to seven disk maser galaxies, if the cluster lifetime derived from the Plummer fit parameters is significantly shorter than the age of the host galaxy a SMBH is instead required to account for the central mass. In their argument Kuo et al. (2011) implicitly assume the central region forms early and evolves together with the host galaxy, whereas in principle a very recently formed nuclear cluster in an older galaxy is still possible (e.g., after an episode of high-mass accretion due to a minor merger event).

The models fit to the maser angular position and kinematic data are summarized below. A detailed description of the models and their parameters may be found in Appendix A.4. Each model was fit independently of the others. The same models below were also applied to data of another disk maser galaxy, IC 2560, presented in the next Chapter.

**Plummer** – The Plummer toy model (see Eq. A.22 in Appendix A.4) and the model parameters, namely  $\beta_P = (M_\infty, x_0, y_0, V_0, \alpha, r_c)$ , were fit to position and velocity data excluding systemic masers. A zero peculiar velocity was assumed for the galaxy. A published distance was adopted for  $D_A$ . The standard non-linear least squares (NLLS) with a trust region algorithm (NLLS-TR; Coleman & Li 1996; Yuan 2000) as provided by Mathworks Matlab<sup>®</sup> (2010)<sup>1</sup> was chosen as the method for parameter fitting and post-fit parameter confidence interval estimation.

**Kepler I** – For a comparison with the Plummer model, the same input data as above were used for a NLLS-TR fit of the Keplerian model (Eq. A.14) with parameters  $\beta_{K1} = (M_{\text{BH}}, x_0, y_0, V_0, \alpha, \gamma)$ . The model assumes a warp-free disk seen at a  $90^\circ$  inclination.

---

<sup>1</sup><http://www.mathworks.com/help/optim/ug/lsqlcurvefit.html>

## 6.9 Model Fit Results and Discussion

The basic Plummer and Keplerian I models (again, see the Appendix A.4) were fit to the maser spot data selected with  $\text{SNR} \geq 6$ , without including the (zero) accelerations that were observed with the GBT for the UGC 3193 water masers. The best-fit Plummer cluster parameters are listed in Table 6.3. The corresponding Kepler I fits are given in Table 6.4. Notably, both of these simple models achieved similar coefficients of determination,  $R^2$ , indicating that both described the HV maser data equally well.

Table 6.3. Plummer model fit to the UGC 3193 rotation curve without accelerations.

	$N$	PA (deg)	$M_\infty \pm 1\sigma$ ( $10^6 M_\odot$ )	$\rho$ ( $M_\odot \text{pc}^{-3}$ )	$\hat{m}_\star$ ( $M_\odot$ )	$r_c$ (pc)	$N_c$ ( $10^6$ )	$t_{\text{coll}}$ (Gyr)	$R^2$
inner ring	12	-66.78	$1.91 \pm 0.25$	$0.34 \times 10^9$	$\leq 0.59$	0.11	$\geq 3.2$	$< 0.3$	0.995
outer ring	40	-32.01	$1.26 \pm 0.07$	$0.01 \times 10^9$	$\leq 4.60$	0.43	$\geq 0.3$	$> 3.5$	0.987
all masers	52	-31.96	$0.68 \pm 0.01$	$5.87 \times 10^9$	$\leq 0.044$	0.03	$\geq 17.5$	$< 0.3$	0.975

Note. — Col 2 ( $N$ ): the number of strong maser features ( $\text{SNR} \geq 6$ ) used in the model fit. Col 3 (PA): the best-fit disk position angle. Col 4 ( $M_\infty$ ): the cluster mass and  $1\sigma$  uncertainty. Col 5 ( $\rho$ ): the cluster density (Eq. A.23). Col 6 ( $m_\star$ ): upper limit on stellar constituent mass (Eq. A.24). Col 7 ( $r_c$ ): cluster radius. Col 8 ( $N_c$ ): number of cluster members. Col 9 ( $t_{\text{coll}}$ ): collisional timescale (Eq. A.25). Col 10 ( $R^2$ ): the coefficient of determination of the model fit.

Table 6.4. Kepler I model fit to the UGC 3193 rotation curve without accelerations.

	$N$	PA (deg)	$M_{\text{BH}} \pm 1\sigma$ ( $10^6 M_\odot$ )	$\rho$ ( $M_\odot \text{pc}^{-3}$ )	$\gamma$	$R^2$
inner ring	12	-66.78	$0.61 \pm 0.49$	$0.1 \times 10^9$	0.5	0.998
outer ring	40	-32.01	$0.60 \pm 0.83$	$0.7 \times 10^6$	0.5	0.960
all masers	52	-31.96	$0.61 \pm 0.17$	$2.4 \times 10^8$	0.5	0.974

Note. — Col 2 ( $N$ ): the number of fit maser features ( $\text{SNR} \geq 6$ ). Col 3: the best-fit disk PA. Col 4: the SMBH mass. Col 5 ( $\rho$ ): the volume density. Col 6 ( $\gamma$ ): the Keplerian rotation parameter,  $v \propto r^{-\gamma}$ . Col 7 ( $R^2$ ): the coefficient of determination of the fit.



### 6.9.1 Plummer Fit Results

The Plummer toy model fit to the UGC 3193 data and the collision and evaporation timescale arguments (Appendix A.4) ruled out a cluster in UGC 3193. Lacking optical  $\sigma_*$  data, the maser rather than stellar velocity dispersion of  $95 \text{ km s}^{-1}$  was used. The value is typical for the stellar velocity dispersion measured in other disk maser galaxies, e.g., McConnell et al. (2011).

The stellar mass limit determined for the inner ring ( $\hat{m}_* \leq 0.6 M_\odot$ ) allows for a population of white dwarfs ( $m_* \leq 1.4 M_\odot$ ), main sequence stars, or red dwarfs. However, the resulting short cluster lifetime of 0.3 Gyr for main sequence stars relative to the time for leaving the main sequence are likely to rule out a Plummer cluster – unless the cluster formed very recently. The outer ring ( $\hat{m}_* \leq 4.6 M_\odot$ ) allows for neutron stars ( $1.4 M_\odot \leq m_* \leq 3 M_\odot$ ), and for all stellar constituents had a lifetime in favor of a cluster. However, the full disk ( $\hat{m}_* < 0.04 M_\odot$ ) had cluster lifetimes shorter than 0.3 Gyr for all respective stellar types, ruling out a cluster.

### 6.9.2 Keplerian Disk Fit Results

The PA and maser impact parameters were estimated with a generalized least squares fit through the strong VLBI maser features with  $\text{SNR} \geq 6$ .

Two fits to a Keplerian edge-on disk were performed, first with a fixed SMBH position equal to the mean of the maser spatial distribution, and then with a free SMBH position (Kepler I). Fitting the strong  $\text{SNR} \geq 6$  maser spots of the entire disk, the inner ring only, and the outer ring only, with impact parameters defined along the axis of the respective PA's, produced a weighted average  $M_{\text{BH}}$  (Eq. A.13) and central volume density (Eq. A.23) for the fixed-SMBH fit of  $0.8 \pm 0.5 \times 10^6 M_\odot$  and  $3.4 \times 10^8 M_\odot \text{ pc}^{-3}$ , or  $0.7 \pm 0.5 \times 10^6 M_\odot$  and  $1.2 \times 10^8 M_\odot \text{ pc}^{-3}$ , or  $0.8 \pm 0.4 \times 10^6 M_\odot$  and only  $9.0 \times 10^5 M_\odot \text{ pc}^{-3}$ , respectively. The masses are within 25 % of the respective Kepler I fits (see Table 6.4) that had general relativistic (GR) corrections and a free SMBH position. A Kepler I fit to all HV groups suggests a SMBH mass of  $0.61 \pm 0.17 \times 10^6 M_\odot$ .

The above mass corresponds to a mean Eddington luminosity,  $L_E \simeq 1.26 \times 10^{38} M / M_\odot \text{ erg s}^{-1}$ , or  $0.77 \times 10^{44} \text{ erg s}^{-1}$ . With the X-ray luminosity limit of  $L_X < 10^{42} \text{ erg s}^{-1}$  found by Walther (2012), the Eddington ratio,  $\lambda = L_X / L_E$ , is  $\lambda < 0.01$ . This is typical of a LLAGN. Using the  $L_X$  upper limit, the accretion rate  $\dot{M}$  can be estimated from disk obliquity  $\mu = \sin(11^\circ) = 0.19$  (see § 6.7.1) by equating the 1.06 pc outer disk radius with the critical radius,  $R_{\text{cr}}$ , within which the disk midplane becomes molecular, given by  $R_{\text{cr}} = 0.04 L_{41}^{-0.426} (\dot{M}_{-5} / \alpha)^{0.809} \mu^{-0.383} M_8^{0.617}$  (cf. Neufeld & Maloney 1995), where  $|\alpha| < 1$  is the accretion model dependent viscosity parameter. We find a  $\dot{M} < 0.05 \alpha M_\odot \text{ yr}^{-1}$  limit on the accretion rate. This is relatively large for LLAGN, but not near the rate of  $\sim 1 M_\odot \text{ yr}^{-1}$  where disk self-gravity becomes significant and leads to gravitational instability. This does not rule out past disk instabilities, however, nor outwards-propagating disruptions of the disk near the SMBH, either of which may have been a driver of

the detected warped disk structure with two distinct rings.

## 6.10 Summary and Conclusions

This Chapter presented spectra, velocity drifts and a VLBI image for the 22 GHz H<sub>2</sub>O megamasers first detected by Braatz & Gugliucci (2008) towards UGC 3193.

The Plummer cluster toy model was ruled out as a description for the observed UGC 3193 maser features unless the cluster formed recently in the last  $\sim 1$  Gyr. Given the good consistency of the data with Keplerian models, and the high central volume densities, we conclude that UGC 3193 hosts a SMBH in its nuclear region. No masers were detected at the systemic velocity, thus a geometric distance determination to the galaxy is not possible.

The temporal drifts in maser central velocities in the four HV maser groups hinted at a slight, near-zero negative mean acceleration for the blueshifted HV groups and an oppositely directed slightly greater positive mean acceleration for the redshifted HV features. These near-zero accelerations may also be an artefact of the very sparse temporal spacing of the GBT single-dish epochs, noise ( $\sim 4$  mJy channel<sup>-1</sup> rms typical in these GBT spectra) and slight variability in the relatively low ( $\sim 5$ – $90$  mJy) maser flux densities, and the most robust conclusion is a non-detection of acceleration in the HV maser features. The acceleration data and the VLBI map indicate that the HV masers are located along the midline of a masing accretion disk.

The main finding of the Keplerian (Kepler I) model fit is a peculiarly low SMBH mass of  $0.61 \pm 1.57 \times 10^6 M_{\odot}$  (or  $0.8 \pm 0.5 \times 10^6 M_{\odot}$  for the less complex model) and a volume density of about  $2.4 \times 10^8 M_{\odot} \text{ pc}^{-3}$ , no resolved structure emitting a 22 GHz continuum, and a maser distribution best described by two masing accretion disks/rings inclined relative to each other that form a wide 7.35 mas (2.12 pc) warped disk. The kinematics, maser distribution and X-ray data favor the presence of a LLAGN with a relatively low-mass SMBH surrounded by a masing accretion disk, rather than extranuclear kilomasers in star formation regions. A SMBH is also suggested by the high nuclear volume density.

The maser velocity dispersion of  $95 \text{ km s}^{-1}$  would place the SMBH in UGC 3193 at the undermassive end of the  $M_{\text{BH}}-\sigma_{\star}$  relation, like other maser galaxies (cf. Greene et al. 2010). A measurement of the actual *stellar* velocity dispersion in the galactic bulge (or pseudo-bulge) is to be carried out in a future observation.

# 7 An Angular Diameter Distance to the Megamaser Galaxy IC 2560

This Chapter presents results on the water megamasers in IC 2560 ( $2913 \text{ km s}^{-1}$ ) that were measured under the Megamaser Cosmology Project (MCP), as were the two MCP maser galaxies NGC 23 and UGC 3193 in the previous Chapters. It should however be mentioned that the recent M.Sc. thesis by Meyer (2013) presents an independent reduction of one of the archival interferometric tracks on IC 2560. It should thus be noted that this Ph.D thesis necessarily has some overlap (though a fully independent work) that at the same time confirms the results of Meyer (2013) and presents additional results on IC 2560 that are indeed new and original. This Chapter partially follows a paper to be submitted to the ApJ.

## 7.1 Abstract

The AGN at the core of the galaxy IC 2560 hosts a warped circumnuclear Keplerian accretion disk that is traced by water maser emission over parsec to sub-parsec scales. The analysis of the maser observations in this Chapter finds drifts in the central velocities (accelerations) of the red and blue high-velocity (HV) maser features that are small but non-zero and of opposite sign, with a  $5\sigma$  tension between the accelerations of the two maser groups. The acceleration signature agrees with a  $5.3^\circ \pm 0.1^\circ$  spiral pitch angle under the Maoz–McKee spiral model where masers trace pattern velocities, implying a minor 0.4 % correction may be necessary for parameters derived from observables under the assumption that masers trace orbital rather than pattern velocities. Geometric Keplerian disk models were fit to the maser data and suggest a disk with a  $49.4^\circ \pm 0.7^\circ$  position angle (PA). The data further indicate a central mass in the inner 0.1 pc of  $5.4_{-0.6}^{+0.9} \times 10^6 M_\odot$ , in agreement also with optical measurements of the stellar velocity dispersion in the galactic bulge and the  $M_{\text{BH}}-\sigma_\star$  relation of maser galaxies.

In addition, via a direct geometric measurement of the maser distribution, this Chapter finds

an angular diameter distance to IC 2560 of  $47.9^{+11.3}_{-9.2}$  Mpc and provides a new measurement of the value of the Hubble constant of  $67.7^{+11.6}_{-8.9}$  km s<sup>-1</sup> Mpc<sup>-1</sup>. If combined with the Hubble constant,  $H_0$ , of two other maser galaxies of the MCP project, UGC 3789 and NGC 6264, the new IC 2560 measurement updates the maser-based estimate of  $H_0$  to  $68.4 \pm 5.3$  km s<sup>-1</sup> Mpc<sup>-1</sup> (8 %).

Table 7.1. Recent  $H_0$  Estimates for flat  $\Lambda$ CDM with  $w \equiv -1$ 

$H_0 \pm 1\sigma$ (km s <sup>-1</sup> Mpc <sup>-1</sup> )	Method	Reference
$70.4 \pm 2.5$	WMAP 7 MASTER fit	Komatsu et al. (2011)
$74.3 \pm 2.1$	Cepheid + HST + Spitzer parallax	Freedman et al. (2012)
$70.0 \pm 2.2$	WMAP 9 C <sup>-1</sup> fit	Hinshaw et al. (2013)
$69.33 \pm 0.88$	WMAP 9 + BAO + $H_0$ prior	Hinshaw et al. (2013)
$67.4 \pm 1.4$	Planck 2013 (without WMAP or lensing)	The Planck Collaboration (2013)
$73.1^{+2.4}_{-3.1}$	RXJ1131–1231 lensing + WMAP 7	Suyu et al. (2013)
$67.5 \pm 2.8$	LSS + gal. BAO + Ly- $\alpha$ BAO	Addison et al. (2013)
$69.3 \pm 1.0$	ACT+WMAP7+BAO+HST	Sievers et al. (2013)
$72.0 \pm 3.0$	NGC 4258 maser ( $7.6 \pm 0.23$ Mpc) & Cepheid	Humphreys et al. (2013)
$68.9 \pm 7.1$	UGC 3789 maser ( $49.6 \pm 5.1$ Mpc)	Reid et al. (2013) (MCP Paper IV)
$68.0 \pm 9.0$	NGC 6264 maser ( $114 \pm 19$ Mpc)	Kuo et al. (2013) (MCP Paper V)
$67.7^{+11.6}_{-8.9}$	IC 2560 maser ( $47.9^{+11.3}_{-9.2}$ Mpc)	this Chapter (MCP Paper, in prep.)
$68.4 \pm 5.3$	Weighted average of the maser galaxies above	
$69.5 \pm 0.5$	Weighted average of all results above	

## 7.2 Introduction

By the end of the last century, observational data have suggested that the expansion of the Universe is not slowing down, as would be expected from attractive gravity, but is speeding up. Recent supernova observations show that expansion switches from deceleration to acceleration around a redshift,  $z$ , of below  $0.752 \pm 0.041$  (Suzuki et al. 2012). The discovery implies that our most basic notions about gravity fail on cosmological distance scales and that the Universe is not dominated by matter, but instead contains an unknown weak inflationary constituent, Dark Energy (DE).

Several cosmological models successfully describe the accelerating expansion, including  $\Lambda$ CDM,  $w$ CDM and  $w(z)$ CDM. They model expansion in terms of a changing scale factor  $a(t)$  in the Einstein–Friedmann equations. For the known types of energy the time evolution of  $a$  is known precisely. Models differ in the time evolution of  $a$  dependent on the type of DE (Bamba et al. 2012; Weinberg et al. 2013). There is not yet sufficiently accurate data to rule out different

kinds of DE. To test DE and cosmological models, fractional energy densities ( $\Omega_{\text{DE}}$ ,  $\Omega_{\text{m}}$ ,  $\Omega_{\text{r}}$ ,  $\Omega_{\text{k}}$ ), neutrino mass, and the Hubble parameter ( $H \equiv \dot{a}/a$ ) have to be measured to high accuracy. Measuring the current Hubble parameter,  $H_0$  at time  $t=0$ , independently of any particular cosmology, would be the most important complement to measurements at higher redshifts (e.g. Hu 2005; Olling 2007; Mortonson et al. 2010).

Further details are given in Appendix A.4.2 on page 217.

Current  $H_0$  measurements are based on Type Ia supernovae (SN Ia at  $z < 2$ ), weak lensing ( $z \approx 1-5$ ), baryon acoustic oscillations (BAO) imprinted on the distribution of luminous matter ( $z > 0.1$ ), Lyman  $\alpha$  absorbers ( $z \approx 2-4$ ), or cosmic microwave background (CMB) anisotropies ( $z \approx 1100$ ). At low  $z$ , commonly SN Ia are used as “standard candles”, relying on an intricate calibration ladder to measure distances and  $H_0$ . For a detailed review, see Weinberg et al. (2013).

Recently, disk water megamasers in active galaxies within 200 Mpc have shown promise for directly and independently measuring and refining the value of  $H_0$ . They are unique probes into the sub-parsec scales of active galactic nuclei (AGN) and allow for accurate measurements of the geometric distance to the host galaxy, while also yielding the black hole (BH) mass (Reid et al. 2013). The prototypical disk maser galaxy, NGC 4258, contains a thin edge-on sub-parsec masing accretion disk around the AGN. Very long baseline interferometry (VLBI) of the maser distribution in the disk has determined the mass of the BH,  $M_{\text{BH}}$ , at sub-0.2 pc scales (Miyoshi et al. 1995), well within its gravitational sphere of influence of about 1 pc.

Similarly,  $M_{\text{BH}}$  has been measured in 8 other maser galaxies, including Mrk 1419 (a LINER), UGC 3789, and others (Kuo et al. 2011; Impellizzeri et al. 2012; Reid et al. 2013; Kuo et al. 2013), with  $M_{\text{BH}}$  generally below  $10^8 M_{\odot}$  but in the range of  $10^5-10^9 M_{\odot}$  of supermassive black holes (SMBHs). Maser SMBH masses provide important observational data for the  $M_{\text{BH}}-\sigma_{\star}$  relation between  $M_{\text{BH}}$  and the stellar velocity dispersion,  $\sigma_{\star}$ , in the galactic bulge (Greene et al. 2010; McConnell et al. 2011), and the  $M_{\text{BH}}-L_{\text{bulge}}$  bulge luminosity relation. In LINER galaxies, maser  $M_{\text{BH}}$  can also be compared to the  $M_{\text{BH}}$  determined via sub-0.05 pc reverberation mapping of the AGN broad line region (Collin et al. 2006).

For observational cosmology, masing circumnuclear disks in AGN are ideal as “standard rulers”, references of known or readily inferred linear size. The linear scale is set by the accelerations along the disk and its angular extent in VLBI images, and allows a geometric measurement of the angular diameter distance,  $D_{\text{A}}$ , to the galaxy. Combined with the optical redshift, this gives a metric distance and  $H_0$ . The method was pioneered by Herrnstein et al. (1999) for NGC 4258. Its recent maser distance of  $7.60 \pm 0.22$  Mpc, and a recalibration of the Cepheid period-luminosity relation for the cosmic distance ladder, updated the “standard candle”-based  $H_0$  to  $72.0 \pm 3.0 \text{ km s}^{-1} \text{ Mpc}^{-1}$  (Humphreys et al. 2013).

While NGC 4258 is not in the Hubble flow, more distant disk maser galaxies are suited for

a direct  $H_0$  measurement that bypasses the complex cosmic distance ladder. At around  $z = 0.18$  the peculiar velocities (non-Hubble redshifts) of clusters fall below 1% of the Hubble flow (Planck Collaboration 2013). However, the redshift “sweet spot”, where inferred distances are insensitive to the radial peculiar velocities and uncertain energy densities of DE and Dark Matter, is lower and at  $0.03 < z < 0.1$  (Weinberg et al. 2013). At 50 Mpc the recessional velocity is over 90% due to cosmological expansion. Current 22 GHz VLBI has sufficient sensitivity and linear scale resolution to detect and positionally resolve individual point-like masing regions in edge-on sub-pc disks of nearby ( $z < 0.06$ ) galaxies within this “sweet spot”. The Megamaser Cosmology Project (MCP) measures  $H_0$  for a sample of disk maser galaxies at 50 Mpc to 200 Mpc and will ultimately combine the results of 10 or more galaxies to reach an  $H_0$  accurate to 3% (Braatz et al. 2009). The MCP project has published distances and  $H_0$  for two galaxies, NGC 6264 and UGC 3789 (see Table 7.1), with several others in preparation.

This Chapter presents a distance to the disk maser galaxy IC 2560. The SMBH mass in IC 2560 was of additional interest, as its value is uncertain (Yamauchi et al. 2012). Like in other maser galaxies, the SMBH mass lies seemingly far below the usual  $M_{\text{BH}}-\sigma_*$  relation given the stellar velocity dispersion  $\sigma_*$  in the bulge measured by Greene et al. (2010, Fig. 8). Greene et al. also suspect that instead of a classic bulge (a centrally concentrated galaxy center of the elliptical type), IC 2560 may contain a disk-like bulge (“pseudobulge”) that are often seen in spiral galaxies. These tend to have “undermassive” SMBH. This may indicate a different AGN feedback mechanism. For example, theoretical investigations find  $M_{\text{BH}} \propto \sigma_*^5$  for mechanical and  $M_{\text{BH}} \propto \sigma_*^4$  for momentum exchange feedback (Silk & Rees 1998; Murray et al. 2005; see also Hu 2008 and Nayakshin et al. 2012).

Below we first introduce IC 2560 (§ 7.3), the single dish observations and data reduction (§ 7.4), the interferometric observations and data reduction (§ 7.8), and the VLBI results (§ 7.9). Finally, we combine these data and present the results of model fitting (§ 7.11).

The geometric and kinematic models fit to the acceleration and VLBI data, namely Keplerian and Plummer cluster models with relativistic corrections, are given in Appendix A.4.

**Conventions:** We denote  $H_0 = 100 h \text{ km s}^{-1} \text{ Mpc}^{-1}$ . Velocities are in the kinematic local standard of rest reference frame (LSR) and use the optical definition. Distances are angular diameter distances,  $D_A$ , unless noted otherwise. Distances adopted from the NASA/IPAC Extragalactic Database (NED) are in the cosmology used by NED at the time of writing ( $h = 0.73$  with density parameters  $\Omega_\Lambda = 0.73$  for dark energy and  $\Omega_m = 0.27$  for baryonic and dark matter). For the geometric model fitting we adopt the recent WMAP9 parameters of  $\Omega_\Lambda = 0.719$  and  $\Omega_m h^2 = 0.28$  for  $h = 0.697$  (see Hinshaw et al. 2013, Table 2). In the nearby Universe the density parameters for relativistic species and curvature are  $\Omega_r, \Omega_k \simeq 0$ .

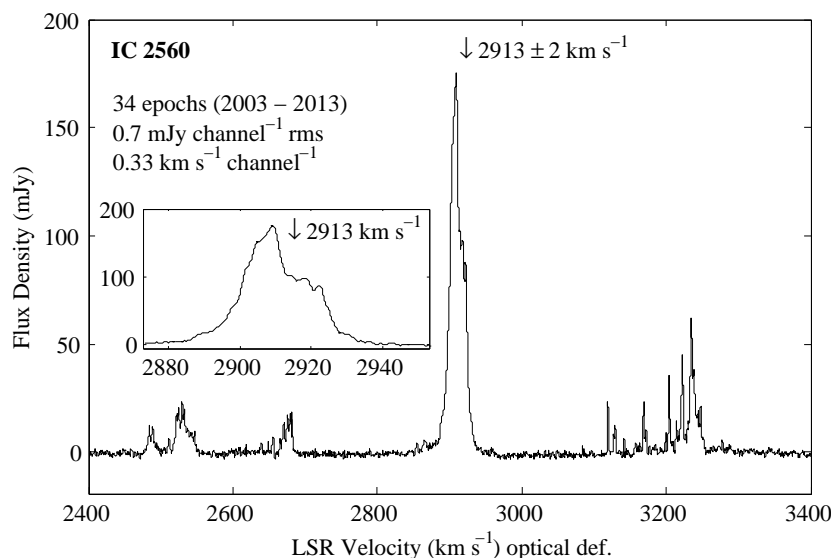


**Fig. 7.1:** The integrated GBT spectrum of H<sub>2</sub>O masers detected towards IC 2560. The inset shows detail on the systemic maser group that is at the recessional velocity of the galaxy.

### 7.3 The Water Maser Galaxy IC 2560

The maser galaxy IC 2560 ( $2913 \pm 2 \text{ km s}^{-1}$ ; Theureau et al. 1998) in the Antlia cluster is a barred spiral galaxy that hosts a Sy 2 nucleus (de Vaucouleurs et al. 1991; Fairall 1986; Véron-Cetty & Véron 2006). The galaxy has three redshift-independent distances: a Tully-Fisher luminosity distance that corresponds to an angular diameter distance of  $46.0 \pm 1.7 \text{ Mpc}$  (Springob et al. 2009), a “sosie” look-alike distance of  $31.0 \pm 2.4 \text{ Mpc}$  (Terry et al. 2002), and a maser distance of  $31^{+12}_{-14} \text{ Mpc}$  (Yamauchi et al. 2012). The galaxy IC 2560 has an infra-red luminosity of  $10^{10.42} L_{\odot}$  and a warm IRAS color ( $S_{60\mu\text{m}}/S_{25\mu\text{m}} = 3.4$ ) with an AGN-dominated nuclear optical spectrum (Wouterloot & Walmsley 1986b; Moshir et al. 1990). An optical emission-line observation by Schulz & Henkel (2003) confirms Sy 2 activity. They find asymmetric line wings suggestive of outflow and estimate a Keplerian mass of  $\sim 10^7 M_{\odot}$  inside an inner radius of 100 pc.

Regarding AGN activity, the *ASCA* X-ray satellite observation by Ishihara et al. (2001) finds a 2–10 keV luminosity,  $L_{2-10}$ , of  $1.0^{+1.0}_{-0.4} \times 10^{41} \text{ erg s}^{-1}$ , confirmed by Walther (2012). Recent *Chandra* and *XMM-Newton* X-ray data provide further evidence of a low-luminosity AGN with a  $L_{2-10}$  of  $\sim 10^{41} \text{ erg s}^{-1}$  and an obscuring column density towards the X-ray core in excess of  $3 \times 10^{24} \text{ cm}^{-2}$  (Iwasawa et al. 2002; Madejski et al. 2006; Tilak et al. 2008). They also detect a cold reflector (the putative disk) and a warm scattered continuum component (disk corona or wind), see also the schematic illustration (Fig. 1.10) in the introduction to this thesis in § 1.5.

The luminous “disk water masers” towards IC 2560 were first detected by Braatz et al.

(1996). The time integrated maser spectrum of all GBT observations to date is shown in Fig. 7.1. It has a symmetric profile with emission at the systemic velocity and by two high-velocity (HV) groups, with a total integrated line profile of  $6.2 \text{ Jy km s}^{-1}$  ( $\sim 280 L_{\odot}$ ).

Ishihara et al. (2001) conducted single dish and VLBI observations between 1996 and 2000. For the systemic masers they report an average drift in central velocity of  $+2.62 \pm 0.09 \text{ km s}^{-1} \text{ yr}^{-1}$ , and  $0.0 \pm 0.5 \text{ km s}^{-1} \text{ yr}^{-1}$  for the redshifted HV features. They infer a central mass of  $2.8 \times 10^6 M_{\odot}$  within  $0.068 \text{ pc}$  and a volume density of at least  $2.1 \times 10^9 M_{\odot} \text{ pc}^{-3}$ . They did not detect the HV masers in VLBI, but find a radio continuum component that coincides with the systemic maser location and that has an AGN-like brightness temperature,  $T_b$ , of  $2.7 \times 10^{11} \text{ K}$ .

The follow-up observations by Yamauchi et al. (2012) during 1995 to 2006 also detect a faint unresolved continuum component with a peak flux density of  $1.8 \pm 0.3 \text{ mJy beam}^{-1}$  and that did not extend more than the  $2.17 \times 1.18 \text{ mas}$  beam size, corresponding to a  $T_b$  of  $> 10^6 \text{ K}$ . Yamauchi et al. find systemic masers, a redshifted feature, and a single blueshifted feature offset by  $0.2 \text{ pc}$  towards the southwest. The blueshifted maser coincides with the location of the continuum component and Yamauchi et al. associate it with a putative jet launched by the AGN in IC 2560. The systemic and redshifted masers indicate a disk position angle (PA) of  $-46^{\circ}$  and a disk thickness of  $2H \leq 0.025 \text{ pc}$ . From their single-dish data Yamauchi et al. find an systemic maser velocity drift of  $+2.57 \pm 0.04 \text{ km s}^{-1} \text{ yr}^{-1}$ . Using the angular offset of the redshifted maser feature they estimate a SMBH mass at the center of a Keplerian masing disk of  $3.5 \times 10^6 M_{\odot}$  and determine an angular diameter distance to IC 2560 of  $31_{-14}^{+12} \text{ Mpc}$ .

Lastly, Greene et al. (2010) measure a stellar velocity dispersion,  $\sigma_{\star}$ , of  $134 \pm 12 \text{ km s}^{-1}$ , consistent with the  $144 \pm 20 \text{ km s}^{-1}$  measured by Cid Fernandes et al. (2004). The  $M_{\text{BH}}-\sigma_{\star}$  relation for spiral galaxies (cf. McConnell et al. 2011) would suggest a SMBH mass of  $\sim 1.6 \times 10^7 M_{\odot}$ . As mentioned in the introduction, however, maser galaxies tend to have systematically “under-massive” SMBHs relative to the mass suggested by the  $M_{\text{BH}}-\sigma_{\star}$  relation.

## 7.4 Single-Dish Observations and Data Reduction

We conducted 22 GHz single dish monitoring with the National Radio Astronomy Observatory (NRAO<sup>1</sup>) Robert C. Byrd Green Bank Telescope (GBT). We also used NRAO GBT archival data. The Nobeyama 45 m data of Yamauchi et al. (2012) were not included. The GBT epochs, 34 in total, are listed in Appendix A.5 in Table A.5.1.

The same setup and data reduction as in Braatz et al. (2010) and as in § 5.3 was followed. The masers in IC 2560 were observed with the dual-polarization K-band Focal Plane Array receiver and the GBT spectrometer backend in either a dual beam-switched mode or a position-

---

<sup>1</sup>The National Radio Astronomy Observatory is a facility of the National Science Foundation operated under cooperative agreement by Associated Universities, Inc.



switched mode. The flux density scale was calibrated using noise injection ( $T_{\text{cal}}$ ) and accounting for pointing errors was accurate to about 15 %. The GBT spectrometer backend setup had 8192 channels, a bandwidth of 200 MHz, and either two identical and overlaid frequency windows for an increased sensitivity in Stokes I, or two only slightly overlapped frequency windows for a wider velocity coverage. The spectra were calibrated in GBTIDL. Bad sub-integrations and bad channels were flagged. Smoothed reference spectra were subtracted to remove standing waves and ripple. Third order baseline fits were removed from individual sub-integrations prior to averaging them into a final spectrum for each epoch.

## 7.5 Single-Dish Results

In total 34 GBT epochs were available and were observed from 2003 March to 2012 November (see Fig. 7.2). Seven GBT epochs were either corrupted by strong bandpass ripple or had too low sensitivity, however 27 epochs produced good spectra. Out of these, 24 epochs of the first 7 years of monitoring had a sufficiently short time spacing to cross-identify individual maser features and fit accelerations.

The rms-weighted average of all 34 GBT epochs (see Fig. 7.1) reached a total on-source integration time of about 21 hours and a sensitivity of 0.7 mJy rms in  $0.33 \text{ km s}^{-1}$  wide channels. The flux density integrated over the velocity range of the blueshifted HV group was  $0.68 \text{ Jy km s}^{-1}$  with an equivalent isotropic luminosity of about  $30 L_{\odot}$ . The integrated flux density of the redshifted group was  $0.90 \text{ Jy km s}^{-1}$  ( $40 L_{\odot}$ ) and the systemic masers had an integrated flux density of  $3.98 \text{ Jy km s}^{-1}$  ( $180 L_{\odot}$ ). The total equivalent isotropic flux density was thus about  $250 L_{\odot}$ . The luminosity estimates are for an adopted luminosity distance of 44.9 Mpc (NED) that is based on the redshift by Theureau et al. (1998).

The symmetry of the IC 2560 maser profile suggests that the HV and systemic maser groups originate in a rotating edge-on disk. The systemic masers were well-centered on the  $2913 \pm 2 \text{ km s}^{-1}$  LSR recessional velocity (see inset in Fig. 7.1). The blue-systemic peak flux density is roughly twice that of the red-systemic peak.

Spaans (2005) postulates such an asymmetry that should occur due to a general relativistic (GR) redshift that partially compensates the Keplerian blueshift and thereby extends the velocity coherent paths in the blue-systemic portion of the disk, while conversely shortening the coherent path lengths in the disk region traced by the red-systemic masers. An inspection of the long-term integrated GBT spectra of the disk masers in NGC 4258, and the long-term integrated spectra of the MCP project disk maser galaxies such as UGC 3789, Mrk 1419, NGC 6264 and NGC 6323 (also, D. Pesce, private comm. on additional maser galaxies) did not, however, reveal any consistent asymmetry in systemic flux densities.

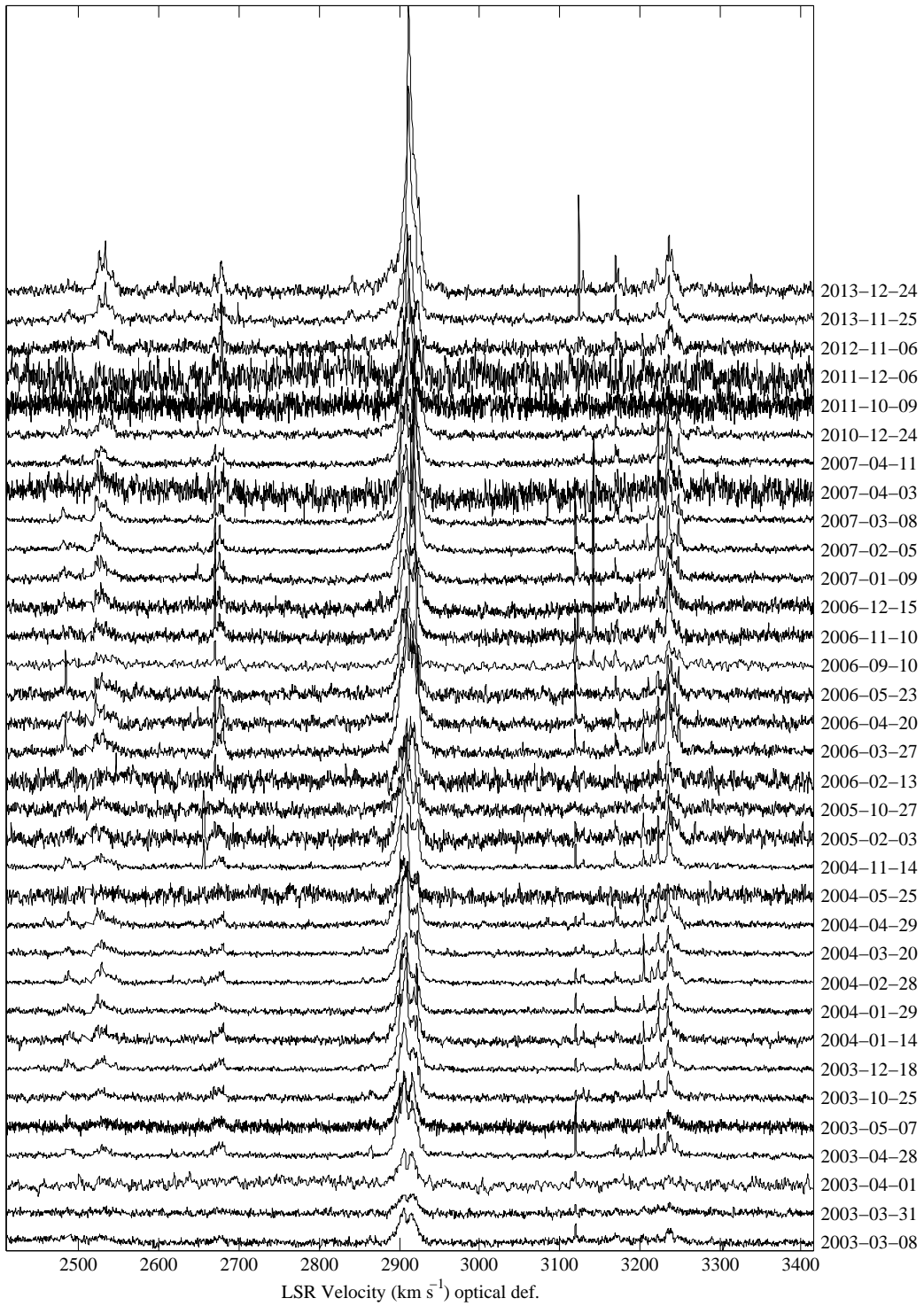


Fig. 7.2: Spectra of all GBT maser epochs on IC 2560. See Fig. 7.1 for the integrated spectrum.

## 7.6 Maser Acceleration Fitting

The drifts in the central velocities of individual lines, or groups of lines, were determined for the maser features that were detected in several epochs. Finding accurate accelerations for the systemic masers is complicated by their time variable flux densities and their tendency to form heavily blended broad lines. This is seen in, e.g., NGC 4258 (Humphreys et al. 2008), and was taken into account with a composite multi-Gaussian model during acceleration fitting. The same fitting methods introduced in the previous Chapter, namely Accel I, Accel II, and Accel IIIa/b (for details, see § 6.3), were used to fit the IC 2560 single-dish maser data.

The time variability in maser flux densities and the occasional long gaps between some of the epochs required that the maser accelerations were fit in up to five subsets of the available epochs. The acceleration estimates given by the relatively manual Accel I and Accel II fits were adopted as the rough a priori starting values for the iterative least squares fit with the Accel IIIa and Accel IIIb methods. For the heavily blended systemic masers in IC 2560, the Accel IIIa and IIIb methods produced acceleration solutions with a comparable goodness of fit. However, the acceleration slope with velocity,  $da/dv$ , fitted by the IIIb method came closer to the relatively smooth gradient expected for a uniform distribution of radii of the systemic masers, and the transverse rotation of these masers through the line of sight (LOS).

Regarding the precision of the acceleration fits, Bragg et al. (2000) note that the velocity drifts of the HV features can be very small and on the order of  $0.1 \text{ km s}^{-1} \text{ yr}^{-1}$ . Bragg et al. find that the Doppler tracking in the AIPS software (Bridle & Greisen 1994) and the CfA Planetary Ephemeris Program agree within the quoted uncertainty of the AIPS routine ( $0.004 \text{ km s}^{-1} \text{ yr}^{-1}$ ). They conclude that any long-term accelerations observed in the maser features above this level must be due to a real physical effect. Without any more recent verification of their comparison we assume that the conclusion by Bragg et al. continues to hold and is valid for the GBT data and the interferometric data observed in the years from 2003 to 2013.

## 7.7 Maser Accelerations Results

The best-fit accelerations are given in Table 7.2. The weighted arithmetic mean accelerations,  $\hat{a}_w$ , were calculated for each maser group and are given as  $\hat{a}_w \pm \sigma_{\hat{a}} \pm \sigma_w$ , where  $\sigma_{\hat{a}}$  is the unbiased standard deviation of the weighted mean, and  $\sigma_w$  is the weighted standard deviation of the data.

The outlier accelerations at the maser central velocities of 2484.8, 2854.8, 2656–2681, and 3230.3  $\text{km s}^{-1}$  (in parentheses in Table 7.2) stem from maser features that were present in 4 or fewer epochs, perhaps due to time variability. Variability at a month time scale suggests that some of these maser features might be associated with the southwest-aligned VLBI jet reported by Yamauchi et al. (2012), considering that similar short timescales are seen for the narrow lines

## 7.7 Maser Accelerations Results

Table 7.2. Accelerations of the maser features in IC 2560.

Blue group		Systemic group		Red group	
$v_{\text{LSR}}$ (km s <sup>-1</sup> )	$a \pm \sigma_a$ (km s <sup>-1</sup> yr <sup>-1</sup> )	$v_{\text{LSR}}$ (km s <sup>-1</sup> )	$a \pm \sigma_a$ (km s <sup>-1</sup> yr <sup>-1</sup> )	$v_{\text{LSR}}$ (km s <sup>-1</sup> )	$a \pm \sigma_a$ (km s <sup>-1</sup> yr <sup>-1</sup> )
2475.45	+0.2812 ± 0.2170	(2854.85	+0.9862 ± 0.2557)	3119.49	-0.2885 ± 0.0146
2483.25	+0.2418 ± 0.2075	2898.17	+2.4435 ± 0.0365	3119.49	-0.2922 ± 0.0146
(2484.78	+3.2434 ± 0.4018)	2899.66	+2.5202 ± 0.0548	3129.22	+0.0961 ± 0.1377
2486.07	+0.2590 ± 0.2107	2902.31	+2.9037 ± 0.0475	3141.86	-0.0464 ± 0.0194
2488.34	+0.2787 ± 0.2137	2903.18	+3.1411 ± 0.0256	3168.83	+0.0310 ± 0.0329
2491.77	+0.2831 ± 0.2151	2904.35	+3.1959 ± 0.0402	3171.82	+0.0310 ± 0.0329
2499.50	+0.2721 ± 0.2155	2906.57	+3.6122 ± 0.0183	3176.25	+0.0314 ± 0.0329
2504.66	+0.2750 ± 0.2151	2907.52	+3.6524 ± 0.0329	3199.25	-0.0438 ± 0.1461
2508.65	+0.2790 ± 0.2118	2909.67	+4.0432 ± 0.0183	3201.92	-0.0709 ± 0.0121
2517.70	+0.2765 ± 0.2137	2910.29	+4.0542 ± 0.0292	3204.06	-0.1497 ± 0.0219
2527.79	+0.2648 ± 0.2086	2913.71	+4.5436 ± 0.0329	3204.09	-0.0763 ± 0.0121
2528.14	+0.2579 ± 0.2137	2913.83	+4.6203 ± 0.0183	3206.51	-0.1497 ± 0.0219
2529.74	+0.2747 ± 0.2129	2918.76	+5.3070 ± 0.0292	3208.56	-0.0997 ± 0.0124
2534.24	+0.2867 ± 0.2170	2918.79	+5.2777 ± 0.0511	3216.24	-0.0760 ± 0.0121
2541.43	+0.2608 ± 0.2155	2922.66	+5.8475 ± 0.0402	3220.97	-0.0844 ± 0.0121
2543.99	+0.2801 ± 0.2126	2923.26	+5.9206 ± 0.0694	3222.20	-0.1421 ± 0.0245
2551.41	+0.2937 ± 0.2126	2925.87	+6.2931 ± 0.0475	3222.55	-0.2695 ± 0.0256
2553.86	+0.2323 ± 0.2100	2928.15	+6.6255 ± 0.0913	3225.06	-0.0877 ± 0.0124
2556.94	+0.3324 ± 0.2374	...	...	3230.28	+0.1534 ± 0.3579
2656.56	+0.1278 ± 0.2228	...	...	3233.04	-0.0632 ± 0.0124
(2670.96	-0.2177 ± 0.2743)	...	...	3235.00	-0.0800 ± 0.0121
(2675.25	-0.2484 ± 0.0734)	...	...	3237.13	-0.0964 ± 0.0121
(2680.72	-0.0329 ± 0.0438)	...	...	3243.37	-0.0774 ± 0.0117
...	...	...	...	3245.23	-0.1056 ± 0.0121
...	...	...	...	3249.23	-0.1048 ± 0.0124
...	...	...	...	3257.91	-0.0895 ± 0.0110
...	...	...	...	3259.82	-0.0950 ± 0.0110
$\hat{a}_w$ : +0.038 ± 0.041 ± 0.218		+4.105 ± 0.219 ± 0.954		-0.104 ± 0.012 ± 0.065	
(or +0.266 ± 0.009 ± 0.038)					

Note. — Accelerations of maser features that were detected in only 4 or fewer epochs are given in parentheses. Weighted mean accelerations,  $\hat{a}_w$ , are shown below each respective group. The uncertainties are the unbiased standard deviation of the weighted mean and the weighted standard deviation of the data, respectively. The blue acceleration outlier (+3.2 km s<sup>-1</sup> yr<sup>-1</sup>) is excluded from the weighted mean. The mean blue acceleration given in the second row, in parentheses, also excludes the three negative blue accelerations.

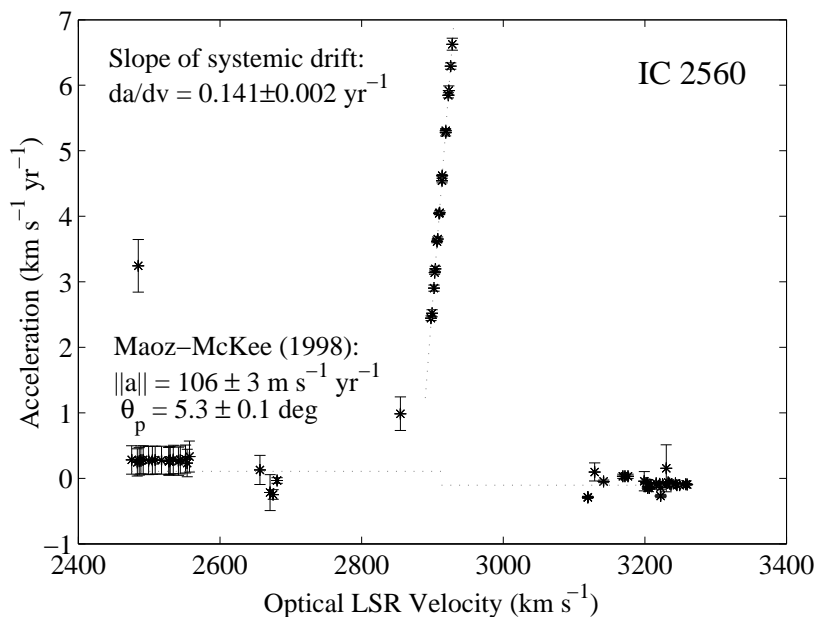


**Fig. 7.3:** IC 2560 maser accelerations against velocity. Accelerations of the Maoz–McKee spiral model fit are overlaid (dotted line).

of some jet-associated masers as in, e.g., NGC 1052 (Kameno et al. 2005).

The best-fit accelerations are shown against velocity in Fig. 7.3. The LOS accelerations of the systemic masers in IC 2560 spanned about  $2.5 \text{ km s}^{-1} \text{ yr}^{-1}$  to  $6.5 \text{ km s}^{-1} \text{ yr}^{-1}$  and had a slope of  $0.141 \pm 0.002 \text{ yr}^{-1}$ . This range of accelerations is wider than the drifts in NGC 4258 of  $7.7 \text{ km s}^{-1} \text{ yr}^{-1}$  to  $8.9 \text{ km s}^{-1} \text{ yr}^{-1}$  (Humphreys et al. 2008), but similar to UGC 3789 with systemic maser accelerations of  $0.51 \text{ km s}^{-1} \text{ yr}^{-1}$  to  $7.29 \text{ km s}^{-1} \text{ yr}^{-1}$  (Braatz et al. 2010). The drift pattern of the systemic masers was consistent with masers located along different radii at the near end of a rotating disk.

For the HV maser features very low LOS velocity drifts were measured, as expected for emission from the midline of a rotating disk. Interestingly, the weighted mean accelerations,  $\hat{a}_w$ , of the blueshifted and redshifted HV groups, with outliers excluded, were non-zero (Table 7.2). This is already indicated in the findings by Yamauchi et al. (2012) who report HV maser accelerations of  $+0.28 \pm 0.23$  and  $-0.09 \pm 0.15 \text{ km s}^{-1} \text{ yr}^{-1}$ , respectively. In comparison, we find  $+0.266 \pm 0.038$  and  $-0.104 \pm 0.065 \text{ km s}^{-1} \text{ yr}^{-1}$ , respectively, consistent with Yamauchi et al.

The fitted HV maser accelerations of Table 7.2 reveal a  $5\sigma$  tension between the redshifted and blueshifted maser velocity drifts. This HV acceleration signature agrees with the prediction by Maoz & McKee (1998) who propose that the accretion disk may form spiral density waves and that this spiral pattern is traced by shocks, with HV maser emission arising in narrow post-

## 7.8 VLBI Observations and Data Reduction

shock regions where the spiral arms are tangent to the LOS. For a logarithmic spiral with pitch angle,  $\phi_p$ , Maoz & McKee predict a drift in the HV maser central velocities towards the systemic velocity at a rate of  $|a_{\text{spiral}}| \approx 0.05(\phi_p/2.5^\circ) \text{ km s}^{-1} \text{ yr}^{-1}$ . They derive a  $\cos \phi_p^{-1}$  correction factor for the true disk radius, circular velocity, and central mass, relative to their values derived without the assumption of a spiral density wave model.

A weighted fit of the HV accelerations in IC 2560, with the outliers excluded (as indicated in Table 7.2), yields a drift of  $|a_{\text{spiral}}| = 106 \pm 3 \text{ m s}^{-1} \text{ yr}^{-1}$ . This corresponds to a pitch angle of  $5.3^\circ \pm 0.1^\circ$ , a correction factor of 0.4 %, and respective in-disk maser azimuth angles (angular positions) of the redshifted and blueshifted HV maser groups of  $-5.3^\circ \pm 0.1^\circ$  and  $174.7^\circ \pm 0.1^\circ$ , respectively. In comparison, the weighted mean azimuth angles derived directly from the measured accelerations (see Eq. A.16 in Appendix A.4) were  $-15.8^\circ \pm 16.4^\circ$ ,  $171.3^\circ \pm 2.7^\circ$ , and  $90.9^\circ \pm 0.6^\circ$  for the redshifted, blueshifted, and systemic masers, respectively. These are consistent with the fitted Maoz–McKee model azimuth angles although the uncertainties are large.

Table 7.3. The K-band VLBI water maser observations for IC 2560s.

Source	Date	Array	Project	Beam size (mas x mas)	PA (deg)	Sensitivity (mJy beam <sup>-1</sup> )
IC 2560	2004 Dec 30	VLBA+VLA+GBT	BG155 <sup>a</sup>	–	–	> 50
IC 2560	2007 Jan 24	VLBA+VLA+GBT	BG169C	2.0 × 0.2	-16°	≈ 4–9 <sup>b</sup>

Note. — <sup>a</sup>The NRAO archival track BG155 failed due to multiple HSA array issues. <sup>b</sup>The rms sensitivity in 0.84 km s<sup>-1</sup> wide channels in the single polarization IFs.

## 7.8 VLBI Observations and Data Reduction

The masers in IC 2560 were mapped in two K-band VLBI observations that were carried out with the NRAO Very Long Baseline Array (VLBA) in its High Sensitivity Array (HSA) configuration that includes the GBT and the phased Karl G. Jansky Very Large Array (VLA). The two VLBI observations are listed in Table 7.3. Both VLBI tracks are previously unpublished NRAO archival data. The principal investigator (PI) and co-investigators of the archival VLBI tracks are L. Greenhill together with others, including J. Braatz, the PI of the MCP project.

Both VLBI tracks were scheduled to contain two types of blocks: a maser observation in dual circular polarization, and two “geodetic” blocks (see, e.g., Brunthaler et al. 2005) in a single polarization. The maser blocks employed phase referencing to calibrate the rapid atmospheric

phase fluctuations. Eight 16 MHz wide frequency windows (IFs) covered the maser emission with a velocity spacing of  $0.84 \text{ km s}^{-1}$  per channel and 256 channels per IF. The raw telescope data were correlated in dual polarization but without forming cross-polarization products (some IFs were single-polarization). The integration time was 2.0 seconds.

The scheduling of the VLBI tracks, the frequency setup, the geodetic blocks before and after the main maser block, and the data reduction closely followed the same route as for the maser galaxy UGC 3193. See § 6.5.2 in the previous Chapter for details.

Both VLBI tracks on IC 2560 produced good geodetic (atmospheric) solutions for most stations, with occasional exceptions due to poor local weather. The first HSA track (BG155) suffered from VLA phasing problems and poor weather at the southern VLBA stations and did not reach a sufficient sensitivity to detect the overall relatively low flux density maser emission. However, the second HSA track (BG169) was successful and produced a strong detection.

The best sensitivity was reached in self-calibration rather than phase-referencing mode. The calibrated visibility data were imaged in Stokes I (for dual-polarized IFs) using a  $0.03 \text{ mas}$  cell size. The channels were averaged with a 50% overlapped sliding boxcar that produced an effective output velocity resolution of about  $1.68 \text{ km s}^{-1}$  for the image cubes. The convolving beam size was  $2.0 \times 0.2 \text{ mas}$  with a  $-16^\circ$  beam position angle (PA). In those IFs that had only single polarization data, the sensitivity in the image cubes was about  $4 \text{ mJy beam}^{-1} \text{ rms}$  to  $9 \text{ mJy beam}^{-1} \text{ rms}$  over  $0.84 \text{ km s}^{-1}$  channels prior to averaging to  $1.68 \text{ km s}^{-1}$ . The sensitivity in Stokes I in the dual-polarized IFs was about a factor of  $\sqrt{2}$  better.

Each velocity slice of the image cubes was fit by 2D Gaussians in AIPS (Bridle & Greisen 1994) to estimate the diameter, integrated flux density, signal-to-noise ratio (SNR), position, and position uncertainty of the compact unresolved maser features. The maser positions and velocities of the strongly detected maser features with a  $\text{SNR} \geq 5$  were analyzed and combined with GBT acceleration data to fit a geometric Keplerian disk model.

## 7.9 VLBI Results

Curiously, no 22 GHz continuum was detected in IC 2560 in the averaged image cubes. The non-detection sets a  $3\sigma$  upper limit on the 22 GHz continuum of  $0.9 \text{ mJy beam}^{-1} \text{ rms}$ , and it is possible that variability in the continuum produced a non-detection of the  $1.8 \pm 0.3 \text{ mJy beam}^{-1}$  continuum emission found by Yamauchi et al. (2012) with the VLBA in 1998.

The water maser emission, however, was strongly detected. The peak flux density of the maser detection was about  $110 \text{ mJy beam}^{-1}$ . The distribution of the water masers is shown in Fig. 7.4. The coordinates of the image are relative to the unweighted mean position of all maser features. The mean uncertainty in the maser positions is  $0.030 \times 0.084 \text{ mas}$  ( $1\sigma_X \times 1\sigma_Y$ ). The

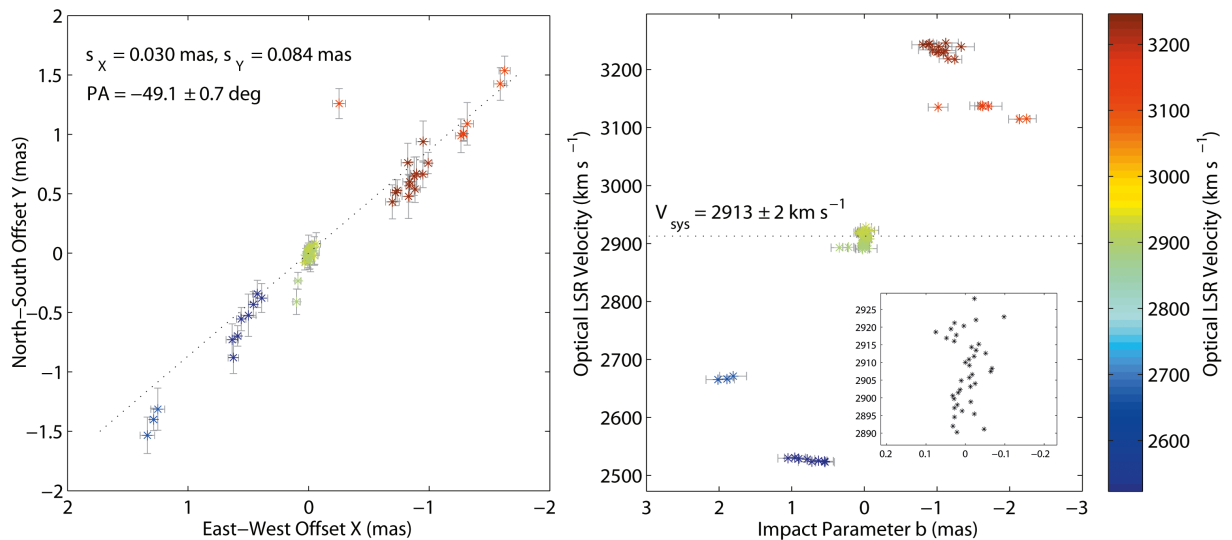


**Fig. 7.4:** The VLBI image of the disk maser distribution in IC 2560 (left) and the maser position–velocity diagram (right) with a close-up view on the systemic masers (right inset; the two outlier systemic masers are not shown). Error bars indicate  $1\sigma$  uncertainties. Coordinates are relative to the mean of the maser distribution. No continuum emission was detected. The panels show the strong maser features with  $\text{SNR} \geq 5$ .

maser group in the image center also coincides with the recessional velocity of the galaxy,  $V_{\text{LSR}}$ , of  $2913 \pm 2 \text{ km s}^{-1}$ .

### Maser Positions

The list of maser positions, their uncertainties, and their SNR is given in its entirety in Table A.6.4, see Appendix A.6. As already suggested by Fig. 7.4 the maser distribution was found to trace an elongated, disk-like structure. It has an estimated position angle,  $\alpha$ , of  $-49.4^\circ \pm 0.7^\circ$ . The PA is based on the strong maser features with  $\text{SNR} > 5$  and excludes the redshifted feature that is found offset by  $(-0.3, 1.3)$  mas from the image center.

Adopting an angular diameter distance of  $43.9 \text{ Mpc} \pm 6\%$  from NED that is based on the redshift by Theureau et al. (1998) the inner diameter (0.50 mas) and the outer diameter (4.25 mas) of the presumably edge-on disk correspond to respective linear distances of 0.11 pc and 0.90 pc.

### Slope of the Systemic Masers

The sub-pc scale of the maser distribution, and the maser position–velocity diagram (P–V diagram) shown in Fig. 7.4 that is suggestive of a Keplerian rotation curve, both indicate that masers



originate in a circumnuclear accretion disk. The systemic masers in the P–V diagram (inset in Fig. 7.4) appear to trace two groups (e.g., two masing rings), but accounting for the position (impact parameter) uncertainties of about 0.09 mas, the comparable maser separations do not robustly support two maser groups.

One may attempt to estimate the distance to the galaxy via a fit of the P–V diagram slope of the systemic masers,  $\Omega$ , the average systemic maser acceleration ( $+4.1 \pm 0.2 \text{ km s}^{-1} \text{ yr}^{-1}$ ), and a rotation curve parameter,  $k$ , derived from the HV masers in the P–V diagram.

For details on the method, see Braatz et al. (2010, § 4) or Appendix A.4 (§ A.4.1 Eq. A.7).

A linear fit through the 13 brightest systemic features with a SNR of  $>20$ , using the York generalized least squares method (York et al. 2004) and the maser position uncertainties and a conservative  $1.8 \text{ km s}^{-1}$  uncertainty in the VLBI maser velocities equal to the velocity resolution, yielded an estimates of the slope. The best-fit P–V slope  $\Omega$  was  $-215.9 \pm 91.3 \text{ km s}^{-1} \text{ mas}^{-1}$ . When a different SNR cut, with SNR  $> 5$  as in Yamauchi et al. (2012), was applied the best-fit slope was  $-478.2 \pm 209.0 \text{ km s}^{-1} \text{ mas}^{-1}$ . This is in agreement with Meyer (2013) who find  $-477 \pm 74 \text{ km s}^{-1} \text{ mas}^{-1}$ . Although Yamauchi et al. (2012) provide no estimate of the slope, a linear fit through their combined 1998 and 2000 VLBI maser data yielded a slope of  $-986 \pm 636 \text{ km s}^{-1} \text{ mas}^{-1}$ . The Yamauchi et al. data are consistent with two systemic populations; the first ( $2890\text{--}2917 \text{ km s}^{-1}$ ) with a slope of  $-471 \pm 225 \text{ km s}^{-1} \text{ mas}^{-1}$ , and the other ( $2917\text{--}2930 \text{ km s}^{-1}$ ) with a  $-85.4 \pm 39.2 \text{ km s}^{-1} \text{ mas}^{-1}$  slope determined solely by 7 maser features in the 1998 epoch that are “exiting” the LOS and are undetected in the 2000 epoch. Combining the former slopes with the slope in this Chapter, we find a weighted average over the 1998, 2000, and 2007 VLBI epochs of  $\Omega = -477 \pm 67 \text{ km s}^{-1} \text{ mas}^{-1}$ .

The rotation curve parameter,  $k$ , necessary for an angular diameter distance as mentioned earlier, was determined as part of a Keplerian rotation curve fit, shown later.

## 7.10 Geometric Models Fit to IC 2560 Maser Data

The same models introduced for UGC 3193 in § 6.8 of the previous Chapter were also fit to the IC 2560 maser data. Just as for the models fit to UGC 3193 data, each model was fit independently of the others. A description of the model parameters and the detailed geometric models may be found in Appendix A.4. The systemic masers and their accelerations allow the following more complex models to be fit to the maser data. These fits allow to determine the Hubble constant,  $H_0$ , and the distance to the galaxy,  $D_A$ . The more complex models are, briefly, with details in Appendix A.4:

**Kepler II** – To solve for  $D_A$  and thereby for  $H_0$  using the simplest geometric model with the fewest parameters (but also the most assumptions), the systemic masers and accelerations were

included in a warp-free disk model fit. Compared to Kepler I, the model parameter set is expanded to  $\beta_{K2} = (M_{\text{BH}}, x_0, y_0, V_0, \alpha, i, H_0, \gamma)$ , with fixed in-disk maser positions that are not part of the free parameters. Instead, the systemic maser radii were solved from Eq. A.13 (§ A.4.1). In the Kepler II fit the residuals (model vs. data) of the accelerations were weighted by the average ratio of velocity and acceleration uncertainties.

The corrections applied by the model to the observed maser line frequencies included special relativistic (SR) and general relativistic (GR) redshifts. The model assumes a  $\Lambda$ CDM cosmology to determine the final distance  $D_A$  of the galaxy (Eq. A.5 in § A.4.1). A standard non-linear least squares fitting technique (Coleman & Li 1996; Yuan 2000) was used and the fits converged in about  $10^3$  to  $10^5$  iterations.

To avoid overfitting the data, and to estimate confidence intervals for  $H_0$ ,  $M_{\text{BH}}$ , and other parameters, the parameters were fit to data in a repeated Leave-N-Out bootstrap with  $N=2$  (see, e.g., Efron & Gong 1983). The confidence intervals determined this way do not contain any propagated uncertainties of the input data, but rather, they provide lower limits on the precision attainable for the given model and data set.

**Kepler III** – The Markov chain Monte Carlo (MCMC) fitting program by Reid et al. (2013) was used to fit the full model parameters (Eq. A.2) of a warped disk together with the now free in-disk maser position parameters. For  $N$  maser features the model has  $4N - 2N - 15$  degrees of freedom that is typically relatively large, 50 to 150, not accounting for the non-linearity of the model. Solving for the best fitting parameters is a highly multi-dimensional problem. It can be solved efficiently with the MCMC fitting technique (see, e.g., Katzgraber 2009). MCMC is a type of Bayesian inference that uses a (nearly-)random walk in the parameter space and numerical integration to find the most likely and best-fitting parameter values and their posterior probability distributions given a set of observations and their uncertainties, and the prior probability distributions of the parameters themselves, e.g., normal and uniform distributions and their a prior parameters such as mean and standard deviation.

All the model parameters subject to the fit are given Gaussian priors. Only  $H_0$  (or, equivalently,  $D_A$ ) are given an unconstrained, uniform prior distribution. One can adopt an independent  $M_{\text{BH}}$  estimate as an a priori parameter value, including its uncertainties, if H $\alpha$  kinematics or stellar velocity dispersion data ( $M_{\text{BH}}-\sigma_*$  relation) are available.

The MCMC fitter by Reid et al. uses SR velocity addition and derives a distance  $D_A$  in a flat  $\Lambda$ CDM cosmology. Compared to Reid et al. (2013) the MCMC program was extended to support unlimited MCMC iterations. The Numerical Recipes random number generator (RAN1 1992) was replaced with the Mersenne Twister (Matsumoto & Nishimura 1998) suited for long MCMC simulations (Katzgraber 2010).

Since objective criteria for assessing MCMC chain convergence are a classic nontrivial prob-

lem, parallel chains and  $\gtrsim 200 \cdot 10^6$  MCMC iterations were used, and the fitting progress was manually monitored via an online calculation of the chain statistics (e.g., Ling 1974).

Strongly correlated parameters, such as  $M_{\text{BH}}$  and  $H_0$ , as well as  $H_0$  and  $V_{\text{pec,r}}$ , typically slow down the convergence. This was compensated with a mix of correlated and independent random walk updates. Lastly, a SR Doppler correction was applied to  $V_{\text{pec,r}} = a\dot{\chi}$ , but not to the GR effect of  $V_0 = \dot{a}\chi$ . Model parameter  $V_0$  was instead equated with the cosmological redshift ( $cz_0$  in  $\text{km s}^{-1}$  units), allowing for several redundant iterative conversions between velocity definitions to be removed from the MCMC program. These latter changes were conceptual, and only changed the interpretation of  $V_{\text{pec,r}}$ . Trial fits that compared the fitter in Kuo et al. (2013) to its modified version i.e. Kepler III produced consistent results. The changes did not invalidate earlier results of the MCMC model, for which intensive simulation and evaluation of systematic errors and internal correlations has been done (Humphreys et al. 2013).

## 7.11 Model Fit Results and Discussion

The basic Plummer and Kepler I models do not include the maser acceleration data nor the systemic maser data. Conversely, the more complex Kepler II and III models include these data. The GBT maser accelerations were interpolated onto the VLBI maser positions; the GBT data had a  $\sim 0.3 \text{ km s}^{-1}$  velocity resolution, higher than VLBI data resolution of  $1.6 \text{ km s}^{-1}$ .

Each fit produces an estimate of the central mass and central mass density. The more complex models also solve for the distance of the galaxy. The fits are given below, first for the Plummer toy model, then the Kepler I model, the traditional method based on the systemic maser slope,  $\Omega$ , that was already determined in § 7.9, and finally, the Kepler II and Kepler III models.

### 7.11.1 Plummer and Kepler I Fit Results

The basic Plummer and Kepler I models in Appendix A.4 were fit to the strongly detected ( $\text{SNR} \geq 6$ ) maser spots. The best-fit Plummer cluster parameters are listed in Table 7.4. The corresponding Kepler I fits are given in Table 7.5 and are also shown in Fig. 7.5. Notably, both of these simple models achieved similar coefficients of determination,  $R^2$ , indicating that both models describe the HV maser data equally well.

The Plummer fit and the collision and evaporation timescale arguments (Appendix A.4) yield an upper stellar mass limit of  $\hat{m}_\star \leq 0.4 M_\odot$ , and a longest cluster lifetime of 0.4 Gyr for a cluster of red dwarfs, white dwarfs, or main sequence stars, a lifetime is much shorter than the age of the host galaxy. For another estimate of the collision timescale we also adopted the known stellar velocity dispersion,  $\sigma_\star$ , of  $134 \pm 12 \text{ km s}^{-1}$  (Greene et al. 2010), and also used the maser velocity dispersion traced by the HV masers in the cluster of  $176 \text{ km s}^{-1}$ , with the same outcome for the

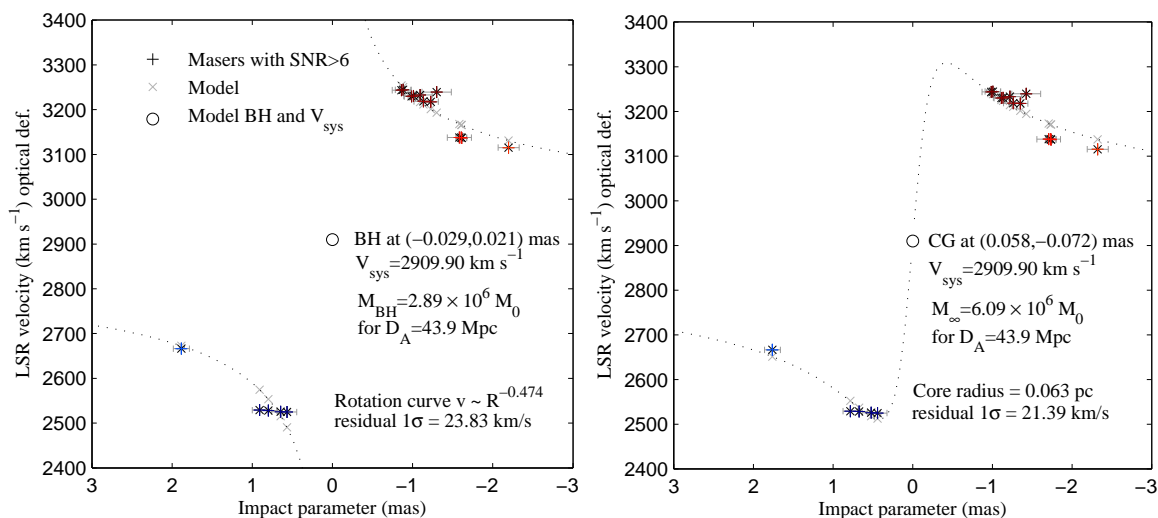


**Fig. 7.5:** The best-fit (near-)Keplerian I model (left) and Plummer cluster model (right). The best-fit parameters are indicated in each panel. The acceleration data are not included in these model fits.

Table 7.4. Plummer model fit to the IC 2560 rotation curve without accelerations.

	$N$	PA (deg)	$M_\infty \pm 1\sigma$ ( $10^6 M_\odot$ )	$\rho$ ( $M_\odot \text{ pc}^{-3}$ )	$\hat{m}_\star$ ( $M_\odot$ )	$r_c$ (pc)	$N_c$ ( $10^6$ )	$t_{\text{coll}}$ (Gyr)	$R^2$
HV only	17	-54.18	$6.05 \pm 1.31$	$5.94 \times 10^9$	$\leq 0.40$	0.062	$\geq 15.1$	$< 0.4$	0.995
HV + syst.	54	-47.69	$5.58 \pm 1.48$	$0.76 \times 10^9$	$\leq 1.13$	0.12	$\geq 5.0$	$< 4.0$	0.860

Note. — Col 2 ( $N$ ): the number of strong maser features ( $\text{SNR} \geq 6$ ) used in the model fit. Col 3 (PA): the best-fit disk position angle. Col 4 ( $M_\infty$ ): the cluster mass. Col 5 ( $\rho$ ): the cluster density (Eq. A.23). Col 6 ( $\hat{m}_\star$ ): upper limit on stellar constituent mass (Eq. A.24). Col 7 ( $r_c$ ): cluster radius. Col 8 ( $N_c$ ): number of cluster members. Col 9 ( $t_{\text{coll}}$ ): collisional timescale (Eq. A.25). Col 10 ( $R^2$ ): the coefficient of determination of the model fit.

cluster lifetime. This strongly rules out a dense dark cluster in the nuclear region of IC 2560.

When systemic masers were included, the more complex Kepler II model (§ 7.11.3) described the data considerably better than the Plummer model, with respective  $R^2$  of 0.995 and 0.860, and Adjusted  $R^2$  of 0.991 and 0.842, whereas the Plummer model did not explain the systemic maser distribution. This too suggests that the masers do not trace a dense dark cluster.

### 7.11.2 Result for the Traditional Distance Fitting Method

For an initial estimate of the SMBH mass a distance of  $43.9 \text{ Mpc} \pm 6\%$  was adopted first to set the linear scale of the disk. Assuming Keplerian rotation (Eq. A.13) and fitting the impact

Table 7.5. Kepler I model fit to the IC 2560 rotation curve without accelerations.

	$N$	PA (deg)	Mass ( $10^6 M_\odot$ )	$\rho$ ( $M_\odot \text{pc}^{-3}$ )	$\gamma$ ( $v \propto r^{-\gamma}$ )	$R^2$
HV, no syst., Keplerian	17	-51.18	$5.04 \pm 0.42$	$3.4 \times 10^8$	0.5	0.991
HV, near-Keplerian	17	-54.18	$2.89 \pm 0.33$	$2.0 \times 10^8$	0.474	0.994

Note. — The first row shows the Keplerian fit ( $\gamma \equiv 0.5$ ), the second row shows the near-Keplerian fit. Col 2 ( $N$ ): the number of fit maser features ( $\text{SNR} \geq 6$ ). Col 3: the best-fit disk PA. Col 4: the SMBH mass. Col 5 ( $\rho$ ): the volume density. Col 6 ( $\gamma$ ): the Keplerian rotation parameter,  $v \propto r^{-\gamma}$ . Col 7 ( $R^2$ ): the coefficient of determination of the fit.

parameters and velocities of the 17 strongest ( $\text{SNR} \geq 6$ ) HV features the weighted average estimate for the SMBH mass is  $4.5 \pm 0.3 \times 10^6 M_\odot$ . The Kepler I model fits (Table 7.5) had a slightly larger  $M_{\text{BH}}$  of  $5.0 \pm 0.4 \times 10^6 M_\odot$  for an edge-on Keplerian disk, and a lower  $2.9 \times 10^6 M_\odot$  for a best-fit sub-Keplerian rotation curve that follows  $v \propto r^{-0.474}$ .

The Keplerian rotation parameter  $k$  (Eq. A.7) that best fit the HV features in the P–V diagram was  $301 \pm 42 \text{ km s}^{-1} \text{ mas}^{0.5}$ , determined with a non-linear least squares method. Similarly, a MCMC-based fit by Meyer (2013) of independently reduced IC 2560 maser data finds  $305 \pm 40 \text{ km s}^{-1} \text{ mas}^{0.5}$ . Although the triplet of best-fit parameters ( $k$ ,  $\Omega$ ,  $a$ ) can yield a distance  $D_A$  (Eq. A.7), the parameter uncertainties were too large for a meaningful distance estimate. Overall, the precision of the slope  $\Omega$  was limited as the systemic group was comparable in size to the VLBI synthetic beam and had a narrow velocity span of  $45 \text{ km s}^{-1}$ . This reduces the “lever arm” in the linear slope fit compared to, e.g., the systemic masers in UGC 3789 that span an almost twice wider range of  $85 \text{ km s}^{-1}$  (Braatz et al. 2010). In addition, the lower maser flux density and the shorter velocity span of the HV features reduce the precision of  $k$ . In effect, a sub-1 % accuracy constraint on  $k$  as in UGC 3789 (Braatz et al. 2010) can not be reached for IC 2560.

Instead of using the averaged maser data and linear fits as above that necessarily lose some of the maser information, we proceeded by fitting the full maser data.

### 7.11.3 Kepler II Fit Result

For a first estimate of the angular diameter distance and the Hubble constant the Kepler II model parameters were fit to the full maser data including also the systemic maser accelerations. The Hubble constant  $H_0$  was left unbounded for the fit, but a fixed disk inclination of  $90^\circ$  had to be assumed due to its strong anti-correlation with  $M_{\text{BH}}$ , and because the Kepler II model (and also Kepler III) does not account for the maser beam opening angle (e.g.,  $7^\circ$  in NGC 4258; Miyoshi et al. 1995) that reduces the observed intensity with decreasing disk inclination.

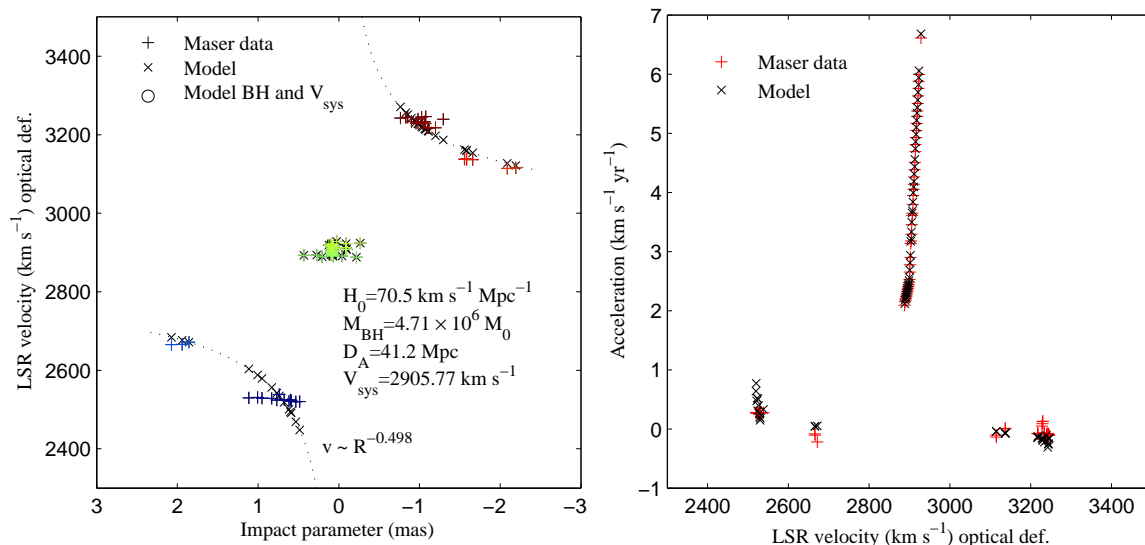


**Fig. 7.6:** The IC 2560 maser impact parameters and velocities (left), and accelerations (right; also see Fig. 7.3), for the Kepler II model fit with free parameters including  $H_0$  and  $M_{\text{BH}}$ . The fit and model data are overlaid.

The Kepler II model included full relativistic corrections. The corrections were small; relative to IC 2560’s cosmological GR redshift, the SR Doppler shift due to the maser orbital speed was below 0.03 %, the GR gravitational redshift was below 0.05 %, and the difference in distance  $D_A$  with and without an assumed a priori  $\Lambda$ CDM cosmology (Eqs. A.4 vs. A.5) was 1.2 %.

The best Kepler II fit ( $R^2 = 0.993$ ) is shown in Fig. 7.6. It yielded a value for  $D_A$  of 41.2 Mpc that also agrees with Yamauchi et al. (2012) within their  $1\sigma$  uncertainty, and a SMBH mass  $M_{\text{BH}}$  of  $4.7 \times 10^6 M_\odot$ , with masers tracing a practically Keplerian rotation curve with  $\gamma = -0.498$ . The fit absorbed the Maoz–McKee -like HV acceleration signature relatively well into an azimuth offset of about  $10^\circ$ . In addition, the fit finds a value for the Hubble constant  $H_0$  of  $70.5 \text{ km s}^{-1} \text{ Mpc}^{-1}$ , and a recessional velocity of the galaxy of  $2905.8 \text{ km s}^{-1}$ . Note that in the CMB reference frame (the “preferred” frame for  $H_0$ ) the observed IC 2560 radial velocities are  $V_{\text{CMB}} \approx V_{\text{LSR}} + 335 \pm 23 \text{ km s}^{-1}$  (Fixsen et al. 1996). The difference between the fitted recessional velocity of  $2905.8 \text{ km s}^{-1}$  and the optical recessional velocity of  $2913 \text{ km s}^{-1}$  LSR is attributed to the peculiar velocity of the galaxy and the CMB–LSR frame offset.

The HV masers covered larger radii (0.1 pc to 0.4 pc, based on the distance) compared to the systemic masers (0.05 pc to 0.10 pc, based on their accelerations and the fitted SMBH mass).

The outer systemic masers at 0.1 pc have an estimated orbital period,  $T = 2\pi(r^3/GM_{\text{BH}})^{-1/2}$ , of about 1400 yr, with a  $450 \text{ km s}^{-1}$  circular velocity that is approximately that of the inner HV masers at 0.1 pc, i.e., the bluest HV features in the GBT spectra. For a LOS velocity change

equal to the  $45 \text{ km s}^{-1}$  width of the systemic group, masers traverse  $\Delta\phi \sim 6^\circ$  of in-disk azimuth (Eq. A.14), indicating a full-width beaming angle of between  $3^\circ$  and  $6^\circ$ . Systemic masers would then pass through the  $6^\circ$  azimuthal slice in 5 to 100 years, depending on their radius.

To estimate uncertainties due to overfitting the Keplerian model into the necessarily incomplete maser data (e.g., additional VLBI epochs and better sensitivity can detect other maser spots along the disk, markedly changing the optimal parameters if the model was overfitted), 550 iterations of a Leave-2-Out bootstrap on Kepler II model fit were run. The measurement uncertainties of the input data are not fully propagated, however, because Kepler II performs an unweighted fit. Rather, the bootstrap method estimates the sensitivity to changes in the data set, or the quality of the current fit in light of “new” maser data. The arithmetic modes of the best-fit parameters, including  $H_0$ , remained similar over the bootstrap iteration. The arithmetic means (of lesser interest in this fit) were somewhat smaller. With the uncertainty estimate from the bootstrap the best-fit  $H_0$  was  $68.1 \pm 5.2 \text{ km s}^{-1} \text{ Mpc}^{-1}$  (8%). The bootstrap method provides an error floor of 8% on the  $H_0$  obtainable with the current maser data under a Keplerian model. The Kepler III model includes more parameters and their degeneracies effectively increase the error floor. A future VLBI follow-up at a higher sensitivity might reduce the uncertainty on  $H_0$ , especially if it can detect more of the low flux density HV maser features.

### 7.11.4 Kepler III Fit Result

Unlike the earlier models, the Kepler III model fit also solves for disk warp and the in-disk azimuth angles and radii,  $(\phi_i, r_i)$ , of all maser features. This means the introduction of over 100 new free parameters to the fit. The primary purpose of the Kepler I and Kepler II fits was to verify the consistency of the results of two low complexity models, compare them to the Plummer cluster model, estimate the precision attainable from the IC 2560 maser data set, and provide a reference baseline for the plausibility of the results given by the highly complex Kepler III model fit. To avoid a bias the best-fit parameters determined in the two independent Kepler I/II fits were not propagated to the Kepler III fit, i.e., the Kepler III fit was also done independently.

The MCMC technique for the Kepler III model fit propagates all a priori uncertainties in, e.g., the galaxy’s recessional velocity, the maser positions, maser velocities, and maser accelerations into the final parameter estimates including  $H_0$ .

Two MCMC fits with different parameter a priori constraint sets were carried out:

**Fit 1** Gaussian priors for  $\phi_i$  and  $r_i$ , no disk warp, no maser orbit eccentricity,  $e = 0$ , and

**Fit 2** Gaussian priors for  $\phi_i$  and for warped disk parameters  $\partial i/\partial r$  and  $\partial \alpha/\partial r$ ,  $e = 0$ .

For every constraint set, four to five parallel MCMC chains with identical settings but different initial chain starting points were run for a duration of  $500 \times 10^6$  iterations per MCMC chain.

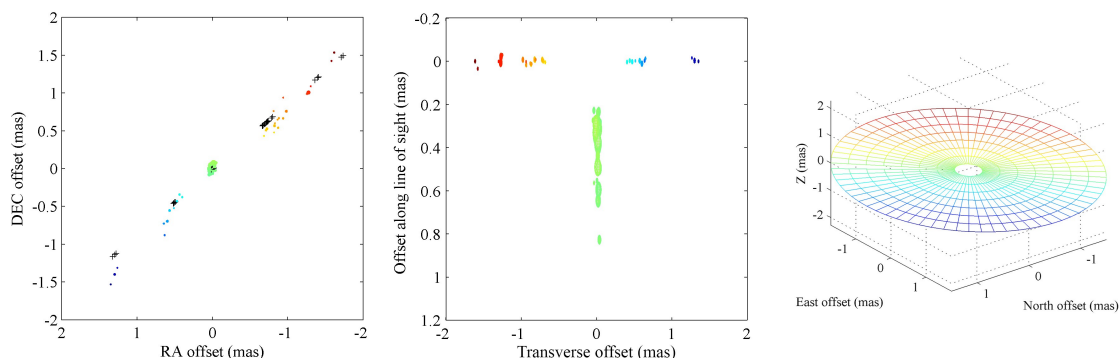


**Fig. 7.7:** The masing disk geometry for Fit 1: The original IC 2560 maser sky positions (left) with the model overlaid (crosses), the maser in-disk positions (middle), and the warp-free disk (right).

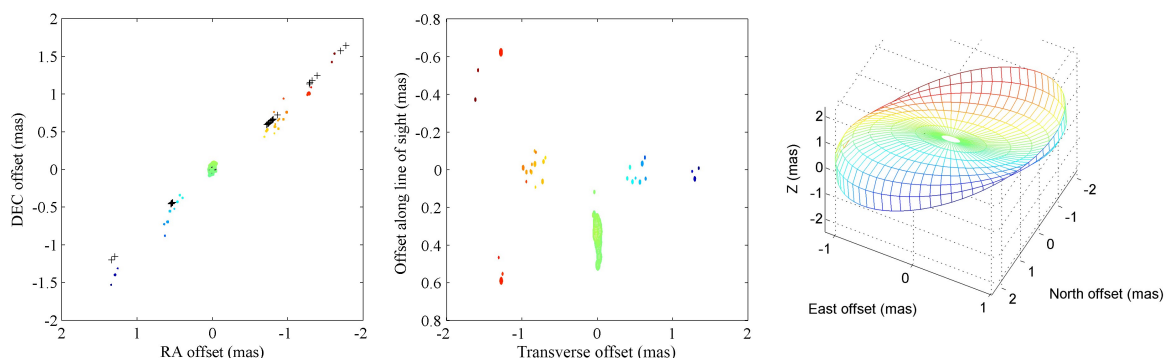


**Fig. 7.8:** The masing disk geometry for Fit 2: The original IC 2560 maser sky positions (left) with the model overlaid (crosses), the maser in-disk positions (middle), and the disk warp exaggerated by factor 10 (right).

After the run the chains were merged and the parameter posterior distributions were derived from the chain statistics. This essentially entailed histogram binning of the over  $500 \times 10^6$  total parameters values that were sampled and output by the MCMC chain. Properties such as the peak (the most likely parameter value), the shape of the histogram (the closest-matching type of posterior probability distribution, e.g., Gaussian or skew normal), and the spread in each parameter (confidence intervals) can be directly deduced from the histogram.

The posterior distributions of the parameters determined in Fits 1 and 2 are shown in the series of Figures in Appendix A.7 (page 232ff.). The joint distributions (e.g.,  $M_{\text{BH}}$  against  $H_0$ ) are also shown in Appendix A.7. The maser positions in the disk and the geometry of the disk as determined by the two MCMC fits are illustrated in Fig. 7.7 (Fit 1) and in Fig. 7.8 (Fit 2).

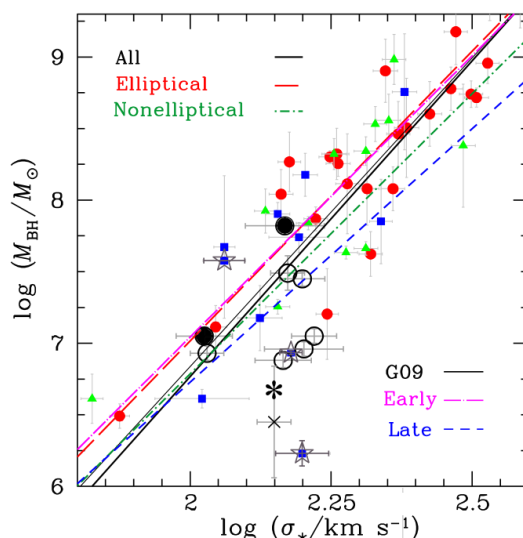
The a priori parameters that were used for the fit, and the best-fit posterior parameters and their uncertainties are given in Table 7.6.



Table 7.6. Best-fit parameters of the Keplerian disk model for the IC 2560 maser position and acceleration data, determined with the MCMC method.

MCMC Fit	Parameters					
Fit 1 Priors	$H_0 \sim \mathcal{F}(65)$	$M_{\text{BH}} \sim \mathcal{N}(0.44, 1.0)$	$V_{\text{LSR}} \sim \mathcal{N}(2913, 3)$	$x_0 \sim \mathcal{N}(0, 0.1)$	$y_0 \sim \mathcal{N}(0, 0.1)$	
	$i \sim \mathcal{N}(90, 0.5)$	$\alpha \sim \mathcal{N}(-49.4, 1.0)$	$V_{\text{pec,r}} \sim \mathcal{N}(335, 300)$	$\phi_i \sim \mathcal{N}(0, 1.0)$		
	Posteriors	$\tilde{H}_0 = 71.37 \pm 10.82$	$\tilde{M}_{\text{BH}} = 0.51 \pm 0.07$	$\tilde{V}_{\text{LSR}} = 2906.72 \pm 0.90$	$\tilde{x}_0 = -0.01 \pm 0.00$	$\tilde{y}_0 = 0.00 \pm 0.01$
		$\tilde{H}_0 = 69.75^{+12.10}_{-9.40}$	$\tilde{M}_{\text{BH}} = 0.49^{+0.09}_{-0.06}$	$\tilde{V}_{\text{LSR}} = 2906.70^{+0.85}_{-0.86}$	$\tilde{x}_0 = -0.01^{+0.00}_{-0.00}$	$\tilde{y}_0 = 0.00^{+0.01}_{-0.01}$
		$\tilde{i} = 89.30 \pm 0.40$	$\tilde{\alpha} = -49.41 \pm 0.58$	$\tilde{V}_{\text{pec,r}} = 345.52 \pm 199.48$		
$\tilde{i} = 89.40^{+0.30}_{-0.48}$	$\tilde{\alpha} = -49.40^{+0.57}_{-0.58}$	$\tilde{V}_{\text{pec,r}} = 357.37^{+193.50}_{-205.39}$				
Shape	$H_0 : 0.33, 0.19$	$M_{\text{BH}} : 0.58, 0.64$	$V_{\text{LSR}} : 0.01, 0.00$	$x_0 : -0.01, 0.00$	$y_0 : -0.00, 0.00$	
	$i : -0.49, -0.12$	$\alpha : -0.03, -0.01$	$V_{\text{pec,r}} : -0.03, -0.07$			
Fit 2 Priors	$H_0 \sim \mathcal{F}(65)$	$M_{\text{BH}} \sim \mathcal{N}(0.44, 1.0)$	$V_{\text{LSR}} \sim \mathcal{N}(2913, 3)$	$x_0 \sim \mathcal{N}(0, 0.1)$	$y_0 \sim \mathcal{N}(0, 0.1)$	
	$i \sim \mathcal{N}(90, 0.5)$	$\partial i / \partial r \sim \mathcal{N}(0, 0.5)$	$\alpha \sim \mathcal{N}(-49.4, 1.0)$	$\partial \alpha / \partial r \sim \mathcal{N}(0, 1.0)$	$V_{\text{pec,r}} \sim \mathcal{N}(335, 200)$	
	Posteriors	$\tilde{H}_0 = 69.39 \pm 10.34$	$\tilde{M}_{\text{BH}} = 0.56 \pm 0.08$	$\tilde{V}_{\text{LSR}} = 2910.53 \pm 1.09$	$\tilde{x}_0 = -0.01 \pm 0.00$	$\tilde{y}_0 = 0.00 \pm 0.01$
		$\tilde{H}_0 = 67.74^{+11.63}_{-8.89}$	$\tilde{M}_{\text{BH}} = 0.54^{+0.09}_{-0.06}$	$\tilde{V}_{\text{LSR}} = 2910.55^{+1.00}_{-1.09}$	$\tilde{x}_0 = -0.01^{+0.00}_{-0.00}$	$\tilde{y}_0 = 0.00^{+0.01}_{-0.01}$
		$\tilde{i} = 89.29 \pm 0.40$	$\tilde{\partial i} / \partial r = 0.50 \pm 0.50$	$\tilde{\alpha} = -49.98 \pm 0.59$	$\tilde{\partial \alpha} / \partial r = 2.66 \pm 0.79$	$\tilde{V}_{\text{pec,r}} = 343.99 \pm 200.48$
$\tilde{i} = 89.38^{+0.31}_{-0.47}$	$\tilde{\partial i} / \partial r = 0.49^{+0.51}_{-0.49}$	$\tilde{\alpha} = -49.98^{+0.59}_{-0.58}$	$\tilde{\partial \alpha} / \partial r = 2.68^{+0.78}_{-0.80}$	$\tilde{V}_{\text{pec,r}} = 343.73^{+200.36}_{-200.50}$		
Shape	$H_0 : 0.35, 0.18$	$M_{\text{BH}} : 0.53, 0.51$	$V_{\text{LSR}} : -0.01, 0.00$	$x_0 : -0.02, 0.00$	$y_0 : -0.00, 0.00$	
	$i : -0.48, -0.11$	$\partial i / \partial r : 0.01, -0.03$	$\alpha : -0.01, -0.00$	$\partial \alpha / \partial r : -0.03, -0.01$	$V_{\text{pec,r}} : -0.01, -0.05$	

Note. — Refer to the Appendix (§ A.4) for parameter descriptions. The black hole mass,  $M_{\text{BH}}$ , is in units of  $10^7 M_{\odot}$ . Priors have uniform  $X \sim \mathcal{U}(a, b)$  or normal  $X \sim \mathcal{N}(\mu, \sigma)$  probability distributions parameterized by the lower and upper limits,  $a$  and  $b$ , or the mean,  $\mu$ , and the standard deviation  $\sigma$  (not the variance  $\sigma^2$ ). The flat prior  $X \sim \mathcal{F}(x_0)$  is essentially “free”,  $X \sim \mathcal{U}(-\infty, +\infty)$ , with an initial MCMC sample value of  $x_0$ . The priors for in-disk azimuth angles  $\phi_i$  denote an offset relative to the default line of sight and midline azimuth angles. The number of MCMC iterations,  $N$ , goodness of fit in terms of reduced  $\chi^2$ ,  $\chi_{\text{red}}^2$ , with a fiducial degrees of freedom of about 124 (not compensated for model non-linearities and strong parameter correlations), and the arithmetic means and modes of the parameters,  $\bar{X} \pm 1\sigma$  and  $\tilde{X} \pm 34\%$  confidence intervals, are shown for each fit. The skewness and excess kurtosis,  $\gamma_1$  and  $\gamma_2$ , of the parameter distributions (see also Figs. A.7.1 and A.7.3) are given in the shape row (e.g.,  $H_0 : \gamma_1, \gamma_2$ ). While a perfect normal distribution has zero skewness and kurtosis, the limited maser data and the internal correlation between model parameters can lead to a skewed probability distribution.



**Fig. 7.9:** The best-fit  $M_{\text{BH}}-\sigma_*$  power laws in a figure adopted from Greene et al. (2010). The  $M_{\text{BH}}-\sigma_*$  power law fits through all galaxies (solid) or sub-samples of galaxies (dashed, dotted) are shown. Maser galaxies categorized by Greene et al. as having a pseudo-bulge (open large circles) or a classic bulge (filled large circles) are indicated, as is the Greene et al. measurement of  $\sigma_* \approx 10^{2.15 \pm 0.03}$  in IC 2560 (horizontal location of cross; note, Greene et al. provide no reference for their adopted SMBH mass and state error bars are “heuristic only”). The new maser-based  $M_{\text{BH}}$  mass of Fit 2 is overlaid (asterisk) and has a  $3\sigma$  uncertainty of about the diameter of the asterisk.

The flat disk model without a warp produced the most plausible in-disk maser positions.

In the warped model seven red HV masers appeared offset in azimuth from the disk midline. However, overall the parameters of the warped disk Fit 2 described the maser data best ( $\chi_{\text{red}}^2 = 1.8$ ) and thus the Fit 2 is adopted as the final parameter set.

We find a best-fit  $H_0$  of  $67.7^{+11.6}_{-8.9}$  km s $^{-1}$  Mpc $^{-1}$  and a SMBH mass of  $5.4^{+0.9}_{-0.6} \times 10^6 M_{\odot}$  stated with  $1\sigma$  uncertainties.

The SMBH mass occupies the low-mass range of the  $M_{\text{BH}}-\sigma_*$  relation for elliptical and spiral galaxies. With a stellar velocity dispersion of  $134 \pm 12$  km s $^{-1}$  (Greene et al. 2010), the SMBH mass in IC 2560 lies by a factor of 10 below the mass predicted by the  $M_{\text{BH}}-\sigma_*$  relations for non-maser galaxies (see Fig. 7.9). That is, IC 2560 appears systematically undermassive like some other H $_2$ O megamaser galaxies, in particular those classified by Greene et al. as having a pseudo-bulge (open circles in Fig. 7.9). The undermassive SMBHs are thought to be the result of a quiescent merger history or a low efficiency of the host galaxy at feeding the SMBH (Greene et al. 2010; McConnell et al. 2011).

## 7.12 Summary and Conclusions

This Chapter presented spectra, velocity drifts and VLBI images for 22 GHz H<sub>2</sub>O megamasers detected towards IC 2560, first detected by Braatz et al. 1996. The Plummer cluster toy model was ruled out as a description of the observed IC 2560 maser features. Given the good consistency of the data with Keplerian models, and the high central volume densities, we conclude that IC 2560 hosts a SMBH in its nuclear region.

The systemic disk masers in IC 2560 had a velocity gradient of  $\Omega = -477 \pm 67 \text{ km s}^{-1} \text{ mas}^{-1}$  (combined with Yamauchi et al. (2012) VLBI data), and the disk masers showed Keplerian rotation with a Keplerian parameter  $k = 301 \pm 42 \text{ km s}^{-1} \text{ mas}^{0.5}$ . The HV maser groups had non-zero accelerations with a sign change and a  $5\sigma$  tension between the positive and negative accelerations. The acceleration was consistent with the signature predicted by the Maoz–McKee spiral model, described by a spiral pitch angle of  $5.3 \pm 0.1^\circ$ . In a detailed Markov Chain Monte Carlo model fit (used for the propagation of full input data uncertainties and parameter prior uncertainties) the maser data agreed closest with a slightly warped Keplerian disk.

The IC 2560 maser data yielded a SMBH mass of  $5.4_{-0.6}^{+0.9} \times 10^6 M_\odot$  and a Hubble constant,  $H_0$ , of  $67.7_{-8.9}^{+11.6} \text{ km s}^{-1} \text{ Mpc}^{-1}$ . This improves upon Yamauchi et al. (2012) via higher-sensitivity VLBI data, longer single-dish monitoring, newer models with relativistic corrections, and Bayesian fitting methods. A weighted average of the result from IC 2560 and the recent values for  $H_0$  determined by the MCP project for the disk maser galaxies UGC 3789 and NGC 6264 (Reid et al. 2013; Kuo et al. 2013), see Table 7.1, yields a new entirely maser-based  $H_0$  value of  $68.4 \pm 5.3 \text{ km s}^{-1} \text{ Mpc}^{-1}$  (8%). When we further include the recent  $H_0$  measurements that are based on other methods (listed in Table 7.1 in the introduction to this Chapter), the weighted average value of the Hubble constant becomes  $69.5 \pm 0.5 \text{ km s}^{-1} \text{ Mpc}^{-1}$  (0.8%).

Both the water maser-based  $H_0$  and the general  $H_0$  average are consistent with the median statistic is significantly more robust to systematic errors. The median statistic applied by Crandall & Ratra (2013) yields a value of  $68_{-14}^{+8} \text{ km s}^{-1} \text{ Mpc}^{-1}$  taken over 124 measurements from 1990 to 2010. The result of Crandall & Ratra is also consistent with the median statistic of  $68 \pm 2.8 \text{ km s}^{-1} \text{ Mpc}^{-1}$  derived from 553 measurements by Chen & Ratra (2011). All estimates are in good agreement with the  $1\sigma$  region for an equation of state parameter  $w$  of  $-1.0$  in a flat  $\Lambda$ CDM cosmology.

The still relatively weak MCP constraints on the Hubble constant (8%) do not, by themselves, falsify  $\Lambda$ CDM nor do they entirely rule out different competing models for Dark Energy that predict a  $w \neq -1.0$  or a redshift-dependent  $w$ . Additional disk maser galaxies are required to improve the precision of the maser-based Hubble constant and to eventually reach the sub-2% precision that is required to constrain  $w$  and to falsify  $\Lambda$ CDM (Mortonson et al. 2010). For this reason new disk maser galaxies are currently being observed and analyzed in the MCP project.

## 8 Deeper into AGN: $\lambda 1.3$ mm-VLBI

This final Chapter reports the results of the first successful very long baseline interferometry (VLBI) observation with the Atacama Pathfinder Experiment (APEX) telescope. The Chapter follows a paper to be published in A&A (Wagner, Roy, Krichbaum *et al.*) and includes the data analysis and the tentative results of a 230 GHz VLBI ( $\lambda 1.3$  mm) fringe finder observation (PI: T. P. Krichbaum) of the blazar 3C 279 using the APEX telescope. The observation was conducted in 2012 May with two stations of the Global mm-VLBI Array (GMVA) and the Event Horizon Telescope (EHT) project. The challenging but successful experiment increased the current mm-VLBI angular resolution of about  $60 \mu\text{as}$  to now  $28.6 \mu\text{as}$ . This allows future observations to resolve the last-photon ring around the Galactic Center SMBH event horizon, and also probe radio jet formation, acceleration and collimation down to a resolution of a few gravitational radii in galaxies like M 87.

The results of the observation include spatially resolved 3C 279 inner region core/jet structure, an APEX station position measurement and verification of the native polarization. The Chapter contains some technical topics due to this being the first VLBI observation with APEX, and a number of issues were encountered that should be presented, as they make some of the presented findings on 3C 279 fine-scale structure highly tentative.



**Fig. 8.1:** The APEX 12 m telescope (214–1390 GHz) in Atacama, Chile, jointly operated by the MPIfR (50%), OSO (23%), and ESO (27%).

## 8.1 Abstract

We observed 3C 279 on 2012 May 7 in one 5 hour VLBI track with APEX, SMA and the ARO SMT (baseline lengths of 3200 M $\lambda$  to 6800 M $\lambda$ ) with a 28.6  $\mu$ s finest fringe spacing and  $< 50$  mJy beam $^{-1}$  sensitivity ( $3\sigma$ ). The necessary on-site VLBI equipment installation prior to the observation was done by A. L. Roy and myself, and M. Lindqvist assisted in the observation.

We detected fringes on all baselines with SNRs of 12 to 55 in 420 s. The 230 GHz total flux density of 3C 279 was 19.79 Jy and the VLBI correlated flux density on the longest baseline averaged about 300 mJy beam $^{-1}$ . No circular cross-hand fringes were detected. The SMA used linear polarization and visibilities had a mixed polarization. The amplitude and ‘‘closure phase’’ were non-zero and non-linear. They implied a spatially resolved asymmetric source structure with at least three components.

We model fitted initial models in Difmap that we derived from quasi-simultaneous super-resolved 43 GHz ( $\lambda$ 7 mm) and 86 GHz ( $\lambda$ 3 mm) images. Our polarization uncertainties and sparse uv coverage did not allow finding complete and unique source models. Instead, we used 3 mm and 7 mm images for guided but highly tentative modelfits. The best-fitting model had six compact components in the inner 3 pc. The modelfit was suggestive of a northwest-southeast oriented jet with a position angle (PA) of  $168 \pm 25^\circ$ , and brightness temperatures,  $T_b$ , of  $10^{10}$  K to  $10^{11}$  K for the presumed jet components. Other models produced  $T_b$  in the same range. These  $T_b$  appear to agree with a Doppler boosted intrinsic  $T_{\text{int}}$  close to an equipartition  $T_{\text{eq}}$  of  $\simeq 10^{10.5}$  K, and the component  $\beta_{\text{app}}$  of 2.9 and 5.2 estimated from their non-ballistic, superluminal motion in six 43 GHz VLBA epochs. The  $168 \pm 25^\circ$  PA tentatively agreed with the 1.3 mm EHT PA from 2011 accounting for the motion seen in 43 GHz components. However, shorter baseline  $\lambda$ 1.3 mm to  $\lambda$ 1.3 cm data suggest complex polarized structure that are likely to impact our tentative results, especially due to our polarization uncertainties. To confirm the structure in the inner parsecs of 3C 279, follow-up observations with APEX and five other mm-VLBI stations have been conducted (March 2013) with a consistent polarization setup. The new data are being analyzed and will be presented in a later paper, not part of this thesis.

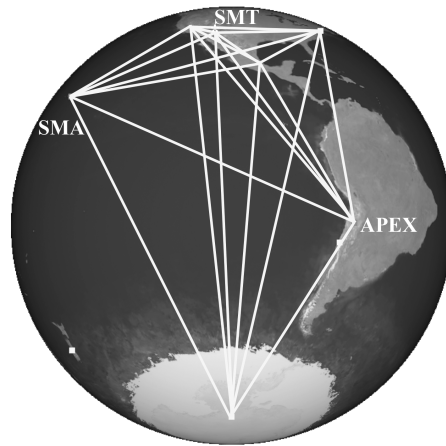


**Fig. 8.2:** The future 1 mm VLBI array seen from above the western hemisphere. Adopted from Doeleman (astro2010).

## 8.2 Introduction

The optically violent variable blazar 3C 279 is one of the brightest quasars at all wavelengths and is one of the best monitored flat-spectrum quasars since it was the first object to exhibit superluminal motion. It has a central black hole mass,  $M_{\text{BH}}$ , of about  $0.54 \times 10^9 M_{\odot}$  (Nilsson et al. 2009). This corresponds to a Schwarzschild radius,  $R_s$ , of 10 AU. At a redshift of  $z = 0.5362$  (Marziani et al. 1996), the angular diameter distance is 1321 Mpc and the linear scale is  $1.0 \mu\text{as} \cong 0.0064 \text{ pc} \cong 130 R_s$ , assuming a flat  $\Lambda$ CDM cosmology with  $H_0 = 69.7 \text{ km s}^{-1} \text{ Mpc}^{-1}$ ,  $\Omega_m = 0.281$ , and  $\Omega_{\Lambda} = 0.719$  (Hinshaw et al. 2013).

The source of the strong emission from radio to VHE  $\gamma$ -ray is a relativistic jet ejected from the black hole. The large-scale structure and jet have been studied in great detail. The 3C 279 core, jet base and components are compact and are well-resolved in earlier lower frequency VLBI observations. The VLBI jet extends towards the southwest and is closely aligned to the line of sight at an angle as small as  $< 0.5^\circ$  (Jorstad et al. 2004). The jet base was previously presumed to coincide with a stationary component offset by 0.95 mas from the core. Both linear and circular polarized emission from the jet is detected with VSOP at 4.8 GHz with 500  $\mu\text{as}$  resolution (Pant et al. 2009) and with CMVA at 86 GHz with 520  $\mu\text{as}$  resolution (Attridge 2001) and with the VLBA at 22 GHz (Gabuzda & Cawthorne 2000) and at 24 GHz and lower frequencies (Homan et al. 2009). These polarimetric observations see about 1 % circular polarization at 15 GHz and 24 GHz over a component triplet in the inner 1 mas near the core, and a linear polarization degree of about 5 % for the core and about 20 % for the inner jet components at 22 GHz and at 86 GHz.

It is thought that viewing angle effects create apparent different classes of astronomical objects and blazars (like 3C 279) may be quasars (QSOs) viewed down the relativistic jet. Relativistic jets are presumed to have a jet base located close to the AGN accretion disk and a central supermassive black hole (SMBH). Synchrotron radiation emitted by relativistic electrons spiraling in the jet magnetic field gives rise to strong radio emission. The 3C 279 radio flaring and high variability on hour to year time-scales in total flux density is strongly correlated across all frequencies and has been monitored for decades (MOJAVE project, Lister et al. 2009; Boston University monitoring project, Jorstad et al. 2011 Fermi Symposium, eConf C110509). While variability is well-described by multi-shock models with shocks propagating in the jet, the actual mechanisms at the heart of a quasar that initiate, launch and collimate jets such as in 3C 279 are currently not understood. These mechanisms can be probed by high resolution mm-VLBI. The competing models for jet launching mechanisms are distinguished by a wide or very compact opening angle at the jet base (in the Blandford-Payne (BP) and Blandford-Znajek (BZ) models, respectively; Blandford & Znajek 1977; Blandford & Payne 1982) with characteristic flux variability time-scales or distinct radial brightness temperature profiles. In single-dish monitoring

both inner jet and core emission merge in the beam and variability time-scale arguments cannot be applied conclusively to constrain the linear scale of the jet base to discern between BP and BZ models. At cm-wavelength VLBI, component blending and opacity-dependent effects such as core shift also preclude a direct measurement. However, core shift data of over 20 sources including M 87 suggest that core opacity decreases with frequency (O’Sullivan & Gabuzda 2009; Sokolovsky et al. 2011; Hada et al. 2011) and we see deeper into the central engine. Using mm-VLBI above 43 GHz the opacity effects become negligible and the observed fine-scale structure resembles closely the emission’s true position and diameter.

Our primary motivation for mm-VLBI on 3C 279 using the Atacama Pathfinder Experiment (APEX) 12 m telescope<sup>1</sup> was to show APEX readiness for imaging of Sgr A\* and M 87 core regions by demonstrating first 1.3 mm VLBI fringes at extremely long baselines (7170 km to 9450 km). Apart from the technical motivation our science goal was to detect emission from the jet base and components in the inner small-scale structure of 3C 279. This extends earlier work with shorter baselines on the Global mm-VLBI Array (GMVA)<sup>2</sup> (e.g., Krichbaum et al. 2008; 2013), and work by Fish et al. (2011), Doeleman et al. (2012) and Lu et al. (2013). The latter groups made detections of Sgr A\*, M 87 and 3C 279 with the new mm-VLBI network, the Event Horizon Telescope (EHT)<sup>3</sup>, at that time without the southern APEX telescope. The EHT is an open collaboration led by the MIT Haystack observatory with several partners including the MPIfR Bonn and the Onsala Space Observatory, Chalmers University of Technology.

There were two earlier independent attempts to improve the resolution of the GMVA network and the EHT from  $\approx 60\text{--}150\ \mu\text{s}$  to  $< 30\ \mu\text{s}$  by including a new southern sub-mm VLBI station. Few southern stations with 230 GHz and 345 GHz receivers are equipped for VLBI. The ASTE and APEX telescopes in Chile were used exclusively for single dish observations and required significant VLBI hardware installation work before attempting mm- and sub-mm VLBI. The first attempt by Honma et al. (NAOJ) in 2010 using the 10 m ASTE telescope at Chajnantor did not produce fringes. The second was our 2011 observation with APEX (MPIfR, OSO) that failed due to an unknown large clock offset.

After receiver and VLBI system improvements at APEX in 2012 (for technical details, see Roy et al. 2013) we detected first fringes at 230 GHz. We achieved the currently highest angular resolution of  $28.6\ \mu\text{s}$ . The improvements at APEX critically extend the resolution of mm-VLBI. As the first station with (sub-)mm-VLBI capability located in the southern hemisphere, APEX improves uv plane coverage, and provides the critical angular resolution of  $< 50\ \mu\text{s}$  (230 GHz) required to resolve the emission associated with the Galactic Center (GC) black hole and M 87

<sup>1</sup>This work is based on data acquired with the Atacama Pathfinder Experiment (APEX). APEX is a collaboration between the Max-Planck-Institut für Radioastronomie, the European Southern Observatory, and the Onsala Space Observatory.

<sup>2</sup><http://www3.mpifr-bonn.mpg.de/div/vlbi/globalmm/>

<sup>3</sup><http://www.eventhorizontelescope.org>

in order to detect the last-photon emission ring around its shadow ( $\approx 40 \mu\text{as}$ ) with a beam size equivalent to a spatial resolution of 2 to 10 Schwarzschild radii (Doeleman et al. 2012). The same angular resolution can be used to probe the structure in the inner parsec of other nearby and high redshift ( $z > 2$ ) QSOs. Several such sources will be observed over the next years.

### 8.3 Zero Spacing Flux Density

The SMA 230 GHz flux density monitoring program (Gurwell et al. 2007) includes 3C 279. On 2012 May 7 an interferometric flux density measurement with the SMA on 3C 279 yielded a total flux density of 19.79 Jy at 230 GHz. This value agreed well with the phased-SMA data from the SMA flux density monitoring program where a similar flux density was seen on 2012 April 27 and May 11. The SMA 1 mm and 860  $\mu\text{m}$  light curves<sup>1</sup> showed 3C 279 to be in a flaring state, with the VLBI observation around the middle of a double-peaked flare.

### 8.4 VLBI Observation

We observed 3C 279 in the 230 GHz (1.3 mm) VLBI session on 2012 May 7, DOY 128, UT 02:00 to UT 06:52, under good atmospheric conditions. Three stations participated in the observation (Table 8.2). The first was the 12 meter APEX telescope (jointly operated by the MPIfR, ESO and OSO) at 5104 meters altitude on the Chajnantor plateau in Atacama, Chile (see Güsten et al. 2006), close to the new ALMA array and the ASTE telescope. The second was the Arizona Radio Observatory (ARO) that operates the 10 meter Heinrich Hertz Sub-millimeter Telescope (ARO SMT) at 3159 meters altitude on Mount Graham, Arizona. The third was the Submillimeter Array (SMA; CfA and ASIAA) with eight 6 meter dishes at 4115 meters on Mauna Kea, Hawaii. The phased SMA had an effective aperture of 12.5 m assuming a typical 0.69 aperture efficiency and 0.9 phasing efficiency. The observation started at UT 02:00 with the single APEX–ARO SMT baseline. The SMA joined at UT 03:15.

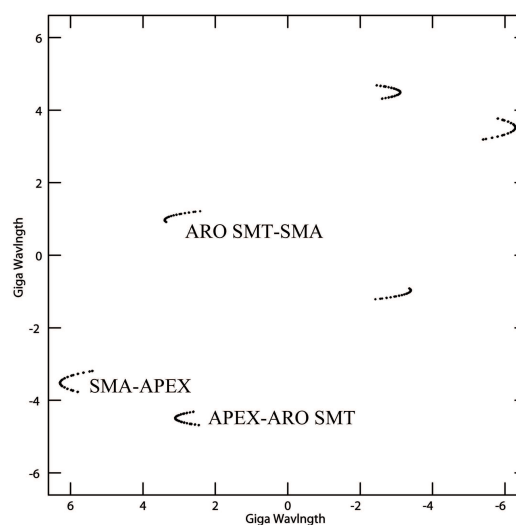


**Fig. 8.3:** The sparse UV coverage on 3C 279 for the APEX 1.3 mm VLBI experiment on 2012 May 7 from UT 02:00 to UT 07:00.

<sup>1</sup>The proprietary SMA light curve data is available at <http://sma1.sma.hawaii.edu/>



**Table 8.1:** Fringe spacings and baseline sensitivities.

Baseline	B (km)	B (M $\lambda$ )	$\theta_B$ ( $\mu$ as)	Data Hours	$dS_{230}$ (mJy)
SMT–SMA	4627	3200	58.4	1.75 (1.52)	2.6
APEX–SMT	7174	5400	37.7	2.33 (2.03)	4.0
SMA–APEX	9447	6800	28.6	1.75 (1.22)	2.0

**Notes.** Resolution is given as baseline fringe spacings,  $\theta_B$ . Sensitivity  $dS_{230}$  at  $1\sigma$  is based on unflagged, good data hours (in parentheses), station SEFD and a bandwidth of 480 MHz. SMT is the ARO SMT.

We sampled a 512 MHz contiguous bandwidth in lower sideband at 229.330 GHz with 2 bit depth using two FPGA-based data acquisition systems, the DBE1 (see, e.g., the Digital Backend Memo Series, MIT Haystack) and the DBBC (Tuccari et al. 2012). The polyphase filterbank algorithm that was used limited the usable bandwidth to 480 MHz. We recorded the resulting APEX data stream at 2 Gbps with Mark 5 recorders (see, e.g., Memo#12 of the VLBA Sensitivity Upgrade, MIT Haystack/NRAO, 2008). The recorded data were correlated at the MPIfR Bonn correlator by H. Rottmann, A. Bertarini and myself, until fringes were found on all baselines.

The antennas, baseline length and resolution, and total hours of baseline data are listed in Table 8.1. The uv coverage on 3C 279 is shown in Figure 8.3. The angular resolution (fringe spacing on the longest baseline) was 28.6  $\mu$ as.

### 8.4.1 Polarization

The polarization was effectively a single hand of circular. ARO SMT recorded both RCP and LCP throughout UT 02:00 to UT 06:52. The SMA recorded in linear polarization because quarter-wave plates ( $\lambda/4$  plates) were not inserted. APEX recorded LCP for the first half of the experiment and RCP for the second half.

APEX used the single-polarization facility receiver (APEX-1 SHeFI at 230 GHz; see Belitsky et al. 2007; Vassilev et al. 2008) and we inserted a  $\lambda/4$  plate into the optical path to convert linear into circular polarization. The effective APEX handedness after 9 mirror reflections (Wieching 2010, private comm.) was likely to be LCP but as this marked the first APEX VLBI observation an experimental confirmation was still required. To determine the effective handedness at APEX, we rotated the  $\lambda/4$  plate from 45° anti-clockwise (seen in the direction of propagation) to 45° clockwise half way through the experiment at UT 04:30.

**Table 8.2:** Telescopes and data acquisition in the 2012 May 7 VLBI session.

Telescope	Altitude	Position (WGS84/ITRF2005)	Receiver	Data acquisition
APEX	5104.47 m	23°00'20.8037"S 67°45'32.9035"W <b>2225039.5297 -5441197.6292 -2479303.3597</b>	APEX-1 SHeFI	DBBC2+DBE1 2 x Mark5C
ARO SMT	3158.70 m	32°42'05.8"N 109°53'28"W -1828796.2000 -5054406.8000 3427865.2000	facility	DBE1 2 x Mark5B+
SMA	4115.06 m	19°49'27.2"N 155°28'39"W -5464555.4930 -2492927.9890 2150797.1760	facility	DBE1 2 x Mark5B+

**Notes.** The new APEX position for VLBI, given in Earth-centered Earth-fixed Cartesian coordinates (X, Y, Z), was measured in 2011 using dual-band GPS and is accurate to 1 cm ( $1\sigma$ ). HatLab DBBC2 and Haystack DBE1 backends had 512 MHz 16-channel polyphase filterbanks for 2 Gbps.

### 8.4.2 APEX Station Position

A high precision APEX station position is required for mm-VLBI. A position error causes residual fringe rate during correlation, and coherence loss during time integration. To keep the coherence loss below 10% for 1 s integration requires the residual fringe rate to be  $< 0.25$  Hz, corresponding to a position error of  $< 3$  m for a future 345 GHz VLBI sky frequency.

A low-accuracy position (3 m rms uncertainty) was derived from observations logged over a one-month period in 2010 by a single-band TrueTime XL-AK GPS timing receiver already mounted outside on the upper platform of the telescope. For better accuracy Onsala supplied a dual-band Ashtech Micro-Z GPS receiver. We used a choke-ring GPS antenna, lent by TIGO in Concepción.

To fully sample coordinates along the telescope azimuth track we logged dual-band GPS data over several days in March 2011 while other observations took place. Initial solutions for the kinematic center of the GPS data were derived while at APEX by fitting a circle into the azimuth track to determine its center to 50 cm accuracy. Later, R. Haas (Onsala Space Observatory) performed a similar fit. The final kinematic position solutions were determined by J. Johansson (Onsala Space Observatory) using standard GPS analysis software, and we determined the final circle center giving the position of the azimuth axis with 0.3 mm accuracy. The circle center positions were adjusted upward by  $46 \pm 0.5$  cm, which is the altitude difference between the reference plane of the GPS antenna and the telescope elevation axis, measured by optical sighting along a level. The final single- and dual-band GPS station positions agreed to 20 cm, well within their error bounds. The resulting position of the axis intersection is shown in Table 8.2.

### 8.4.3 APEX Receiver Decoherence and Phase Calibration Tone

We tested the phase coherence of the receiver system by injecting a single sky frequency pilot tone (PCal) into the receiver optics via a horn antenna. The tone was tuned to near 230 GHz and phase-locked to the maser 10 MHz reference. The tone was mixed down to 10 kHz by the IF system and compared to a 10 kHz tone derived directly from the maser 10 MHz reference. This revealed 60 degree rms phase fluctuations, measured manually using an HP 3561A audio analyzer to measure the sideband-to-carrier power ratio of the tone at 10 kHz, corresponding to a coherence of 60 % in 1 second. The measurements also revealed a linear phase drift rate of 13.3 mHz that in a comparison of synthesizers was likely attributed to the maser-locked synthesizer that produced the local oscillator tone for the 230 GHz receiver. The receiver coherence measurement of 2012 was repeated in 2013, with identical results.

The tone injector assembly increased  $T_{\text{sys}}$  by 3 K by scattering ambient noise; the tone power itself was 37 dB below the system noise in the 512 MHz sampled bandwidth and so made negligible contribution to noise. We estimated the beam blockage caused by the tone injector by measuring the antenna efficiency and  $T_{\text{sys}}$  on a primary calibrator (Saturn) with and without the tone injector assembly installed. This yielded values of 190 K and 0.026 K/Jy with the tone injector; and only 3 K lower  $T_{\text{sys}}$  and no change in sensitivity without the tone injector, equal to the nominal APEX 230 GHz sensitivity of 0.026 K/Jy. This shows the beam blockage was close to negligible.

We injected the PCal tone during the 3C 279 VLBI observation. We used the tone phase detected in the Mark 5 recordings to test the correction of fringe visibility phases during post processing to increase instrumental coherence to > 95 % in 1 s and remove the linear 13.3 mHz phase drift (standard fringe fitting was also successful at removing the drift). The PCal tone power provided a SNR of 1000 in a 488 Hz wide tone channel and 21 ms integration time. The PCal in actual Mark 5 data, rather than measured with the HP 3561A, had a slightly lower 50 degree rms, corresponding to a coherence of 70 % in 1 s. The coherence remained stable with < 5 % deviations in each Mark 5 recording, and was consistent across scans. The phase noise

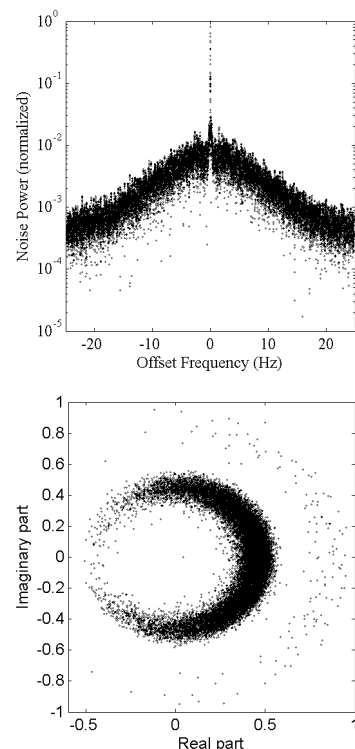


**Fig. 8.4:** Typical phase noise characteristics measured for the APEX receiver. Top: The phase noise spectrum of the extracted PCal tone. Bottom: The extracted PCal signal shown in the complex plane.

**Table 8.3:** Overview of the 3C 279 VLBI observation on 2012 May 7

Time UT	Station polarization and source elevation						Notes
	APEX	EI <sup>a</sup>	ARO SMT	EI	SMA	EI	
02:00-03:15	LCP	72	LCP+RCP	30	–	–	–
03:15-03:30	LCP		LCP+RCP		(X)	11	SMA phasing problem
03:30-03:45	LCP		LCP+RCP		X	15	–
03:45-04:00	(LCP)		LCP+RCP		X		AP Doppler on <sup>b</sup>
04:03-04:15	LCP	62	LCP+RCP	48	X	22	Early AP Doppler <sup>b</sup>
04:30-05:00	RCP		LCP+RCP		X		AP $\lambda/4$ rotated
05:00-05:15	(RCP)		LCP+RCP		X		AP Doppler on
05:15-06:52	RCP	25	LCP+RCP	46	X	57	–

**Notes.** <sup>(a)</sup> Elevation of 3C 279 in degrees from SCHED schedule summary. <sup>(b)</sup> The APEX system enabled Doppler correction which shifted the band, causing a loss of fringes.

characteristic due to the receiver chain, and to an unknown part due to the tone synthesizer, is shown in Fig. 8.4 (top) after removing the 13.3 mHz drift. The receiver phase appeared stable i.e. did not unwind over time (Fig. 8.4 bottom), but had the already mentioned  $\sim 50$  degree rms deviations around zero phase. The impact considering future VLBI observations is an APEX fringe amplitude loss that can be calibrated.

#### 8.4.4 Known Issues

There were no critical issues during the observation. A summary is shown in Table 8.3. About 89 % of raw APEX data were good. The SMA observed in a linear polarization instead of circular polarization since  $\lambda/4$  plates were inadvertently not inserted into the beam. The recorded raw data of one polarization hand were lost and SMA data were thus single polarization. The SMA also had phasing issues during the first scan. In total about 85 % of VLBI baseline data and  $> 95$  % of a priori calibration data were usable.

## 8.5 VLBI Data Reduction

For the 3C 279 observation we had only three VLBI baselines, hence the source visibility function is badly undersampled (e.g., Fig. 8.3). Complex source structure cannot be recovered directly. Instead we used quasi-simultaneous 3 mm and 7 mm VLBI images as templates for the probable small-scale structure. We then followed standard methods (e.g., Rogers et al. 1974) of model fitting Gaussian components into 1.3 mm uv visibility data and closure phase, and derived constraints for the brightness temperature, angular size and spatial distribution of the sub-parsec emission regions in 3C 279.

Station data were correlated at the MPIfR Bonn using the Swinburne DiFX-2 software correlator (Deller et al. 2011). We reduced baseline visibilities using three different software packages: NRAO AIPS 31DEC12 for initial phase and amplitude calibration including fringe fitting, the Haystack Observatory Postprocessing System 3.8 (HOPS; G. Crew, private copy) for specialized mm-VLBI data reduction but no amplitude calibration, and Caltech Difmap (Shepherd 1997) for model fitting into fully calibrated visibility data. Three DiFX correlator runs were necessary to compare the AIPS and HOPS data reduction: 1) 64 channels and a 0.02 s averaging period (AP), 2) 64 channels and a 0.32 s AP allowed by AIPS, 3) 64 channels and the minimum integer 1.0 s AP required by the HOPS data reduction.

The 0.02 s AP dataset was fringe fitted using the basic HOPS fringe fitting software that we had modified to read and apply the APEX phase solutions. This improved the APEX coherence to  $> 95\%$  in 1 s. Unfortunately, the full HOPS mm-VLBI data reduction path did not support such short AP for the input data. Similar restrictions were also imposed by AIPS. We left short AP's as an area of future software improvement work. Instead, the AIPS and HOPS data reduction used the shortest practical AP of 0.32 s and 1.0 s, respectively, and the stable APEX decoherence loss was accounted for with a constant gain correction factor.

### 8.5.1 A Priori Calibration Data

Weather was logged at all stations. Stations performed independent gain calibrations on the Moon and Saturn. Most calibration data were assembled manually. A summary is shown in Table 8.4. Water vapor radiometers (WVR) at each station provided densely spaced zenith opacity,  $\tau_0$ , measurements. APEX antenna gain in kelvin per flux density unit (DPFU),  $g_1$ , is based on the beam brightness temperature of 30.6 K measured on Saturn and the Saturn 230 GHz flux density of 1160.53 Jy computed by the IRAM GILDAS package<sup>1</sup>. The DPFU is corrected for the beam filling factor (Saturn had a diameter of 18.75'' on 2012 May and was in the APEX 27''

**Table 8.4:** Summary of the a priori station calibration data.

Station	$g_0$ (V/V)	$\tau_0$	$T_{\text{sys}}$ (K)	$g_1$ (K/Jy)	SEFD (Jy)
APEX	1/0.7	0.06–0.09	170–185;180	0.0281	6410
ARO SMT	1.0	0.21–0.33	230–300;250	0.0182	13740
SMA	$\sqrt{2}$	0.03–0.06	85–125;95	0.0445	2130

**Notes.** Gains  $g_0$  correct for APEX 70 % decoherence and SMA linear polarization. Atmospheric opacities  $\tau_0$  are based on water vapor radiometer data.  $T_{\text{sys}}$  is shown in a “min–max;mean” format. The ARO SMT system temperatures are double-sideband  $T_{\text{sys}}$ , and the SMA  $T_{\text{sys}}$  is an average of antennas 1 to 7.

<sup>1</sup><http://www.iram.fr/IRAMFR/GILDAS/>

FWHM primary beam) and atmospheric opacity at a Saturn elevation of  $57.9^\circ$  and a  $\tau_0$  of 0.067. The ARO SMT gain and the aperture efficiency,  $\eta_{\text{ap}}$ , agreed with earlier data. SMA antenna gain measurement data were not available, so Table 8.4 shows an estimate for  $g_1$  derived assuming antenna diameters of 6 m, constant  $\eta_{\text{ap}}$  of 0.69 and phasing efficiency,  $\eta_{\text{phasing}}$ , of 0.9 for the 7 (out of 8) phased dishes.

We had no information on the gain-elevation dependence so we assumed the change was negligible for all three stations. This is plausible at the relatively low frequency of 230 GHz compared to the THz operating range of these telescopes. Using a constant antenna gain and using the measured  $T_{\text{sys}}$  values we calibrated the fringe visibility amplitudes from degree of first-order coherence into flux density.

Without previous 230 GHz polarimetry we estimated the mixed-hand baselines to have a  $\sqrt{2}$  amplitude loss, compensated by  $g_0$  in station calibration Table 8.4, not accounting for cross-polarization leakage terms at the stations that are typically low.

### 8.5.2 Fringe Detection

The primary goal of the 3C 279 fringe finder experiment was to detect APEX fringes. We verified the APEX data acquisition system by operating two backends (DBE1 and DBBC) in parallel, sampling two copies of the same signal. Correlating these recordings yielded correlation coefficients  $> 0.95$ , confirming that the backends operated correctly. We then used HOPS for a coarse fringe search in uncalibrated data. All baselines produced fringes and had SNRs between 12 and 55.

The clock rate of APEX was found to be  $-7.523 \times 10^{-8}$  s/s and the rate of ARO SMT was  $6.051 \times 10^{-12}$  s/s relative to the SMA. The high APEX clock rate was due to the APEX H-maser that was locked and stable but had a slightly detuned cavity. There was insufficient time to go through a lengthy cavity tuning process just prior to the experiment. Fortunately DiFX can handle much higher clock rates since it adds the clock rate to the geometrical rate, and the experiment was correlated successfully.

Both APEX–ARO SMT parallel hands (LCP–LCP, RCP–RCP) produced strong fringes with similar fringe amplitudes and with SNRs between 12 and 35. The APEX–ARO SMT cross-hands (LCP–RCP, RCP–LCP) produced no fringes. The ARO SMT ratio  $LR/\sqrt{LL \cdot RR}$  of autocorrelation amplitudes was  $\approx 5\%$ . This indicated a low instrumental polarization leakage. Polarization leakage at APEX has not been characterized. We defer speculations about the lack of cross-hand fringes to the Results section.

On mixed-hand APEX–SMA and ARO SMT–SMA baselines (LCP–X, RCP–X) strong fringes were found. The APEX–SMA baseline had fringe SNRs again between 12 and 35, and ARO SMT–SMA had SNRs up to 55. Regarding ARO SMT dual-circular data, LCP–X fringe amplitude on

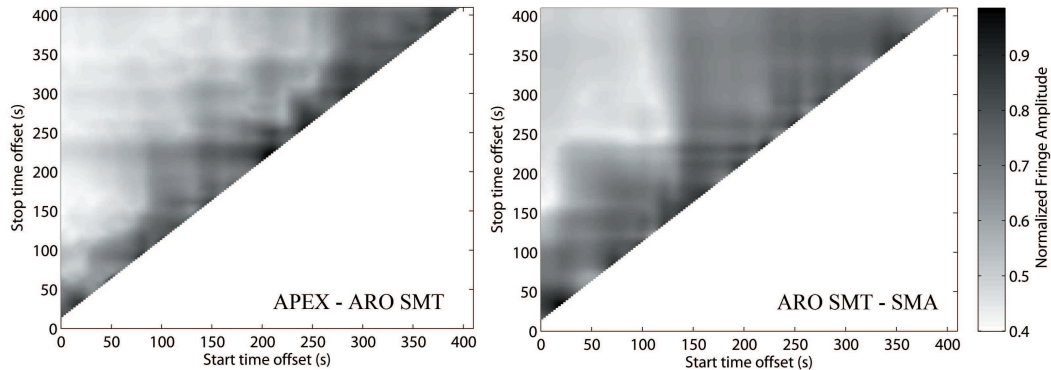


**Fig. 8.5:** Example of fringe amplitudes on the APEX–ARO SMT (left) and ARO SMT–SMA (right) baseline, without APEX receiver PCal phase corrections. Vertical stretches of nearly constant fringe amplitude characterize the coherence time. The amplitude maps are normalized to their peaks. Each fringe amplitude point is the result of a fringe fit over a certain start and stop time range, or “sub-scan”, within the same 420 s scan.

the ARO SMT–SMA baseline was about 10 % to 25 % higher than the RCP–X fringe amplitude. This can still be absorbed into the estimated amplitude calibration uncertainty of 10 % and may not be intrinsic to 3C 279.

### 8.5.3 Phase Stability on the Baselines

At mm-VLBI frequencies the atmospheric and tropospheric signal propagation is dominated by rapid phase fluctuations that quickly cause complete decoherence. No-loss coherence times are often less than a few tens of seconds. Sources with a low flux density are often not detectable within the coherence time. In mm-VLBI a combination of coherent and incoherent time averaging is often able to extend time integration across the coherence time limit and can recover sufficient SNR to detect and fit fringes. The method requires a good coherence time estimate.

A short coherence time of 10 to 50 seconds with fast variability at 1 minute time-scales or longer was seen on the APEX baselines. The SMA–ARO SMT baseline was stable, with coherence times longer than 100 s and slow variability at 3 minute time-scales or longer. The APEX PCal phase corrections were not applied. The APEX coherence times reflect a combination of a stable (in time) instrumental decoherence and a time varying atmosphere, and agreed with data from the ALMA site characterization that reports coherence times of 20 s to 120 s for the May–July winter time (Holdaway 1997).

We initially estimated phase stability and coherence time,  $t_{\text{coh}}$ , in APEX–SMA and APEX–ARO SMT visibility data using HOPS. HOPS has a heuristic approach for producing a single  $t_{\text{coh}}$  estimate for the length of an entire scan (420 s for 3C 279). The approach consists of

multi-timescale fringe fitting, multi-timescale incoherent averaging, and finally inspecting fringe amplitude over the discrete time-scales and locating the time at which fringe amplitude first starts decreasing. The time  $t_{\text{coh}}$  in HOPS follows not the usual definition of e-folding decay time, but rather is the time  $t_{\text{coh}}$  at which fringe amplitude  $a(t)$  starts decreasing from a constant plateau  $a_0$  at rate  $a_1$  (model:  $a(t) = a_0 + u(t \geq t_{\text{coh}}) \cdot a_1 \log_{10}(t/t_{\text{coh}})$ ). The  $t_{\text{coh}}$  estimate is used by the HOPS fringe fit algorithm to improve the SNR during the final fringe fit.

The scan coherence times in HOPS were between 3 s and 100 s, but the fits did not match the underlying fringe amplitude data. I then performed a more sophisticated analysis. The HOPS fixed-timescale fringe fitter was used to produce a grid of about 900 fringe fit solutions per scan, each solution for a different time range within a scan and with 10 s time granularity. A  $t_{\text{coh}}$  time according to the HOPS definition was fitted into the grid results. A typical fit for a single 420 s scan is shown in Figure 8.6.

The grid method produced  $t_{\text{coh}}$  values of 10 s to 50 s on the APEX baselines that were consistent with underlying data. It also revealed slow variability in  $t_{\text{coh}}$ , reflected in maps of the gridded fringe amplitude. A typical  $t_{\text{coh}}$  fit on the APEX–ARO SMT baseline is shown in Figure 8.6, and two fringe amplitude maps representative of the conditions on the stable SMA–ARO SMT baseline and the faster-varying APEX–ARO SMT baseline are shown in Figure 8.5.

#### 8.5.4 Calibration in HOPS

The variability in  $t_{\text{coh}}$  was inconsequential for calibration in AIPS (which unlike HOPS does not alter and average the visibility data), but it affected fringe rate, delay and phase solutions in HOPS and initially lead to erratic HOPS results. To calibrate data in HOPS, instead of using HOPS  $t_{\text{coh}}$  estimates we took  $t_{\text{coh}}$  estimated by the grid method. For each scan we chose the longest stable time ranges in the fringe amplitude maps and those that gave the best fringe SNR. We then re-ran HOPS fringe fitting with these  $t_{\text{coh}}$  and time range settings.

Phase, rate and delay of each scan in the final calibrated HOPS dataset were well-behaved. We did not apply amplitude calibration in HOPS.

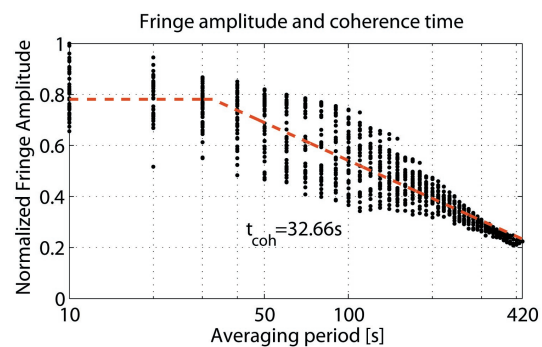


**Fig. 8.6:** Representative example of coherence time,  $t_{\text{coh}}$  (the fringe amplitude knee point), fitted into fringe fit solutions determined by HOPS 3.8 on the APEX–ARO SMT baseline. The fringe fits over different sections of a 420 s scan at 10 s time granularity produce the roughly 900 data points shown.



### 8.5.5 Calibration in AIPS

We used AIPS to apply calibrations to 3C 279's visibilities before exporting them to Difmap model fitting. We performed the same steps on the 0.32 s AP and 1.0 s AP correlator outputs to confirm consistency. The correlated flux density of 3C 279 was sufficiently high for a  $\text{SNR} > 5$  detection within the atmospheric coherence time and allowed fringe fitting in AIPS.

In AIPS the 3C 279 zero spacing Stokes I flux density was set to the value found in the course of flux monitoring at the SMA (19.79 Jy). Constant a priori gains  $g_0$  in Table 8.4 were applied, including SMA linear polarization loss, and adjusted APEX decoherence losses in 1 s for the 0.32 s AP and 1.0 s AP data where the APEX PCal tone phase corrections were not applied. The APEX on-site radiometer<sup>1</sup> measured the zenith atmospheric opacity,  $\tau_0$ , at 60 s intervals. We corrected visibilities by interpolating the  $\tau_0$  data over the elevation track of 3C 279 to estimate the gain correction  $g_\tau = \sqrt{e^{+\tau_0/\sin(\text{el})}}$ . The atmospheric opacity remained low with an increase to 0.09 towards the end of the observation. At the ARO SMT,  $\tau_0$  averaged 0.250 but degraded towards the end. Next we applied  $T_{\text{sys}}$  and DPFU gain data to adjust the flux density scale. Note that APEX  $T_{\text{sys}}$  and DPFU data automatically corrects for the inserted  $\lambda/4$  plate loss. To complete the gain and absolute flux density scale calibration we then applied sampler threshold corrections derived from autocorrelations (AIPS ACCOR; Kogan 1995). We also applied Earth orientation parameter corrections, resulting in small corrections ( $< 50$  ps) to station delays. About 15 % of visibilities corrupted due to issues at APEX or the SMA, see § 8.4.4, were flagged.

The final phase calibrations in AIPS consisted of a baseline-based, combined IF fringe fit with a bounded rate-delay window. In order to use the same visibilities as the HOPS data reduction, scans were fringe fitted over optimal time ranges indicated by highest SNR or best fringe amplitude stability found by the grid method described in the previous section. The best solution interval for fringe fitting was 20 s, approximately twice the shortest overall coherence time on the two APEX baselines. AIPS fringe fitting succeeded for a few more scans than HOPS fringe fitting. A small residual phase slope across the full continuum band was removed with a per-IF phase self-calibration on a point source model and single solutions for each 420 s scan.

Calibrated 0.32 s and 1.0 s AP data were frequency averaged from 15 IFs and 64 channels down to a single IF with one channel. The averaged calibrated data were written to a FITS file. Comparisons in AIPS using cross power spectra, amplitude against uv distance and closure phase showed good consistency between the 0.32 s and 1.0 s AP datasets.

### 8.5.6 Closure Phase

A powerful interferometric observable is the complex triple product (bispectrum) of visibilities in a triangle of three connected baselines. In VLBI the bispectrum magnitude and argument

<sup>1</sup><http://www.apex-telescope.org/weather/>

are called closure quantities, namely closure amplitude and closure phase. Closure phase is invariant under translation of the VLBI image (i.e. shifts of the interferometric phase center), but is not invariant under rotation. It is robust against statistically independent delay or phase errors at the telescopes, such as clock offsets and the local atmosphere. It is however sensitive to baseline-based errors (e.g., instrumental polarization impurities), as well as asymmetries in source structure. This allows conclusions about source structure.

For a source that is unresolved or has point symmetry, the bispectrum is real-valued and the closure phase is  $0^\circ$  or  $180^\circ$ . Other closure phases imply a skewed source brightness distribution that is not point symmetric. A complex-valued bispectrum can be used to infer resolved and skewed asymmetric source structure (see, e.g., Rogers et al. 1974; Monnier 2007).

A large number of independent triangles is required to capture a significant fraction of the source phase information carried by the equivalent Fourier phases of all baseline visibilities but without telescope-based errors. With one independent triangle as in our VLBI observation, 33 % of clean Fourier phase information is recovered by closure phase, and multiple source models, if they are complex, can describe the same phase data. Incidentally, for imaging purposes source Fourier phases carry the majority of information about source structure, and amplitude data including systematic amplitude calibration errors generally give only a small contribution to the source angular structure reconstructed from visibility data (e.g., Ni & Huo 2007). Amplitude errors tend to scatter power in the image. This may change the peak amplitudes of unresolved point sources, but does not affect their location, which can be determined within the overall angular precision limit,  $\theta_{\text{lim}}$ , set by the fringe spacing and fringe SNR (Kovalev et al. 2005; Lobanov 2005), of

$$\theta_{\text{lim}} = b_\phi \cdot 0.939 \sqrt{\ln \text{SNR}/(\text{SNR} - 1)}$$

The half-power beam sizes,  $b_\phi$ , and lowest SNRs on the APEX–ARO SMT–SMA triangle, result in angular precision limits  $\theta_{\text{lim}}$  of  $\lesssim 15 \mu\text{s}$ . Next inspected closure phase in both datasets, the first calibrated and fringe fitted in AIPS, the other fringe fitted in HOPS.

## 8.6 Results

### 8.6.1 Closure Phase and Baseline Amplitudes

We inspected the closure phase for 3C 279 on the APEX–ARO SMT–SMA triangle, and found good agreement between visibility data fringe fitted with HOPS and with AIPS. The closure phase was distinctly non-zero and had a slow swing from about  $+50^\circ$  to  $-100^\circ$  over 3 h. The scan average closure phases in the HOPS calibrated data are shown in the left panel of Figure 8.7.

The closure phases in AIPS-calibrated data that was self-calibrated in Difmap on a point-source model, flagged, and averaged to 10 s intervals are shown in the right panel of Figure 8.7.

Note that SMA had linear polarization, while APEX and ARO SMT were circularly polarized. The amplitude loss in mixed polarization visibilities is about  $\sqrt{2}$  for a polarized source with only a weak linear component to the radiation, i.e. no correlation between circular cross-hands (e.g., similar to the lack of APEX–ARO SMT cross-circular fringes). The  $\sqrt{2}$  loss was accounted for during amplitude calibration. The effect of mixed polarization visibilities on closure phase is more challenging to quantify. While any antenna-based phase errors cancel out in the closure phase, cross-polarization leakage (instrumental polarization) combined with source polarization creates baseline-based, non-canceling closure phase errors that follow the parallactic angle and that mimic source structure (e.g., Massi et al. 1996).

The closure phase error caused by a cross-polarization leakage  $p$  and a source component with linear polarization  $m$  is at most  $\arg(1 + 2 p m \sqrt{-1})$  (this maximizes the phase error of the visibility, see the second line of Eq. 10 in Massi et al. 1996). There is an additional contribution of  $\arg(1 + p p \sqrt{-1})$  due to the leakage terms, yielding an uncertainty in closure phase,  $\Delta\Phi$ , of about

$$\Delta\Phi \lesssim \arg(1 + 2 p m \sqrt{-1}) + \arg(1 + p p \sqrt{-1})$$

The polarization cross-talk of the SMA at 230 GHz when  $\lambda/4$  plates are inserted is  $p = 3\%$  (Marrone 2006), and is lower without  $\lambda/4$  plates. The instrumental polarization of the ARO SMT

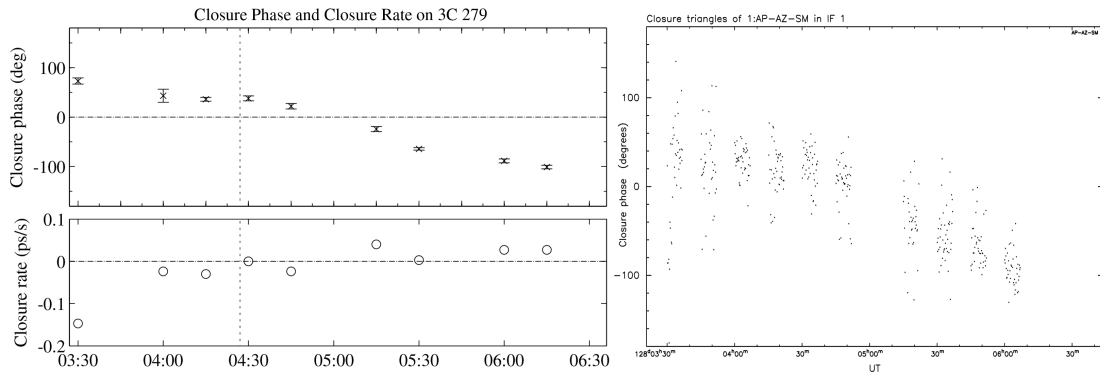


**Fig. 8.7:** Closure phase (degrees) on the APEX–ARO SMT–SMA triangle determined for visibilities fringe fitted in HOPS (top left) and in AIPS (right). Closure phases are in LCP–LCP–X polarization and switch to RCP–RCP–X at UT 04:30 (vertical dotted line). HOPS closure phases are 420 s scan averages. The closure rate is below  $\pm 0.2$  ps/s (bottom left). The AIPS closure phases are 10 s averages.

is similar. APEX is optimized for low cross-polarization leakage, too, but the leakage has not been characterized with the  $\lambda/4$  plate in place. Adopting a 10 % leakage the closure phase error is about  $0.6^\circ$ .

Knowledge of the polarization degree of the inner components in 3C 279 would be required to estimate closure phase errors due to the SMA. The source polarization is somewhat uncertain. For the 3C 279 inner jet components at 22 GHz and 86 GHz, past observations by Gabuzda & Cawthorne (2000) and Attridge (2001) find  $m = 5\%$  to  $m = 20\%$ . Two 43 GHz epochs of the Boston blazar monitoring data were close to our 1.3 mm observation. The polarization degrees of the 7 mm core and the northern component in the inner 1 mas region were about 14 % and 3 %, respectively, and were fairly stable between 2012 April 28 and May 26, whereas the polarization degree of the southern component increased from below 1 % to about 9 % (S. Jorstad, private comm.).

Initial reductions of 230 GHz EHT data from 2013 suggest a high linear polarization fraction on the 2-4 G $\lambda$  baselines between ARO SMT and Hawaii, with a possible swing along the uv track from nearly unpolarized to 60 %. We thus adopt a high polarization degree of 60 % as an average over all components. With an instrumental polarization of 3 % this yields a closure phase uncertainty of  $3^\circ$ , or more conservatively  $6^\circ$ . The detected closure phases were notably larger than this uncertainty. These small errors to closure phase are unlikely to notably affect the source image or our model fitting in § 8.6.2. In addition, the parallactic angles and their sum did not follow the closure phase swing, nor did the closure phase jump with the switch to RCP recording at APEX at UT 4:30 (Fig. 8.7). This increased our confidence that the overall closure phase characteristics did capture structure in 3C 279.

Based on the non-zero closure phase, and fringes detected on all three baselines, we argue that we see spatially resolved structure in 3C 279 described by at least three components with angular sizes below 60  $\mu\text{as}$ . The non-zero closure phase implies that source structure is not point symmetric. While the simplest description are two point sources with unequal flux density, we did not detect the fast  $180^\circ$  phase flips that occur with binary components when one VLBI baseline traverses a null in their visibility pattern. Instead, the smooth

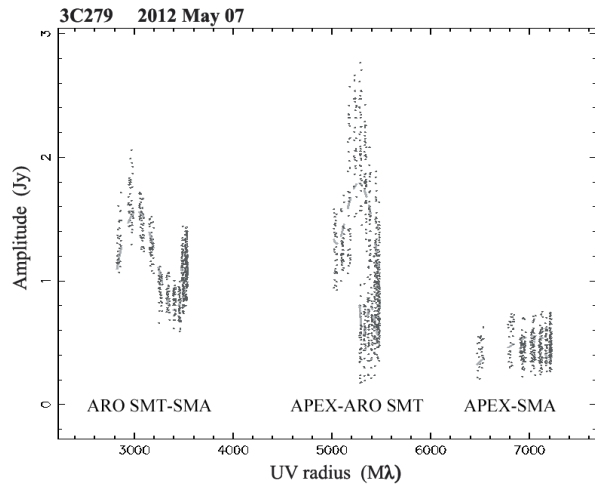


**Fig. 8.8:** The detected amplitude (Jy) against uv distance ( $M\lambda$ ) on 3C 279.

and non-linear evolution of the closure phase, with changes larger than the  $< 17^\circ$  uncertainty due to instrumental polarization, implies that at least three components were detected.

The visibility amplitudes against uv distance are shown in Figure 8.8. They exhibited large variations that were suggestive of source structure. The variations were not synchronous in time between baselines. This increased our confidence that they were not due to the telescope amplitude calibration uncertainties of  $< 20\%$ . To test whether variations are explained by a flat flux density over uv distance, we fit a linear model with  $\nu = N - 2$  degrees of freedom and a  $5 \cdot 1\sigma$  uncertainty in flux density into the visibility amplitudes on the shortest baseline (SMA–ARO SMT;  $5\sigma = 15 \text{ mJy beam}^{-1} \text{ rms}$ ) that exhibited the strongest variations. For the fit residual  $S$  we found  $P(\chi^2 \geq S/\nu) = 0.31\%$ , and rejected the linear model at 3 sigma confidence. We conclude the observed baseline amplitudes indicate resolved source structure on the SMA–ARO SMT baseline with at least two components. The smaller amplitude variations on the APEX baselines did not allow a similar conclusion. However, the amplitude and closure phase data, when combined, indicated at least three components.

### 8.6.2 Model Fitting

Our most robust finding is the detection of fringes on 3C 279 and a closure phase that implies resolved source structure with at least three components  $\leq 60 \mu\text{as}$  in size. The inner region of 3C 279 could not be imaged directly, because of the sparse three-baseline uv coverage. To explore tentative models for the 1.3 mm fine-scale structure we used Difmap model fitting of basic unpolarized models, and included a priori information from high resolution 3 mm (17 May) and 7 mm (26 May) images to support more complex models. Note that the 1.3 mm amplitude calibration uncertainties would, via Fourier theory, predominantly affect the flux density of the fitted components. The SMA linear polarization however introduces phase uncertainties (spatial uncertainties). Thus the models described further below are tentative and need a confirmation from a new 1.3 mm observation.

We fit the calibrated 1.3 mm datasets using Difmap (Shepherd 1997). In Difmap each source component is described by six parameters: the flux density, the three shape parameters of a 2D Gaussian, and its 2D position. We fit source models that contained between 1 and 6 components, with a lower bound for the component diameters of  $15 \mu\text{as}$ . The component positions and flux densities were left unconstrained.

The Difmap reduction steps were as follows. The original calibrated visibility data were first phase self-calibrated on a point-source model with 2 s and then 10 s solution intervals, followed by Levenberg-Marquardt damped least-squares fitting to a candidate model consisting of the resulting image’s clean components. Next, phase self-calibration was repeated at 10 s and 40 s solution intervals, and data were coherently averaged to 10 s, about half the typical coherence

time seen during the experiment. Next, phase self-calibration and model fitting were repeated alternately until the model parameters converged and the lowest reduced chi-squared ( $\chi_{\text{red}}^2$ ) was attained. The formal uncertainties for the model parameters were determined from the parameter covariance matrix (the inverse of the Hessian matrix estimated by Difmap's Levenberg-Marquardt fitter). The variances were multiplied by the  $\chi_{\text{red}}^2$  of the fit.

Initially, candidate models were constructed without a priori data on 3C 279 structure. The 1.3 mm closure phase and baseline amplitudes were used to build the most likely initial models. These initial models were then fit to the data. The closure phase indicated a model with at least three components, and we fit simple models with 1 to 3 components. Models with 4 to 6 components were however found to describe the dataset best, both subjectively, and in terms of  $\chi_{\text{red}}^2$  at a nominal degrees of freedom of about 3200.

Table 8.5: Best-fitting Difmap modelfits of APEX  $\lambda 1.3$  mm VLBI visibility data.

Model	$\chi^2_{\text{red}}$	Beam size and PA ( $\mu\text{as}$ ) x ( $\mu\text{as}$ ) x (deg)	ID	Flux (Jy)	$T_b$ ( $\log_{10}$ K)	r ( $\mu\text{as}$ )	$\theta$ (deg)	Component size and PA maj ( $\mu\text{as}$ ) x min ( $\mu\text{as}$ ) (deg)
1k.mod3	6.00	15.0 x 36.9 x 26.2	1	1.43 $\pm$ 1 %	11.3	0.0	0.0	15.6 x 15.6 $\pm$ 3 % 0.0
1k.mod2	3.87	15.0 x 36.9 x 26.2	1	7.88 $\pm$ 6 %	11.0	0.0	0.0	51.3 x 25.1 $\pm$ 14 % 40.4 $\pm$ 4 %
2k.mod2	3.01	15.0 x 36.9 x 26.2	1	9.07 $\pm$ 6 %	11.4	0.0	0.0	52.2 x 25.9 $\pm$ 9 % 39.3 $\pm$ 3 %
			2	0.34 $\pm$ 2 %	10.7	323.7 $\pm$ 2 %	177.1 $\pm$ 1 %	15.0 x 15.0 0.0
3k.mod1	2.82	14.1 x 39.2 x 26.9	1	2.03 $\pm$ 3 %	11.4	0.0	0.0	17.3 x 18.3 $\pm$ 3 % 0.0
			2	5.59 $\pm$ 4 %	11.3	137.4 $\pm$ 1 %	-166.0 $\pm$ 1 %	30.8 x 30.8 $\pm$ 2 % 0.0
			3	4.76 $\pm$ 4 %	11.3	104.3 $\pm$ 2 %	-176.3 $\pm$ 1 %	29.1 x 29.1 $\pm$ 2 % 0.0
4k.mod2	2.27	14.1 x 39.2 x 26.9	1	4.37 $\pm$ 3 %	11.52	0.0	0.00	21.2 x 21.2 $\pm$ 3 % 0.0
			2	4.66 $\pm$ 4 %	11.42	68.8 $\pm$ 2 %	-167.58 $\pm$ 1 %	24.4 x 24.4 $\pm$ 3 % 0.0
			3	2.46 $\pm$ 6 %	11.31	112.1 $\pm$ 1 %	-154.38 $\pm$ 1 %	20.1 x 20.1 $\pm$ 6 % 0.0
			4	0.85 $\pm$ 5 %	10.77	416.0 $\pm$ 1 %	-161.03 $\pm$ 1 %	22.1 x 22.1 $\pm$ 4 % 0.0
4k.mod-jan6	2.64	15.0 x 36.9 x 26.2	1	1.87 $\pm$ 2 %	11.02	0.0	0.00	24.4 x 24.4 0.0
			2	1.45 $\pm$ 1 %	11.33	57.6 $\pm$ 1 %	-170.30 $\pm$ 1 %	15.0 x 15.0 0.0
			3	1.26 $\pm$ 2 %	11.00	198.0 $\pm$ 5 %	-150.50 $\pm$ 1 %	20.7 x 20.7 0.0
			4	0.67 $\pm$ 3 %	10.35	369.2 $\pm$ 5 %	-123.07 $\pm$ 1 %	31.8 x 31.8 0.0
5k.mod-jan6	2.54	15.0 x 36.9 x 26.2	1	0.24 $\pm$ 4 %	10.84	195.9 $\pm$ 4 %	3.98 $\pm$ 1 %	10.7 x 10.7 0.0
			2	4.88 $\pm$ 10 %	11.02	0.0	0.00	39.5 x 39.5 $\pm$ 5 % 0.0
			3	2.49 $\pm$ 5 %	11.34	54.4 $\pm$ 1 %	-171.69 $\pm$ 1 %	19.6 x 19.6 $\pm$ 4 % 0.0
			4	0.52 $\pm$ 7 %	11.01	199.8 $\pm$ 1 %	-149.94 $\pm$ 1 %	13.0 x 13.0 $\pm$ 12 % 0.0
			5	0.80 $\pm$ 11 %	10.39	382.6 $\pm$ 1 %	-129.86 $\pm$ 1 %	33.1 x 33.1 $\pm$ 11 % 0.0

5k.mod-jan7flg	2.13	14.9 x 37.0 x 26.5	1	1.32 ± 3 %	10.94	263.4 ± 1 %	5.83 ± 1 %	22.5 x 22.5 ± 3 %	0.0
			2	0.99 ± 4 %	11.16	0.0	0.00	15.1 x 15.1 ± 5 %	0.0
			3	0.46 ± 4 %	10.64	183.7 ± 1 %	-84.66 ± 2 %	19.0 x 19.0 ± 7 %	0.0
			4	0.89 ± 2 %	11.47	59.9 ± 1 %	-168.69 ± 1 %	10.0 x 10.0	0.0
			5	0.65	11.11	196.5 ± 1 %	-150.35 ± 1 %	13.0 x 13.0	0.0
6k.mod4	1.88	13.9 x 40.0 x 27.3	1/S1	1.8 ± 4 %	10.9	0.0	0.0	28.0 x 28.0	0.0
			2/N1	2.6 ± 2 %	11.0	306.6 ± 1 %	-11.8 ± 1 %	40.2 x 21.5	58.2
			3/C	2.3 ± 3 %	10.9	61.9 ± 2 %	11.4 ± 1 %	33.1 x 27.4	-31.4
			4	2.2 ± 2 %	11.1	137.7 ± 1 %	-12.1 ± 1 %	31.0 x 19.2	12.4
			5	9.7 ± 2 %	11.2	255.4 ± 1 %	-95.6 ± 2 %	57.9 x 33.9	35.2
			6	1.2 ± 4 %	11.2	353.5 ± 1 %	-124.0 ± 1 %	38.4 x 6.5	-87.1

**Notes.** Source models for 1.3 mm 3C 279's visibility data produced by model fitting in Difmap. The goodness of fit ( $\chi^2_{\text{red}}$  with about 3200 degrees of freedom) is as reported by Difmap. Beam sizes are Difmap estimates and vary by flagged data. Component positions are in polar coordinates ( $r$ ,  $\theta$ ). The overall model fit position accuracy is  $< 20 \mu\text{as}$ . Formal fractional uncertainties (68 % CI) are based on the Difmap covariance matrix conservatively multiplied by  $\chi^2_{\text{red}}$ , and are stated for the free parameters of the last model fit step. The flux densities have an additional  $\sim 20\%$  uncertainty due to the absolute calibration ( $T_{\text{sys}}$  and gain). The apparent brightness temperatures  $T_b$  are at the mid-band frequency of 229.090 GHz. The best 5-component fit is 5k.mod-jan6, but the southern component at 0.4 mas may be ill-constrained as it corresponds to the amplitude up-turn in the first SMA scan. If this first SMA scan is removed, the best fit is 5k.mod-jan7flg. For the 6-component fit the likely 3 mm and 7 mm VLBI counterparts to C, S1 and N1 (Figure 8.10) are indicated in the ID column.



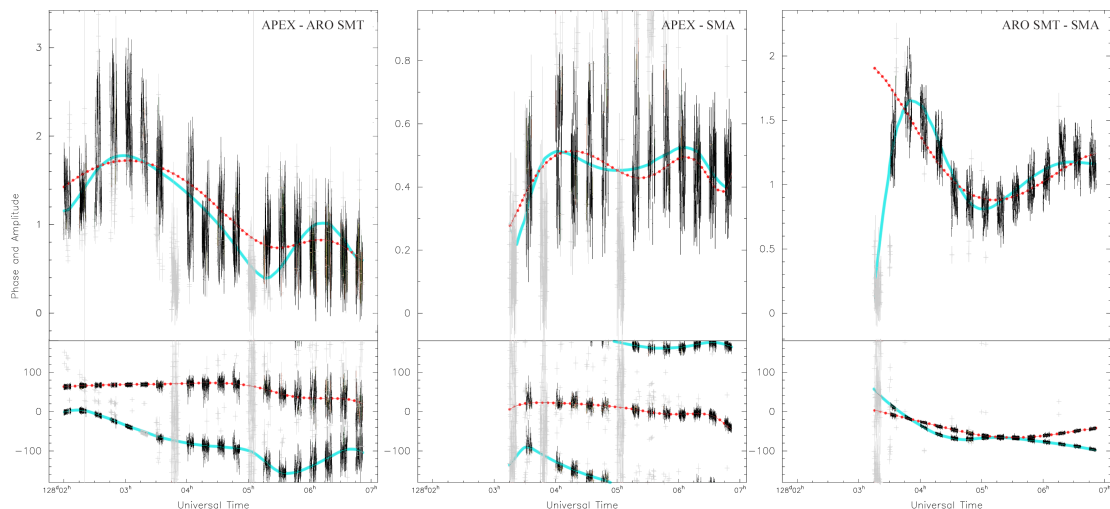


**Fig. 8.9:** Visibility data after fitting the four- and six-component models, *4k.mod2* and *6k.mod4*, shown in Table 8.5 and Figure 8.10. The four-component (red, dotted) and six-component (cyan, solid) models are overlaid. Grey data are flagged. The phases have been self-calibrated against the model. Data are 10 s averages.

To get a priori information of the core region structure, we super-resolved 7 mm and 3 mm VLBI images to a resolution comparable to that of the 1.3 mm VLBI beam. Super-resolving can be summarized thus: The most common imaging algorithm in VLBI (CLEAN) produces images by approximating underlying sparse visibility data with a superposition of identical 2D Gaussian (or beam-shaped) components, scaled for amplitude. Super-resolving an image then amounts to reducing the diameter of these superposed components. Although super-resolving may create spiral-shaped artifacts, these occur farther out from the image center. The core region remains unaffected (see, e.g., Tateyama 2009). We set uv tapers and super-resolved six public 7 mm VLBI images<sup>1</sup> from 2011 October to 2012 May using a 0.08 mas restoring beam. The original 7 mm beam size was about 0.3 mas. We also used a 3 mm GMVA image from 2012 May 17 (Krichbaum et al. 2013), matched its uv range to that of the 7 mm image, and super-resolved it with the same 0.08 mas restoring beam. In addition to super-resolving the 3 mm and 7 mm images, we also removed their original CLEAN components and used Difmap to fit the core region with 7 components. The model fits showed good agreement with the visibility data.

The core region in the two super-resolved and near-contemporaneous 3 mm (17 May) and 7 mm (26 May) images were largely consistent. Both images showed an inner component with an approximately flat spectrum, located between two steeper components in a North-South orientation, with a second pair of North-South oriented components that was offset by 0.4 mas to

<sup>1</sup>[http://www.bu.edu/blazars/VLBA\\_GLAST/3c279.html](http://www.bu.edu/blazars/VLBA_GLAST/3c279.html)

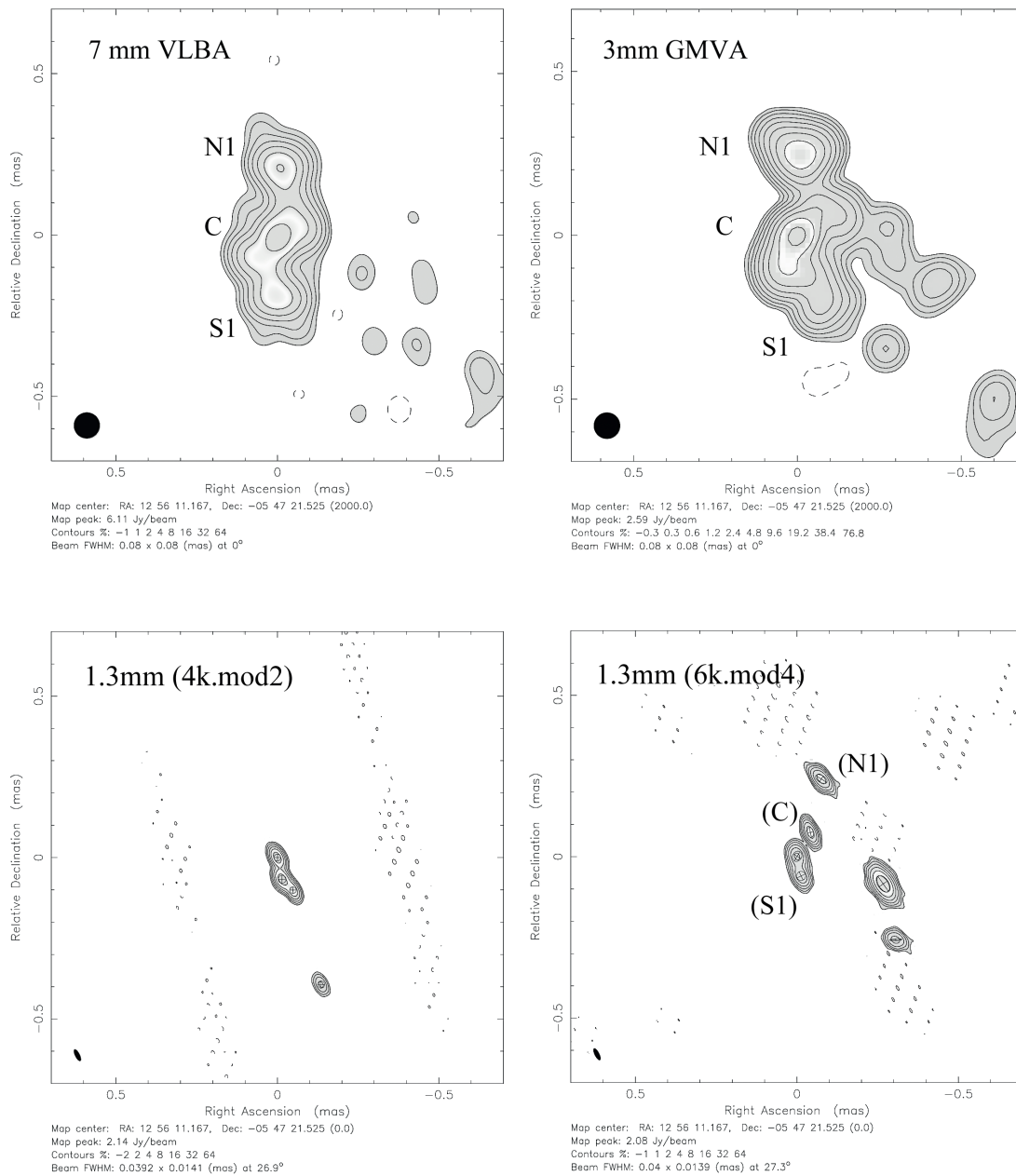


**Fig. 8.10:** Quasi-simultaneous 43 GHz VLBA and 86 GHz GMVA images of 3C 279 super-resolved with a  $80 \mu\text{s}$  FWHM clean beam (top) and two 230 GHz model fits (bottom). Contours are at -2, 4, 8, 16, 32, 64 and 96% from the peak. *Top left:* 43 GHz image, 2012 May 26. The image was produced from public uv data observed by Marscher under the Boston IAR blazar monitoring program ([http://www.bu.edu/blazars/VLBA\\_GLAST/3c279.html](http://www.bu.edu/blazars/VLBA_GLAST/3c279.html)). *Top right:* 86 GHz image, 2012 May 17. The image was produced from uv data of Krichbaum et al. (2013). *Bottom left:* best 230 GHz modelfit of four circular Gaussians with a  $\chi_{red}^2$  of 2.27. *Bottom right:* best 230 GHz modelfit of six elliptical Gaussians with a  $\chi_{red}^2$  of 1.88, with the initial model based on 3 mm and 7 mm images.

the southwest along the direction of the cm-VLBI jet. As the SMA 1 mm and 0.85 mm monitoring indicated that 3C 279 was in a double-peaked flaring state, and as the single-wavelength epochs had a relatively long time separation, no solid conclusions on core/jet association can be drawn from the component spectral indices.

Compared to the super-resolved images, the two respective 3 mm and 7 mm modelfits produced a similar inner structure, with two components (N1 and S1) aligned roughly along North-South from the presumed core, and a second pair of components also aligned North-South that were offset by 0.4 mas to the southwest of C.

For the 1.3 mm modelfits with 4 to 6 components, we located the presumed core (C) and brightest jet components (N1 and S1) in the inner  $\pm 1.0$  mas region of the 3 mm and 7 mm images, and used the component positions and flux densities to construct several initial models.

The final 1.3 mm modelfits are shown in Table 8.5. If we were not to trust the closure phase data, the simplest model (*1k.mod2* in Table 8.5) is a single elliptical component that has a flux density of 7.88 Jy, with an apparent brightness temperature of  $10^{11}$  K estimated at the mid-band frequency of 229.090 GHz.

Conversely, assuming that closure phases reliably reflected the source structure, the simplest fit would contain three asymmetrically distributed components with flux densities and brightness temperatures similar to those of the single component fit. The best simple fit (*3k.mod1*) had three components in a sub-parsec region.

The models with 4 to 6 components that were based upon the a priori data from 3 mm and 7 mm VLBI fit the 1.3 mm data better in overall morphology and in  $\chi_{\text{red}}^2$ . The two near-contemporaneous super-resolved 7 mm and 3 mm images and modelfits, the best six-component modelfit (*6k.mod4* with a  $\chi_{\text{red}}^2$  of 1.88), and the four-component modelfit (*4k.mod2* with a  $\chi_{\text{red}}^2$  of 2.27) are shown in Figure 8.10.

Our images based on the model fits are to be considered highly tentative and need confirmation from new 1.3 mm observations with a larger array.

### 8.6.3 Comparison to 7 mm Jet

The inner 1 mas region in the 3 mm image and in the six 7 mm images showed a consistent southern (S1) and northern (N1) component that were oriented approximately along a North-South axis. Several components with lower flux densities were located westward of the presumed core (C). The super-resolved 2012 May 17 3 mm and 2012 May 26 7 mm images are shown in Figure 8.10. For the other 7 mm images, see the IAR Boston project pages by A.P. Marscher, or see Jorstad et al. (in preparation).

We estimated the proper motions  $\mu$  for S1 and N1 in the six super-resolved 7 mm images via a 3D orthogonal linear regression based on principal component analysis of the data, fitting

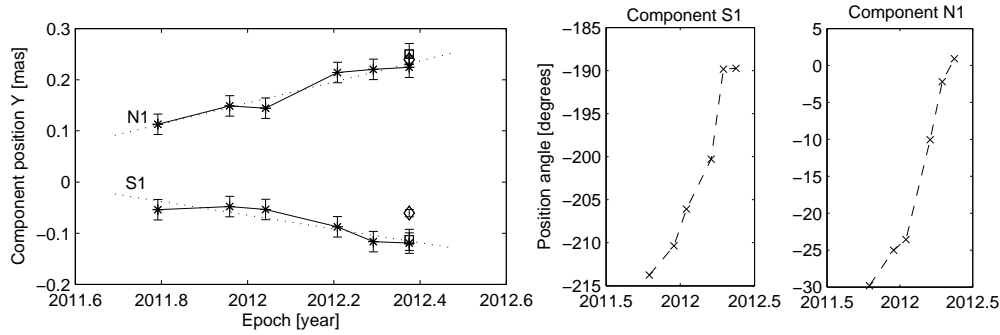


**Fig. 8.11:** Positions of southern and northern components 3D-fitted (time, RA, DEC) for proper motion, and their position angle in super-resolved 7 mm images. The six 7 mm epochs are 2011 Oct to 2012 May (Marscher; public Boston IAR data). Fitted proper motions  $\mu$  (solid lines) relative to the core are  $\mu_{S1} = 0.14 \pm 0.02$  mas/yr ( $2.9 c$ ), and  $\mu_{N1} = 0.25 \pm 0.05$  mas/yr ( $5.2 c$ ), with a slow change in position angles indicating non-ballistic motion. Positions from the 2012 May 3 mm image (squares) and the 1.3 mm 6-component modelfit (diamonds) are overlaid.

epochs in years against the angular component offsets relative to the presumed core. We found the component trajectories to be well described by a radially linear motion relative to the core (C), but with a drift in time of the position angle (PA). The proper motions were  $\mu_{S1} = 0.14 \pm 0.02$  mas yr $^{-1}$  for S1, and  $\mu_{N1} = 0.25 \pm 0.05$  mas yr $^{-1}$  for N1. These correspond to apparent velocities in the plane of the sky of  $v_{\perp,S1} = 0.90 \pm 0.13$  pc yr $^{-1}$  and  $v_{\perp,N1} = 1.60 \pm 0.32$  pc yr $^{-1}$ , or Doppler factors of  $\beta_{app} = 2.9$  and  $\beta_{app} = 5.2$ , respectively. The 7 mm positions and the fitted proper motions are shown in Figure 8.11. The 3 mm and the six-component (*6k.mod4*) 1.3 mm modelfit positions are overlaid.

We found that the 7 mm components S1 and N1 followed an outwards trajectory with a position angle (PA) that gradually drifted over six epochs at a rate of about  $+25^\circ$  yr $^{-1}$ . This intrinsic non-ballistic motion bent westwards for N1 and eastwards for S1. Compared to the kiloparsec scale southwest oriented jet seen in cm-VLBI, the 7 mm and 3 mm VLBI data suggested a change in the jet direction, with an inner jet that extended southeast near the core.

We also estimated spectral indices,  $\alpha = d \log(S)/d \log(\nu)$ , of the 3 mm and 7 mm modelfit components, and the simplest 1.3 mm modelfit with 4 components (*4k.mod-jan6*). Note that the epochs were several weeks apart, and that the 1.3 mm components were a modelfit with a poor uv coverage and with calibration uncertainties. We tentatively found that N1 had a steep spectrum, C was flat, the southern component S1 was mildly steep, and a second southern component (S2) was flat or mildly steep. For the 6 component modelfit (*6k.mod4*) we found tentative spectral indices consistent with flat spectrum, or possibly with a mild spectral turn-up between 86 GHz to 230 GHz.

If we associate the six-component (*6k.mod4*) 1.3 mm modelfit components C, S1 and N1 of

Figure 8.10 with the core and inner jet (based on geometry, as the near flat spectral indices were inconclusive), and if we propagate the modelfit position uncertainty, we find an inner 1.3 mm jet that tentatively extends towards the southeast with a PA of  $168 \pm 25^\circ$  in the inner sub-3 pc region. In comparison, two-component model (*2k.mod2*) had the second component at a similar position angle of  $177 \pm 18^\circ$ . These PA may indicate a change from the large-scale southwest oriented jet in cm-VLBI towards an inner jet at mm-VLBI that has a southeast orientation.

Alternatively, the 7 mm, 3 mm, and the 1.3 mm data including both 5-component modelfits *5k.mod-jan6* and *5k.mod-jan7flag*, were also consistent with a southwest oriented jet as in cm-VLBI, if the two North-South oriented component pairs and their positions were interpreted as tracing the jet ridgeline.

## 8.7 Discussion

Our primary and most robust finding was the detection of fringes on 3C 279. We further detected a closure phase and varying visibility amplitudes against uv distance that together implied spatially resolved fine-scale structure in the inner 3 pc of 3C 279, described by at least three components  $\lesssim 60 \mu\text{as}$  in size.

The average correlated flux density detected on the SMA–ARO SMT baseline was between 1 Jy and 2 Jy. This agrees with the SMA–ARO SMT flux density found in EHT observations with the SMA, ARO SMT, and other stations from March 2011 to April 2011 by Lu et al. (2013).

The six-component 1.3 mm modelfit showed an inner jet PA of  $168 \pm 25^\circ$ , consistent with the PA of  $177 \pm 18^\circ$  given by the simpler two-component modelfit. In comparison, in their 1.3 mm epoch from year 2011 Lu et al. (2013) find a PA of  $127 \pm 3^\circ$ . Their data have a shortest fringe spacing of about  $60 \mu\text{as}$ , twice that of our observation. Lu et al. fit a two-component model of the inner parsec region using an approach similar to that presented here. Accounting for the rotation in PA by  $+25^\circ \text{ yr}^{-1}$  that we tentatively found over the six 7 mm epochs, our 1.3 mm PA, and the PA measurement in 2011 by Lu et al. agree within 1 sigma.

The lack of crossed circular fringes (see § 8.5.2) on the APEX–ARO SMT baseline suggests a very low linear polarization degree for the emission at the  $40 \mu\text{as}$  fringe spacing. The parallel circular fringes with SNRs of 12 up to 35 reflect the complex sum of polarized and unpolarized radiation (cf. the Appendix in Brown et al. 1989), while the lack of crossed circular fringes (or fringes below the detection threshold, e.g.,  $\text{SNR} < 6$ ) provide an upper limit on the linear polarized radiation. Our non-detection yielded a tentative upper limit of about 20% on the linear polarization degree. This is plausible considering the moderate to weak 3C 279 polarization at lower frequencies (see § 8.6.1), and appears consistent with the polarization seen in the 43 GHz Boston blazar monitoring data near our observation. The initial reduction of the EHT data from 2013 suggests much higher polarization fractions one year later on the Hawaii–ARO SMT

baselines, however, these data were in the uv plane quadrants orthogonal to those of the APEX–ARO SMT baseline.

Our upper limit of 20% on the linear polarization degree at 230 GHz is tentative as we did not characterize APEX instrumental polarization (D-terms) and had no full polarimetry. Future polarimetric VLBI, although challenging at 230 GHz, will be required to sample the source coherence function in all four uv plane quadrants and accurately determine the degree of polarization in the core region of 3C 279.

Regarding brightness temperatures, all 1.3 mm modelfit components had  $T_b$  that were of the order of  $10^{10}$  K to  $10^{11}$  K. The limits on the intrinsic brightness temperature in the rest frame of the component are given by inverse Compton cooling, with  $T_{\text{int}} \lesssim 10^{12}$  K (Kellermann & Pauliny-Toth 1969), or the equipartition temperature ( $T_{\text{int}} \simeq T_{\text{eq}}$ ), for which observational statistics suggest values between  $10^{10.5}$  K and  $10^{11.3}$  K (Readhead 1994; Homan et al. 2006). Our model  $T_b$  agreed with the  $T_{\text{eq}}$  range, including a  $T_{\text{eq}}$  of  $10^{10.5}$  K that is Doppler boosted (e.g., Figure 1 in Homan et al. 2006) by the  $\beta_{\text{app}}$  of 2.9 and 5.2 that we had estimated from the six 7 mm epochs of the Boston VLBA monitoring project.

In addition, the low model  $T_b$  was mildly suggestive of a possible decrease of the core  $T_b$  by frequency, as observed in 3C 279 and PKS B1921-293 over centimeter, 3.5 mm, and 1.3 mm wavelengths (Lee et al. 2008; Lu et al. 2012). This might indicate an intrinsic acceleration of the jet in 3C 279, with higher Doppler factors along the regions further out from the core that, due to opacity effects, are probed by the lower frequencies. Lastly, the low  $T_b$  of all model components agreed tentatively with  $8 \times 10^{10}$  K for the core in the 2011 EHT observation (Lu et al. 2013).

The modelfits are based on a priori knowledge and simple assumptions of the station properties and source sub-structure. To limit the degrees of freedom, our modelfits were necessarily unpolarized. Any actual polarized sub-structure in 3C 279 or instrumental polarization leakage will introduce uncertainties. Although we expect such effects to be small, these assumptions may be incorrect. To quantify the uncertainties, however, we would require a priori polarization data at a better uv coverage and a resolution comparable to that of our experiment. Such data are not yet available. Rather than adopt further assumptions and perform a poorly constrained simulation to estimate the polarization-dependent modelfit uncertainties, a topic well beyond the scope of this paper, it is preferable to concentrate efforts on measuring the actual polarization using future polarimetric ultra-high resolution 1.3 mm VLBI observations.

## 8.8 Conclusions

We presented 1.3 mm VLBI fringes towards the blazar 3C 279. These were the first VLBI fringes on the currently longest baseline of  $6800 M\lambda$  with a  $28.6 \mu\text{as}$  fringe spacing, and were the first fringes involving baselines to the APEX telescope after equipping it for VLBI (for technical

details, see Roy et al. 2013).

The average correlated flux density on the longest baseline (SMA–APEX) on 3C 279 was about  $\approx 300$  mJy out of a total 230 GHz flux density of 19.79 Jy. We found structure in 3C 279 at  $< 60 \mu\text{as}$  angular scales, implied firstly by the detected fringes, and secondly by the non-zero, non-linear amplitude over uv distance and closure phase. The closure phase suggested that the overall emission was resolved into at least three components, and that the fine-scale source structure must have an asymmetric distribution of components with unequal flux densities.

We presented tentative source models that fit the 1.3 mm VLBI data. A more complex model with six components that also produced the smallest  $\chi_{\text{red}}^2$  of 1.88 was supported by information from super-resolved and model-fitted, quasi-simultaneous 3 mm and 7 mm images. The six-component model agreed best with the inner 1 mas structure seen at these longer wavelengths. The model had an inner jet PA of  $168 \pm 25^\circ$ , consistent with the relative PA in the simplest two-component model of  $177 \pm 18^\circ$ , and also consistent with 7 mm VLBA, 3 mm GMVA, and the Lu et al. 1.3 mm EHT data. We thus favored the six component model fit, although it had many free parameters.

Because of the limited uv coverage, uncertainties in the amplitude calibration and the instrumental phase, and uncertainties due to the mixed polarization visibilities on the SMA baselines, our 1.3 mm model fits are tentative. Our tentative findings, including a possible decrease in  $T_b$  by frequency due to, e.g., intrinsic acceleration of the jet, have to be verified by new 1.3 mm observations. The new observations should have a consistent polarization setup and a larger number of telescopes (e.g., APEX with the SMA, ARO SMT, CARMA, and the IRAM telescopes).

New 1.3 mm VLBI observations that include 3C 279, albeit not fully polarimetric, have already been made (March 2013) with the largest array yet available at this frequency, now six stations including APEX.

## 8.9 Future Outlook

The successful APEX mm-VLBI experiment demonstrated that future mm-VLBI observations of the GMVA and the EHT can include APEX for critical resolution. To confirm the structure in the inner parsecs of 3C 279, follow-up observations with APEX and five other mm-VLBI stations have already been conducted (March 2013) and are being analyzed. The new 230 GHz VLBI data also include other sources such as OJ 287, BL Lac, M 87 and Sgr A\*.

Early results of the March 2013 mm-VLBI run are the recent detection of APEX fringes on Sgr A\* and M 87 with an SNR greater than 10. The APEX baselines offer the highest resolution of the array, with a fringe spacing shorter than  $40 \mu\text{as}$ .

The fringes on Sgr A\* and M 87 suggest that emission from spatially resolved fine-scale structure smaller than 10 gravitational radii has been detected in both Sgr A\* and M 87. Al-

though it is much too early for conclusions, we can speculate that the fringes may be related to emission around the SMBH. This is because the APEX baselines (and later, ALMA baselines) towards other EHT or GMVA stations should in theory be able to resolve the anticipated crescent and shadow of the SMBH in M 87 and Sgr A\*, and also probe jet launching in M 87.

As mentioned in the introduction, the above two topics are the main science drivers for the EHT and GMVA mm-VLBI observations (e.g., Fish et al. 2011; Doeleman et al. 2012; Krichbaum et al. 2013). The geometry of the crescent is related to the spin of a SMBH, the spin orientation angle, the accretion disk inclination, and the type of accretion flow. This is illustrated for different models on Sgr A\* in Fig. 8.12.

The recent mm-VLBI data should be able to test the SMBH “no-hair” conjecture and study general relativity in the strong regime, and in M 87, the data should be able to probe jet launching (see, e.g., Dexter & Fragile 2013; Kamruddin & Dexter 2013; Broderick et al. 2014).

Results of the analysis of current data, and possible additional VLBI observations with APEX and ALMA in the EHT or GMVA, will provide fundamental insight into accretion mechanisms and the nature of black holes.

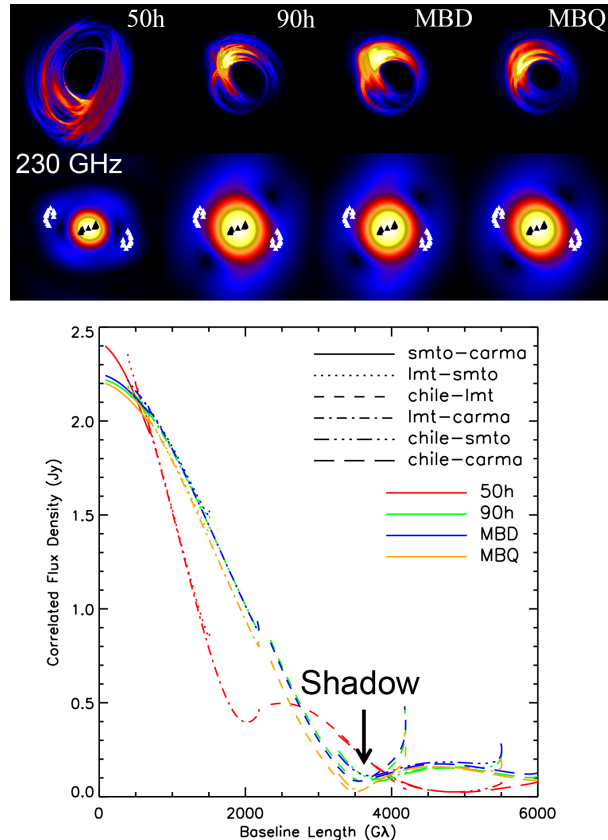


**Fig. 8.12:** Predictions for the emission by the event horizon-scale crescent around the SMBH in Sgr A\* (top) and the corresponding amplitude against uv distance for each model (bottom). The uv ranges covered by different VLBI baselines are indicated through dashed and dotted line segments. Images are adopted from the IAU Symposium 303 talk by J. Dexter (2013), for models see also Dexter & Fragile (2013).





# Bibliography

- G. E. Addison, et al. (2013). ‘Cosmological constraints from baryon acoustic oscillations and clustering of large-scale structure’. *ArXiv e-prints* . 123
- G. B. Airy (1835). ‘On the Diffraction of an Object-glass with Circular Aperture’. *Transactions of the Cambridge Philosophical Society* **5**:283. 13
- W. Alef (2004). ‘A Review of VLBI Instrumentation’. In R. Bachiller, F. Colomer, J.-F. Desmurs, & P. de Vicente (eds.), *European VLBI Network on New Developments in VLBI Science and Technology*, pp. 237–244. 15
- A. Alonso-Herrero, et al. (2009). ‘PMAS optical integral field spectroscopy of luminous infrared galaxies. I. The atlas’. *A&A* **506**:1541–1562. 92, 101, 103
- A. Alonso-Herrero, et al. (2013). ‘Local Luminous Infrared Galaxies. III. Co-evolution of Black Hole Growth and Star Formation Activity?’. *ApJ* **765**:78. 220
- A. Alonso-Herrero, et al. (2012). ‘Local Luminous Infrared Galaxies. II. Active Galactic Nucleus Activity from Spitzer/Infrared Spectrograph Spectra’. *ApJ* **744**:2. 92, 103
- N. Andreasian & D. Alloin (1994). ‘More ultraluminous IRAS galaxies as interacting systems.’. *A&AS* **107**:23–28. 84
- N. K. Andreasian (1992). ‘Rotation curves of two galaxies with megamaser radiation’. In S. S. Holt, S. G. Neff, & C. M. Urry (eds.), *American Institute of Physics Conference Series*, vol. 254 of *American Institute of Physics Conference Series*, pp. 617–620. 84, 85
- R. Antonucci (1993). ‘Unified models for active galactic nuclei and quasars’. *ARA&A* **31**:473–521. 4, 5, 6, 92
- I. Aretxaga, et al. (1999). ‘Seyfert 1 Mutation of the Classical Seyfert 2 Nucleus NGC 7582’. *ApJ* **519**:L123–L126. 6
- M. K. Argo, et al. (2007). ‘OH main line masers in the M82 starburst’. *MNRAS* **380**:596–608. 77
- R. Athreya (2009). ‘A New Approach to Mitigation of Radio Frequency Interference in Interferometric Data’. *ApJ* **696**:885–890. 31
- J. M. Attridge (2001). ‘86 GHz Very Long Baseline Polarimetry of 3C 273 and 3C 279 with the Coordinated Millimeter VLBI Array’. *ApJ* **553**:L31–L34. 149, 163
- W. A. Baan (2010). ‘Setting the stage - layers of RFI Mitigation’. In *RFI 2010 – Proceedings of the RFI mitigation workshop*. PoS. 24
- W. A. Baan & J. A. Irwin (1995). ‘The Nuclear Structure of NGC 3079’. *ApJ* **446**:602. 77
- W. A. Baan, et al. (1982). ‘Broad hydroxyl emission in IC 4553’. *ApJ* **260**:L49–L52. 8
- U. Bach, et al. (2002). ‘Proper motion in Cygnus A’. In E. Ros, R. W. Porcas, A. P. Lobanov, & J. A. Zensus (eds.), *Proceedings of the 6th EVN*

- Symposium*, p. 155. 47, 51
- K. Bamba, et al. (2012). ‘Dark energy cosmology: the equivalent description via different theoretical models and cosmography tests’. *Ap&SS* **342**:155–228. 123, 217, 219
- A. Baudry & N. Brouillet (1996). ‘Spatial distribution and nature of H<sub>2</sub>O masers in Messier 82.’. *A&A* **316**:188–195. 77
- C. Beaudoin, et al. (2013). ‘Receiver Upgrade for the GGAO 12m VLBI system’. In N. Zubko & M. Poutanen (eds.), *Proceedings of the 21st Meeting of the European VLBI Group for Geodesy and Astrometry*, pp. 13–16. EVGA. 26
- V. Belitsky, et al. (2007). ‘Facility heterodyne receiver for the Atacama Pathfinder Experiment Telescope’. In *Infrared and Millimeter Waves, 2007 and the 2007 15th International Conference on Terahertz Electronics. IRMMW-THz. Joint 32nd International Conference on*, pp. 326–328. 152
- J. F. Bell, et al. (2000). ‘Summary of the Elizabeth and Frederick White Conference on radio frequency interference mitigation strategies’. In J. B. . L. Kewley (ed.), *The Elizabeth & Fredrick White Conference on Radio Frequency Interference Mitigation Strategies*. 24
- J. F. Bell, et al. (2001). ‘Base Band Data for Testing Interference Mitigation Algorithms’. *PASA* **18**:105–113. 31, 32
- N. Bennert, et al. (2009). ‘A Search for H<sub>2</sub>O Megamasers in High-z Type-2 Active Galactic Nuclei’. *ApJ* **695**:276–286. 77, 80
- S. Bianchi, et al. (2012). ‘AGN Obscuration and the Unified Model’. *Advances in Astronomy* **2012**. 4, 6, 92
- M. D. Bica, et al. (1995). ‘A multifrequency radio continuum and IRAS faint source survey of markarian galaxies’. *ApJS* **98**:369–440. 101
- J. Binney & S. Tremaine (2008). *Galactic Dynamics: Second Edition*. Princeton University Press. 118, 219, 220
- R. D. Blandford & D. G. Payne (1982). ‘Hydromagnetic flows from accretion discs and the production of radio jets’. *MNRAS* **199**:883–903. 6, 149
- R. D. Blandford & R. L. Znajek (1977). ‘Electromagnetic extraction of energy from Kerr black holes’. *MNRAS* **179**:433–456. 149
- J. A. Braatz, et al. (2009). ‘Cosmology with Water-vapor Megamasers’. In *Astro2010: The Astronomy and Astrophysics Decadal Survey*, vol. 2010 of *ArXiv Astrophysics e-prints*, p. 23. 11, 12, 125, 218, 219
- J. A. Braatz & N. E. Gugliucci (2008). ‘The Discovery of Water Maser Emission from Eight Nearby Galaxies’. *ApJ* **678**:96–101. 9, 77, 91, 92, 93, 94, 97, 104, 105, 106, 107, 121
- J. A. Braatz, et al. (2010). ‘The Megamaser Cosmology Project. II. The Angular-diameter Distance to UGC 3789’. *ApJ* **718**:657–665. 94, 102, 106, 108, 110, 127, 132, 136, 140, 211, 214
- J. A. Braatz, et al. (1996). ‘A Survey for H<sub>2</sub>O Megamasers in Active Galactic Nuclei. I. Observations’. *ApJS* **106**:51. 126, 146
- J. A. Braatz, et al. (1997). ‘A Survey for H<sub>2</sub>O Megamasers in Active Galactic Nuclei. II. A Comparison of Detected and Undetected Galaxies’. *ApJS* **110**:321. 9, 77
- A. E. Bragg, et al. (2000). ‘Accelerations of Water Masers in NGC 4258’. *ApJ* **535**:73–89. 10, 108, 130, 216
- A. F. Bridle & E. W. Greisen (1994). ‘The NRAO AIPS Project – A Summary’. Technical Memo AIPS Memo 87, National Radio Astronomical Observatory, Charlottesville, VA. 36, 49, 94, 111, 130, 134
- F. H. Briggs, et al. (2000). ‘Removing Radio Interference from Contaminated Astronomical Spectra Using an Independent Reference Sig-

- nal and Closure Relations'. *AJ* **120**:3351–3361. 62, 63
- F. H. Briggs & J. Kocz (2005a). 'Overview of technical approaches to radio frequency interference mitigation'. *Radio Science* **40**:5. 24
- F. H. Briggs & J. Kocz (2005b). 'Overview of Technical Approaches to RFI Mitigation'. *ArXiv Astrophysics e-prints* . 58
- A. E. Broderick, et al. (2014). 'Testing the No-hair Theorem with Event Horizon Telescope Observations of Sagittarius A\*'. *ApJ* **784**:7. 175
- L. F. Brown, et al. (1989). 'Global fringe fitting for polarization VLBI'. *AJ* **97**:1522–1531. 172
- A. Brunthaler, et al. (2005). 'Atmosphere-Corrected Phase-Referencing'. In J. Romney & M. Reid (eds.), *Future Directions in High Resolution Astronomy*, vol. 340 of *Astronomical Society of the Pacific Conference Series*, p. 455. 95, 112, 133
- P. Castangia, et al. (2013). 'New Compton-thick AGN in the circumnuclear water maser hosts UGC3 789 and NGC 6264'. *ArXiv e-prints* . 82
- H. Chamberlin (1985). *Musical Applications of Microprocessors*. Hayden Books, 2 edn. 37
- R. Chellappa & S. Theodoridis (2013). *Academic Press Library in Signal Processing: Volume 3: Array and Statistical Signal Processing*. Academic Press. 59
- G. Chen & B. Ratra (2011). 'Median Statistics and the Hubble Constant'. *PASP* **123**:1127–1132. 146
- E. Churchwell, et al. (1977). 'Detection of H<sub>2</sub>O maser emission in the Galaxy M 33'. *A&A* **54**:969–971. 8
- R. Cid Fernandes, et al. (2004). 'The star formation history of Seyfert 2 nuclei'. *MNRAS* **355**:273–296. 127
- M. J. Claussen, et al. (1998). 'The Water Masers in the Elliptical Galaxy NGC 1052'. *ApJ* **500**:L129. 92
- T. Coleman & Y. Li (1996). 'An Interior Trust Region Approach for Nonlinear Minimization Subject to Bounds'. *SIAM Journal on Optimization* **6**(2):418–445. 118, 137
- S. Collin, et al. (2006). 'Systematic effects in measurement of black hole masses by emission-line reverberation of active galactic nuclei: Eddington ratio and inclination'. *A&A* **456**:75–90. 124
- J. J. Condon, et al. (2002). 'Radio Sources and Star Formation in the Local Universe'. *AJ* **124**:675–689. 47, 106
- J. J. Condon, et al. (1998). 'The NRAO VLA Sky Survey'. *AJ* **115**:1693–1716. 101, 106
- J. J. Condon, et al. (1991). 'Compact starbursts in ultraluminous infrared galaxies'. *ApJ* **378**:65–76. 98
- J. E. Conway & P. R. Blanco (1995). 'H<sub>i</sub> Absorption Toward the Nucleus of the Powerful Radio Galaxy Cygnus A: Evidence for an Atomic Obscuring Torus?'. *ApJ* **449**:L131. 47, 51, 52
- E. A. Corbett, et al. (2003). 'COLA. II. Radio and Spectroscopic Diagnostics of Nuclear Activity in Galaxies'. *ApJ* **583**:670–688. 94
- T. Cornwell & E. B. Fomalont (1989). 'Self-Calibration'. In R. A. Perley, F. R. Schwab, & A. H. Bridle (eds.), *Synthesis Imaging in Radio Astronomy*, vol. 6 of *Astronomical Society of the Pacific Conference Series*, p. 185. 95
- S. Crandall & B. Ratra (2013). 'Median statistics cosmological parameter values'. *ArXiv e-prints* . 146
- J. Dattorro (1997). 'Effect Design: Part 1 Reverbator and Other Filters'. *AES Journal* **45**(9):660–684. 37, 38
- M. L. Davies, et al. (2013). 'The radio source count at 93.2 GHz from observations of 9C sources using AMI and CARMA'. *MNRAS* **430**:1961–1969. 95
- T. M. Davis & C. H. Lineweaver (2004). 'Ex-

- panding Confusion: Common Misconceptions of Cosmological Horizons and the Superluminal Expansion of the Universe’. *Publications of the Astron. Soc. Australia* **21**:97–109. 213, 221
- G. de Vaucouleurs, et al. (1991). *Third Reference Catalogue of Bright Galaxies. Volume I: Explanations and references. Volume II: Data for galaxies between 0<sup>h</sup> and 12<sup>h</sup>. Volume III: Data for galaxies between 12<sup>h</sup> and 24<sup>h</sup>*. Springer, New York, NY (USA). 83, 105, 126, 211
- H. Dejonghe (1987). ‘A completely analytical family of anisotropic Plummer models’. *MNRAS* **224**:13–39. 118, 212, 219
- A. Deller (2010). ‘Software correlators as testbeds for RFI algorithms’. In *RFI Mitigation Workshop PoS (RFI2010)* 35. 34
- A. T. Deller, et al. (2011). ‘DiFX-2: A More Flexible, Efficient, Robust, and Powerful Software Correlator’. *PASP* **123**:275–287. 30, 34, 156
- F. X. Desert & M. Dennefeld (1988). ‘The link between IRAS spectra and near-infrared emission features in external galaxies’. *A&A* **206**:227–236. 106
- J. Dexter & P. C. Fragile (2013). ‘Tilted black hole accretion disc models of Sagittarius A\*: time-variable millimetre to near-infrared emission’. *MNRAS* **432**:2252–2272. 4, 175
- G. P. di Benedetto (2008). ‘The Cepheid distance to the Large Magellanic Cloud and NGC 4258 by the surface brightness technique and improved calibration of the cosmic distance scale’. *MNRAS* **390**:1762–1776. 211
- P. J. Diamond (1995). ‘VLBI Data Reduction in Practice’. In J. A. Zensus, P. J. Diamond, & P. J. Napier (eds.), *Very Long Baseline Interferometry and the VLBA*, vol. 82 of *Astronomical Society of the Pacific Conference Series*, p. 227. 50
- P. J. Diamond, et al. (1999). ‘Global VLBI Observations of the Compact OH Megamaser Emission from III ZW 35 and IRAS 17208-0014’. *ApJ* **511**:178–184. 53
- S. G. Djorgovski, et al. (2008). ‘The Origins and the Early Evolution of Quasars and Supermassive Black Holes’. In H. Kleinert, R. T. Jantzen, & R. Ruffini (eds.), *The Eleventh Marcel Grossmann Meeting On Recent Developments in Theoretical and Experimental General Relativity, Gravitation and Relativistic Field Theories*, pp. 340–367. 220
- S. S. Doeleman, et al. (2012). ‘Jet-Launching Structure Resolved Near the Supermassive Black Hole in M87’. *Science* **338**:355–. 4, 6, 150, 151, 175
- M. A. Dopita & R. S. Sutherland (2003). *Astrophysics of the diffuse universe*. Springer. 96
- R. J. H. Dunn, et al. (2010). ‘The radio properties of a complete, X-ray selected sample of nearby, massive elliptical galaxies’. *MNRAS* **404**:180–197. 61
- B. Efron & G. Gong (1983). ‘A Leisurely Look at the Bootstrap, the Jackknife, and Cross-Validation’. *The American Statistician* **37**(1):36–48. 137
- M. Elitzur (ed.) (1992). *Astronomical masers*, vol. 170 of *Astrophysics and Space Science Library*. 7
- M. Elitzur (2007). ‘Recent developments in maser theory’. In J. M. Chapman & W. A. Baan (eds.), *IAU Symposium*, vol. 242 of *IAU Symposium*, pp. 7–16. 7
- M. Elitzur (2012). ‘On the Unification of Active Galactic Nuclei’. *ApJ* **747**:L33. 6
- M. Elitzur & T. de Jong (1978). ‘A model for the maser sources associated with H II regions’. *A&A* **67**:323–332. 9
- M. Elitzur & I. Shlosman (2006). ‘The AGN-obscuring Torus: The End of the “Doughnut” Paradigm?’. *ApJ* **648**:L101–L104. 6
- S. W. Ellingson (2005). ‘Introduction to special section on Mitigation of Radio Frequency In-

- interference in Radio Astronomy'. *Radio Science* **40**:5. 24
- A. P. Fairall (1986). 'Some new bright southern Seyfert galaxies'. *MNRAS* **218**:453–455. 126
- X. Fan, et al. (2006). 'Constraining the Evolution of the Ionizing Background and the Epoch of Reionization with  $z \sim 6$  Quasars. II. A Sample of 19 Quasars'. *AJ* **132**:117–136. 4
- V. L. Fish, et al. (2011). '1.3 mm Wavelength VLBI of Sagittarius A\*: Detection of Time-variable Emission on Event Horizon Scales'. *ApJ* **727**:L36. 150, 175
- D. J. Fixsen, et al. (1996). 'The Cosmic Microwave Background Spectrum from the Full COBE FIRAS Data Set'. *ApJ* **473**:576. 141
- L. Flöer, et al. (2010). 'RFI mitigation for the Effelsberg Bonn HI Survey (EBHIS)'. In *RFI Mitigation Workshop (RFI2010)* 42. 64
- D. T. Frayer, et al. (1998). 'OH satellite-line masers in the nucleus of NGC 253'. *AJ* **115**:559. 77
- W. L. Freedman, et al. (2012). 'Carnegie Hubble Program: A Mid-infrared Calibration of the Hubble Constant'. *ApJ* **758**:24. 123
- A. M. Fridman, et al. (2005). 'The orientation parameters and rotation curves of 15 spiral galaxies'. *A&A* **430**:67–81. 103
- P. A. Fridman & W. A. Baan (2001). 'RFI mitigation methods in radio astronomy'. *A&A* **378**:327–344. 24
- D. C. Gabuzda & T. V. Cawthorne (2000). 'VLBI polarization images of eight compact active galactic nuclei at  $\lambda=1.3\text{cm}$ '. *MNRAS* **319**:1056–1066. 149, 163
- J. F. Gallimore, et al. (2004). 'The Parsec-Scale Radio Structure of NGC 1068 and the Nature of the Nuclear Radio Source'. *ApJ* **613**:794–810. 47
- J. F. Gallimore, et al. (1996). 'H 2O and OH Masers as Probes of the Obscuring Torus in NGC 1068'. *ApJ* **462**:740. 46, 47, 48, 52, 53, 77, 92
- T. Garn, et al. (2007). 'Deep 610-MHz Giant Metrewave Radio Telescope observations of the Spitzer extragalactic First Look Survey field - I. Observations, data analysis and source catalogue'. *MNRAS* **376**:1251–1260. 39, 54
- M. A. Garrett & C. Greenwood (2012). 'Resolving The Sky (RTS 2012) - Radio Interferometry: Past, Present and Future'. In *Resolving The Sky - Radio Interferometry: Past, Present and Future*. 16
- R. W. Garwood, et al. (1987). 'Arecibo observations of IRAS galaxies at 21 and 18 centimeters'. *ApJ* **322**:88–100. 83
- R. Giovanelli & M. P. Haynes (1993). 'A survey of the Pisces-Perseus supercluster. VI - The declination zone +15.5 deg to 21.5 deg'. *AJ* **105**:1271–1290. 85
- M. Gliozzi, et al. (2003). 'On the origin of the X-rays and the nature of accretion in NGC 4261'. *A&A* **408**:949–959. 84
- J. D. Goldader, et al. (1997). 'Heavily Obscured Star Formation in the II ZW 96 Galaxy Merger'. *AJ* **113**:1569–1579. 85
- O. González-Martín, et al. (2009). 'Fitting Liner Nuclei within the Active Galactic Nucleus Family: A Matter of Obscuration?'. *ApJ* **704**:1570–1585. 84, 90
- J. E. Greene, et al. (2010). 'Precise Black Hole Masses from Megamaser Disks: Black Hole-Bulge Relations at Low Mass'. *ApJ* **721**:26–45. 11, 104, 121, 124, 125, 127, 138, 145, 195
- L. J. Greenhill (2007). 'Masers in AGN environments'. In J. M. Chapman & W. A. Baan (eds.), *IAU Symposium*, vol. 242 of *IAU Symposium*, pp. 381–390. 8
- L. J. Greenhill, et al. (2003). 'A Warped Accretion Disk and Wide-Angle Outflow in the Inner Parsec of the Circinus Galaxy'. *ApJ* **590**:162–173.

- 6, 83, 84
- L. J. Greenhill, et al. (2008). ‘Prevalence of High X-Ray Obscuring Columns among AGNs that Host H<sub>2</sub>O Masers’. *ApJ* **686**:L13–L16. 78
- E. Groten (2004). ‘Fundamental Parameters and Current (2004) Best Estimates of the Parameters of Common Relevance to Astronomy, Geodesy, and Geodynamics by Erwin Groten, IPGD, Darmstadt’. *Journal of Geodesy* **77**(10-11):724–797. 22
- M. A. Gurwell, et al. (2007). ‘Monitoring Phase Calibrators at Submillimeter Wavelengths’. In A. J. Baker, J. Glenn, A. I. Harris, J. G. Mangum, & M. S. Yun (eds.), *From Z-Machines to ALMA: (Sub)Millimeter Spectroscopy of Galaxies*, vol. 375 of *Astronomical Society of the Pacific Conference Series*, p. 234. 151
- R. Güsten, et al. (2006). ‘The Atacama Pathfinder EXperiment (APEX) - a new submillimeter facility for southern skies -’. *A&A* **454**:L13–L16. 151
- K. Hada, et al. (2011). ‘An origin of the radio jet in M87 at the location of the central black hole’. *Nature* **477**:185–187. 150
- M. P. Haynes, et al. (2011). ‘The Arecibo Legacy Fast ALFA Survey: The  $\alpha$ .40 H I Source Catalog, Its Characteristics and Their Impact on the Derivation of the H I Mass Function’. *AJ* **142**:170. 92
- C. Henkel, et al. (2005). ‘H<sub>2</sub>O Megamasers: Accretion Disks, Jet Interaction, Outflows or Massive Star Formation?’. *Ap&SS* **295**:107–116. 9, 77
- C. Henkel, et al. (2004). ‘Water vapor in the starburst galaxy NGC 253: A new nuclear maser?’. *A&A* **414**:117–122. 77
- J. R. Herrnstein, et al. (1996). ‘The Warp in the Subparsec Molecular Disk in NGC4258 as an Explanation for Persistent Asymmetries in the Maser Spectrum’. *ApJ* **468**:L17. 211
- J. R. Herrnstein, et al. (1999). ‘A geometric distance to the galaxy NGC4258 from orbital motions in a nuclear gas disk’. *Nature* **400**:539–541. 124, 211
- G. Hinshaw, et al. (2013). ‘Nine-year Wilkinson Microwave Anisotropy Probe (WMAP) Observations: Cosmological Parameter Results’. *ApJS* **208**:19. 123, 125, 149, 218
- P. Hofner, et al. (2006). ‘H<sub>2</sub>O Maser Emission in the Starburst Galaxy NGC 253’. *AJ* **131**:2074–2077. 92
- J. A. Högbom (1974). ‘Aperture Synthesis with a Non-Regular Distribution of Interferometer Baselines’. *A&AS* **15**:417. 18, 19
- J. Hogden, et al. (2012). ‘Comparison of Radio-frequency Interference Mitigation Strategies for Dispersed Pulse Detection’. *ApJ* **747**:141. 24, 27
- D. W. Hogg (1999). ‘Distance measures in cosmology’. *ArXiv Astrophysics e-prints*. 213
- M. A. Holdaway (1997). ‘Atmospheric Coherence Times at Chajnantor’. Tech. Rep. 169, NRAO. 158
- D. Hollenbach, et al. (2009). ‘Water, O<sub>2</sub>, and Ice in Molecular Clouds’. *ApJ* **690**:1497–1521. 78
- D. C. Homan, et al. (2006). ‘Intrinsic Brightness Temperatures of AGN Jets’. *ApJ* **642**:L115–L118. 173
- D. C. Homan, et al. (2009). ‘Full Polarization Spectra of 3C 279’. *ApJ* **696**:328–347. 149
- P. F. Hopkins & E. Quataert (2010). ‘How do massive black holes get their gas?’. *MNRAS* **407**:1529–1564. 3
- U. Hopp, et al. (2000). ‘The Hamburg/SAO survey for emission-line galaxies . III. The third list of 81 galaxies’. *A&AS* **142**:417–423. 82
- J. Hu (2008). ‘The black hole mass-stellar velocity dispersion correlation: bulges versus pseudo-bulges’. *MNRAS* **386**:2242–2252. 125
- W. Hu (2005). ‘Observing Dark Energy’. *ASP*

- Conf. Ser.* **339**:215. 124
- M. Huarte-Espinosa, et al. (2013). ‘Mass loading and knot formation in AGN jets by stellar winds’. *Mem. Soc. Astron. Italiana* **84**:725. 102
- A. Hubbard & E. G. Blackman (2006). ‘Active galactic nuclei jet mass loading and truncation by stellar winds’. *MNRAS* **371**:1717–1721. 102
- J. P. Huchra, et al. (1999). ‘The CFA Redshift Survey: Data for the South Galactic CAP’. *ApJS* **121**:287–368. 47, 92
- E. M. L. Humphreys, et al. (2005). ‘First Detection of Millimeter/Submillimeter Extragalactic H<sub>2</sub>O Maser Emission’. *ApJ* **634**:L133–L136. 8
- E. M. L. Humphreys, et al. (2008). ‘Toward a New Geometric Distance to the Active Galaxy NGC 4258. II. Centripetal Accelerations and Investigation of Spiral Structure’. *ApJ* **672**:800–816. 96, 102, 108, 110, 130, 132, 211, 213
- E. M. L. Humphreys, et al. (2013). ‘Toward a New Geometric Distance to the Active Galaxy NGC 4258. III. Final Results and the Hubble Constant’. *ApJ* **775**:13. 123, 124, 138, 211, 215, 221
- C. Impellizzeri (2008). *Molecular absorption in the cores of AGN: On the unified model*. Ph.D. thesis, Bonn University. 6, 46, 47, 77, 78, 81, 84, 87, 88, 90
- C. M. V. Impellizzeri, et al. (2012). ‘Mrk 1419 - a new distance determination’. In R. S. Booth, W. H. T. Vlemmings, & E. M. L. Humphreys (eds.), *IAU Symposium*, vol. 287 of *IAU Symposium*, pp. 311–315. 102, 124
- H. Inami, et al. (2010). ‘The Buried Starburst in the Interacting Galaxy II Zw 096 as Revealed by the Spitzer Space Telescope’. *AJ* **140**:63–74. 85
- Y. Ishihara, et al. (2001). ‘Water-Vapor Maser Emission from the Seyfert 2 Galaxy IC 2560: Evidence for a Super-Massive Black Hole’. *PASJ* **53**:215–225. 126, 127, 219, 220
- K. Iwasawa, et al. (2002). ‘A Chandra observation of the H<sub>2</sub>O megamaser IC 2560’. *MNRAS* **336**:L71–L74. 126
- S. Jogee (2006). ‘The Fueling and Evolution of AGN: Internal and External Triggers’. In D. Alloin (ed.), *Physics of Active Galactic Nuclei at all Scales*, vol. 693 of *Lecture Notes in Physics*, Berlin Springer Verlag, p. 143. 3
- S. Jorstad, et al. (2011). ‘Parsec-Scale Behavior of Blazars during High Gamma-Ray States’. *2011 Fermi Symposium proceedings - eConf C110509* arXiv:1111.0110. 149
- S. G. Jorstad, et al. (2004). ‘Change in Speed and Direction of the Jet near the Core in the Quasar 3C 279’. *AJ* **127**:3115–3120. 149
- S. Kameno, et al. (2005). ‘Emergence of a Narrow H<sub>2</sub>O Maser Feature in NGC 1052’. *ApJ* **620**:145–150. 132
- A. B. Kamruddin & J. Dexter (2013). ‘A geometric crescent model for black hole images’. *MNRAS* **434**:765–771. 175
- H. G. Katzgraber (2009). ‘Introduction to Monte Carlo Methods’. *ArXiv e-prints*. 137
- H. G. Katzgraber (2010). ‘Random Numbers in Scientific Computing: An Introduction’. *ArXiv e-prints*. 137
- K. I. Kellermann & M. H. Cohen (1988). ‘The origin and evolution of the N.R.A.O.-Cornell VLBI system’. *JRASC* **82**:248–265. 15
- K. I. Kellermann & J. M. Moran (2001). ‘The Development of High-Resolution Imaging in Radio Astronomy’. *ARA&A* **39**:457–509. 15
- K. I. Kellermann & I. I. K. Pauliny-Toth (1969). ‘The Spectra of Opaque Radio Sources’. *ApJ* **155**:L71. 173
- J. Kerp, et al. (2011). ‘The Effelsberg Bonn H I Survey (EBHIS)’. *Astronomische Nachrichten* **332**:637. 64
- F. J. Kerr & D. Lynden-Bell (1986). ‘Review of galactic constants’. *MNRAS* **221**:1023–1038.



- 47
- M. Kesteven (2003). ‘Adaptive Filters for RFI Mitigation in Radioastronomy’. In Y. C. Minh (ed.), *New technologies in VLBI*, vol. 306 of *Astronomical Society of the Pacific Conference Series*, p. 93. 60, 63
- M. Kesteven (2010). ‘Overview of RFI mitigation methods in existing and new systems’. In *RFI 2010 – Proceedings of the RFI mitigation workshop*. PoS. 24
- M. Kettenis, et al. (2006). ‘ParselTongue: AIPS Talking Python’. In C. Gabriel, C. Arviset, D. Ponz, & S. Enrique (eds.), *Astronomical Data Analysis Software and Systems XV*, vol. 351 of *Astronomical Society of the Pacific Conference Series*, p. 497. 113
- H. Klöckner (2004). *Extragalactic Hydroxyl*. Ph.D. thesis, Rijksuniversiteit Groningen. 77, 78, 83, 85, 87, 90
- H.-R. Klöckner & W. A. Baan (2004). ‘An embedded circumnuclear disk in Mrk 273’. *A&A* **419**:887–896. 8
- J. Kocz, et al. (2010). ‘Radio Frequency Interference Removal through the Application of Spatial Filtering Techniques on the Parkes Multi-beam Receiver’. *AJ* **140**:2086–2094. 58
- K. Kogan (1995). ‘Effect of Digitizer Errors on the Cross and Auto Correlation Response of an FX Correlator’. Tech. Rep. 9, NRAO. 113, 160
- E. Komatsu, et al. (2011). ‘Seven-year Wilkinson Microwave Anisotropy Probe (WMAP) Observations: Cosmological Interpretation’. *ApJS* **192**:18. 123
- S. Komissarov (2012). *Central Engines: Acceleration, Collimation and Confinement of Jets*, pp. 81–114. Wiley-VCH Verlag GmbH & Co. KGaA. 5
- P. T. Kondratko, et al. (2006). ‘Discovery of Water Maser Emission in Five AGNs and a Possible Correlation Between Water Maser and Nuclear 2-10 keV Luminosities’. *ApJ* **652**:136–145. 9, 77, 78
- J. Kormendy & D. Richstone (1995). ‘Inward Bound—The Search For Supermassive Black Holes In Galactic Nuclei’. *ARA&A* **33**:581. 3
- Y. Y. Kovalev, et al. (2005). ‘Sub-Milliarcsecond Imaging of Quasars and Active Galactic Nuclei. IV. Fine-Scale Structure’. *AJ* **130**:2473–2505. 161
- T. P. Krichbaum, et al. (2008). ‘Towards millimeter VLBI’. *ArXiv e-prints*. 150
- T. P. Krichbaum, et al. (2013). ‘Zooming towards the Event Horizon - mm-VLBI today and tomorrow’. In *Proceedings of the 11th European-VLBI Network Symposium, October 2012*. <http://pos.sissa.it/cgi-bin/reader/conf.cgi?confid=178>. 150, 168, 169, 175
- J. H. Krolik & M. C. Begelman (1988). ‘Molecular tori in Seyfert galaxies - Feeding the monster and hiding it’. *ApJ* **329**:702–711. 6
- G. P. Kuiper (1950). ‘The Diameter of Pluto’. *PASP* **62**:133. 20
- C. Y. Kuo, et al. (2011). ‘The Megamaser Cosmology Project. III. Accurate Masses of Seven Supermassive Black Holes in Active Galaxies with Circumnuclear Megamaser Disks’. *ApJ* **727**:20. 11, 83, 118, 124, 211, 212, 216, 219, 220
- C. Y. Kuo, et al. (2013). ‘The Megamaser Cosmology Project. V. An Angular-diameter Distance to NGC 6264 at 140 Mpc’. *ApJ* **767**:155. 102, 110, 123, 124, 138, 146, 233, 239
- S.-S. Lee, et al. (2008). ‘a Global 86 GHz VLBI Survey of Compact Radio Sources’. *AJ* **136**:159–180. 173
- A. Leshem, et al. (2000). ‘Multichannel Interference Mitigation Techniques in Radio Astronomy’. *ApJS* **131**:355–373. 57, 58, 61
- R. F. Ling (1974). ‘Comparison of Several Algo-

- rithms for Computing Sample Means and Variances’. *Journal of the American Statistical Association* **69**(348):859–866. 138
- M. L. Lister, et al. (2009). ‘MOJAVE: Monitoring of Jets in Active Galactic Nuclei with VLBA Experiments. V. Multi-Epoch VLBA Images’. *AJ* **137**:3718–3729. 149
- M. L. Lister, et al. (2013). ‘MOJAVE. X. Parsec-scale Jet Orientation Variations and Superluminal Motion in Active Galactic Nuclei’. *AJ* **146**:120. 4
- K. Y. Lo (2005). ‘Mega-Masers and Galaxies’. *ARA&A* **43**:625–676. 78
- A. P. Lobanov (2005). ‘Resolution limits in astronomical images’. *ArXiv Astrophysics e-prints*. 161
- R.-S. Lu, et al. (2013). ‘Fine-scale Structure of the Quasar 3C 279 Measured with 1.3 mm Very Long Baseline Interferometry’. *ApJ* **772**:13. 150, 172, 173
- R.-S. Lu, et al. (2012). ‘Resolving the Inner Jet Structure of 1924–292 with the Event Horizon Telescope’. *ApJ* **757**:L14. 173
- G. Madejski, et al. (2006). ‘X-Ray Emission from Megamaser Galaxy IC 2560’. *ApJ* **636**:75–82. 126
- P. R. Maloney, et al. (1996). ‘Radiation-driven Warping: The Origin of WARPS and Precession in Accretion Disks’. *ApJ* **472**:582. 117
- P. J. Manners (2007). ‘Measuring the RFI environment of the South African SKA site’. Master’s thesis, Rhodes University. 24, 25
- D. Maoz, et al. (1995). ‘Detection of compact ultraviolet nuclear emission in liner galaxies’. *ApJ* **440**:91–99. 212
- E. Maoz (1995). ‘Spiral Structure in the Circumnuclear Disk at the Center of NGC 4258’. *ApJ* **455**:L131. 118, 211, 213
- E. Maoz (1998). ‘Dynamical Constraints on Alternatives to Supermassive Black Holes in Galactic Nuclei’. *ApJ* **494**:L181. 118, 212, 219
- E. Maoz & C. F. McKee (1998). ‘Doppler Shift Asymmetry in High-Velocity Maser Emission from Shocks in Circumnuclear Disks’. *ApJ* **494**:218. 132, 133, 213
- D. P. Marrone (2006). *Submillimeter Properties of Sagittarius A\*: The Polarization and Spectrum from 230 to 690 GHz and the Submillimeter Array Polarimeter*. Ph.D. thesis, Harvard University. 162
- J.-M. Martin, et al. (1989). ‘Discovery of nine new extragalactic OH megamasers - The role and efficiency of far-infrared radiation’. *Academie des Sciences Paris Comptes Rendus Serie Sciences Mathematiques* **308**:287–292. 83, 86
- P. Marziani, et al. (1996). ‘Comparative Analysis of the High- and Low-Ionization Lines in the Broad-Line Region of Active Galactic Nuclei’. *ApJS* **104**:37. 149
- M. Massi, et al. (1996). ‘Baseline errors on European VLBI Network measurements. II. Instrumental polarization.’. *A&AS* **116**:167–176. 162
- Matlab® (2010). *version 7.10.0 (R2010a)*. The MathWorks Inc., Natick, Massachusetts. 35, 37, 108, 118
- M. Matsumoto & T. Nishimura (1998). ‘Mersenne twister: a 623-dimensionally equidistributed uniform pseudo-random number generator’. *ACM Trans. Model. Comput. Simul.* **8**(1):3–30. 137
- J. McBride & C. Heiles (2013). ‘An Arecibo Survey for Zeeman Splitting in OH Megamaser Galaxies’. *ApJ* **763**:8. 83
- J. N. McCallum, et al. (2009). ‘Probing the microarcsecond structure of the Circinus megamasers through diffractive interstellar scintillation’. *MNRAS* **392**:1339–1362. 83
- N. J. McConnell, et al. (2011). ‘Two ten-billion-solar-mass black holes at the centres of giant elliptical galaxies’. *Nature* **480**:215–218. 11,

- 104, 120, 124, 127, 145
- D. N. McLintock (1980). *Very long baseline interferometry and geodetic applications*. Ph.D. thesis, University of Nottingham. 17, 22
- S. Meyer (2013). ‘The Structure of the Water Megamaser in the Galaxy IC2560 Bachelor’s thesis, Department of Astronomy, Harvard College, Cambridge, MA’. Master’s thesis, Department of Astronomy, Harvard College, Cambridge, MA. 122, 136, 140
- V. Migenes, et al. (2011). ‘Optical and OH megamaser observations of the starburst galaxy IIZw 096’. *MNRAS* **416**:1267–1273. 85
- S. K. K. Mitra (2000). *Digital Signal Processing: A Computer-Based Approach*. McGraw-Hill Higher Education, 2nd edn. 31, 35, 36
- M. Miyoshi, et al. (1995). ‘Evidence for a black hole from high rotation velocities in a sub-parsec region of NGC4258’. *Nature* **373**:127–129. 124, 140
- J. D. Monnier (2007). ‘7. Phases in interferometry’. In F. Malbet & G. Perrin (eds.), *Observation and Data Reduction with the VLT Interferometer*, vol. 51 of *New Astronomy Reviews*, pp. 604–616. 161
- J. M. Moran, et al. (1973). ‘Very long baseline interferometric observations of the H<sub>2</sub>O sources in W49N, W3(OH), Orion A, and VY Canis Majoris.’. *ApJ* **185**:535–567. 15
- H. W. Morsi & W. Reich (1986). ‘A new 32 GHz radio continuum receiving system for the Effelsberg 100-m telescope’. *A&A* **163**:313–320. 24
- M. J. Mortonson, et al. (2010). ‘Testable dark energy predictions from current data’. *Phys. Rev. D* **81**(6):063007. 124, 146, 218
- M. Moshir, et al. (1990). ‘IRAS Faint Source Catalogue, version 2.0.’. In *IRAS Faint Source Catalogue, version 2.0 (1990)*, p. 0. 92, 105, 126
- D. Mudd, et al. (2012). ‘XMM-Newton Observations of Three Interacting Luminous Infrared Galaxies’. *ApJ (submitted)*. 85
- N. Murray, et al. (2005). ‘On the Maximum Luminosity of Galaxies and Their Central Black Holes: Feedback from Momentum-driven Winds’. *ApJ* **618**:569–585. 125
- N. Nakai, et al. (1995). ‘Search for Extremely-High-Velocity H<sub>2</sub>O Maser Emission Seyfert Galaxies’. *PASJ* **47**:771–799. 9, 77
- S. Nayakshin, et al. (2012). ‘The Observed M- $\sigma$  Relations Imply That Super-massive Black Holes Grow by Cold Chaotic Accretion’. *ApJ* **753**:15. 125
- D. A. Neufeld, et al. (1995). ‘Thermal Balance in Dense Molecular Clouds: Radiative Cooling Rates and Emission-Line Luminosities’. *ApJS* **100**:132. 8, 9
- D. A. Neufeld & P. R. Maloney (1995). ‘The Mass Accretion Rate through the Masing Molecular Disk in the Active Galaxy NGC 4258’. *ApJ* **447**:L17. 10, 117, 120
- D. A. Neufeld, et al. (1994). ‘Water maser emission from X-ray-heated circumnuclear gas in active galaxies’. *ApJ* **436**:L127. 83, 117
- X. Ni & X. Huo (2007). ‘Statistical interpretation of the importance of phase information in signal and image reconstruction’. *Statistics & Probability Letters* **77**(4):447–454. 161
- K. Nilsson, et al. (2009). ‘The host galaxy of 3C 279’. *A&A* **505**:601–604. 149
- C. Nixon, et al. (2013). ‘Tearing up the disc: misaligned accretion on to a binary’. *MNRAS* **434**:1946–1954. 117
- C. J. Nixon & A. R. King (2012). ‘Broken discs: warp propagation in accretion discs’. *MNRAS* **421**:1201–1208. 117
- K. Noguchi, et al. (2009). ‘A New Sample of Buried Active Galactic Nuclei Selected from the Second XMM-Newton Serendipitous Source Catalogue’. *ApJ* **705**:454–467. 90

- R. C. Nongpiur, et al. (2013). ‘Improved Design Method for Nearly Linear-Phase IIR Filters Using Constrained Optimization’. *IEEE Transactions on Signal Processing* **61**:895–906. 38
- A. R. Offringa, et al. (2012). ‘Post-correlation filtering techniques for off-axis source and RFI removal’. *MNRAS* **422**:563–580. 22, 33
- R. P. Olling (2007). ‘Accurate extragalactic distances and dark energy: anchoring the distance scale with rotational parallaxes’. *MNRAS* **378**:1385–1399. 124
- T. Oosterloo, et al. (2010). ‘The latest on Apertif’. In *ISKAF2010 Science Meeting*. 61
- S. P. O’Sullivan & D. C. Gabuzda (2009). ‘Magnetic field strength and spectral distribution of six parsec-scale active galactic nuclei jets’. *MNRAS* **400**:26–42. 150
- J. Ott, et al. (2013). ‘Discovery of Nuclear Water Maser Emission in Centaurus A’. *ApJ* **771**:L41. 92, 103
- F. N. Owen, et al. (1997). ‘The Cluster of Galaxies Surrounding Cygnus A’. *ApJ* **488**:L15. 47
- F. Panessa, et al. (2006). ‘On the X-ray, optical emission line and black hole mass properties of local Seyfert galaxies’. *A&A* **455**:173–185. 101
- N. D. Pant, et al. (2009). ‘A Complete Set of VSOP Observations of 3C279’. In Y. Hagiwara, E. Fomalont, M. Tsuboi, & M. Yasuhiro (eds.), *Approaching Micro-Arcsecond Resolution with VSOP-2: Astrophysics and Technologies*, vol. 402 of *Astronomical Society of the Pacific Conference Series*, p. 213. 149
- R. Parra, et al. (2010). ‘COLA. III. Radio Detection of Active Galactic Nucleus in Compact Moderate Luminosity Infrared Galaxies’. *ApJ* **720**:555–568. 94
- A. Parsons & PAPER Team (2009). ‘Developing A Low-frequency Interferometer For Detecting The Epoch Of Reionization: Correlation, Calibration, And High Dynamic-range Imaging With Paper’. In *American Astronomical Society Meeting Abstracts #213*, vol. 41 of *Bulletin of the American Astronomical Society*, p. 348. 40
- A. R. Parsons, et al. (2010). ‘The Precision Array for Probing the Epoch of Re-ionization: Eight Station Results’. *AJ* **139**:1468–1480. 40
- R. K. Pearson (2005). *Mining Imperfect Data: Dealing with Contamination and Incomplete Records*. SIAM: Society for Industrial and Applied Mathematics. 113
- A. B. Peck, et al. (2003). ‘The Flaring H<sub>2</sub>O Megamaser and Compact Radio Source in Markarian 348’. *ApJ* **590**:149–161. 46, 92
- B. Petrachenko (2010). ‘The Impact of Radio Frequency Interference (RFI) on VLBI2010’. In R. Navarro, S. Rogstad, C. E. Goodhart, E. Sigman, M. Soriano, D. Wang, L. A. White, & C. S. Jacobs (eds.), *Sixth International VLBI Service for Geodesy and Astronomy. Proceedings from the 2010 General Meeting, "VLBI2010: From Vision to Reality"*. Held 7-13 February, 2010 in Hobart, Tasmania, Australia. Edited by D. Behrend and K.D. Baver. NASA/CP 2010-215864., p.434-438, pp. 434–438. 26
- W. T. Petrachenko, et al. (2010). ‘VLBI2010: Next Generation VLBI System for Geodesy and Astrometry’. *AGU Fall Meeting Abstracts* p. B6. 27
- Y. M. Pihlström (2005). ‘OH Megamaser Galaxies at High Angular Resolution’. In J. Romney & M. Reid (eds.), *Future Directions in High Resolution Astronomy*, vol. 340 of *Astronomical Society of the Pacific Conference Series*, p. 224. 8
- Planck Collaboration (2013). ‘Planck intermediate results. XIII. Constraints on peculiar velocities’. *ArXiv e-prints* . 125
- H. C. Plummer (1915). ‘The distribution of stars in globular clusters’. *MNRAS* **76**:107–121. 118,

- 219
- A. J. Poulson, et al. (2005). ‘Programmable Real-Time Cancellation of GLONASS Interference with the Green Bank Telescope’. *AJ* **130**:2916–2927. 27
- J. E. Pringle (1996). ‘Self-induced warping of accretion discs’. *MNRAS* **281**:357–361. 117
- J. E. Pringle (1997). ‘Self-induced warping of accretion discs - Non-linear evolution and application to AGN’. *MNRAS* **292**:136. 117
- C. Ramos Almeida, et al. (2011). ‘Testing the Unification Model for Active Galactic Nuclei in the Infrared: Are the Obscuring Tori of Type 1 and 2 Seyferts Different?’. *ApJ* **731**:92. 6
- A. C. S. Readhead (1994). ‘Equipartition brightness temperature and the inverse Compton catastrophe’. *ApJ* **426**:51–59. 173
- M. J. Reid, et al. (2009). ‘The Megamaser Cosmology Project. I. Very Long Baseline Interferometric Observations of UGC 3789’. *ApJ* **695**:287–291. 95, 113
- M. J. Reid, et al. (2013). ‘The Megamaser Cosmology Project. IV. A Direct Measurement of the Hubble Constant from UGC 3789’. *ApJ* **767**:154. 11, 77, 109, 123, 124, 137, 146, 213, 216
- M. Rioja, et al. (2012). ‘The Impact of Frequency Standards on Coherence in VLBI at the Highest Frequencies’. *AJ* **144**:121. 21
- G. Risaliti, et al. (1999). ‘The Distribution of Absorbing Column Densities among Seyfert 2 Galaxies’. *ApJ* **522**:157–164. 90
- J. Rissanen, et al. (1978). ‘Modeling by Shortest Data Description’. *Automatica* **14**(5):465–471. 60
- A. E. E. Rogers, et al. (1974). ‘The structure of radio sources 3C 273B and 3C 84 deduced from the ‘closure’ phases and visibility amplitudes observed with three-element interferometers’. *ApJ* **193**:293–301. 155, 161
- A. E. E. Rogers, et al. (1967). ‘The Positions and Angular Extent of OH Emission Associated with the H II Regions W3, W24, W49, and NGC 6334’. *ApJ* **147**:369. 15
- D. A. Roshi & R. A. Perley (2003). ‘A New Technique to Improve RFI Suppression in Radio Interferometers’. In Y. C. Minh (ed.), *New technologies in VLBI*, vol. 306 of *Astronomical Society of the Pacific Conference Series*, p. 109. 28, 29, 33, 34, 57
- A. L. Roy, et al. (2013). ‘VLBI at APEX: First Fringes’. In *Proceedings of 11th EVN Symposium 2012*, vol. 057 of *EVN Symposium Proceedings*. 150, 174
- G. Ruiz, et al. (2005). ‘Algorithms for Multi-Beam Receiver Data Analysis’. In D. Danesy (ed.), *4th European Conference on Space Debris*, vol. 587 of *ESA Special Publication*, p. 89. 28, 64
- M. Ryle (1955). ‘The application of interferometric methods in radio astronomy’. *Vistas in Astronomy* **1**:532–541. 14
- M. Ryle (1957). ‘The Mullard Radio Astronomy Observatory, Cambridge’. *Nature* **180**:110–112. 14
- M. Ryle (1962). ‘The New Cambridge Radio Telescope’. *Nature* **194**:517–518. 14
- M. Ryle & A. Hewish (1960). ‘The synthesis of large radio telescopes’. *MNRAS* **120**:220. 14
- M. Ryle & A. C. Neville (1962). ‘A radio survey of the North Polar region with a 4.5 minute of arc pencil-beam system’. *MNRAS* **125**:39. 15
- M. Ryle & D. D. Vonberg (1946). ‘Solar Radiation on 175 Mc./s.’. *Nature* **158**:339–340. 15
- S. Sachdev & N. Udaya Shankar (1995). ‘Strategy for interference removal at Mauntyus Radio Telescope’. *Bulletin of the Astronomical Society of India* **23**:574–575. 34
- D. B. Sanders, et al. (2003). ‘The IRAS Revised Bright Galaxy Sample’. *AJ* **126**:1607–1664. 92

- S. Sawada-Satoh, et al. (2008). ‘Positional Coincidence of H<sub>2</sub>O Maser and a Plasma-Obscuring Torus in Radio Galaxy NGC 1052’. *ApJ* **680**:191–199. 6, 46, 85, 88, 92, 99
- R. O. Schmidt (1986). ‘Multiple emitter location and signal parameter estimation’. *IEEE Transactions on Antennas and Propagation* **34**:276–280. 59
- H. Schulz & C. Henkel (2003). ‘Rotation and outflow in the central kiloparsec of the water-megamaser galaxies IC 2560, NGC 1386, NGC 1052, and Mrk 1210’. *A&A* **400**:41–62. 126
- P. F. Scott, et al. (1961). ‘First results of radio star observations using the method of aperture synthesis’. *MNRAS* **122**:95–111. 15
- S. L. Shapiro & S. A. Teukolsky (1983). *Black holes, white dwarfs, and neutron stars: The physics of compact objects*. Wiley-Interscience. 220
- M. C. Shepherd (1997). ‘Difmap: an Interactive Program for Synthesis Imaging’. In G. Hunt & H. Payne (eds.), *Astronomical Data Analysis Software and Systems VI*, vol. 125 of *Astronomical Society of the Pacific Conference Series*, p. 77. 156, 164
- J. L. Sievers, et al. (2013). ‘The Atacama Cosmology Telescope: Cosmological parameters from three seasons of data’. *ArXiv e-prints*. 123
- J. Silk & M. J. Rees (1998). ‘Quasars and galaxy formation’. *A&A* **331**:L1–L4. 125
- C. Simpson, et al. (1996). ‘An Ionization Cone and Dusty Disk in Markarian 348: The Obscuring Torus Revealed?’. *ApJ* **457**:L19. 46
- M. F. Skrutskie, et al. (2006). ‘The Two Micron All Sky Survey (2MASS)’. *AJ* **131**:1163–1183. 98, 111
- K. V. Sokolovsky, et al. (2011). ‘A VLBA survey of the core shift effect in AGN jets. I. Evidence of dominating synchrotron opacity’. *A&A* **532**:A38. 150
- M. Spaans (2005). ‘The Impact of Gravitational Redshift on Systemic Water Maser Emission in NGC 4258’. *ArXiv Astrophysics e-prints*. 128
- C. M. Springob, et al. (2005). ‘A Digital Archive of H I 21 Centimeter Line Spectra of Optically Targeted Galaxies’. *ApJS* **160**:149–162. 92
- C. M. Springob, et al. (2009). ‘SFI++ II: A New I-Band Tully-Fisher Catalog, Derivation of Peculiar Velocities and Data Set Properties’. *ApJS* **182**:474–475. 126
- S. Stanko, et al. (2005). ‘A field programmable gate array spectrometer for radio astronomy. First light at the Effelsberg 100-m telescope’. *A&A* **436**:391–395. 65
- L. Staveley-Smith, et al. (1992). ‘A southern OH megamaser survey’. *MNRAS* **258**:725–737. 87, 90
- S. H. Suyu, et al. (2013). ‘Two Accurate Time-delay Distances from Strong Lensing: Implications for Cosmology’. *ApJ* **766**:70. 123
- N. Suzuki, et al. (2012). ‘The Hubble Space Telescope Cluster Supernova Survey. V. Improving the Dark-energy Constraints above  $z > 1$  and Building an Early-type-hosted Supernova Sample’. *ApJ* **746**:85. 123
- E. R. Switzer, et al. (2013). ‘Determination of  $z \sim 0.8$  neutral hydrogen fluctuations using the 21 cm intensity mapping autocorrelation’. *MNRAS* **434**:L46–L50. 58
- Y. Tan, et al. (2012). ‘On the nature of X-ray “unobscured” Seyfert 2 galaxies’. *Science in China G: Physics and Astronomy* **55**:2482–2491. 6, 90
- A. Tarchi, et al. (2007). ‘The water megamaser in the merger system Arp 299’. *New A Rev.* **51**:67–70. 77
- A. Tarchi, et al. (2011). ‘New H<sub>2</sub>O masers in Seyfert and FIR bright galaxies. IV. Interferometric follow-ups’. *A&A* **525**:A91. 78, 85, 87
- A. Tarchi, et al. (2004). ‘Extragalactic Water

- Masers in Bright IRAS Sources’. In S. Aalto, S. Huttemeister, & A. Pedlar (eds.), *The Neutral ISM in Starburst Galaxies*, vol. 320 of *Astronomical Society of the Pacific Conference Series*, p. 199. 87
- J. M. Tarongi & A. Camps (2009). ‘Normality Analysis for RFI Detection in Microwave Radiometry’. *Remote Sensing* **2**(1):191–210. 27
- C. E. Tatemaya (2009). ‘Study of BL Lac VLBA Data at 8 and 15 GHz in a Super-resolution Mode’. *ApJ* **705**:877–884. 168
- G. B. Taylor, et al. (eds.) (1999). *Synthesis Imaging in Radio Astronomy II*, vol. 180 of *Astronomical Society of the Pacific Conference Series*. 17, 21
- J. H. Taylor, et al. (1993). ‘Catalog of 558 pulsars’. *ApJS* **88**:529–568. 64
- J. Tennyson (2011). *Astronomical Spectroscopy: An Introduction to the Atomic and Molecular Physics of Astronomical Spectra*. World Scientific Publishing Company, 2 edn. 7
- J. N. Terry, et al. (2002). ‘Local velocity field from sosie galaxies. I. The Peebles’ model’. *A&A* **393**:57–68. 126
- The Planck Collaboration (2013). ‘Planck 2013 results. XVI. Cosmological parameters’. *ArXiv e-prints*. 123
- G. Theureau, et al. (1998). ‘Kinematics of the local universe. VII. New 21-cm line measurements of 2112 galaxies’. *A&AS* **130**:333–339. 126, 128, 135
- G. Theureau, et al. (2007). ‘Kinematics of the Local Universe. XIII. 21-cm line measurements of 452 galaxies with the Nançay radiotelescope, JHK Tully-Fisher relation, and preliminary maps of the peculiar velocity field’. *A&A* **465**:71–85. 105
- A. R. Thompson, et al. (2001). *Interferometry and Synthesis in Radio Astronomy, 2nd Edition*. Wiley-Interscience, 2 edn. 17, 19, 21, 22
- D. R. Thompson, et al. (2011). ‘Detection of Fast Radio Transients with Multiple Stations: A Case Study Using the Very Long Baseline Array’. *ApJ* **735**:98. 27, 34
- A. Tilak, et al. (2008). ‘A Deep 0.3-10 keV Spectrum of the H<sub>2</sub>O Maser Galaxy IC 2560’. *ApJ* **678**:701–711. 11, 12, 126
- S. C. Trager, et al. (2000). ‘The Stellar Population Histories of Local Early-Type Galaxies. I. Population Parameters’. *AJ* **119**:1645–1676. 84
- L. N. Trefethen & D. Bau (1997). *Numerical Linear Algebra*. SIAM: Society for Industrial and Applied Mathematics. 58
- G. Tuccari, et al. (2012). ‘The DBBC environment for millimeter radioastronomy’. In *The DBBC environment for millimeter radioastronomy*, vol. 8452, pp. 84522W–84522W–11. 152
- C. M. Urry & P. Padovani (1995). ‘Unified Schemes for Radio-Loud Active Galactic Nuclei’. *PASP* **107**:803. 6
- P. H. van Cittert (1934). ‘Die Wahrscheinliche Schwingungsverteilung in Einer von Einer Lichtquelle Direkt Oder Mittels Einer Linse Beleuchteten Ebene’. *Physica* **1**:201–210. 17, 18
- A.-J. van der Veen & A.-J. Boonstra (2004). ‘Spatial filtering of RF interference in radio astronomy using a reference antenna’. In *Acoustics, Speech, and Signal Processing, 2004. Proceedings. (ICASSP '04). IEEE International Conference on*, vol. 2, pp. ii–189–92 vol.2. 62
- W. van Driel, et al. (2001). ‘H I line observations of luminous infrared galaxy mergers’. *A&A* **368**:64–73. 85
- H. J. van Langevelde, et al. (2000). ‘A thin H i circumnuclear disk in NGC 4261’. *A&A* **354**:L45–L48. 81, 84, 90
- V. Vassilev, et al. (2008). ‘A Swedish heterodyne facility instrument for the APEX telescope’. *A&A* **490**:1157–1163. 152

- R. V. Vasudevan, et al. (2013). ‘X-Ray Properties of the Northern Galactic Cap Sources in the 58 Month Swift/BAT Catalog’. *ApJ* **763**:111. 90
- M. A. W. Verheijen, et al. (2008). ‘Apertif, a focal plane array for the WSRT’. In R. Minchin & E. Momjian (eds.), *The Evolution of Galaxies Through the Neutral Hydrogen Window*, vol. 1035 of *American Institute of Physics Conference Series*, pp. 265–271. 16
- M.-P. Véron-Cetty & P. Véron (2006). ‘A catalogue of quasars and active nuclei: 12th edition’. *A&A* **455**:773–777. 126
- J. Wagner (2011). ‘EU FP7 ALBiUS WP6 MPI Project Documentation for DiFX Multirate Filtering’. Tech. rep., MPIfR. 35
- R. C. Walker (1995). ‘What the VLBA Can Do For You’. In J. A. Zensus, P. J. Diamond, & P. J. Napier (eds.), *Very Long Baseline Interferometry and the VLBA*, vol. 82 of *Astronomical Society of the Pacific Conference Series*, p. 133. 24
- C. Walter & S. Chatterjee (1999). ‘Ionospheric Corrections Using GPS Based Models’. Tech. Rep. 23, NRAO. 113
- J. Walther (2012). *Untersuchung von Masergalaxien im harten Röntgenbereich*. Ph.D. thesis, Univ. Würzburg. 101, 106, 120, 126
- W. D. Watson & B. K. Wallin (1994). ‘Evidence from masers for a rapidly rotating disk at the nucleus of NGC 4258’. *ApJ* **432**:L35–L38. 211, 216
- M. Wax & T. Kailath (1985). ‘Detection of signals by information theoretic criteria’. *Acoustics, Speech and Signal Processing, IEEE Transactions on* **33**(2):387–392. 61
- D. H. Weinberg, et al. (2013). ‘Observational probes of cosmic acceleration’. *Phys. Rep.* **530**:87–255. 123, 124, 125, 213, 217, 218
- J. B. Whiteoak & F. F. Gardner (1974). ‘Observations of OH in NGC 4945 and NGC 253’. *Astrophys. Lett.* **15**:211. 8
- K. W. Willett, et al. (2011). ‘Mid-infrared Properties of OH Megamaser Host Galaxies. II. Analysis and Modeling of the Maser Environment’. *ApJ* **730**(1):56. 87, 90
- J. G. A. Wouterloot & C. M. Walmsley (1986a). ‘H<sub>2</sub>O masers associated with IRAS sources in regions of star formation’. *A&A* **168**:237–247. 83
- J. G. A. Wouterloot & C. M. Walmsley (1986b). ‘H<sub>2</sub>O masers associated with IRAS sources in regions of star formation’. *A&A* **168**:237–247. 105, 126
- Q. Wu, et al. (2013). ‘Warping of an accretion disc and launching of a jet by a spinning black hole in NGC 4258’. *MNRAS* **436**:1278–1285. 117
- Y. Yaji, et al. (2010). ‘Evidence of Non-thermal X-ray Emission from Radio Lobes of Cygnus A’. *ApJ* **714**:37–44. 47
- A. Yamauchi, et al. (2012). ‘Water-Vapor Maser Disk at the Nucleus of the Seyfert 2 Galaxy IC 2560 and its Distance’. *PASJ* **64**:103. 108, 110, 125, 126, 127, 130, 132, 134, 136, 141, 146
- D. York, et al. (2004). ‘Unified equations for the slope, intercept, and standard errors of the best straight line’. *American Journal of Physics* **72**(3):367–375. 136, 214
- A. J. Young, et al. (2002). ‘A Chandra X-Ray Study of Cygnus A. II. The Nucleus’. *ApJ* **564**:176–189. 46
- Y. Yuan (2000). ‘A review of trust region algorithms for optimization’. In *Proceedings of the Fourth International Congress on Industrial & Applied Mathematics*, ICIAM 99 (Edinburgh), p. 271. Oxford University Press. 118, 137
- M. S. Yun, et al. (2001). ‘Radio Properties of Infrared-selected Galaxies in the IRAS 2 Jy Sample’. *ApJ* **554**:803–822. 83
- J. A. Zensus, et al. (eds.) (1995). *Very Long Baseline Interferometry and the VLBA*, vol. 82 of



- Astronomical Society of the Pacific Conference Series*. 17, 18
- J. S. Zhang, et al. (2006). 'Extragalactic H<sub>2</sub>O masers and X-ray absorbing column densities'. *A&A* **450**:933–944. 78
- G. Zhu, et al. (2011). 'Optical Properties of Host Galaxies of Extragalactic Nuclear Water Masers'. *ApJ* **742**:73. 101

# List of Figures

1.1	A typical spectram energy distribution for normal and active galaxies. . . . .	3
1.2	The energy levels and radiative transitions of ortho and para isomers of water. .	5
1.3	Structure of the accretion disk near the black hole. . . . .	5
1.4	Stimulated emission in a masing molecule. . . . .	7
1.5	The energy levels and radiative transitions of ortho and para isomers of water. .	7
1.6	Abundances of O, O <sub>2</sub> , and H <sub>2</sub> O as a function of temperature. . . . .	8
1.7	Schematic illustration of the disk water masers and accretion disk in NGC 4258.	10
1.8	Schematic illustration of the disk water masers and accretion disk in NGC 4258.	10
1.9	The $M_{\text{BH}}-\sigma_{\star}$ relations for different types of galaxies. . . . .	11
1.10	Illustration of possible accretion disk geometries in maser galaxy IC 2560. . . .	12
2.1	The interferometric fringe pattern of a VLBI baseline. . . . .	13
2.2	The effect of longer baselines on fringe spacing. . . . .	14
2.3	Example of the scales of array resolution on Cygnus A. . . . .	15
2.4	Three types of common radio astronomical interferometric arrays. . . . .	16
2.5	The effect of an incompletely filled synthetic aperture. . . . .	17
2.6	Examples of temporal and spatial coherence. . . . .	18
2.7	Example uv plane coverage with the VLA and the VLBA, and the uv trajectory in time and frequency. . . . .	20
3.1	Radio frequency interference at Effelsberg at 1.6 GHz and at APEX at 230 GHz.	23
3.2	The allocation of the 3 GHz to 300 GHz radio spectrum in the UK. . . . .	24
3.3	Schematic illustration of “fringe stopping”: a phasor diagram of two visibilities.	30
3.4	Time evolution of visibilities in an ATCA array observation of an OH maser in presence of RFI from a GLONASS satellite. . . . .	32
3.5	Example of fringe rate filtering and the time trajectories of complex visibilities in data from the ATCA array. . . . .	33

3.6	Example of the correlator output with and without fringe rate filtering for ATCA data with GLONASS RFI and an OH maser. . . . .	34
3.7	The magnitude and phase response of two VLBI fringe rate filters, compared to no additional filtering. . . . .	36
3.8	The structure of the Digital State Variable Filter . . . . .	38
3.9	Results of a simulation in AIPY of the effect of RFI fringe component aliasing in visibility data. . . . .	39
3.10	The GPS modulation scheme. . . . .	40
3.11	The fringe frequency spectrum of synthetic 1.6 GHz VLBI data with GPS RFI seen on the Ef–Wb baseline. . . . .	42
3.12	The single-channel, full fringe frequency spectrum of the synthetic GPS RFI dataset after fringe-stopping in DiFX. . . . .	42
3.13	The fringe frequency spectrum in three channels around the GPS interferer. . . . .	44
3.14	The full fringe frequency spectrum of DiFX fringe stopped 1.6 GHz data with GPS RFI after fringe rate filtering. . . . .	45
3.15	Three EVN VLBI image of Cygnus A by Bach et al. shown for reference. . . . .	47
3.16	The uv coverage on Cygnus A in the 1.6 GHz EVN VLBI experiment EW014. . . . .	48
3.17	Example of trunk DiFX and RFI DiFX processed EVN VLBI visibility data. . . . .	51
3.18	The EVN 1.6 GHz VLBI continuum image of Cygnus A. . . . .	52
3.19	The EVN 1.6 GHz VLBI continuum image of NGC 1068 and the spectrum over the southern component showing the main-line OH non-detection. . . . .	53
3.20	A diagram of the antenna signals contributing to the array coherence matrix. . . . .	57
3.21	The coherence matrix eigenvalue spectra and RFI “nulling” in 1.49 GHz APERTIF phased array feed data . . . . .	59
3.22	The result of “nulling” RFI in 1.49 GHz APERTIF phased array feed data, showing an image towards Virgo A. . . . .	60
3.23	Effelsberg $\lambda 21$ cm 7-beam receiver and beam spectrograms. . . . .	65
3.24	The geometry of the simulated uniform 64-antenna array. . . . .	66
3.25	An example synthetic array coherence matrix produced by the simulation model. . . . .	68
3.26	Images for a subjective performance comparison of the four RFI subtraction methods based on synthetic array coherence data. . . . .	71
3.27	Comparison of the residual errors of the four RFI subtraction methods for arrays, show for 1 interferer and 2 reference antennas. . . . .	74
3.28	Comparison of the residual errors of the four array RFI subtraction methods for 2 interferers and 2 reference antennas. . . . .	74
3.29	Comparison of the residual errors of the four array RFI subtraction methods for 2 interferers and 3 reference antennas. . . . .	75

3.30	Comparison of the residual errors of the four array RFI subtraction methods for 3 interferers and 3 reference antennas. . . . .	75
4.1	Water megamasers detected towards 2MFGC 13581, IRAS 17526+3253, NGC 4261, and IRAS 20550+1656. . . . .	81
4.2	Equivalent isotropic luminosities and upper limits for all 95 sources now searched for OH and H <sub>2</sub> O maser emission. . . . .	86
5.1	The rms-weighted integrated spectrum of the water masers in NGC 23. . . . .	93
5.2	Five GBT epochs of the water masers in NGC 23 with component fits overlaid. . . . .	97
5.3	Multi-wavelength continuum images of NGC 23 and water maser positions. . . . .	100
5.4	Water masers in NGC 23 detected with the VLA and VLBA. . . . .	101
6.1	The integrated spectrum of the 22 GHz GBT water maser detection towards UGC 3193. . . . .	105
6.2	Spectra of the eight 22 GHz epochs on UGC 3193. . . . .	108
6.3	The best-fit maser accelerations in UGC 3193. . . . .	110
6.4	The maser map and position–velocity diagram of the disk masers in UGC 3193. . . . .	116
7.1	Spectrum of H <sub>2</sub> O masers towards IC 2560. . . . .	126
7.2	Spectra of all GBT epochs of the H <sub>2</sub> O masers detected towards IC 2560. . . . .	129
7.3	IC 2560 maser accelerations against velocity. Accelerations of the Maoz–McKee spiral model fit are overlaid. . . . .	132
7.4	The VLBI image of the disk maser distribution in IC 2560. . . . .	135
7.5	The best-fit Keplerian I and Plummer models for masers in IC 2560. . . . .	139
7.6	The maser position–velocity diagram and accelerations for the Kepler II model fit to IC 2560 disk maser data. . . . .	141
7.7	The masing disk geometry for the best-fit parameters of MCMC Fit 1. . . . .	143
7.8	The masing disk geometry for the best-fit parameters of MCMC Fit 2. . . . .	143
7.9	The best-fit $M_{\text{BH}}-\sigma_{\star}$ power laws in a figure adopted from Greene et al. (2010). The $M_{\text{BH}}-\sigma_{\star}$ power law fits through all galaxies (solid) or sub-samples of galaxies (dashed, dotted) are shown. Maser galaxies categorized by Greene et al. as having a pseudo-bulge (open large circles) or a classic bulge (filled large circles) are indicated, as is the Greene et al. measurement of $\sigma_{\star} \simeq 10^{2.15 \pm 0.03}$ in IC 2560 (horizontal location of cross; note, Greene et al. provide no reference for their adopted SMBH mass and state error bars are “heuristic only”). The new maser-based $M_{\text{BH}}$ mass of Fit 2 is overlaid (asterisk) and has a $3\sigma$ uncertainty of about the diameter of the asterisk. . . . .	145

8.1	The APEX 12 m telescope. . . . .	147
8.2	The $\lambda$ 1.3 mm VLBI array during the observation and the future planned full (sub)mm VLBI array. . . . .	148
8.3	UV coverage on 3C 279 for the APEX 1.3 mm VLBI experiment on 2012 May 7. . . . .	151
8.4	The APEX receiver phase noise characteristics. . . . .	154
8.5	Example of the typical evolution in APEX 1.3 mm VLBI coherence time during 7 minutes, showing atmospheric turbulence and APEX receiver decoherence. . . . .	158
8.6	Example of the typical APEX 1.3 mm VLBI coherence time (HOPS “tcoh”) during 7 minutes on the APEX–ARO SMT baseline. . . . .	159
8.7	The 3C 279 1.3 mm VLBI closure phase detected on the APEX–ARO SMT–SMA triangle. . . . .	162
8.8	The detected amplitude (Jy) against uv distance ( $M\lambda$ ) on 3C 279 in APEX 1.3 mm VLBI during 2012. . . . .	163
8.9	The 1.3 mm VLBI visibility data and the four- and six-component modelfits of Table 8.5. . . . .	168
8.10	Super-resolved 43 GHz VLBA and 86 GHz GMVA images of 3C 279, and two APEX 1.3 mm VLBI best-fitting modelfits. . . . .	169
8.11	Proper motions of 3C 279 components in super-resolved 7 mm images. The 3 mm components and the 1.3 mm 6-component modelfit positions are overlaid. . . . .	171
8.12	Predictions event horizon -scale emission from Sgr A*. . . . .	175
A.3.1	Spectra of the GBT water maser non-detections. . . . .	207
A.3.2	Test spectra of the GBT 22 GHz water maser detections in known maser galaxies. . . . .	210
A.4.1	Coordinates of the Keplerian disk model. . . . .	215
A.4.2	The improvement in Dark Energy EoS w constraints by more accurate $H_0$ data. . . . .	218
A.7.1	Normalized posterior probability densities for parameters of the first IC 2560 MCMC model fit (Fit 1). . . . .	232
A.7.2	Joint posterior distributions for parameters of the first IC 2560 MCMC model fit (Fit 1). . . . .	233
A.7.3	Normalized posterior probability densities for parameters of the second IC 2560 MCMC model fit (Fit 2). . . . .	238
A.7.4	Joint posterior distributions for parameters of the first IC 2560 MCMC model fit (Fit 2). . . . .	238

# List of Tables

3.1	Summary 1.6 GHz EVN VLBI experiment. . . . .	48
3.2	Tabulated performance comparison of the four RFI subtraction methods, based on simulations of a 64-element antenna array. . . . .	73
4.1	Epochs of the 22 GHz GBT water maser survey. . . . .	80
4.2	Source sample of the 22 GHz H <sub>2</sub> O maser search . . . . .	89
4.2	continued. . . . .	90
5.1	Single-Dish and Radio Interferometric Epochs on NGC 23. . . . .	94
5.2	Spectral Features in GBT Epochs. . . . .	97
6.1	Single Dish and Interferometric Epochs on UGC 3193. . . . .	107
6.2	The best-fit accelerations of the maser features in UGC 3193. . . . .	111
6.3	Plummer model fit to the UGC 3193 rotation curve without accelerations. . . . .	119
6.4	Kepler I model fit to the UGC 3193 rotation curve without accelerations. . . . .	119
7.1	Recent $H_0$ Estimates for flat $\Lambda$ CDM with $w \equiv -1$ . . . . .	123
7.2	Accelerations of the maser features in IC 2560. . . . .	131
7.3	The K-band VLBI water maser observations for IC 2560s. . . . .	133
7.4	Plummer model fit to the IC 2560 rotation curve without accelerations. . . . .	139
7.5	Kepler I model fit to the IC 2560 rotation curve without accelerations. . . . .	140
7.6	Best-fit parameters of the Keplerian disk model for the IC 2560 maser position and acceleration data, determined with the MCMC method. . . . .	144
8.1	APEX 1.3 mm VLBI fringe spacings and baseline sensitivities. . . . .	152
8.2	Telescopes and data acquisition in the APEX VLBI session in 2012. . . . .	153
8.3	Overview of the 3C 279 $\lambda$ 1.3 mm VLBI observation on 2012 May 7 . . . . .	155
8.4	Summary of station calibration data for the APEX VLBI run in 2012. . . . .	156
8.5	Best-fitting Difmap modelfits of APEX 1.3 mm VLBI visibility data. . . . .	166

A.1.1 The DiFX correlation setup file with RFI related entries. . . . .	202
A.1.2 The new RFI-related entries in the DiFX correlation descriptor file. . . . .	203
A.1.3 The syntax of the new DiFX fringe rate filter coefficients file. . . . .	204
A.2.1 Summary of the source code additions to DiFX that are related to fringe rate filtering. . . . .	205
A.2.2 Summary of the Matlab and Python scripts related to array RFI mitigation and DiFX. . . . .	206
A.5.1 Single Dish and Interferometric Epochs on IC 2560 . . . . .	223
A.6.1 Positions of maser features in NGC 23. . . . .	224
A.6.1 Positions of maser features in NGC 23. . . . .	225
A.6.2 Positions of maser features in UGC 3193. . . . .	226
A.6.3 Positions of maser features in UGC 3193. . . . .	227
A.6.4 Positions of maser features in IC 2560. . . . .	228
A.6.5 Positions of maser features in IC 2560. . . . .	229
A.6.6 Positions of maser features in IC 2560. . . . .	230
A.6.7 Positions of maser features in IC 2560. . . . .	231

# Acknowledgements

There were many great moments throughout the short four years in Bonn and travelling the globe, sometimes working, occasionally even on the thesis. During this time I've received valuable help and support from many people and this is the place to thank at least some of them.

For reviewing this thesis and for their participation in the disputation examination I would like to thank Prof. Dr. A. Eckart, Prof. Dr. A. Zensus, and Prof. Dr. S. Crewell. I'm grateful to both Prof. Eckart and Prof. Zensus for being my doctoral advisors. In particular, I sincerely thank Prof. Zensus as well as W. Alef for their kind support throughout the thesis in various forms, via the IMPRS research school, the EU and RadioNet projects, interesting other projects such as APEX VLBI, and for supporting my travels to NRAO Charlottesville and Green Bank. I feel deeply grateful to Prof. J. Braatz for allowing me to work on the MCP project, for the time spent both in Charlottesville and Green Bank, with thanks also to M. Reid and C. Y. Kuo for their comments, to Christian Henkel for his help, suggestions and support, and to all others in and outside of the MCP project who went through scheduling and observing for nearly ten years worth of MCP maser galaxy data! Thank you also Feng Gao and Jan Pitann for the fun, hiking, and discussions during my NRAO and GBT stays.

In Bonn T. Krichbaum was my first introduction to Difmap and I thank him for the mm-VLBI discussions. A related thanks goes to my excellent supervisor Alan Roy, not only for the first crash course to AIPS, but for his time and friendly advice throughout the Ph.D. time. I'm extremely grateful to Alan for many things, starting from him "bringing" me to the MPIfR Bonn – anywhere else I would've surely never met Yoon nor had that life-changing "event" named Lumi. Thank you for the many inspiring and enlightening times here in Bonn, and for the great memories including Teide and the Atacama! Indeed, a particular highlight was definitely the annual visits with Alan to that high-altitude town and telescope in Chile. Thanks also Michael Lindqvist and Neil Nagar, and APEX folks. At the MPIfR a special thanks also to Amit Bansod, Christian Fromm, and Marios Karouzou for the fun and interesting time in and out of the office, as well as a number of other former Bonn people now scattered around the world for the nice time in Bonn!

Finally, to my beloved Yoon, my "old" and "new" parents, Sofia and Martin, Ulla and H.-J.,



---

and also Oma, I'm immensely grateful for them being always supportive and available, including often taking care of Lumi! Without their continuous loving support this thesis would not have been possible!

Regarding the formal acknowledgements, here they are: I was supported for this research through a stipend from the International Max Planck Research School (IMPRS) for Astronomy and Astrophysics. This research has made use of the NASA/IPAC Extragalactic Database (NED) which is operated by the Jet Propulsion Laboratory, California Institute of Technology, under contract with the National Aeronautics and Space Administration. This research has made use of NASA's Astrophysics Data System. This study makes use of 43 GHz VLBA data from the Boston University gamma-ray blazar monitoring program, funded by NASA through the Fermi Guest Investigator Program. This work is based on data acquired with the Atacama Pathfinder Experiment (APEX). APEX is a collaboration between the Max-Planck-Institut für Radioastronomie, the European Southern Observatory, and the Onsala Space Observatory. VLBI research at the Sub-millimeter Telescope of the Arizona Radio Observatory is partially supported by the NSF University Radio Observatories Program (URO grant AST-1140030) and by AST-0905844. The ARO is a facility of Steward Observatory, University of Arizona. The National Radio Astronomy Observatory is a facility of the National Science Foundation operated under cooperative agreement by Associated Universities, Inc.

# A Appendix

## A.1 DiFX Configuration Files for Fringe Rate Filtering

The main setup file for DiFX correlation with enabled fringe rate filtering is shown in Table A.1.1. The standard DiFX tools convert the main setup file into a series of correlation setup files that describe the actual correlation process. The syntax of these files has been extended by two new entries, shown in Table A.1.2. They specify the location of a user-provided filter coefficients file and specify whether fringe rate filtering should be enabled.

The syntax of the coefficient file is given in Table A.1.3. The filters are serially interconnected in the order that they appear in the file. A serial multi-rate filtering chain is possible via the decimator block.

## A.1 DiFX Configuration Files for Fringe Rate Filtering

```
# Template v2d file for DiFX correlation of W30H
vex = w3oh.vex.clocks
antennas = EF, JB, WB
singleScan = True
# The nChan should never be less than 128.
SETUP default

tInt = 2.048
nChan = 2048
nFFTChan = 2048
xmacLength = 2048 # to prevent FFT split into 16x128 pieces
doPolar = True
doRFI = True # enable RFI filters (default: False)

# Note 1: DiFX can apply filters only to the raw data in one sub-integration
# Note 2: DiFX sums the output of parallel sub-integrations to yield one complete
#         integration (e.g. 4 sub-ints of 0.512s are summed for one 2.048s visibility).
#         If the expected RFI fringe frequency is lower than what can be filtered
#         in a single sub-integration, to reduce aliasing you may need to increase
#         the sub-integration time (at cost of computer main memory).
# Note 3: DiFX is distributed and time-continuous filtering will not work.
#         The filter states are thus always reset at the end of a sub-integration.
# A subint of 0.512s produces 4 subints for one full 2.048s Tint.
subintNS = 512000000 # (optional)

# This, along with SETUP default above, should always be done
RULE default { setup = default} # Stations and file list paths
ANTENNA EF { filelist = filelist.ef }
ANTENNA JB { filelist = filelist.jb }
ANTENNA WB { filelist = filelist.wb }

# Setup place holders
SETUP w3oh.set { }
# Sources (pointing centers) with recorded data
SOURCE W30H { }
```

**Table A.1.1:** Some of the standard entries in a DiFX v2d correlation job meta-descriptor file, used to configure the correlation process, and comments on RFI filtering and the new doRFI setting.

## A.1 DiFX Configuration Files for Fringe Rate Filtering

---

```
# COMMON SETTINGS
...
RFI FILT TYPE:      CHAIN
RFI FILT COEFFS:   /Exps/w3oh/w3oh_01.coeff
```

**Table A.1.2:** The two new entries in the DiFX input correlation descriptor file that are relevant to RFI fringe rate filtering. Specifying a filter type of `CHAIN` enables custom filtering, while specifying `NONE` disables custom filters and enables normal time averaging.

## A.1 DiFX Configuration Files for Fringe Rate Filtering

```

# --- Example filter configuration file
# The total number of cascaded (serially interconnected) filters
5 # i.e, five filters should follow after this. The possible choices are:

# --- Integrator
0 # type: 0=integrator, has no coefficients

# --- Decimation by an integer factor
1 # type: 1=decimator
3 # decimation ratio

# --- Biquad IIR Filter
2 # type: 2=IIR-SOS/biquad
10 # filter order, order 10 requires five 2nd order sections
9.99831172521226110e-6 # input prescaling gain
# filter coefficients in M=order/2 rows (M x 6 coeffs total)
# b0(1) b1(1) b2(1) a0(1) a1(1) a2(1)
# ...
# b0(M) b1(M) b2(M) a0(M) a1(M) a2(M)
1.0 -1.99999451637268070 1.0 1.0 -1.99986529350280760 0.99986535310745239
1.0 -1.99999928474426270 1.0 1.0 -1.99989640712738040 0.99989646673202515
1.0 -1.99999964237213130 1.0 1.0 -1.99993586540222170 0.99993598461151123
1.0 -1.99999976158142090 1.0 1.0 -1.99996757507324220 0.99996769428253174
1.0 -1.99999976158142090 1.0 1.0 -1.99999022483825680 0.99999040365219116

# --- Digital state variable filter
4 # type: 4=DSVF
1.0 # input prescaling gain
0.000773 # tuning f = 2*sin(pi*(1024*(1/0.52)))/16e6
0.5 # quality q = 1/Q for Q = 2.0

# --- Moving average filter
5 # type: 5=MAvg
16 # length L of window
0.0625 # input prescaling gain, gain=1/L gives the moving average

```

**Table A.1.3:** The syntax of the new DiFX fringe rate filter coefficients file. The available filter types and individual filter parameters are listed.

## A.2 Summary of the RFI Mitigation Source Code

The software release, algorithm implementation and the documentation of the DiFX<sup>1</sup> VLBI fringe rate filter and the array RFI mitigation implemented in the first part of this thesis are found in the “rfi” branch of the DiFX source code repository<sup>2</sup>. The documentation can also be found on the pages of the RadioNet EU FP7 ALBiUS project<sup>3</sup>.

A subset of the new files, programs, and their function is listed below for reference.

Source file	Description
<i>filterchain.cpp,.h</i>	Instantiates a chain with one or more filters in series and can also load a filter setup from a text file.
<i>filterhelpers.cpp,.h</i>	Common utility functions.
<i>filter.h</i>	The interface definition of the filter class.
<i>filters.cpp,.h</i>	Derived classes and factory function.
<i>filter_iirsos.cpp</i>	Cascaded bi-quad IIR filter implementation.
<i>filter_dsvf.cpp</i>	Digital State Variable filter.
<i>filter_int.cpp</i>	Integrating filter.
<i>filter_mavg.cpp</i>	Moving average filter.
<i>filter_dec.cpp</i>	Decimator, sample rate reduction.
<i>filter_test.cpp</i>	Tests cases for the filter infrastructure. Also loads an external 1-channel 32-bit floating point data filters it with the filter chain specified in an external coefficients file.
<i>filter_data.cpp</i>	Utility that provides a signal generator (impulse, step, sine, Gaussian noise) and allows the signal to be filtered with an external *.coeff file.
<i>filter_parse.cpp</i>	Utility that checks the validity of a filter coefficient file.

**Table A.2.1:** Summary of the source code additions to DiFX that are related to fringe rate filtering.

<sup>1</sup><http://cira.ivec.org/dokuwiki/doku.php/di fx/>

<sup>2</sup><https://svn.atnf.csiro.au/di fx/>

<sup>3</sup><http://www.radionet-eu.org/fp7/albius.html>

## A.2 Summary of the RFI Mitigation Source Code

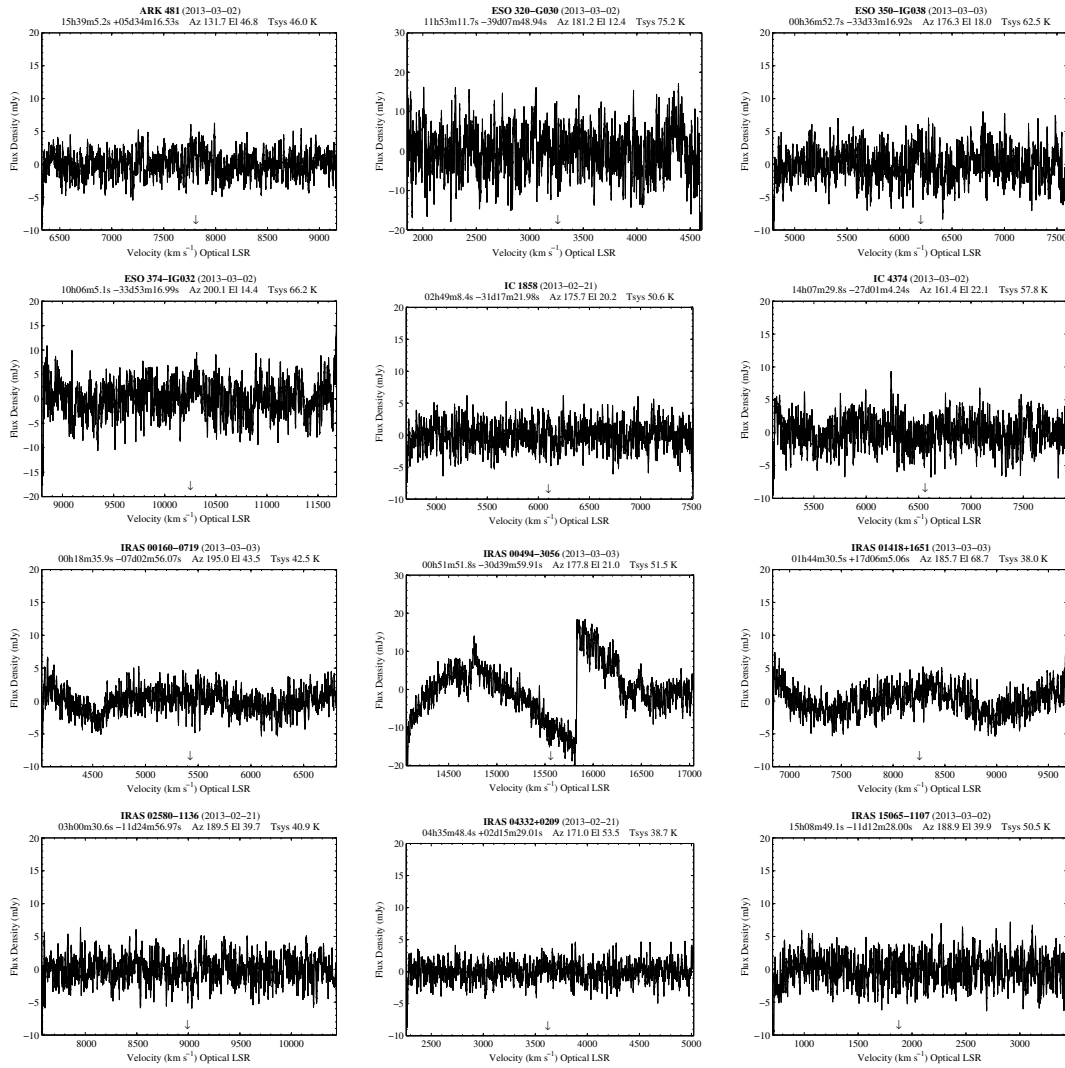
Script	Description
<i>test_dsvf.m</i>	Reference implementation of the Digital State Variable filter.
<i>test_iirsos.m</i>	Reference implementation of the bi-quad IIR filter.
<i>read_mk5b.m</i>	Reads Mark5B data recordings into Matlab.
<i>read_difx_dump.m</i>	Reads a chunk of raw multi-channel cross correlation data from a binary dump file. These files are written by DiFX after fringe stopping (but prior to averaging) when debug dumps are enabled in <code>./src/mode.cpp</code> .
<i>integrate_difx_dump.m</i>	Produces time-integrated autocorrelation from a DiFX dump file.
<i>integrate_difx_dump_xc2.m</i>	Produces time-integrated, and for comparison also low-pass filtered, cross-correlations from two DiFX dump files.
<i>specgram_difx_dump_xc2.m</i>	Reads from two DiFX dump files, produces auto and crosscorrelation spectrograms and a fringe frequency spectrum.
<i>fftdump_fringrates.m</i>	Loads one DiFX dump and displays the time series and fringe frequency spectrum of some or all spectral channels. When only few channels are selected it uses line plots, otherwise a spectrogram plot.
<i>fftdump_fringrates2.m</i>	Loads two DiFX dump files and shows the unfiltered, integrated, and filtered cross correlation time series. Can add a noise and a synthetic tone at a source fringe rate to the data. Includes tests for, e.g, the effect of different filter state initialization schemes.
<i>fftdump_checks.m</i>	Loads two DiFX dump files for analysis. Several plot types can be enabled, e.g., a cross correlation spectrogram, time integrated cross- and autocorrelations, phase/lag plot, and the true cross covariance for non zero-average signals, given by $E \langle s_1 \cdot s_2^* \rangle - E \langle s_1 \rangle E \langle s_2 \rangle^*$ .
<i>subscrfi_*.m</i>	Several scripts found in the “beamformer” package that allow basic imaging of array covariance data (visibilities), array RFI detection, spatio-spectral nulling of RFI, RFI template subtraction, generating of synthetic array data with source and RFI components, DOA estimation.
<i>datagen5b.py</i>	Generates synthetic Mark5B recordings (16 MHz, 8 channels, 2-bit data), with mutually correlated noise, and optionally a correlated RFI in form of a GPS carrier that is optionally modulated by the C/A and Y code sequences. Mutually uncorrelated noise is added to the station data.

**Table A.2.2:** Summary of the Matlab and Python scripts related to array RFI mitigation and DiFX.

### A.3 Spectra of the Water Maser Non-Detections

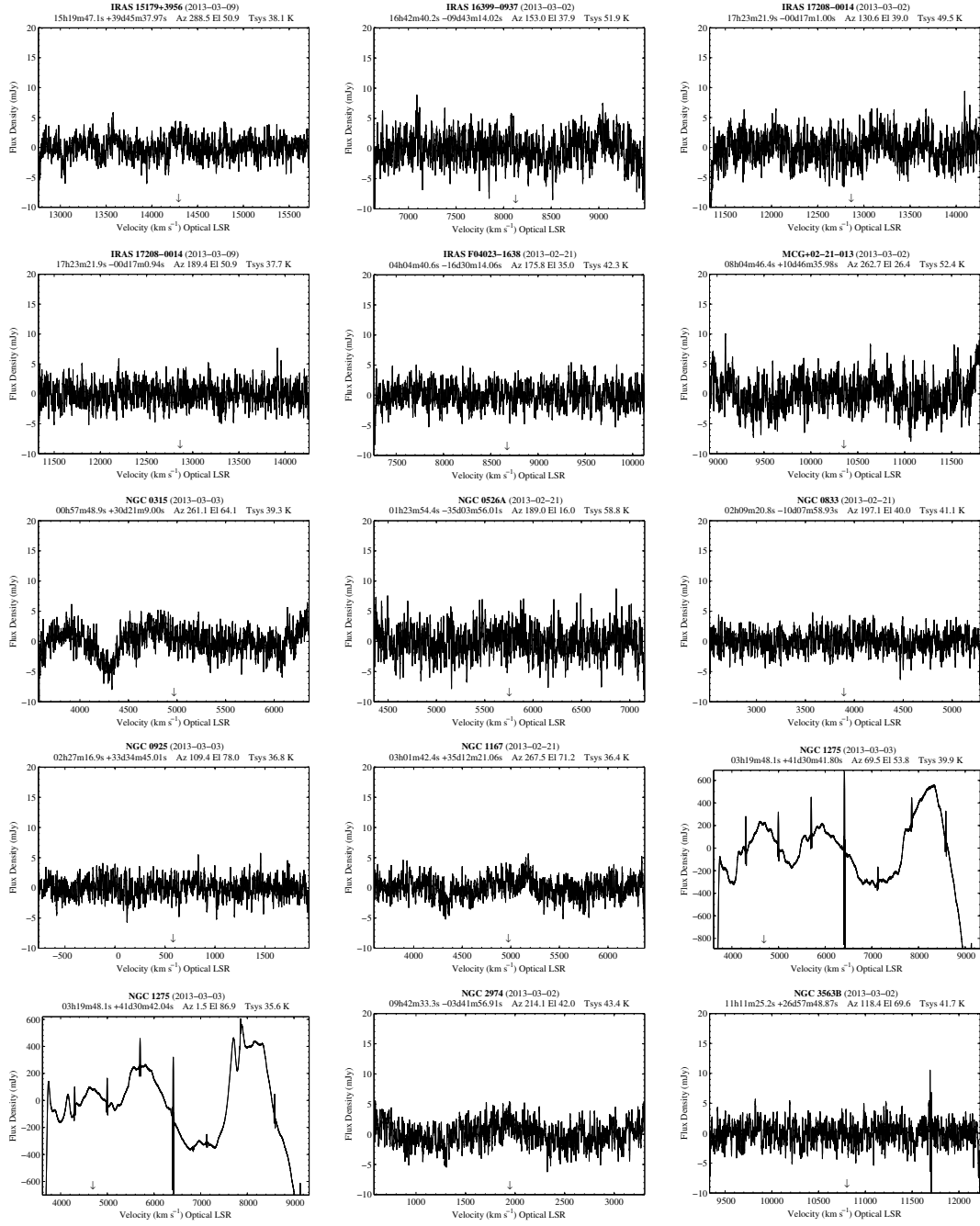
Spectra of the new 22 GHz water maser detections were shown in Table 4.1, see § 4.6. Spectra of the *nondetections* are reproduced below. The upper limits on maser flux density and equivalent isotropic luminosity for the nondetections can be found in Table 4.2 on page 89.

**Fig. A.3.1:** Spectra of the GBT water maser non-detections, smoothed with a shape preserving 3<sup>rd</sup> order  $\sim 5$  km/s Savitzky–Golay filter. Systemic recession velocities are indicated by arrows and are adopted from the NASA/IPAC Extragalactic Database (NED).

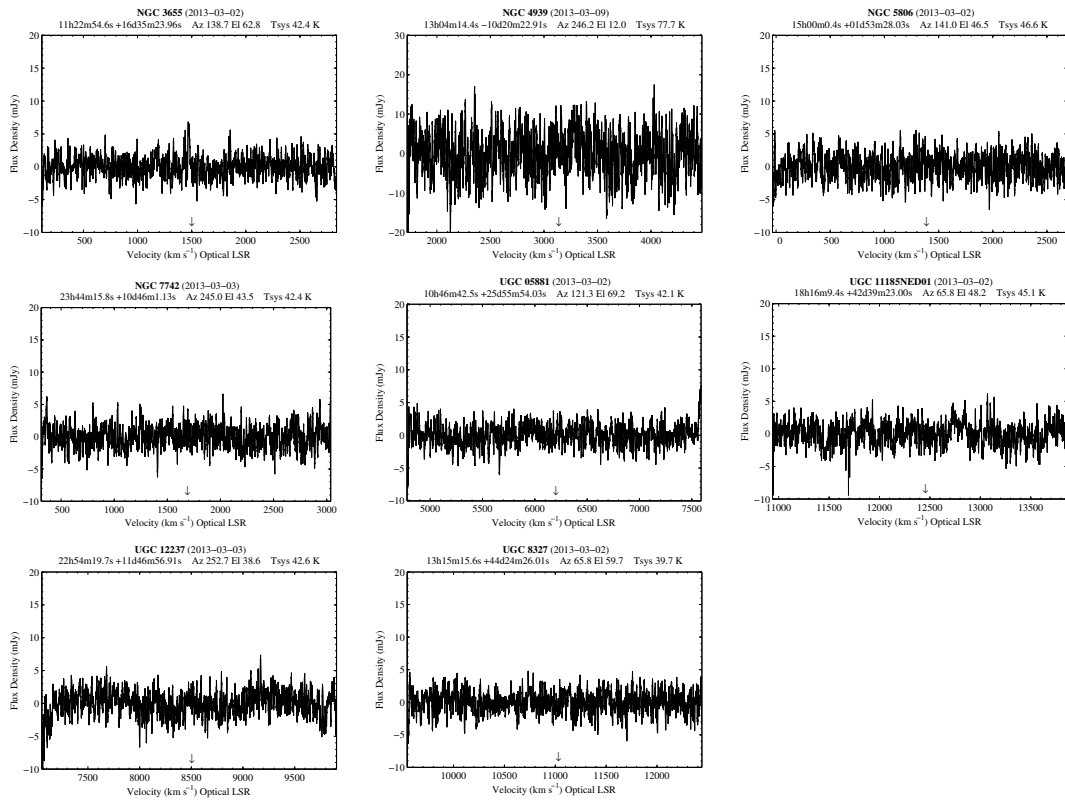




### A.3 Spectra of the Water Maser Non-Detections

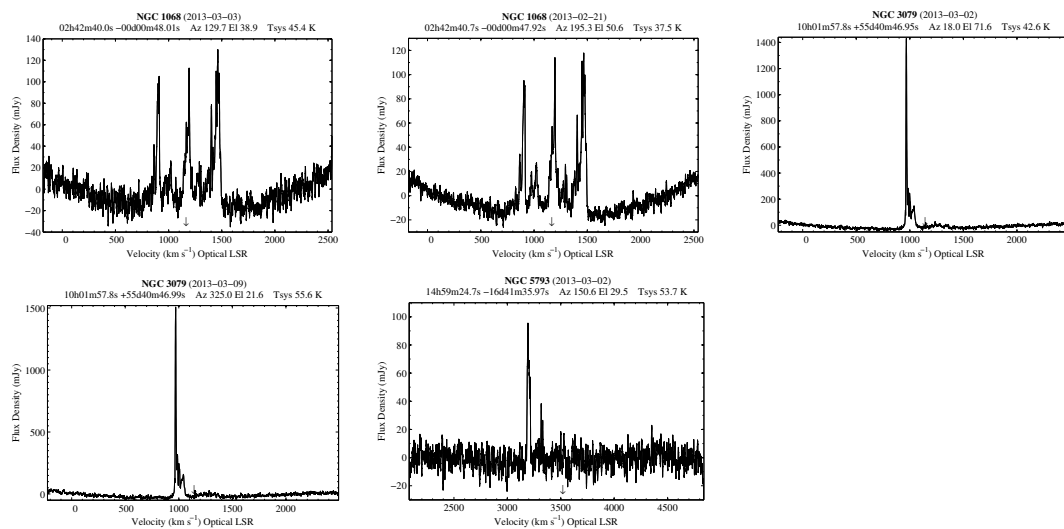


### A.3 Spectra of the Water Maser Non-Detections



### A.3 Spectra of the Water Maser Non-Detections

**Fig. A.3.2:** The spectra of three known 22 GHz water megamaser galaxies that were observed during the water maser survey to verify the GBT spectrometer setup.



## A.4 Geometric Models for the Maser Distribution

This Appendix contains details on the geometric models, special relativistic corrections, and cosmology used in the analysis of UGC 3193 (§ 6) and IC 2560 (§ 7) maser data.

Water megamasers have been detected in the active galactic nucleus (AGN) in galaxies such as NGC 4258 (e.g., Watson & Wallin 1994). The maser emission traces the geometry and kinematics of the circumnuclear accretion disk around the central supermassive black hole (SMBH).

Two observables are of interest to the Megamaser Cosmology Project (MCP)<sup>1</sup>: the maser positions against velocity, and the drift with time of the central velocity of each maser feature.

The former are measured by 22 GHz radio interferometric very long baseline interferometry (VLBI) observations with the Very Long Baseline Array (VLBA), the latter are determined through single-dish monitoring with the Robert C. Byrd Green Bank Telescope (GBT). The rotation curve of the accretion disk is related to the measured VLBI angular offsets from the central SMBH of the high velocity maser features. The orbital accelerations, on the other hand, of the low velocity line of sight (LOS) maser features near the recessional velocity of the galaxy are derived from a time series of GBT spectra. The spectra are taken at intervals of a few weeks or months. The acceleration fit was described earlier in § 6.3 on page 107. The VLBI data reduction steps were outlined in § 6.6 on page 113 and references therein.

There is abundant evidence that the observed maser positions and the maser kinematics (the rotation curve and maser accelerations) in disk maser galaxies can be described by a thin, near-Keplerian accretion disk that has a typically sub-parsec size and that is associated with the circumnuclear accretion disk around the SMBH within in the AGN (Herrnstein et al. 1996; Braatz et al. 2010; Kuo et al. 2011; Humphreys et al. 2013). The spectral line velocities of these “disk masers” are assumed to be projected orbital speeds in the disk, rather than pattern velocities due to e.g. spiral density waves (Maoz 1995; also see the investigation in Humphreys et al. 2008). The assumption, orbital rather than pattern velocities, appears to hold at least for the currently most-studied disk maser galaxy, NGC 4258 ( $z=0.001494$ ; de Vaucouleurs et al. 1991). There is relatively good consistency between its maser proper motion distance of  $7.2 \pm 0.5$  Mpc (Herrnstein et al. 1999), its recent Cepheid luminosity distances, e.g.,  $7.17^{+0.14}_{-0.10}$  Mpc (di Benedetto 2008), and its most recent and highest-precision disk maser distance of  $7.60 \pm 0.23$  Mpc based on 18 VLBI observations (Humphreys et al. 2013).

A Keplerian model fit to the maser data can yield the angular diameter distance, central

---

<sup>1</sup>For the project, maser galaxies, and references to publications, see the project web site at <https://safe.nrao.edu/wiki/bin/view/Main/MegamaserCosmologyProject>

## A.4 Geometric Models for the Maser Distribution

---

mass, and Hubble constant. The linear size of the Keplerian (thin) rotating accretion disk,  $s$ , is constrained by the measured angular positions, maser spectral feature central velocities (projected orbital speeds) and their drift with time (projected centripetal accelerations). Combined with the observed angular size,  $\Theta$ , of the maser distribution, we can infer both the central mass,  $M_{\text{BH}}$ , and the angular diameter distance of the galaxy, defined as

$$D_{\text{A}} \equiv s/\Theta \tag{A.1}$$

The Hubble constant  $H_0$ , or  $H^2 \equiv (\dot{a}/a)^2$  with the scale factor  $a$ , at the present time,  $t = 0$ , is given by  $D_{\text{A}}$  and the optical redshift of the galaxy (Eqs. A.4 and A.5 below).

Increasingly more complex models with fewer assumptions, but more parameters, were fit to the maser data. Models included (near-)Keplerian models and a Plummer cluster toy model. The reason for fitting a Plummer model was stated in § 6.8, see page 6.8, and relates to a discussion in Maoz et al. (1995) who note that the nuclei of some LINER galaxies may be spherically symmetric dense clusters instead of SMBHs. The Plummer toy model is a macroscopic description that hides details of the internal dynamics of a cluster (Dejonghe 1987), and the best-fit model and cluster lifetime arguments detailed in Maoz (1998) may be used to determine if a cluster is a viable alternative to a SMBH for the maser galaxy in question (see also Kuo et al. 2011). While the “elongated”, disk-like distribution of masers in the VLBI maps of “disk maser” galaxies provides some evidence against a spherical cluster, we nevertheless follow the MCP paper by Kuo et al. (2011) and fit the Plummer model into the maser rotation curve.

The fitted models account for the dominant general relativistic (GR) effects (FRW  $d\tau^2 = dt^2 - a(t)^2 dx^2$  metric) and special relativistic (SR) effects ( $d\tau^2 = dt^2 - dx^2$  metric). These effects red-shift the wavelength of a maser in a slowly rotating disk, with the maser located at the shallow end of the SMBH potential (at  $\gg 10^3$  gravitational radii) in a nearby host galaxy ( $\lesssim 200$  Mpc) in practically flat space. The host galaxy is receding in this space due to cosmological expansion and may have a small additional peculiar velocity relative to a “global” reference frame. For the purposes here, the cosmic microwave background (CMB) is a very good approximation of a “global” reference frame. The above effects that stretch the maser wavelength at emission in the AGN to the eventually observed wavelength at time of detection on Earth are, namely, the SR Doppler shift, GR gravitational redshift, and GR cosmological redshift.

Details on the Keplerian and Plummer models are provided below.

### A.4.1 Keplerian Disk Model

A thin Keplerian disk with a radial warp in the PA, and a radial warp in the inclination,  $i$ , can be described with the following parameter set adopted from Reid et al. (2013),

$$\beta = (M_{\text{BH}}, x_0, y_0, H_0, V_0, V_{\text{pec,r}}, i, \partial i / \partial r, \partial^2 i / \partial r^2, \alpha, \partial \alpha / \partial r, \partial^2 \alpha / \partial r^2, e, \omega, \partial \omega / \partial r) \quad (\text{A.2})$$

Parameters include the SMBH mass,  $M_{\text{BH}}$ , the SMBH position,  $(x_0, y_0)$ , the Hubble constant,  $H_0$ , the pure Hubble expansion velocity of the galaxy,  $V_0$ , and the radial line of sight (LOS) component of its peculiar velocity,  $V_{\text{pec,r}}$ , the disk inclination angle,  $i$ , and its radial warp, the disk position angle (PA or  $\alpha$ ), the maser orbit eccentricity,  $e$ , and the periapsis of the orbit,  $\omega$ , and its radial drift. The recessional velocity  $V_{\text{CMB}} = \dot{a}\chi + a\dot{\chi} = V_0 + V_{\text{pec,r}}$  is in the CMB frame, and  $\chi$  is in the co-moving coordinate frame, whereas  $a$  is the scale factor. For simplicity, the  $\lesssim 600 \text{ km s}^{-1}$  offset of the LSR frame relative to the CMB frame can be considered as lumped into  $V_{\text{pec,r}}$ . In addition, patterns like spiral density waves (e.g., Maoz 1995; § 2.1 in Maoz & McKee 1998; and also see Maoz & McKee 1998; Humphreys et al. 2008) can be absorbed by, for example, fitting a non-zero orbit eccentricity,  $e$ , with a radially changing orbit periapsis,  $\omega$ .

The variables of the Keplerian model are the detected maser features,  $(x, y, v, a)$ , and the VLBI and GBT observations provide these data and their uncertainties, given by

$$\mathbf{MK} = \{(x_i \pm \sigma_{x_i}, y_i \pm \sigma_{y_i}, v_i \pm \sigma_{v_i}, a_i \pm \sigma_{a_i}) : i = 1, \dots, N\} \quad (\text{A.3})$$

where  $x_i, y_i$  are the measured maser position,  $v_i$  are the central velocities, and  $a_i$  are the drifts in central velocity of each of the  $N$  maser features, each with their respective  $1\sigma$  uncertainties.

The angular diameter distance of the galaxy,  $D_A$ , is implicitly contained in the model parameters. For nearby objects the angular diameter distance is

$$D_A \simeq cz/H_0 = V_0/H_0 \quad (\text{A.4})$$

where the pure Hubble velocity of the galaxy,  $V_0$ , is in the optical velocity definition. The above is a good approximation for  $z \lesssim 0.3$  without requiring the GR velocity-redshift relation (Davis & Lineweaver 2004). At  $z = 0.01$  the above distance is about 0.5 Mpc larger than the GR distance properly given by the  $\Lambda$ CDM cosmology (Hogg 1999; Weinberg et al. 2013),

$$D_A = \frac{c/H_0}{1+z} \int_0^z \frac{1}{\sqrt{\Omega_m(1+z')^3 + \Omega_\Lambda}} dz' \quad (\text{A.5})$$

Note that the redshift,  $z$ , is the pure GR cosmological redshift and does not contain a SR redshift contamination due to the radial peculiar velocity of the galaxy,  $V_{\text{pec,r}}$ .

The rotation curve of the accretion disk is traced by the maser impact parameters,  $b_i$ , shown against maser velocities,  $v_i$ , in the position–velocity (P–V) diagram. The position angle (PA or  $\alpha$ ) of the disk is needed to determine the maser impact parameters along the disk. The PA is a free parameter of the full disk model. However, initially the PA may be estimated by a standard generalized total least squares (GTLS) linear fit that allows for uncertainties in all parameters, cf. York et al. (2004). The PA is given by the best linear fit through the maser VLBI angular position data, a subset of **MK**,

$$\mathbf{M} = \{(x_i \pm \sigma_{x_i}, y_i \pm \sigma_{y_i}) : i = 1, \dots, N\} \quad (\text{A.6})$$

where  $x_i, y_i$  are the measured positions, and  $\sigma_{x_i}, \sigma_{y_i}$  are the respective measurement uncertainties. The impact parameters are defined as the coordinate along the axis or linear fit through **M** (“along the PA”), and are given by  $b_i = x'_i$  in the set  $\mathbf{M}' = \mathbf{R}(-\alpha)\mathbf{M}$  counter-rotated by the PA, where **R** is simply the rotation matrix.

A first straightforward estimate of the angular diameter distance is provided by the approach described in, e.g., § 4 of Braatz et al. (2010). It assumes the systemic masers occupy a narrow ring at near-identical radii,  $r_i$ , in a fully edge-on and warp-free Keplerian disk. The disk must be spatially well-sampled by several strong HV features located along the disk midline. The measured accelerations,  $a_i$ , of the low velocity systemic LOS features are related to the maser orbit radius,  $r_i \propto a_i^{-0.5}$ . The systemic maser accelerations can be combined with the velocity gradient of the systemic maser features,  $\Omega \simeq \partial v / \partial b$ , and the Keplerian parameter,  $k$ , of the rotation curve  $b_i = b_0 + k^2 / (v_i - V_0)^2$  (where  $V_0$  is the systemic recession velocity), to yield

$$D_A = a^{-1} k^{2/3} \Omega^{4/3} \quad (\text{A.7})$$

with a fractional uncertainty of (Braatz et al. 2010)

$$\sigma_{D_A} \simeq D_A \sqrt{\left(\frac{\sigma_a}{a}\right)^2 + \left(\frac{2}{3} \frac{\sigma_k}{k}\right)^2 + \left(\frac{4}{3} \frac{\sigma_\Omega}{\Omega}\right)^2} \quad (\text{A.8})$$

The velocity gradient  $\Omega$  is given by a linear fit (e.g., GTLS) through the systemic features in the P–V diagram. Because the angular distribution of systemic masers is smaller than the VLBA beam size for galaxies at  $> 10$  Mpc, the precision of  $\Omega$  rapidly decreases with distance.

The Keplerian model with the full set of parameters (Eq. A.2) yields a more accurate distance. The model positions for the disk masers in a flat 2-D disk embedded in a volume of space

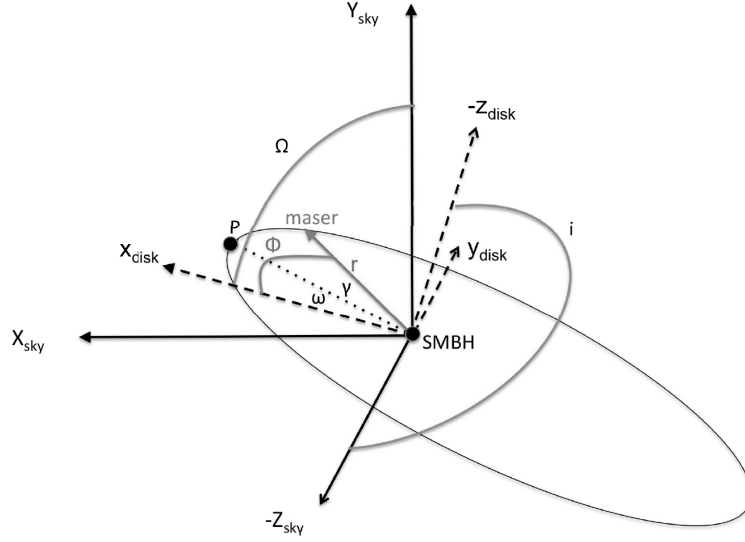


**Fig. A.4.1:** Coordinates of a single maser orbit in the Keplerian disk model. The maser radius,  $r$ , and azimuth,  $\Phi$ , ( $\phi$  in this Appendix), are in polar coordinates. The orbit periapsis angle,  $\omega$ , is towards the periapsis point marked by P. The in-disk coordinates,  $(x, y, z = 0)_{\text{disk}}$ , are centered on the SMBH. The in-sky projection for the maser orbit inclination and disk/orbit position angles, here  $i$  and  $\Omega$  (in this Appendix,  $i$  and  $\alpha$ ), respectively, and their radial warps, result in a predicted position in the plane of the sky of  $(X, Y)_{\text{sky}}$ . The inclination is the angle between  $z_{\text{disk}}$  and  $Z_{\text{sky}}$ . Figure adopted from Humphreys et al. (2013).

are

$$\mathbf{m} = \{(\phi_i, r_i) : i = 1, \dots, N\} \quad (\text{A.9})$$

with azimuth angles,  $\phi_i$ , and milli-arcsecond radii,  $r_i$ . The azimuth angles follow a convention where  $\phi_i \approx 90^\circ$  for the LOS systemic masers, and  $\phi_i \approx 90 \pm 90^\circ$  in the sense of disk rotation for the HV masers. The maser positions are rotated by the disk inclination,  $i$ , and the disk position angle,  $\alpha$ , and their respective radial warps into the natural observer coordinate system in which the 3<sup>rd</sup> coordinate is along the LOS and the other two coordinates are in the plane of the sky. This is a  $\mathbb{R}^3 \mapsto \mathbb{R}^3$  map that is given simply by the Euler rotation angles  $(0^\circ, i_i, \alpha_i)$  where

$$i_i = i + r_i (\partial i / \partial r) + r_i^2 (\partial^2 i / \partial r^2) \quad (\text{A.10})$$

$$\alpha_i = \alpha + r_i (\partial \alpha / \partial r) + r_i^2 (\partial^2 \alpha / \partial r^2) \quad (\text{A.11})$$

The final model positions project out the third coordinate and add the SMBH position  $(x_0, y_0)$ , yielding the in-sky maser distribution,  $\hat{\mathbf{M}} = \{(x_i, y_i) : i = 1, \dots, N\}$ , that depends only on the model parameters  $\hat{\beta}$  and the in-disk positions  $\hat{\mathbf{m}}$ . For a schematic illustration of the coordinates see, e.g., Appendix A in Humphreys et al. (2013), reproduced here in Fig. A.4.1.



## A.4 Geometric Models for the Maser Distribution

The optimal positions  $\hat{\mathbf{m}}$  and model parameters  $\hat{\beta}$  are those that minimize the post-fit residual,  $\|\hat{\mathbf{M}} - \mathbf{M}\|$ , for an observation  $\mathbf{M}$ . The measured maser velocities and accelerations,

$$\mathbf{K} = \{(v_i, a_i) : i = 1, \dots, N\} \quad (\text{A.12})$$

can be used to constrain the model, too. This entails minimizing the post-fit residuals  $\|\hat{\mathbf{K}} - \mathbf{K}\|$  and  $\|\hat{\mathbf{M}} - \mathbf{M}\|$ .

The velocities and accelerations for (near-)Keplerian maser orbits are

$$v_{c,i} = \frac{\sqrt{GM_{\text{BH}}}}{R_i^\gamma} \quad \text{and} \quad a_{c,i} = \frac{v_{c,i}^2}{R_i} \quad (\text{A.13})$$

When seen along the LOS by an observer on Earth, after projection effects, they become

$$v_i = v_{c,i} \cdot \cos \phi_i \sin i_i + V_0 + V_{\text{pec,r}} + \frac{GM_{\text{BH}}}{cR_i} \quad (\text{A.14})$$

$$a_i = a_{c,i} \cdot \sin \phi_i \sin i_i \quad (\text{A.15})$$

For Keplerian orbits,  $\gamma = 0.5$ . The distance  $D_A$  and the model angular radii,  $r_i$ , set the linear-scale radii of the maser orbits,  $R_i = D_A r_i$ . The last term is the GR gravitational redshift.

The in-disk maser azimuth angles may be obtained by dividing Eq. A.15 by the fourth power of the third term in Eq. A.14 (e.g., Bragg et al. 2000),

$$\frac{\sin \phi_i}{\cos^4 \phi_i} = \frac{a_i}{v_i^4} GM_{\text{BH}} \quad (\text{A.16})$$

The last term in Eq. A.14 is the GR gravitational redshift. For SMBH masses below  $2 \times 10^7 M_\odot$  and orbit radii  $R_i$  greater than 5000 AU, as typical of disk maser galaxies, the gravitational redshift is less than  $15 \text{ km s}^{-1}$ . Additional relativistic corrections are applied to Eq. A.14, not directly shown. For disk masers, typically  $v_{c,i} \leq 0.003c$  and the velocities are not relativistic. To maintain accuracy, however, velocities local to the SMBH are propagated to the observed final redshift (or, “optical” redshift velocity,  $v_i$ ) by a series of SR Doppler shifts of the 22.23508 GHz water maser rest frequency,  $\nu_0$ , with frame boosts that transport the reference frame from the maser orbit, the disk kinematic center, and the receding host galaxy to the LSR frame of the observer.

For a detailed description of data and models refer also to Watson & Wallin (1994), Bragg et al. (2000), Kuo et al. (2011) and Reid et al. (2013).

### A.4.2 The Relation between $H_0$ and Dark Energy Models

As mentioned in the Chapter on IC 2560, the expansion of the Universe appears to be accelerating. This requires a new form of negative energy, termed Dark Energy. The evolution of an expanding homogenous and isotropic Universe filled with a perfect fluid is described by the Friedmann-Lemaître-Robertson-Walker (FLRW) metric and the two Friedmann equations for energy-momentum conservation,

$$\left(\frac{\dot{a}}{a}\right)^2 = \frac{8\pi G}{3}\rho - \frac{k}{a^2} \quad (\text{A.17})$$

$$\frac{\ddot{a}}{a} = -\frac{4\pi G}{3}(\rho + 3P) = \frac{4\pi G}{3}(1 + 3w)\rho \quad (\text{A.18})$$

where the scale factor that determines the “stretching” of space is defined as  $a \equiv (1 + z)^{-1}$ . The Hubble parameter is  $H(z) \equiv \dot{a}/a$  and  $k$  is the spatial curvature of either -1, 0, or +1. The pressure and energy density of the perfect fluid are  $P$  and  $\rho$ , respectively. The equation of state parameter  $w$  of the perfect fluid is the ratio of the latter, defined as  $w \equiv P/\rho$  (e.g., Bamba et al. 2012).

For ordinary non-relativistic matter  $w$  equals  $w \approx 0$ , whereas for radiation  $w = 1/3$ . Both result in a decelerating Universe that may initially expand but eventually either coasts along indefinitely or collapses in a Big Crunch. For Eq. A.18 to produce the accelerating Universe observed today, a value of  $w < -1/3$  is required. The cosmological constant  $\Lambda$  added by Einstein to his field equations corresponds to  $w = -1$  and is currently the most favored candidate description of Dark Energy. However, more generic forms of  $w = w(z)$  that are time (or redshift) dependent are also possible under the many different cosmological theories (Bamba et al. 2012).

The current standard cosmic expansion model, flat  $\Lambda$ CDM with zero spatial curvature,  $k = 0$ , contains a fixed cosmological constant and hence has  $w = -1$ .

It is instructive to write the FLRW equations in the form (e.g., Weinberg et al. 2013)

$$\frac{H^2(z)}{H_0^2} = \Omega_m a^{-3} + \Omega_r a^{-4} + \Omega_k a^{-2} + \Omega_\phi \frac{u_\phi(z)}{u_\phi(0)} \quad (\text{A.19})$$

where the Hubble constant is  $H_0 = H(z \equiv 0)$ , and  $\Omega_m, \Omega_r, \Omega_k$  are the present day (i.e. at  $z=0$ ) energy density parameters of matter, radiation, curvature, respectively, and  $\Omega_\phi$  is a generic Dark Energy -like energy density. The curvature energy density is  $\Omega_k = 1 - \Omega_m - \Omega_r - \Omega_\phi$  and in a spatially flat universe it is  $\Omega_k \equiv 0$ . The critical energy density required for flat space, such that

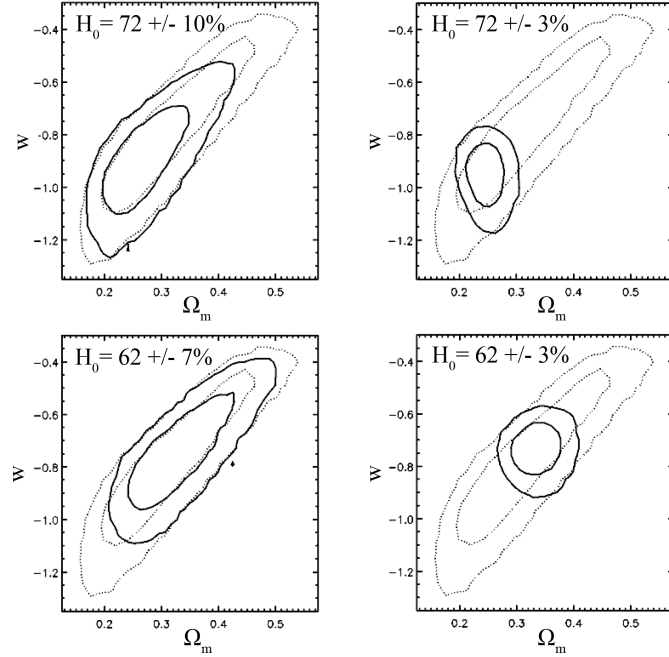


**Fig. A.4.2:** The improvement in constraints on the Dark Energy EoS parameter  $w$  via more accurate  $H_0$  data. The WMAP-7 likelihood contours for the DE equation of state parameter,  $w$ , are shown against the density parameter of matter,  $\Omega_m$ , for two different values and uncertainties of  $H_0$ . The dotted lines represent the “wCDM + no perturbations” model of Spregel et al. (2007). The solid lines show the improvement in terms of a better-constrained  $w$  for a more accurate  $H_0$ . Figure adopted from Braatz et al. (2009).

$k = 0$  when  $\Lambda = 0$ , is given by (e.g., Weinberg et al. 2013)

$$\rho_{\text{crit}} = \frac{3H_0^2}{8\pi G} \quad (\text{A.20})$$

Each of the density parameters  $\Omega_m, \Omega_r$ , and  $\Omega_k$  above is expressed as a ratio of the respective energy density  $u_i$  and the critical density  $\rho_{\text{crit}}$ , i.e.,  $\Omega_i = u_i/c^2\rho_{\text{crit}}$  of the  $i$ th component.

Observations of the cosmic microwave background anisotropies have determined relative density parameters (see, e.g., Hinshaw et al. 2013), such as  $\Omega_m h^2$  where  $h = H_0/100 \text{ km s}^{-1} \text{ Mpc}^{-1}$ . Local  $H_0$  measurements with disk maser galaxies and other methods thus allow to fix  $\Omega_m$ . Notably, the parameters  $H_0$  and  $\Omega_m h^2$  are the only free Dark Energy parameters under  $\Lambda$ CDM. For example, Mortonson et al. (2010) find that  $H_0$  measured to  $\lesssim 2\%$  can provide a sharp practical test to falsify  $\Lambda$ CDM.

If  $\Lambda$ CDM is falsified through precise local measurements of  $H_0$  to  $\lesssim 2\%$  this would indicate

that  $w(z) \neq -1$ . In this case other more complex models of Dark Energy become viable such as, for example, Phantom Energy ( $w < -1$ ). The improved accuracy of  $w$  through a similar improvement in  $H_0$  is also illustrated in Fig. A.4.2, adopted here from the MCP project White Paper (cf. Braatz et al. 2009). A hypothetical measurement of  $72 \text{ km s}^{-1} \text{ Mpc}^{-1}$  to 3 % would, for example, eliminate several competing quintessence models (Bamba et al. 2012) of a variable  $w$  of  $-1 < w < -1/3$ .

The key goal of the MCP project is thus the accurate measurement of  $H_0$  based on distances to individual galaxies to an accuracy of 3 %. The MCP data provide essential tests for the cosmological models (e.g.,  $\Lambda$ CDM) and the Dark Energy candidates (e.g., the cosmological constant), and are based on independent and straightforward methods (Braatz et al. 2009).

### A.4.3 Plummer Cluster Model

In several disk maser galaxies the central mass and density given by the observed rotation curves are typical of massive black holes (Kuo et al. 2011). To rule out astrophysical alternatives to massive black holes, e.g., dense dark clusters of non-luminous gravitating objects, one can fit a general Plummer cluster toy model and use collision and evaporation time scale arguments to support or rule out the cluster hypothesis (Maoz 1998; Kuo et al. 2011). This assumes that the masers are located inside the cluster, rather than in the accretion disk of a SMBH/disk system, and trace the kinematics of the cluster. The Plummer toy model (Plummer 1915; Dejonghe 1987; Binney & Tremaine 2008) is given by

$$v_{p,i} = \left[ \frac{GM_\infty R_i^2}{(r_c^2 + R_i^2)^{3/2}} \right]^{1/2} \quad (\text{A.21})$$

$$v_i = v_{p,i} + V_0 + V_{\text{pec},i} + \frac{GM_\infty}{cR_i} \quad (\text{A.22})$$

for cluster radius,  $r_c$ , and total mass of the cluster,  $M_\infty$ . The linear-scale radius of the maser orbit is given as before by the galaxy distance, and is  $R_i = D_A r_i$ . The cluster volume density is

$$\rho_c = \frac{3}{4\pi} \frac{M_\infty}{[M_\odot]} \left( \frac{r_c}{[\text{pc}]} \right)^{-3} \quad (\text{A.23})$$

The upper limit on the mass of stellar constituents,  $\hat{m}_*$ , can be constrained by requiring that the cluster persists over the approximate age of the host galaxy,  $T_{\text{age}} \approx 10 \text{ Gyr}$ . The cluster persists if it has an evaporation time scale that is significantly longer than  $T_{\text{age}}$ . For shorter time scales Ishihara et al. (2001) and Kuo et al. (2011) argue (for several disk maser galaxies) that a SMBH is more likely to be observed than a cluster.

However, it is still debated whether the galaxy or the central object form first, and the early

## A.4 Geometric Models for the Maser Distribution

growth stages of SMBHs are not yet firmly established (for a review, see Djorgovski et al. 2008). Alonso-Herrero et al. (2013) suggest that the bulk of the central mass growth may start at a later stage, after a star-forming galaxy phase, around a slow transition to an AGN phase where the nucleus becomes increasingly clearly identified as a Seyfert, and there is only moderate star formation in the host galaxy. This could allow recently formed clusters to be detected (as in fact Ishihara et al. 2001 do point out), and the cluster could indeed form quite recently at the onset of a Seyfert stage, even when the cluster evaporation time scale is much shorter than the  $T_{\text{age}}$  of the host galaxy. Thus evidence against a cluster based on timescale arguments might be considered tentative.

Assuming the cluster persists, the upper limit on the mass  $\hat{m}_\star$  (e.g., Binney & Tremaine 2008; Kuo et al. 2011) can be solved numerically from

$$\hat{m}_\star = \frac{(1.305 r_c / [0.01 \text{ pc}])^{3/2}}{\ln(0.1 M_\infty / \hat{m}_\star)} \cdot \sqrt{\frac{M_\infty}{[10^8 M_\odot]}} \quad (\text{A.24})$$

where  $1.305 r_c$  is the approximate radius of half total mass. Likewise, the collision time scale, or the time scale of significant evolution in the stellar mass function that in turn leads to faster evaporation, must be longer than  $T_{\text{age}}$ . The time scale is

$$t_{\text{coll}} = \left[ 16 \sqrt{\pi} \frac{\rho_c}{\hat{m}_\star} \sigma_\star r_\star^2 \cdot \left( 1 + \frac{G \hat{m}_\star}{2 \sigma_\star^2 r_\star} \right) \right]^{-1} \quad (\text{A.25})$$

for the cluster central density,  $\rho_c$  (Eq. A.23), the stellar radius,  $r_\star$ , and stellar rms velocity dispersion,  $\sigma_\star$  (Binney & Tremaine 2008).

The stellar radius  $r_\star$  depends on the type of star and the mass of the star (e.g., Shapiro & Teukolsky 1983). For example, the relation of mass to radius for neutron stars with  $1.4 M_\odot \lesssim m_\star \lesssim 3 M_\odot$  is given by (Shapiro & Teukolsky 1983)

$$m_\star = (r_\star / 15.12 \text{ km})^{-3} M_\odot \quad (\text{A.26})$$

and for white dwarfs with  $0 M_\odot \lesssim m_\star \lesssim 1.4 M_\odot$  is given by

$$m_\star = 0.7011 \left( r_\star / [10^4 \text{ km}] \right)^{-3} (\mu_e / 2)^{-5} M_\odot \quad (\text{A.27})$$

with the mean molecular weight of the electron,  $\mu_e$ , of about 1.18 for a solar composition. For brown dwarfs with  $0 M_\odot \lesssim m_\star \lesssim 0.075 M_\odot$  the relation is

$$r_\star = 2.2 \times 10^4 \left( \frac{m_\star}{[M_\odot]} \right)^{-1/3} \left( 1 + \sqrt{\frac{[0.0032 M_\odot]}{m_\star}} \right)^{-4/3} \text{ km} \quad (\text{A.28})$$

Lastly,  $t_{\text{coll}}$  of Eq. A.25 also depends on the stellar rms velocity dispersion in the cluster. If the cluster is assumed to extend into the galactic bulge, then optical observations can provide the stellar velocity dispersion  $\sigma_{\star}$  in the cluster. On the other hand, based on the Plummer model hypothesis, masers are tracing the actual cluster kinematics. Thus the stellar velocity dispersion in the cluster can also be approximated by the standard deviation of the maser velocities. If the Plummer cluster lifetime for all the above stellar constituents (and others, e.g., main sequence stars and red dwarfs) is shorter than that of the host galaxy, i.e. when  $t_{\text{coll}} < T_{\text{age}}$ , a cluster is tentatively ruled out as a BH/SMBH alternative to the dense nuclear mass, keeping in mind however the caveats mentioned earlier.

### A.4.4 Relativistic Corrections

Relativistic corrections are applied in the models to derive the observed red-shifted wavelength from the emitted wavelength that H<sub>2</sub>O maser rest frequency,  $\nu_0$ , of 22.23508 GHz.

The equations for the Keplerian and Plummer models (Eqs. A.14 and A.22) shown earlier include the GR gravitational redshift ( $v_{\text{grav}} = c z_{\text{grav}} = GM_{\text{BH}}/cR_i$ ) for photons escaping the potential well of the SMBH. Regarding other redshifts, the observed radial recessional velocity of the host galaxy has two constituents,

$$V_{\text{rec}} = \dot{a}\chi + a\dot{\chi} = V_0 + V_{\text{pec,r}} = cz_{\text{rec}} \quad (\text{A.29})$$

where, as before,  $a$  is the cosmological scale factor and the radial LOS coordinate  $\chi$  of the maser galaxy is in the coordinate frame co-moving with the cosmological expansion. The factor  $\dot{a}$  is due to cosmological expansion (GR) and  $\dot{\chi}$  is due to the peculiar velocity of the galaxy (SR).

The models propagate the former term, i.e. the GR cosmological redshift, into the overall redshift of the maser emission. The GR redshift reflects the pure Hubble/cosmological redshift of the maser galaxy, and as usual, the associated optical “velocity”,  $V_0 = cz$ , due to the GR cosmological redshift can be superluminal (Davis & Lineweaver 2004). Thus unlike in the disk maser model of Humphreys et al. (2013), no SR “correction” is applied to the GR redshift here. The redshift of nearby maser galaxies is  $z \ll 1$  and thus the error in Humphreys et al. (2013) for NGC 4258 (at  $z \approx 0.001$ ) is fortunately below 1 %.

Lastly, both Keplerian and Plummer models also propagate the SR Doppler redshifts (in SR the velocities do not exceed the speed of light). The SR redshifts are due to the LOS component of the maser orbital velocity (in the rest frame of the SMBH) and the peculiar velocity of the host galaxy (in the rest frame that is co-moving with the cosmological expansion). To simplify the model, the peculiar velocity of the host galaxy and the observer are lumped into the same velocity parameter. For the SR Doppler shift due to orbital velocity, the change in the observed

frequency is as usual given by

$$v/v_0 = \gamma^{-1} (1 + v_{\parallel}/c)^{-1} \quad \text{where } \gamma = 1/\sqrt{1 - v^2/c^2} \quad (\text{A.30})$$

where  $v_{\parallel}$  is the radial LOS component of the orbital velocity. The radial peculiar velocity of the host galaxy is propagated in an identical manner to the observed redshift.

## A.5 Water Megamaser Epochs on IC 2560

Table A.5.1. Single Dish and Interferometric Epochs on IC 2560

Date	Project	rms (mJy)	Date	Project	rms (mJy)
2003 Mar 06	AGBT02B-018-03	5.1	2006 May 22	AGBT06A-022-06	5.7
2003 Mar 30	AGBT02C-054-01	4.6	2006 Sep 09	AGBT06C-051-02	9.3
2003 Apr 01	AGBT01A-014-05	13.8	2006 Nov 10	AGBT06C-051-05	12.2
2003 Apr 27	AGBT02B-018-06	3.4	2006 Dec 15	AGBT06C-051-08	12.7
2003 May 06	AGBT01A-014-06	5.3	2007 Jan 09	AGBT06C-051-09	8.0
2003 Oct 25	AGBT02A-046-03	5.9	2007 Feb 05	AGBT06C-051-10	7.0
2003 Dec 18	AGBT02A-046-05	2.3	2007 Mar 08	AGBT06C-051-12	6.8
2004 Jan 14	AGBT03C-012-02	4.0	2007 Apr 03	AGBT06C-051-13	14.6
2004 Jan 29	AGBT02A-046-06	2.7	2007 Apr 11	AGBT06C-051-14/15	3.8
2004 Feb 28	AGBT02A-046-07	2.1	2010 Dec 24	AGBT10C-019-04	3.6
2004 Mar 20	AGBT02A-046-08	2.5	2011 Oct 08	AGBT10C-019-27	11.8
2004 Apr 28	AGBT02C-054-06	2.9	2011 Dec 05	AGBT10C-019-35	25.4
2004 May 24	AGBT02A-046-10	12.5	2012 Nov 05	AGBT12A-297-17	10.5
2004 Aug 29	AGBT02A-046-16	n/a	2013 Nov 24	AGBT13A-236-27	4.3
2004 Nov 14	AGBT02C-054-08	2.2	2013 Dec 24	AGBT13A-236-33	5.7
2005 Feb 03	AGBT04C-041-02	7.6			
2005 Oct 26	AGBT05C-051-04	10.1			
2006 Feb 12	AGBT06A-022-01	14.9			
2006 Mar 27	AGBT05C-022-04	4.8			
2006 Apr 19	AGBT05C-022-05	5.6	2007 Jan 24	BG169C HSA	



## A.6 Water Megamaser Positions in NGC 23, UGC 3193 and IC 2560

Table A.6.1. Positions of maser features in NGC 23.

ID	Velocity (km s <sup>-1</sup> )	X ± σ <sub>X</sub> (mas ± mas)	Y ± σ <sub>Y</sub> (mas ± mas)	Size (mas × mas)	SNR
1	4435.50	-0.029 ± 0.062	-0.109 ± 0.104	0.64 × 0.34	2.6
2	4439.00	-0.052 ± 0.039	-0.001 ± 0.066	0.70 × 0.36	4.5
3	4442.50	0.012 ± 0.028	0.009 ± 0.041	0.73 × 0.43	7.5
4	4446.00	-0.005 ± 0.016	0.008 ± 0.024	0.75 × 0.41	13.1
5	4449.50	-0.032 ± 0.016	-0.039 ± 0.023	0.72 × 0.40	13.2
6	4453.00	0.004 ± 0.016	-0.028 ± 0.025	0.73 × 0.41	12.4
7	4456.50	0.004 ± 0.018	0.004 ± 0.030	0.80 × 0.42	11.2
8	4460.00	0.004 ± 0.018	0.007 ± 0.029	0.77 × 0.41	11.3
9	4463.50	-0.007 ± 0.013	0.010 ± 0.023	0.74 × 0.39	13.7
10	4467.00	0.007 ± 0.015	0.028 ± 0.024	0.73 × 0.39	12.8
11	4470.50	0.031 ± 0.015	-0.001 ± 0.023	0.73 × 0.41	13.1
12	4474.00	0.014 ± 0.018	-0.030 ± 0.030	0.84 × 0.44	11.8
13	4477.50	0.018 ± 0.018	0.005 ± 0.031	0.85 × 0.41	11.4
14	4481.00	0.021 ± 0.017	0.004 ± 0.025	0.75 × 0.41	12.3
15	4484.50	0.042 ± 0.017	0.012 ± 0.026	0.75 × 0.41	12.2
16	4488.00	0.043 ± 0.016	0.020 ± 0.023	0.72 × 0.39	12.9
17	4491.50	-0.000 ± 0.015	-0.009 ± 0.023	0.72 × 0.34	12.6
18	4495.00	-0.020 ± 0.016	-0.022 ± 0.027	0.80 × 0.32	12.0
19	4498.50	0.012 ± 0.018	-0.039 ± 0.026	0.77 × 0.39	12.1
20	4502.00	0.014 ± 0.019	-0.032 ± 0.025	0.69 × 0.43	11.4
21	4505.50	-0.025 ± 0.018	-0.031 ± 0.028	0.71 × 0.42	10.9
22	4509.00	-0.019 ± 0.017	-0.011 ± 0.026	0.73 × 0.41	11.7
23	4512.50	0.013 ± 0.016	0.046 ± 0.025	0.73 × 0.39	12.2
24	4516.00	0.025 ± 0.014	0.042 ± 0.022	0.74 × 0.38	14.2
25	4519.50	0.014 ± 0.014	0.043 ± 0.024	0.73 × 0.36	12.8
26	4523.00	0.015 ± 0.018	0.043 ± 0.028	0.73 × 0.37	10.7
27	4526.50	0.025 ± 0.014	0.022 ± 0.021	0.70 × 0.37	14.0
28	4530.00	0.030 ± 0.013	0.030 ± 0.020	0.72 × 0.38	14.4
29	4533.50	0.032 ± 0.013	0.031 ± 0.021	0.77 × 0.37	15.3
30	4537.00	0.019 ± 0.013	0.000 ± 0.022	0.78 × 0.34	14.4

## A.6 Water Megamaser Positions in NGC 23, UGC 3193 and IC 2560

Table A.6.1 (cont'd)

ID	Velocity (km s <sup>-1</sup> )	X ± σ <sub>X</sub> (mas ± mas)	Y ± σ <sub>Y</sub> (mas ± mas)	Size (mas × mas)	SNR
31	4540.50	0.018 ± 0.014	0.001 ± 0.027	0.79 × 0.36	12.4
32	4544.00	-0.020 ± 0.014	0.023 ± 0.027	0.81 × 0.37	12.6
33	4547.50	-0.027 ± 0.013	0.017 ± 0.021	0.73 × 0.37	14.1
34	4551.00	-0.000 ± 0.014	0.017 ± 0.020	0.69 × 0.39	14.2
35	4554.50	-0.002 ± 0.014	0.007 ± 0.020	0.69 × 0.38	14.5
36	4558.00	0.010 ± 0.013	-0.000 ± 0.019	0.70 × 0.36	14.8
37	4561.50	0.017 ± 0.015	0.022 ± 0.024	0.76 × 0.36	13.0
38	4565.00	-0.002 ± 0.016	0.004 ± 0.024	0.77 × 0.38	12.9
39	4568.50	-0.002 ± 0.016	-0.042 ± 0.025	0.76 × 0.36	12.4
40	4572.00	-0.009 ± 0.013	-0.013 ± 0.024	0.81 × 0.33	13.8
41	4575.50	-0.013 ± 0.012	0.001 ± 0.021	0.78 × 0.35	15.1
42	4579.00	-0.014 ± 0.013	-0.009 ± 0.019	0.70 × 0.40	15.3
43	4582.50	-0.033 ± 0.013	-0.002 ± 0.021	0.73 × 0.40	14.9
44	4586.00	-0.018 ± 0.015	-0.001 ± 0.023	0.78 × 0.38	13.9
45	4589.50	0.003 ± 0.015	0.028 ± 0.023	0.76 × 0.39	13.7
46	4593.00	-0.001 ± 0.016	0.037 ± 0.024	0.74 × 0.41	12.8
47	4596.50	0.010 ± 0.015	-0.014 ± 0.025	0.73 × 0.40	12.5
48	4600.00	-0.006 ± 0.015	-0.010 ± 0.027	0.79 × 0.39	12.4
49	4603.50	-0.022 ± 0.018	-0.026 ± 0.031	0.85 × 0.38	11.3
50	4607.00	-0.024 ± 0.022	-0.062 ± 0.034	0.79 × 0.42	9.5
51	4610.50	-0.076 ± 0.056	0.007 ± 0.062	0.67 × 0.46	4.4

Note. — The positions of water maser spots in NGC 23 (VLBI track BG187A) and their 1σ position uncertainties. Velocities are kinematic LSR velocities in the optical definition.

## A.6 Water Megamaser Positions in NGC 23, UGC 3193 and IC 2560

Table A.6.2. Positions of maser features in UGC 3193.

ID	Velocity (km s <sup>-1</sup> )	X ± σ <sub>X</sub> (mas ± mas)	Y ± σ <sub>Y</sub> (mas ± mas)	Size (mas × mas)	SNR
1	4241.56	1.575 ± 0.009	-1.926 ± 0.034	1.75 × 0.42	21.4
2	4243.29	1.564 ± 0.006	-1.921 ± 0.024	1.80 × 0.41	31.8
3	4245.02	1.577 ± 0.007	-1.950 ± 0.027	1.86 × 0.41	28.9
4	4246.76	1.564 ± 0.009	-1.950 ± 0.034	1.81 × 0.40	22.7
5	4349.08	2.570 ± 0.072	-4.009 ± 0.168	2.51 × 0.60	6.0
6	4350.81	2.789 ± 0.026	-4.624 ± 0.072	2.09 × 0.56	12.0
7	4352.55	2.913 ± 0.007	-4.936 ± 0.023	1.81 × 0.47	33.0
8	4354.28	2.936 ± 0.004	-4.889 ± 0.015	1.78 × 0.46	48.6
9	4356.02	2.950 ± 0.003	-4.850 ± 0.010	1.73 × 0.47	69.8
10	4357.75	2.946 ± 0.002	-5.034 ± 0.009	1.82 × 0.45	89.5
11	4359.49	2.943 ± 0.002	-5.048 ± 0.007	1.79 × 0.43	102.3
12	4361.22	2.947 ± 0.002	-4.970 ± 0.007	1.71 × 0.42	102.0
13	4362.96	2.945 ± 0.002	-4.995 ± 0.007	1.68 × 0.42	99.0
14	4364.69	2.937 ± 0.002	-4.982 ± 0.007	1.67 × 0.42	108.3
15	4366.43	2.243 ± 0.021	-3.033 ± 0.068	1.53 × 0.42	9.4
16	4366.43	2.931 ± 0.002	-4.977 ± 0.007	1.66 × 0.41	98.8
17	4368.16	2.272 ± 0.016	-3.073 ± 0.057	1.63 × 0.45	12.1
18	4368.16	2.926 ± 0.003	-4.983 ± 0.010	1.66 × 0.41	69.7
19	4369.90	2.920 ± 0.007	-5.005 ± 0.026	1.64 × 0.43	28.5
20	4369.90	2.320 ± 0.013	-3.048 ± 0.045	1.60 × 0.44	16.3
21	4371.63	2.320 ± 0.013	-3.098 ± 0.039	1.69 × 0.47	18.3
22	4373.37	2.329 ± 0.012	-3.069 ± 0.038	1.63 × 0.49	18.0
23	4375.10	2.308 ± 0.014	-3.139 ± 0.048	1.80 × 0.46	15.7
24	4376.84	2.282 ± 0.012	-3.193 ± 0.040	1.79 × 0.44	18.8
25	4378.57	2.273 ± 0.006	-3.153 ± 0.022	1.73 × 0.42	33.1
26	4380.31	2.258 ± 0.008	-3.095 ± 0.028	1.76 × 0.43	26.0
27	4382.04	2.206 ± 0.032	-3.156 ± 0.091	1.84 × 0.49	8.4
28	4476.67	-0.497 ± 0.007	0.908 ± 0.025	1.83 × 0.43	31.3
29	4478.41	-0.516 ± 0.004	0.924 ± 0.014	1.74 × 0.42	52.3
30	4480.14	-0.515 ± 0.005	0.884 ± 0.016	1.73 × 0.42	44.7
31	4481.88	-0.500 ± 0.005	0.838 ± 0.018	1.81 × 0.43	42.2
32	4483.62	-0.495 ± 0.006	0.876 ± 0.020	1.80 × 0.45	37.5
33	4485.35	-0.437 ± 0.014	0.792 ± 0.040	2.13 × 0.52	22.2
34	4487.09	-0.471 ± 0.022	0.823 ± 0.064	2.39 × 0.51	15.4
35	4488.83	-0.479 ± 0.016	0.848 ± 0.047	2.04 × 0.49	18.0
36	4490.56	-0.594 ± 0.012	1.151 ± 0.033	2.16 × 0.53	27.1
37	4492.30	-0.677 ± 0.007	1.351 ± 0.021	1.98 × 0.49	38.4
38	4494.04	-0.548 ± 0.020	1.112 ± 0.048	2.73 × 0.59	23.0
39	4495.77	-0.149 ± 0.036	0.321 ± 0.087	3.27 × 0.59	15.1
40	4497.51	-0.300 ± 0.021	0.630 ± 0.054	2.87 × 0.55	21.6

## A.6 Water Megamaser Positions in NGC 23, UGC 3193 and IC 2560

Table A.6.3 (cont'd)

ID	Velocity (km s <sup>-1</sup> )	X ± σ <sub>X</sub> (mas ± mas)	Y ± σ <sub>Y</sub> (mas ± mas)	Size (mas × mas)	SNR
41	4499.24	-0.459 ± 0.005	0.975 ± 0.016	1.74 × 0.44	46.0
42	4500.98	-0.467 ± 0.003	0.987 ± 0.011	1.70 × 0.42	65.2
43	4502.72	-0.470 ± 0.004	1.001 ± 0.013	1.68 × 0.41	54.6
44	4504.45	-0.463 ± 0.016	1.005 ± 0.050	1.68 × 0.45	14.0
45	4564.07	0.751 ± 0.045	-1.293 ± 0.162	2.03 × 0.41	5.2
46	4565.80	0.727 ± 0.017	-1.424 ± 0.062	1.80 × 0.41	12.2
47	4567.54	0.799 ± 0.013	-1.629 ± 0.051	1.73 × 0.40	14.4
48	4569.28	0.866 ± 0.018	-1.528 ± 0.068	1.91 × 0.44	11.8
49	4571.01	0.839 ± 0.018	-1.607 ± 0.065	1.86 × 0.45	12.0
50	4572.75	0.837 ± 0.017	-1.684 ± 0.055	1.84 × 0.46	14.0
51	4574.49	0.876 ± 0.023	-1.593 ± 0.081	2.06 × 0.46	10.6
52	4576.23	0.806 ± 0.021	-1.566 ± 0.088	1.89 × 0.39	9.0
53	4577.96	0.773 ± 0.024	-1.549 ± 0.091	1.63 × 0.37	7.6
54	4579.70	0.763 ± 0.032	-1.552 ± 0.115	1.51 × 0.39	5.5

Note. — The maser positions in UGC 3193 (VLBI track BB313Z) and their 1σ position uncertainties. Velocities are kinematic LSR velocities in the optical definition. Positions are relative to the unweighted centroid of all maser features of 4<sup>h</sup>52<sup>m</sup>52<sup>s</sup>.5572, 3°03′25′.738. The size column lists the major and minor axes of the fit 2D Gaussians. All 53 maser features detected by VLBI are shown. They had a SNR > 3. Masers were detected in four high-velocity groups (blue I: IDs 1 to 4, blue II: IDs 5 to 27 red I: IDs 28 to 44, red II: IDs 45 to 54).

## A.6 Water Megamaser Positions in NGC 23, UGC 3193 and IC 2560

Table A.6.4. Positions of maser features in IC 2560.

ID	Velocity (km s <sup>-1</sup> )	X ± σ <sub>X</sub> (mas ± mas)	Y ± σ <sub>Y</sub> (mas ± mas)	Size (mas × mas)	SNR
1	2517.84	0.490 ± 0.087	-0.348 ± 0.257	2.17 × 0.25	3.5
2	2518.70	-0.207 ± 0.052	0.181 ± 0.109	1.19 × 0.19	4.4
3	2519.56	0.423 ± 0.073	-0.176 ± 0.183	2.07 × 0.25	4.6
4	2520.42	0.393 ± 0.070	-0.128 ± 0.200	2.40 × 0.21	4.9
5	2521.27	0.427 ± 0.060	-0.324 ± 0.194	2.17 × 0.20	4.6
6	2522.13	0.431 ± 0.057	-0.392 ± 0.146	1.54 × 0.20	4.3
7	2522.99	0.416 ± 0.050	-0.292 ± 0.122	1.59 × 0.20	5.3
8	2523.84	0.526 ± 0.064	-0.437 ± 0.178	2.30 × 0.25	5.3
9	2524.70	0.452 ± 0.038	-0.257 ± 0.114	1.98 × 0.22	7.1
10	2525.56	0.485 ± 0.037	-0.345 ± 0.108	1.68 × 0.23	6.4
11	2527.27	0.566 ± 0.079	-1.727 ± 0.181	1.92 × 0.19	4.2
12	2528.13	0.585 ± 0.039	-0.469 ± 0.098	1.68 × 0.22	7.0
13	2528.98	0.615 ± 0.030	-0.611 ± 0.086	1.63 × 0.23	7.8
14	2529.84	0.651 ± 0.044	-0.795 ± 0.132	1.78 × 0.21	5.5
15	2530.70	0.660 ± 0.051	-0.642 ± 0.133	1.76 × 0.22	5.4
16	2535.84	0.059 ± 0.042	-1.993 ± 0.111	1.06 × 0.19	3.9
17	2537.55	-0.037 ± 0.077	-0.109 ± 0.238	2.01 × 0.24	3.5
18	2538.41	0.479 ± 0.061	-0.445 ± 0.143	1.61 × 0.17	4.5
19	2663.69	1.680 ± 0.057	-0.770 ± 0.151	1.34 × 0.17	3.6
20	2665.40	1.365 ± 0.061	-1.447 ± 0.153	2.06 × 0.20	5.4
21	2666.26	1.312 ± 0.033	-1.314 ± 0.095	2.07 × 0.20	8.9
22	2671.41	1.277 ± 0.058	-1.228 ± 0.177	2.26 × 0.20	5.2
23	2672.27	1.266 ± 0.077	-1.197 ± 0.224	2.06 × 0.19	3.8
24	2676.56	1.428 ± 0.116	-1.365 ± 0.226	2.07 × 0.36	3.6
25	2679.13	0.833 ± 0.100	-1.127 ± 0.326	3.08 × 0.17	3.9
26	2679.99	0.669 ± 0.073	-0.746 ± 0.189	1.55 × 0.17	3.3
27	2867.07	0.061 ± 0.084	0.328 ± 0.274	2.01 × 0.21	3.0
28	2872.22	-0.584 ± 0.050	-0.687 ± 0.164	1.31 × 0.22	3.3
29	2878.24	-0.129 ± 0.069	-0.723 ± 0.207	1.74 × 0.19	3.5
30	2881.67	0.053 ± 0.079	0.009 ± 0.339	2.52 × 0.21	3.1
31	2887.69	-0.053 ± 0.038	0.290 ± 0.138	1.51 × 0.22	4.6
32	2889.40	0.091 ± 0.066	-0.082 ± 0.142	1.68 × 0.24	4.7
33	2890.26	0.017 ± 0.033	0.042 ± 0.088	1.50 × 0.23	6.9
34	2891.12	-0.020 ± 0.040	0.104 ± 0.121	1.83 × 0.23	6.3
35	2891.98	0.012 ± 0.029	0.020 ± 0.091	1.73 × 0.23	7.9
36	2892.84	0.127 ± 0.030	-0.324 ± 0.108	1.91 × 0.22	7.4
37	2893.70	0.115 ± 0.025	-0.147 ± 0.071	1.54 × 0.23	9.0
38	2894.56	0.051 ± 0.018	0.071 ± 0.055	1.42 × 0.24	10.7
39	2895.42	0.029 ± 0.016	0.123 ± 0.048	1.46 × 0.25	12.8
40	2896.28	0.027 ± 0.015	0.073 ± 0.041	1.54 × 0.26	15.6

## A.6 Water Megamaser Positions in NGC 23, UGC 3193 and IC 2560

Table A.6.5 (cont'd)

ID	Velocity (km s <sup>-1</sup> )	X ± σ <sub>X</sub> (mas ± mas)	Y ± σ <sub>Y</sub> (mas ± mas)	Size (mas × mas)	SNR
41	2897.14	0.036 ± 0.013	0.054 ± 0.036	1.55 × 0.26	17.9
42	2897.99	0.034 ± 0.013	0.063 ± 0.035	1.56 × 0.26	18.3
43	2898.85	0.027 ± 0.014	0.107 ± 0.038	1.57 × 0.27	17.1
44	2899.71	0.045 ± 0.012	0.063 ± 0.035	1.53 × 0.27	18.2
45	2900.57	0.038 ± 0.011	0.050 ± 0.030	1.52 × 0.26	21.1
46	2901.43	0.032 ± 0.010	0.064 ± 0.028	1.60 × 0.26	23.7
47	2902.29	0.032 ± 0.008	0.071 ± 0.023	1.54 × 0.25	28.0
48	2903.15	0.027 ± 0.009	0.106 ± 0.024	1.54 × 0.25	26.2
49	2904.01	0.028 ± 0.009	0.125 ± 0.025	1.54 × 0.26	25.1
50	2904.87	0.039 ± 0.009	0.084 ± 0.025	1.54 × 0.25	25.2
51	2905.73	0.029 ± 0.011	0.103 ± 0.030	1.60 × 0.25	21.7
52	2906.58	0.025 ± 0.010	0.110 ± 0.026	1.54 × 0.26	24.1
53	2907.44	0.002 ± 0.010	0.155 ± 0.028	1.51 × 0.25	22.2
54	2908.30	-0.002 ± 0.011	0.156 ± 0.031	1.52 × 0.24	20.2
55	2909.16	0.018 ± 0.012	0.091 ± 0.032	1.53 × 0.25	19.5
56	2910.02	0.029 ± 0.012	0.088 ± 0.032	1.53 × 0.25	19.5
57	2910.88	0.030 ± 0.012	0.103 ± 0.033	1.56 × 0.24	19.3
58	2911.74	0.024 ± 0.013	0.116 ± 0.035	1.45 × 0.26	16.8
59	2912.60	0.005 ± 0.010	0.139 ± 0.030	1.49 × 0.24	20.6
60	2913.46	0.009 ± 0.009	0.107 ± 0.026	1.53 × 0.23	24.4
61	2914.32	0.017 ± 0.012	0.099 ± 0.031	1.59 × 0.25	21.1
62	2915.18	0.016 ± 0.013	0.125 ± 0.034	1.51 × 0.26	18.4
63	2916.04	0.036 ± 0.018	0.053 ± 0.051	1.59 × 0.28	13.0
64	2916.89	0.033 ± 0.020	0.020 ± 0.057	1.74 × 0.29	12.6
65	2917.75	0.032 ± 0.025	0.056 ± 0.070	1.61 × 0.28	9.5
66	2918.61	0.058 ± 0.022	0.007 ± 0.062	1.39 × 0.27	9.3
67	2919.47	0.042 ± 0.019	0.047 ± 0.053	1.40 × 0.25	10.9
68	2920.33	0.029 ± 0.023	0.082 ± 0.057	1.54 × 0.26	11.1
69	2921.19	0.022 ± 0.034	0.038 ± 0.088	1.54 × 0.28	7.2
70	2922.05	0.027 ± 0.035	0.127 ± 0.111	1.36 × 0.27	5.2
71	2922.91	-0.036 ± 0.036	0.163 ± 0.095	1.20 × 0.27	5.3
72	2923.77	-0.111 ± 0.053	0.333 ± 0.168	1.86 × 0.22	4.6
73	2928.06	-0.022 ± 0.028	0.064 ± 0.073	1.04 × 0.23	5.9
74	2935.80	0.025 ± 0.056	-0.356 ± 0.167	1.42 × 0.18	3.5
75	2938.37	-0.553 ± 0.049	-0.086 ± 0.155	1.26 × 0.18	3.4
76	2947.83	-0.454 ± 0.114	-1.276 ± 0.340	2.67 × 0.20	3.2
77	2948.69	0.536 ± 0.057	-0.557 ± 0.183	1.32 × 0.21	3.0
78	3104.96	-1.512 ± 0.107	2.218 ± 0.248	2.47 × 0.19	4.0
79	3114.42	-1.563 ± 0.054	1.510 ± 0.137	1.97 × 0.23	5.8
80	3115.28	-1.599 ± 0.046	1.621 ± 0.124	1.83 × 0.23	6.0

## A.6 Water Megamaser Positions in NGC 23, UGC 3193 and IC 2560

Table A.6.6 (cont'd)

ID	Velocity ( $\text{km s}^{-1}$ )	$X \pm \sigma_X$ (mas $\pm$ mas)	$Y \pm \sigma_Y$ (mas $\pm$ mas)	Size (mas $\times$ mas)	SNR
81	3117.00	$-1.506 \pm 0.084$	$1.161 \pm 0.206$	$1.86 \times 0.23$	3.6
82	3117.86	$-1.456 \pm 0.116$	$0.960 \pm 0.285$	$2.65 \times 0.18$	3.8
83	3128.19	$-0.802 \pm 0.068$	$1.234 \pm 0.196$	$1.68 \times 0.25$	3.5
84	3132.46	$-0.265 \pm 0.081$	$1.020 \pm 0.265$	$2.17 \times 0.19$	3.4
85	3133.32	$-0.445 \pm 0.126$	$0.641 \pm 0.387$	$3.00 \times 0.16$	3.2
86	3135.04	$-0.226 \pm 0.054$	$1.345 \pm 0.126$	$1.62 \times 0.20$	5.2
87	3135.90	$-0.164 \pm 0.076$	$1.287 \pm 0.245$	$2.36 \times 0.20$	4.0
88	3135.93	$-1.267 \pm 0.087$	$1.078 \pm 0.190$	$1.85 \times 0.34$	3.9
89	3136.76	$-1.288 \pm 0.053$	$1.175 \pm 0.179$	$2.48 \times 0.26$	5.8
90	3136.79	$-1.259 \pm 0.021$	$1.092 \pm 0.058$	$2.14 \times 0.23$	15.1
91	3137.62	$-1.237 \pm 0.047$	$1.074 \pm 0.142$	$2.22 \times 0.24$	6.5
92	3137.65	$-1.255 \pm 0.023$	$1.091 \pm 0.063$	$2.12 \times 0.24$	13.7
93	3159.99	$-1.359 \pm 0.086$	$-0.225 \pm 0.273$	$2.10 \times 0.17$	3.2
94	3166.91	$-1.425 \pm 0.064$	$1.170 \pm 0.221$	$2.00 \times 0.23$	3.8
95	3178.92	$-0.571 \pm 0.066$	$-0.224 \pm 0.224$	$2.40 \times 0.19$	4.4
96	3178.96	$-1.389 \pm 0.081$	$0.374 \pm 0.202$	$1.66 \times 0.17$	3.3
97	3187.53	$-1.705 \pm 0.059$	$-0.216 \pm 0.212$	$1.64 \times 0.15$	3.2
98	3192.69	$-0.850 \pm 0.078$	$0.369 \pm 0.270$	$2.23 \times 0.17$	3.4
99	3194.42	$-0.973 \pm 0.070$	$-0.004 \pm 0.255$	$2.13 \times 0.17$	3.5
100	3197.86	$-0.532 \pm 0.058$	$0.318 \pm 0.162$	$1.53 \times 0.17$	3.9
101	3199.58	$-0.591 \pm 0.102$	$2.092 \pm 0.263$	$2.10 \times 0.15$	3.2
102	3203.02	$-1.018 \pm 0.123$	$0.901 \pm 0.374$	$2.80 \times 0.16$	3.1
103	3205.61	$-0.770 \pm 0.063$	$0.317 \pm 0.162$	$1.70 \times 0.19$	4.3
104	3206.47	$-0.478 \pm 0.114$	$0.225 \pm 0.347$	$2.90 \times 0.15$	3.4
105	3216.80	$-0.914 \pm 0.076$	$0.771 \pm 0.181$	$2.22 \times 0.27$	5.0
106	3217.66	$-0.964 \pm 0.032$	$0.844 \pm 0.090$	$1.97 \times 0.23$	9.0
107	3218.52	$-0.921 \pm 0.040$	$0.750 \pm 0.113$	$1.92 \times 0.23$	7.0
108	3219.38	$-0.871 \pm 0.064$	$0.681 \pm 0.160$	$1.70 \times 0.20$	4.3
109	3227.99	$-0.921 \pm 0.077$	$0.694 \pm 0.177$	$2.12 \times 0.27$	4.8
110	3228.85	$-0.848 \pm 0.053$	$0.734 \pm 0.161$	$2.17 \times 0.20$	5.5
111	3229.71	$-0.809 \pm 0.029$	$0.653 \pm 0.087$	$1.93 \times 0.21$	9.1
112	3230.57	$-0.856 \pm 0.044$	$0.625 \pm 0.112$	$2.14 \times 0.24$	7.7
113	3232.29	$-0.815 \pm 0.083$	$0.606 \pm 0.246$	$2.56 \times 0.31$	4.3
114	3233.15	$-0.867 \pm 0.047$	$0.754 \pm 0.143$	$2.16 \times 0.20$	6.2
115	3234.01	$-0.802 \pm 0.054$	$0.564 \pm 0.186$	$2.49 \times 0.22$	5.5
116	3238.32	$-0.987 \pm 0.087$	$1.154 \pm 0.262$	$2.54 \times 0.19$	4.0
117	3239.18	$-0.923 \pm 0.058$	$1.025 \pm 0.173$	$2.58 \times 0.18$	6.1
118	3240.04	$-0.813 \pm 0.058$	$0.686 \pm 0.170$	$2.34 \times 0.21$	5.7
119	3240.90	$-0.150 \pm 0.057$	$1.228 \pm 0.198$	$1.72 \times 0.19$	3.6
120	3241.76	$-0.555 \pm 0.078$	$0.410 \pm 0.261$	$2.22 \times 0.23$	3.5

## A.6 Water Megamaser Positions in NGC 23, UGC 3193 and IC 2560

Table A.6.7 (cont'd)

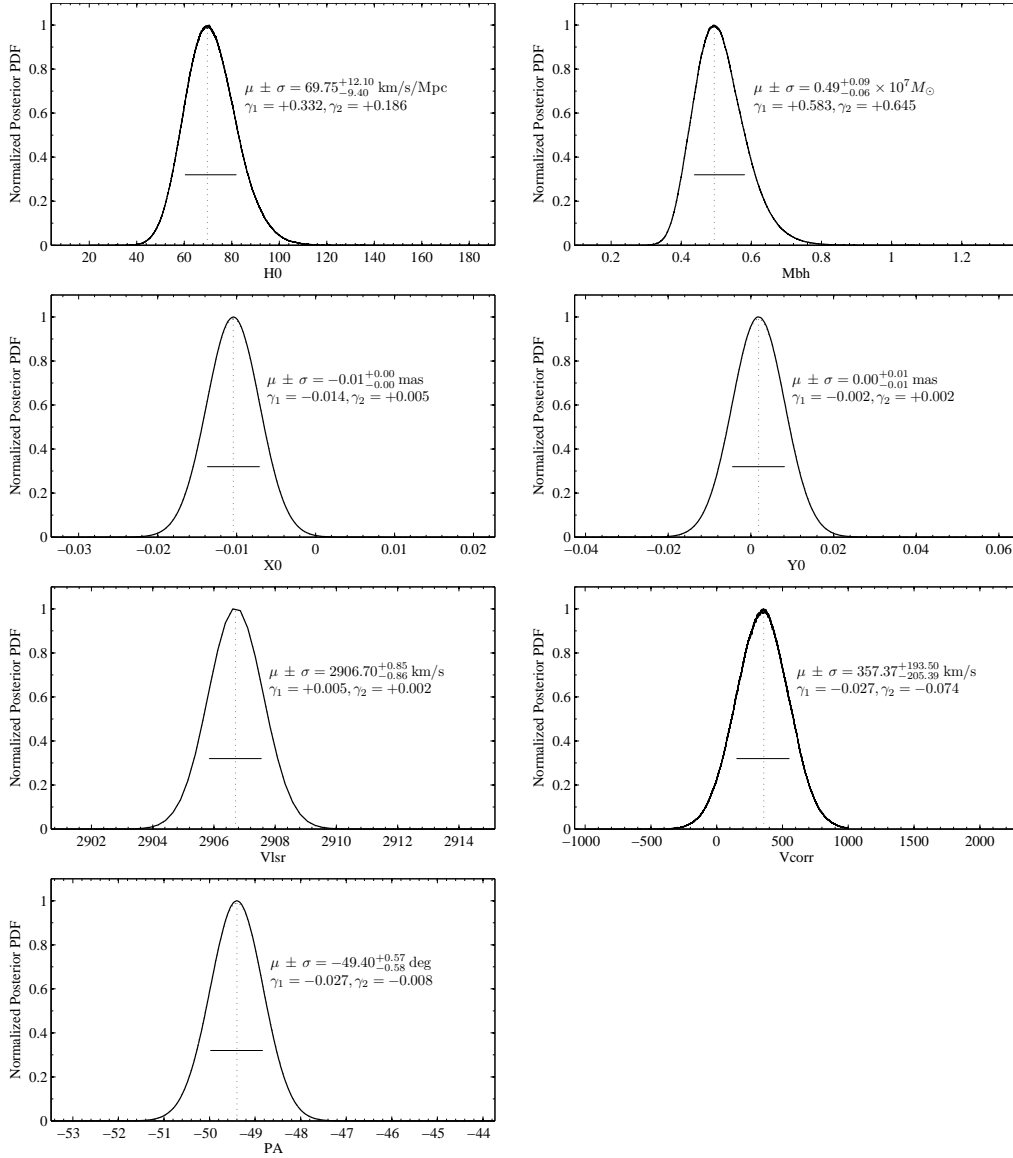
ID	Velocity (km s <sup>-1</sup> )	$X \pm \sigma_X$ (mas $\pm$ mas)	$Y \pm \sigma_Y$ (mas $\pm$ mas)	Size (mas $\times$ mas)	SNR
121	3242.62	$-0.668 \pm 0.056$	$0.518 \pm 0.143$	$2.06 \times 0.23$	5.8
122	3243.49	$-0.695 \pm 0.042$	$0.594 \pm 0.109$	$2.31 \times 0.23$	8.6
123	3244.35	$-0.707 \pm 0.039$	$0.613 \pm 0.091$	$1.72 \times 0.23$	7.7
124	3245.21	$-0.766 \pm 0.061$	$0.804 \pm 0.159$	$1.92 \times 0.21$	4.9
125	3246.07	$-0.795 \pm 0.054$	$0.847 \pm 0.164$	$2.31 \times 0.18$	5.8
126	3246.93	$-0.802 \pm 0.078$	$0.765 \pm 0.235$	$2.36 \times 0.18$	4.1
127	3252.10	$-1.277 \pm 0.084$	$1.276 \pm 0.265$	$2.13 \times 0.15$	3.3
128	3252.96	$-1.283 \pm 0.077$	$1.292 \pm 0.228$	$1.83 \times 0.16$	3.3

Note. — The maser positions in IC 2560 (VLBI track BG169C) and their  $1\sigma$  position uncertainties. The systemic masers have IDs of 27 to 77. Velocities are kinematic LSR velocities in the optical definition. Positions are relative to the unweighted centroid of all maser features of  $10^h 16^m 18^s.71$ ,  $-33^\circ 33' 49''.740$ . The size column lists the major and minor axes of the fit 2D Gaussians. A total of 177 maser features were detected. Only the 128 features with a SNR > 3 are shown here.



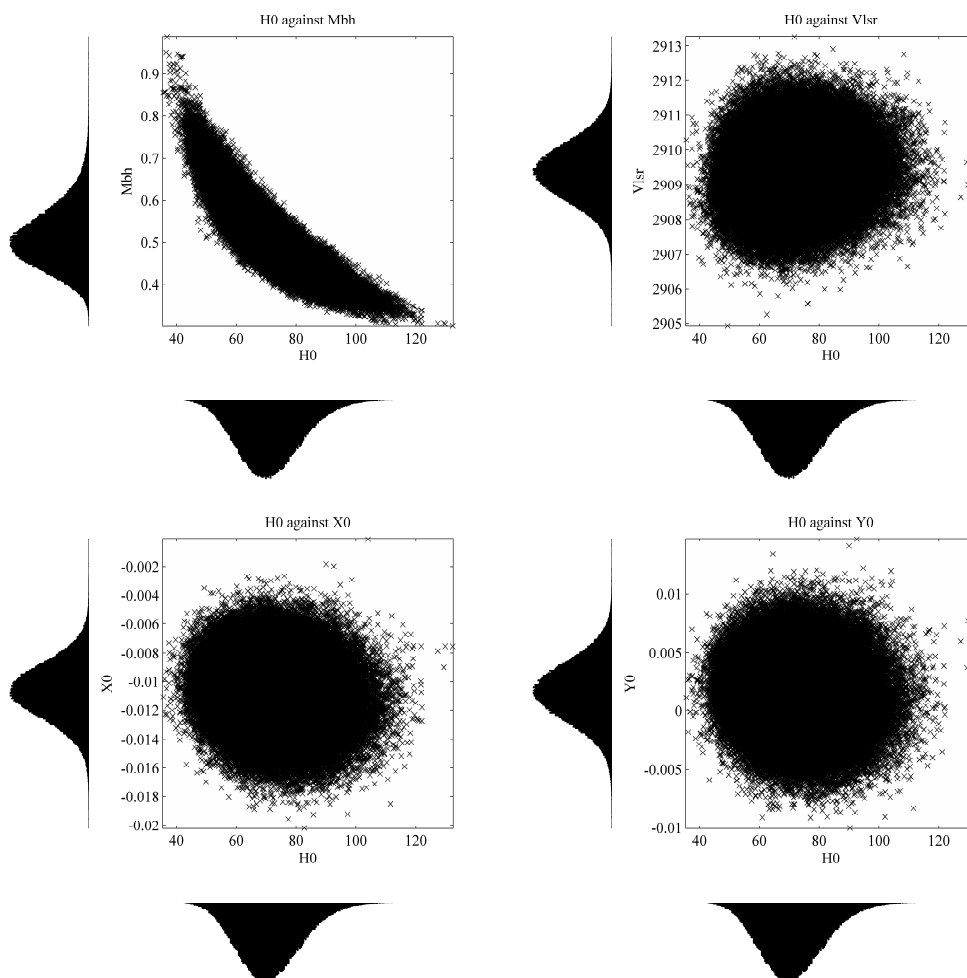
## A.7 Parameter Posteriors for the IC 2560 Disk Maser Model Fit

**Fig. A.7.1:** The normalized posterior probability density functions (PDFs) of the parameters of the first IC 2560 MCMC model fit after  $2.5 \times 10^9$  iterations (Fit 1 in Table 7.6). The peak of each PDF,  $\mu$  (vertical dotted line), the lower and upper single-sided standard deviations, “ $1\sigma$ ” (horizontal line), the skewness of the PDF,  $\gamma_1$ , and the kurtosis of the PDF,  $\gamma_2$ , are shown inside each panel.

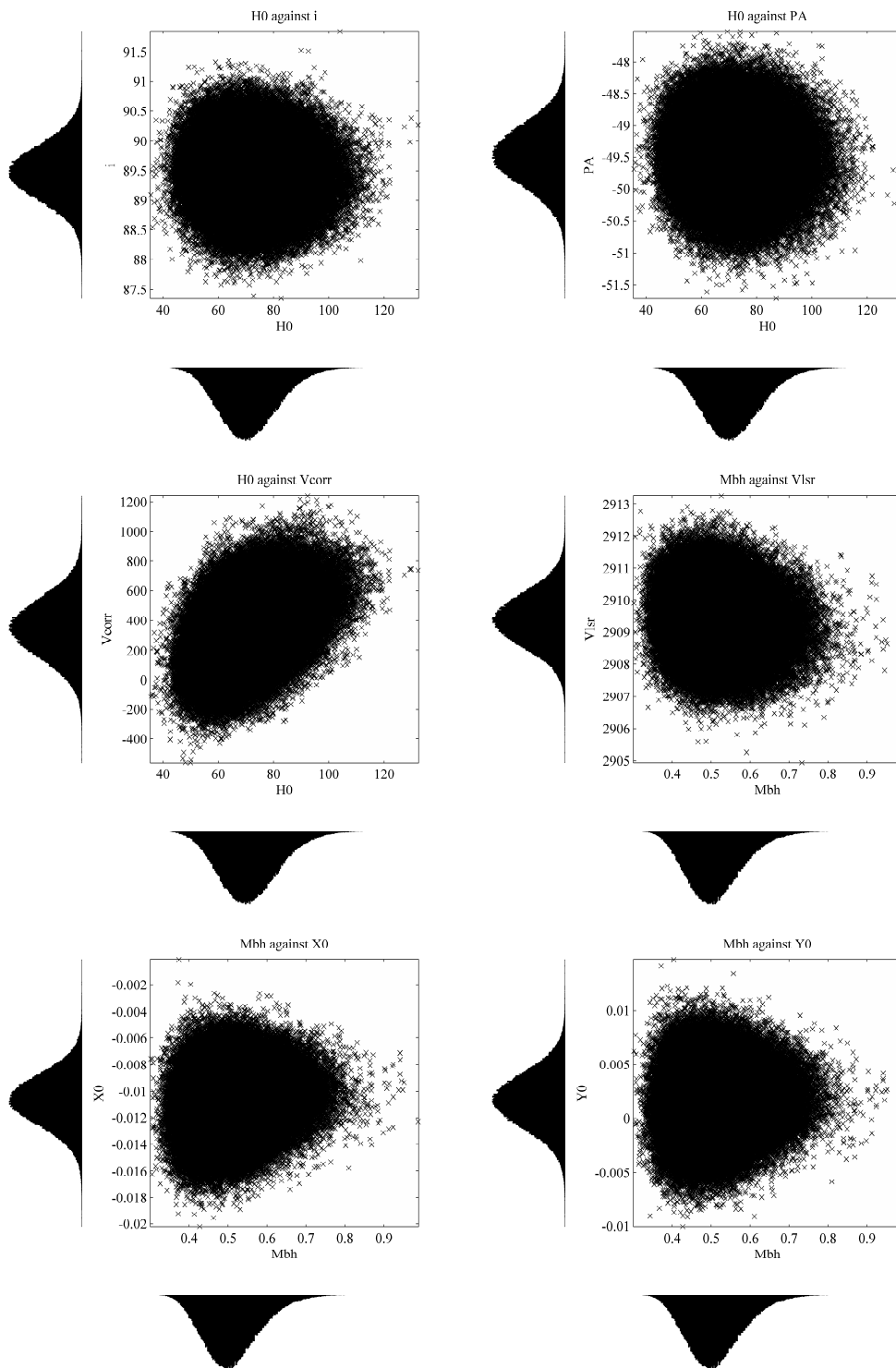


## A.7 Parameter Posteriors for the IC 2560 Disk Maser Model Fit

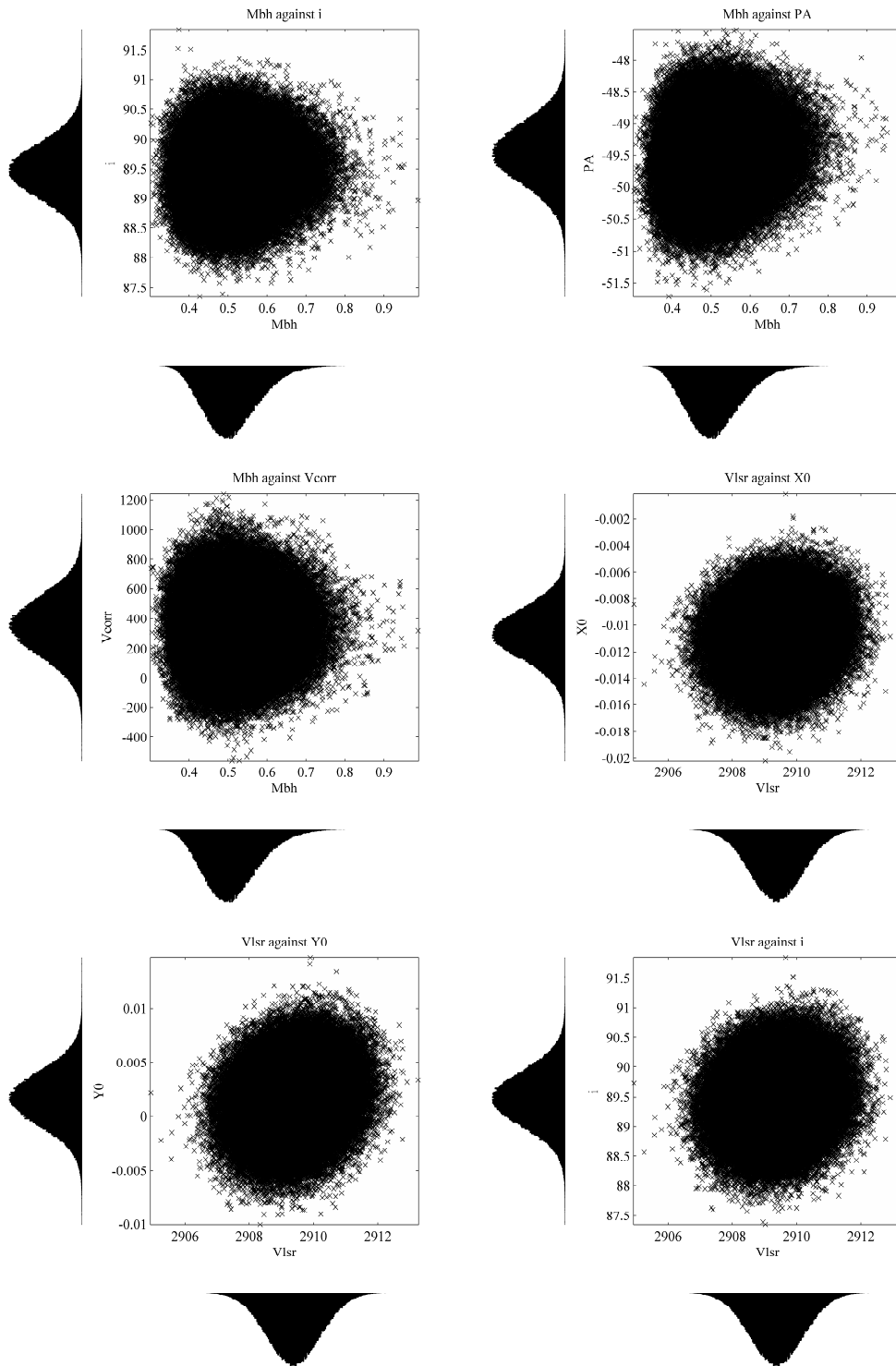
**Fig. A.7.2:** The joint posterior distributions of the parameters of the *first* IC 2560 disk maser Keplerian model MCMC fit (**Fit 1** in Table 7.6). Note that parameters  $M_{\text{BH}}$  and  $H_0$  are anticorrelated; the observed maser velocities and VLBI angular distribution can be explained by lower maser orbits around a smaller model  $M_{\text{BH}}$  with the host galaxy at a closer model distance  $D_A$ . The observed recessional velocity at a closer model  $D_A$  requires a larger  $H_0$  (an vice versa; see also Fig. 8 in Kuo et al. 2013). The systemic maser acceleration data, however, break the  $M_{\text{BH}}-D_A$  degeneracy.



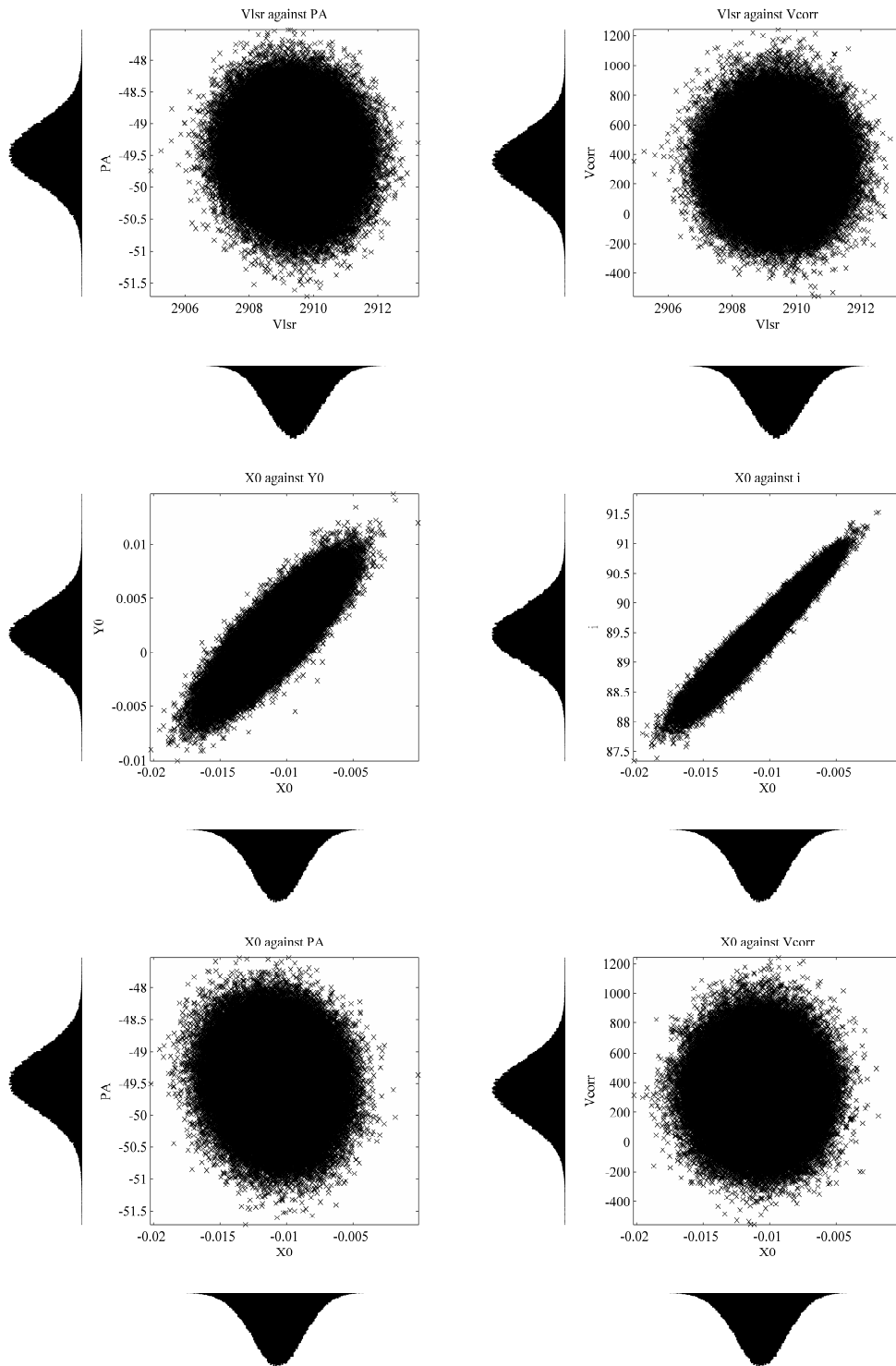
## A.7 Parameter Posteriors for the IC 2560 Disk Maser Model Fit



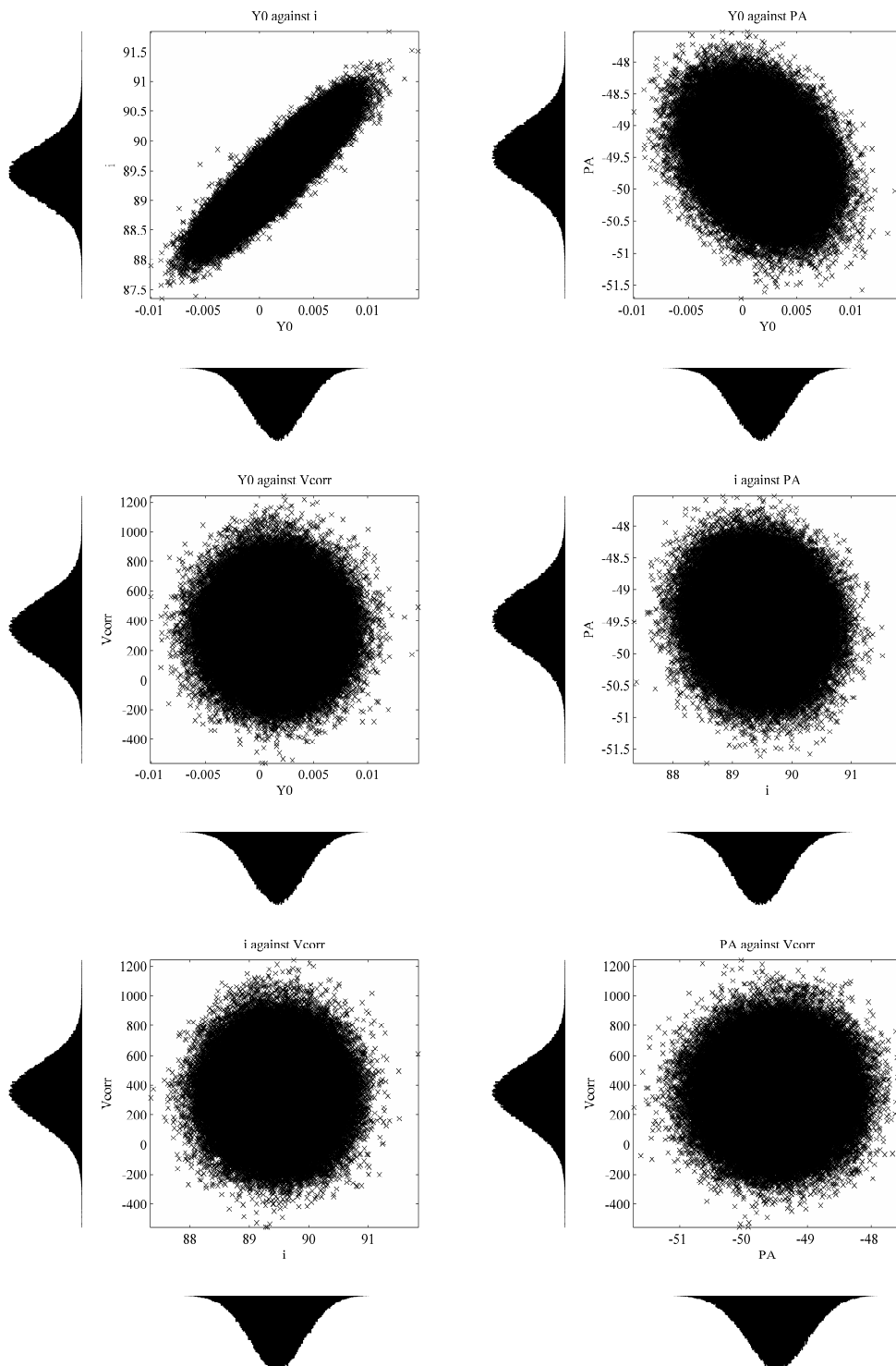
## A.7 Parameter Posteriors for the IC 2560 Disk Maser Model Fit



## A.7 Parameter Posteriors for the IC 2560 Disk Maser Model Fit

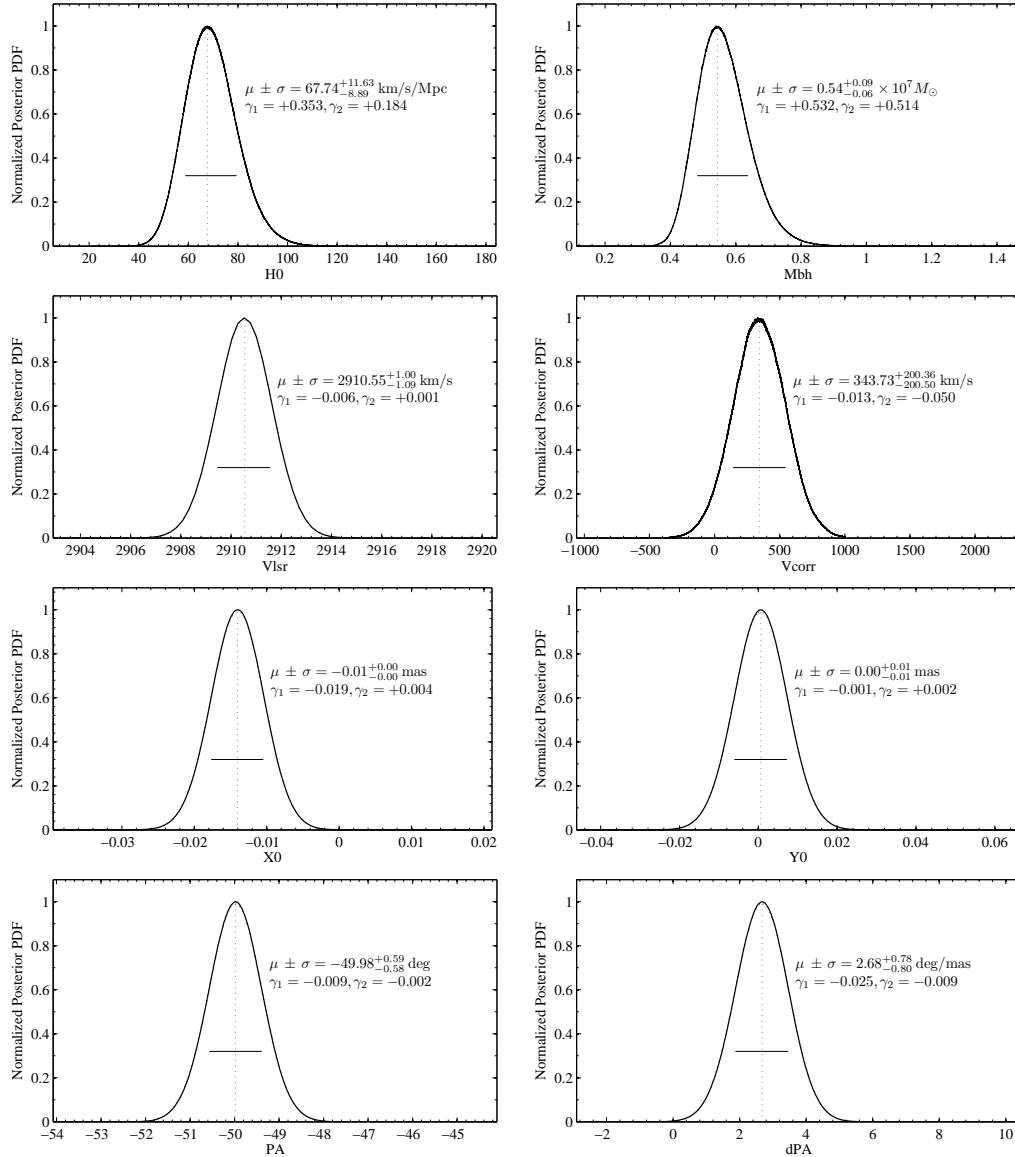


## A.7 Parameter Posteriors for the IC 2560 Disk Maser Model Fit



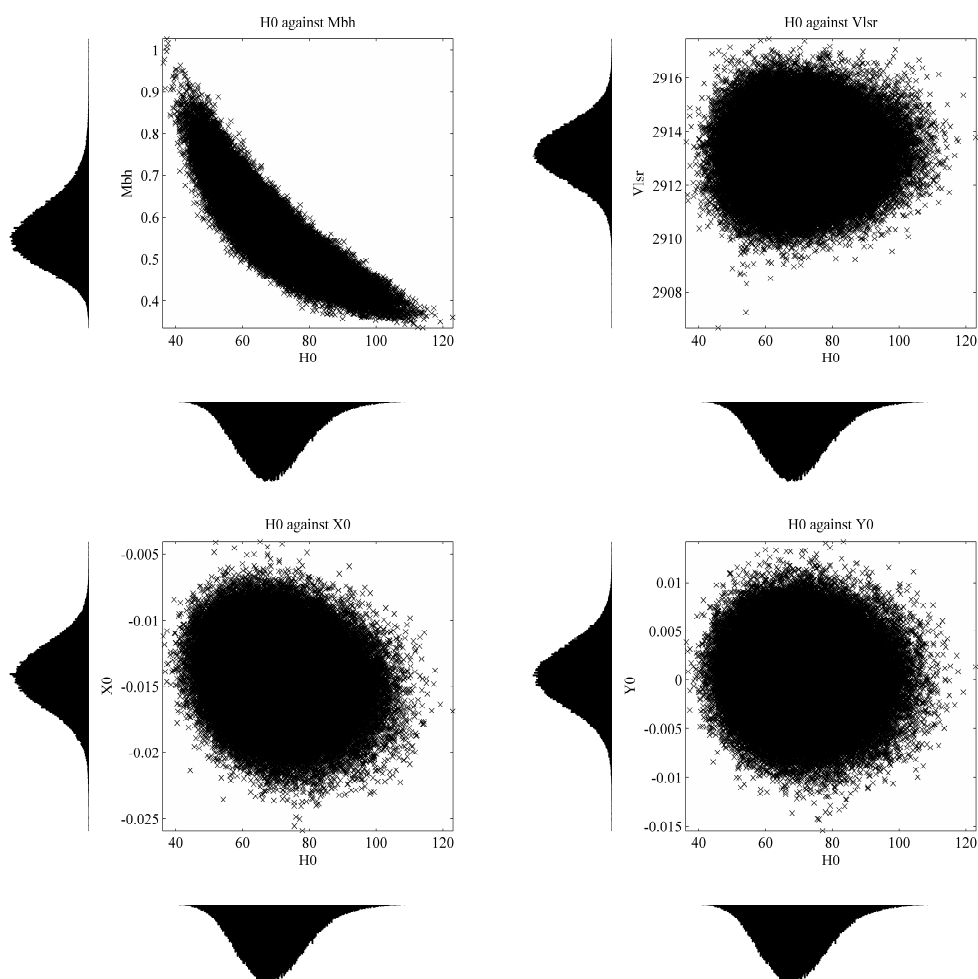
## A.7 Parameter Posteriors for the IC 2560 Disk Maser Model Fit

**Fig. A.7.3:** The normalized posterior probability density functions (PDFs) of the parameters of the second IC 2560 MCMC model fit after  $2.0 \times 10^9$  iterations (Fit 2 in Table 7.6). The peak of each PDF,  $\mu$  (vertical dotted line), the lower and upper single-sided standard deviations, “ $1\sigma$ ” (horizontal line), the skewness of the PDF,  $\gamma_1$ , and the kurtosis of the PDF,  $\gamma_2$ , are shown inside each panel.



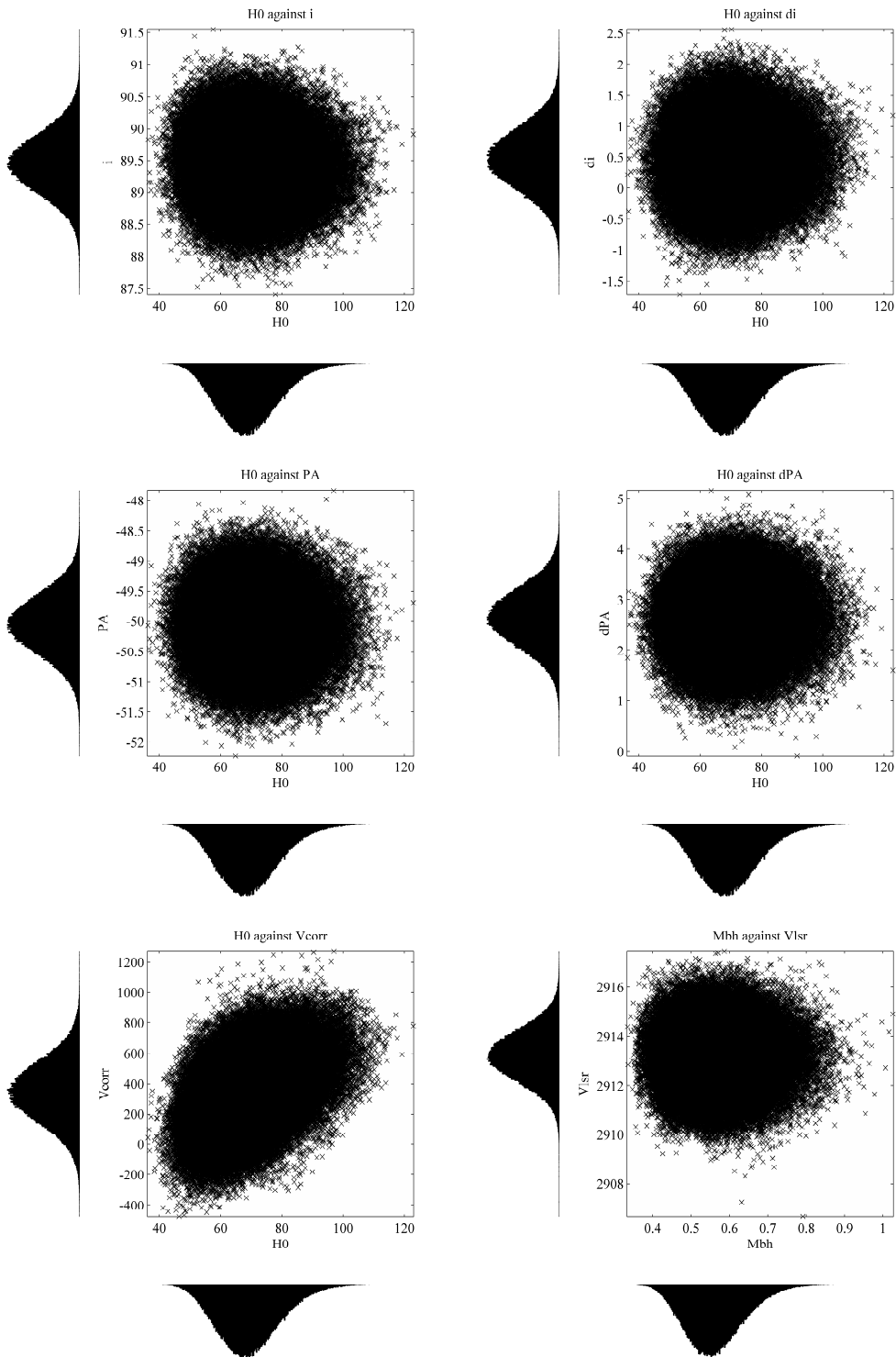
## A.7 Parameter Posteriors for the IC 2560 Disk Maser Model Fit

**Fig. A.7.4:** The joint posterior distributions of the parameters of the *second* IC 2560 disk maser Keplerian model MCMC fit (**Fit 2** in Table 7.6). Note that parameters  $M_{\text{BH}}$  and  $H_0$  are anticorrelated; the observed maser velocities and VLBI angular distribution can be explained by lower maser orbits around a smaller model  $M_{\text{BH}}$  with the host galaxy at a closer model distance  $D_A$ . The observed recessional velocity at a closer model  $D_A$  requires a larger  $H_0$  (an vice versa; see also Fig. 8 in Kuo et al. 2013). The systemic maser acceleration data, however, break the  $M_{\text{BH}}-D_A$  degeneracy.

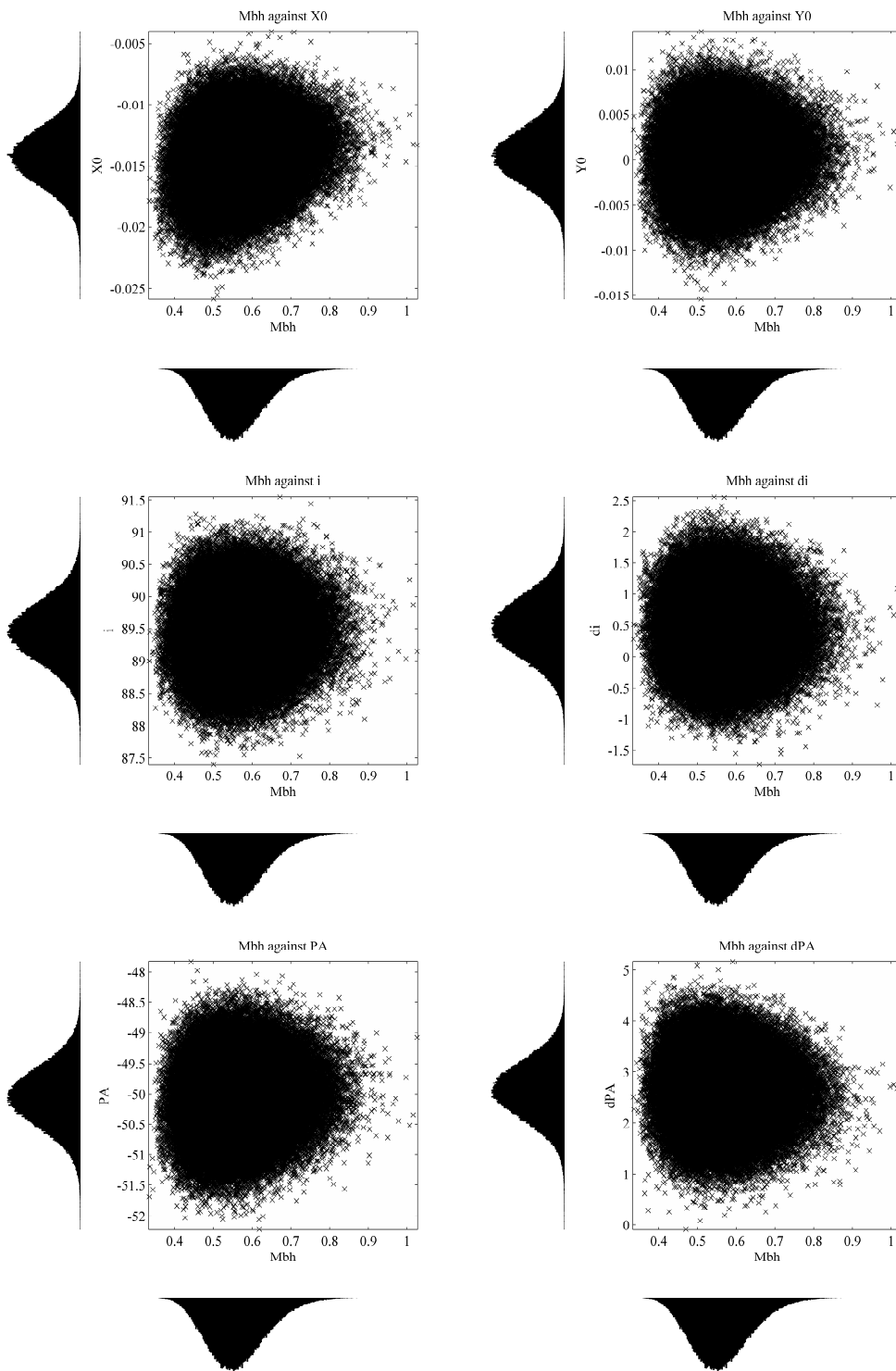




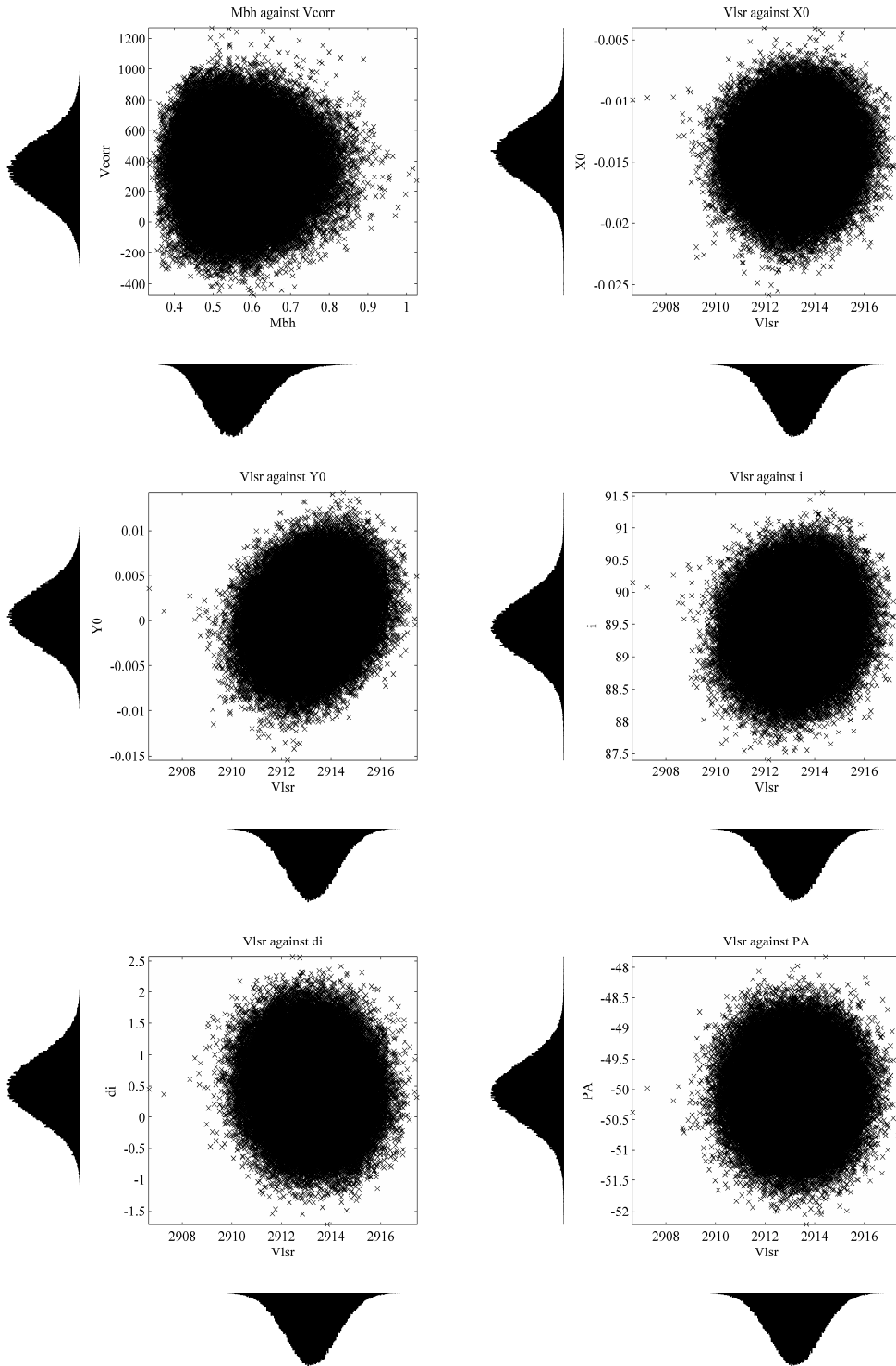
## A.7 Parameter Posteriors for the IC 2560 Disk Maser Model Fit



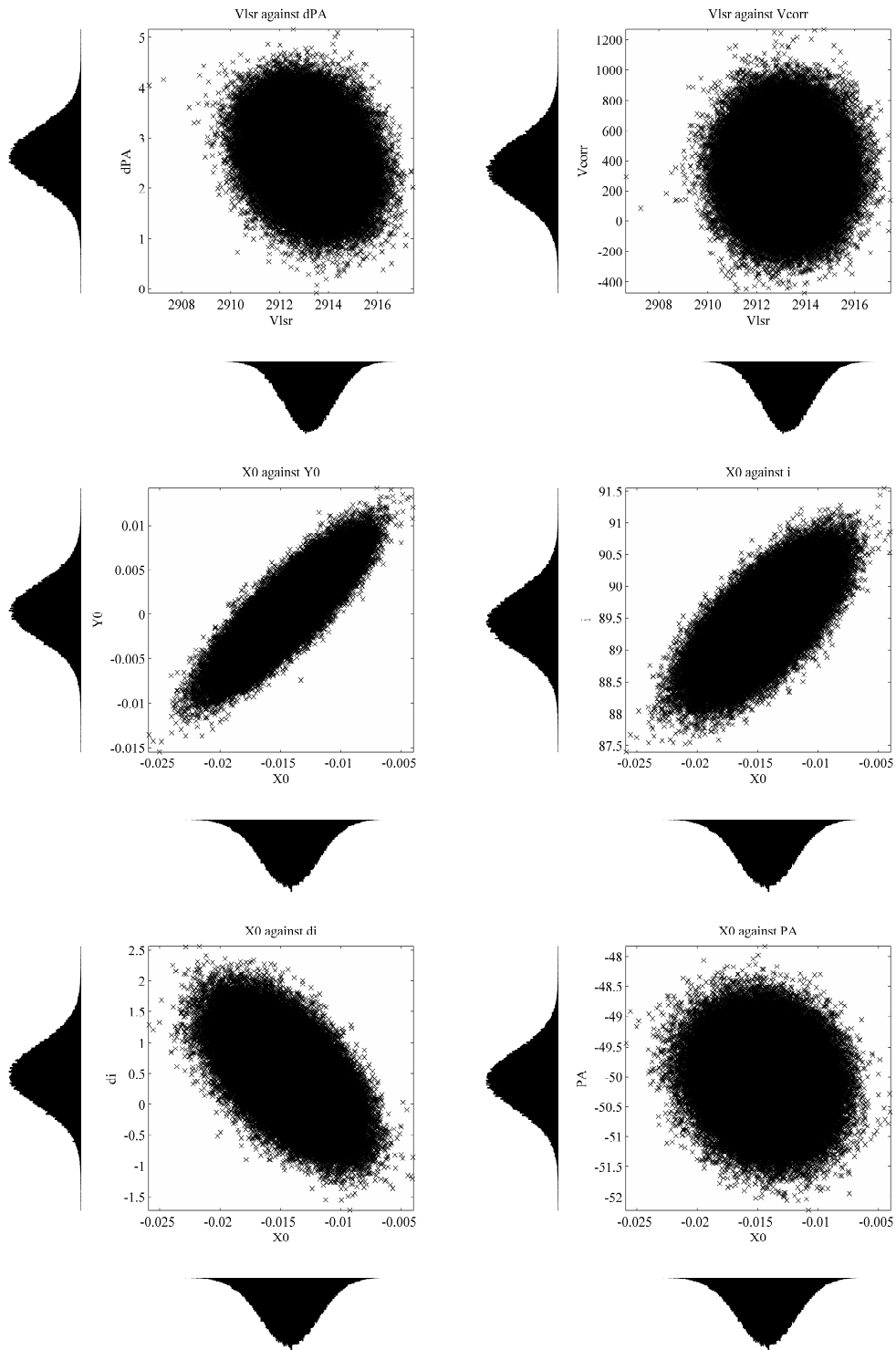
## A.7 Parameter Posteriors for the IC 2560 Disk Maser Model Fit



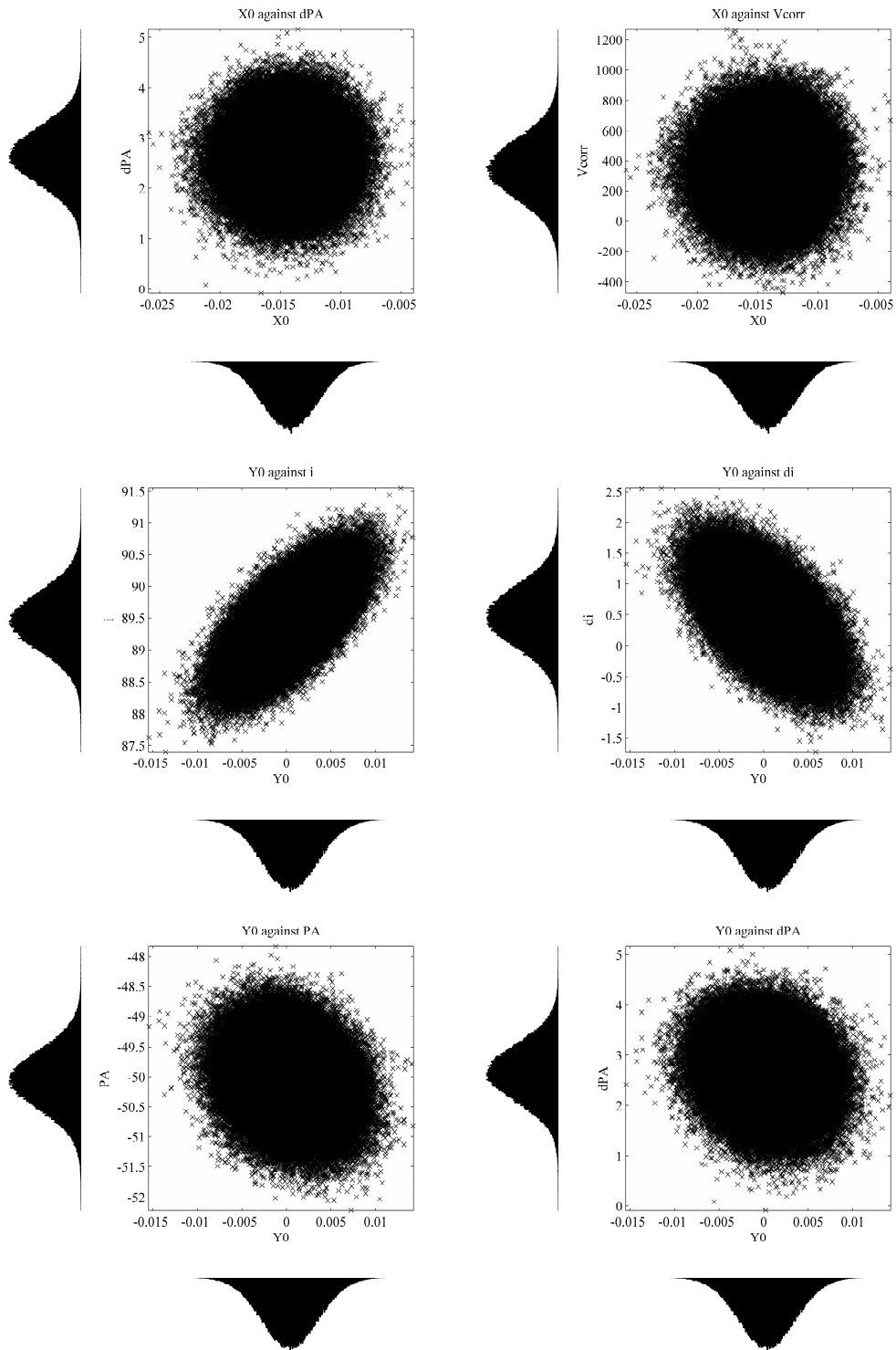
## A.7 Parameter Posteriors for the IC 2560 Disk Maser Model Fit



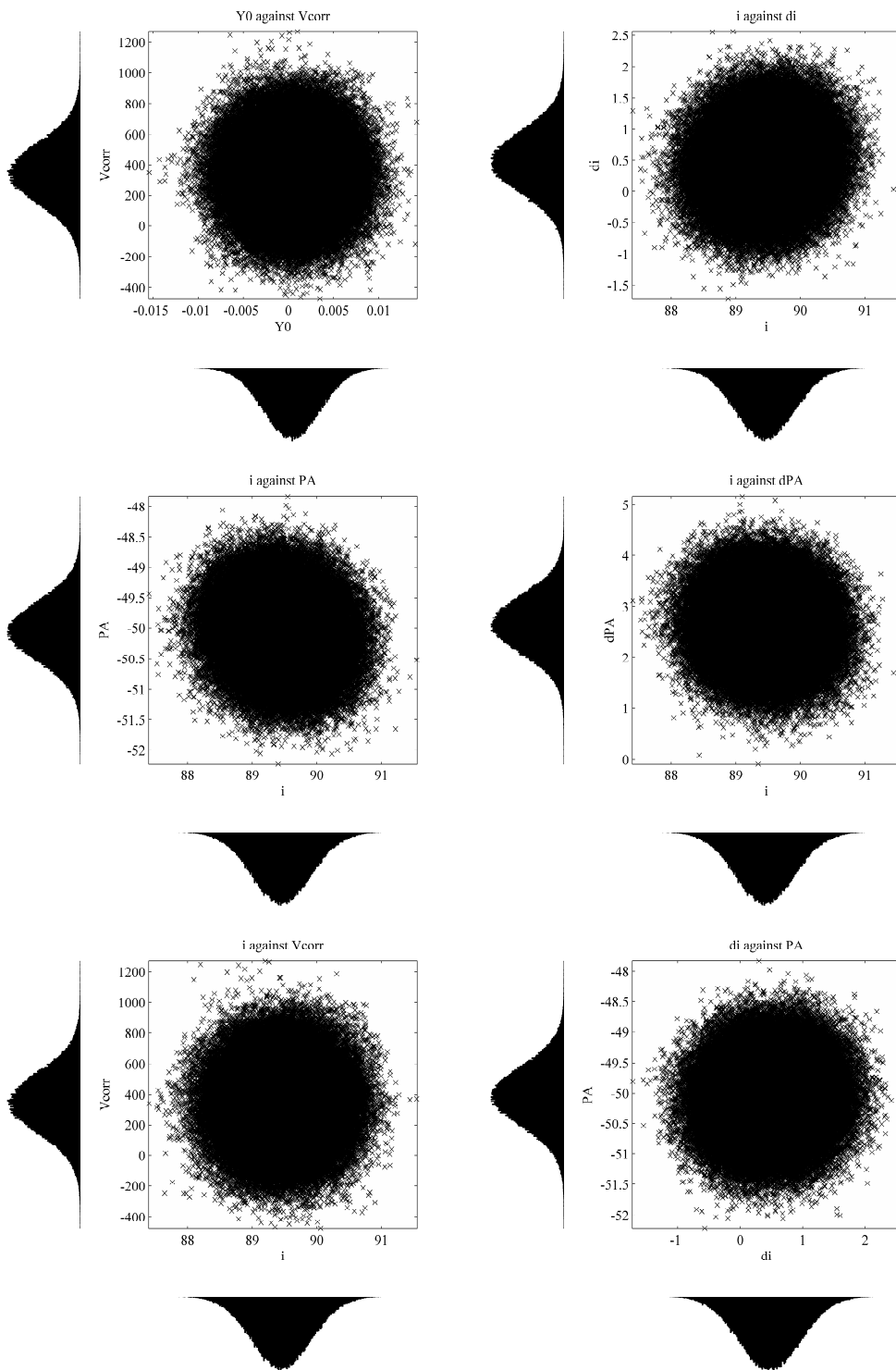
## A.7 Parameter Posteriors for the IC 2560 Disk Maser Model Fit



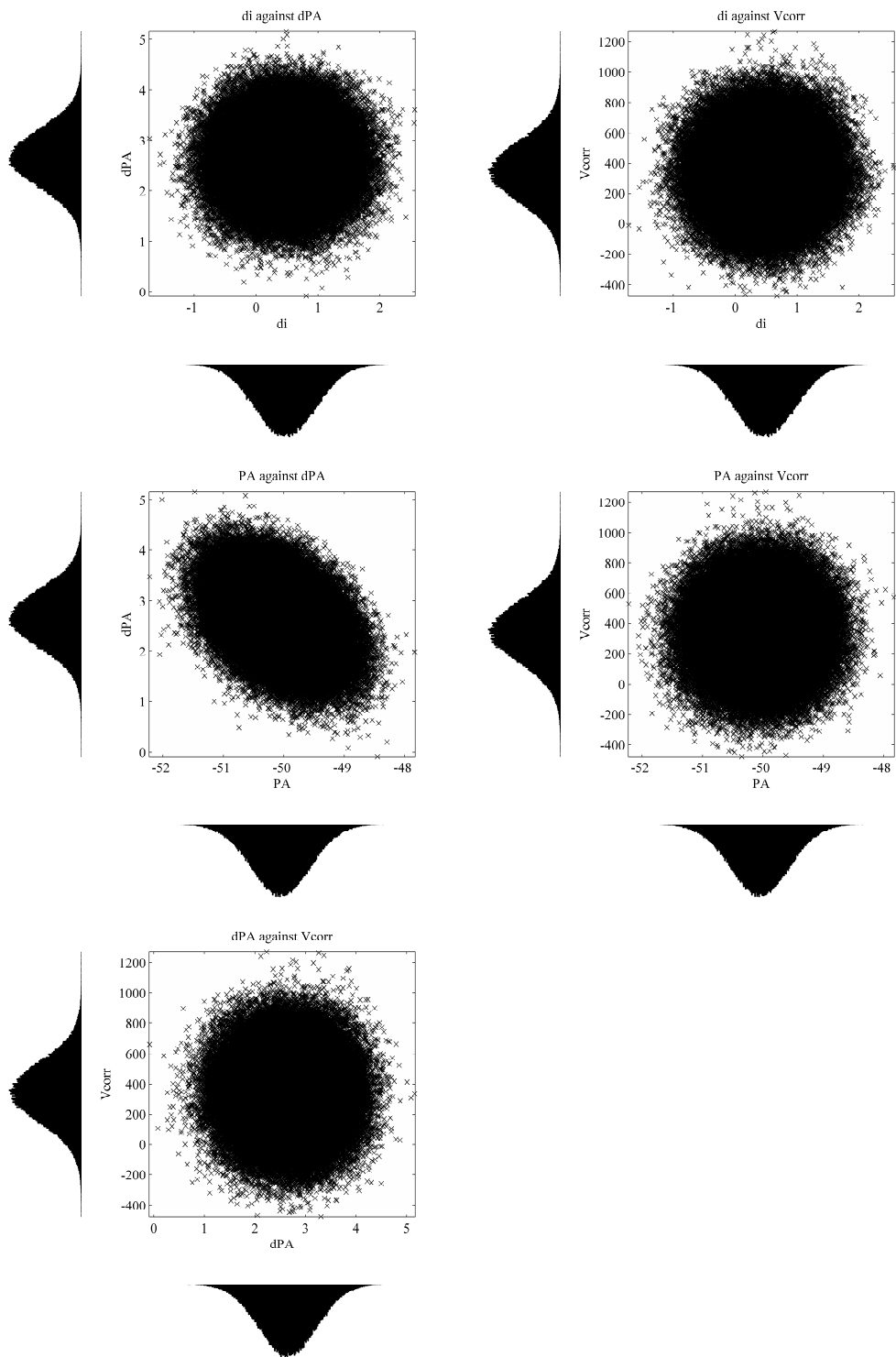
## A.7 Parameter Posteriors for the IC 2560 Disk Maser Model Fit



## A.7 Parameter Posteriors for the IC 2560 Disk Maser Model Fit



## A.7 Parameter Posteriors for the IC 2560 Disk Maser Model Fit







# Erklärung

Ich versichere, dass ich die von mir vorgelegte Dissertation selbständig angefertigt, die benutzten Quellen und Hilfsmittel vollständig angegeben und die Stellen der Arbeit – einschliesslich Tabellen, Karten und Abbildungen – die anderen Werken im Wortlaut oder dem Sinn nach entnommen sind, in jedem Einzelfall als Entlehnung kenntlich gemacht habe; dass ich diese Dissertation noch keiner anderen Fakultät oder Universität zur Prüfung vorgelegen habe; dass sie – abgesehen von unten angegebenen Teilpublikationen – noch nicht veröffentlicht worden ist sowie, dass ich eine solche Veröffentlichung vor Abschluss des Promotionsverfahrens nicht vornehmen werde. Die Bestimmungen dieser Promotionsordnung sind mir bekannt. Die von mir vorgelegte Dissertation ist von Prof. Dr. Andreas Eckart und Prof. h.c. Dr. Anton Zensus betreut worden.

Köln, den 02.07.2014

Teilpublikationen und öffentliche Projektdokumentation:

- Wagner, J., *DiFX Multirate Filtering*, Tech. rep., EU FP7 ALBiUS WP6, 2011
- Wagner, J., *FPA RFI Templates*, Tech. rep., EU FP7 ALBiUS WP6, 2011
- Wagner, J., *C++ Beamformer Library with RFI Mitigation*, Softw. pub., DiFX SVN, EU FP7 ALBiUS WP6, 2011
- Wagner, J., *22 GHz water maser search in 37 nearby galaxies – Four new water megamasers in Seyfert 2 and OH maser/absorber galaxies*, *A&A* 560, A12, 2013.

# Curriculum Vitae

## Persönliche Daten

Name: Jan Florian Wagner  
Anschrift: Max-Planck-Institut für Radioastronomie  
Auf dem Hügel 69, D-53121 Bonn, Deutschland  
Wohnungsadresse: Am Schwanenmorgen 3, D-53121 Bonn, Deutschland  
Telefon: +49 (228) 525-365  
Mobiltelefon: +49 177 1730061  
E-mail: jan.wagner@iki.fi; jwagner@mpifr.de  
Geburtsdatum und -ort: 26.01.1980, Helsinki, Finnland

## Ausbildung

- 2014 Ph.D., Universität Köln, Deutschland: “*RFI Mitigation for VLBI and Arrays Water Megamasers in Active Galaxies*”, VLBI und Astrophysik
- 2009 **Bachelor of Science (B.Sc.), Universität Helsinki, Finnland**, “*Robot Navigation*”  
Erlangt am 15.5.2009, 187 ECTS, Note 4 von max. 5, Informatik, Nebenfach Mathematik
- 2007 **Master of Science (M.Sc. tech.), Helsinki University of Technology, Finnland**: “*Development of Real-Time Very Long Baseline Interferometry Systems at the Metsähovi Radio Observatory*”  
Erlangt am 17.12.2007, 200 ECTS, Note 4 von max. 5, Electronics Engineering and Space Technology, Nebenfächer Computational Engineering, Radio Technology
- 1998 **Abitur, Deutsche Schule Helsinki, Finnland**

---

## Arbeitserfahrung

- 2010 – 2014    **Max-Planck-Institut für Radioastronomie**, Bonn Deutschland  
Diverse Arbeit unter der VLBI-Gruppe, der International Max Planck Research School (IMPRS) for Astronomy and Astrophysics, und EU FP7 ALBiUS: RFI-Mitigation für VLBI und Arrays, Entwicklung am VLBI-Softwarekorrelator, APEX VLBI -Projekt, FILA10G-Projekt, Megamaser Cosmology Projekt, Doktorand
- 2006 – 2010    **Metsähovi Radio Observatory**, Kylmälä, Finnland  
Diverse Arbeit und Projekte, einige werden hier aufgeführt:  
Mit Space Systems Finland Ltd, 2009 – 2010: ESO E-ELT Technical Design Study der Echtzeit-Datenverarbeitung für Adaptive Optik, dazu Infrastruktur für die Datenverarbeitung; V. Bos (SSF), V. Bauvir (ESO) und J. Ritakari.  
Mit dem Finnish Geodetic Institute, 2009 – 2010: technische Arbeit für geodätisches VLBI und Entwicklungsprojekt für Satellite Laser Ranging; Dr. M. Poutanen, Dr. K. Arsov (FGI). Unter JIVE PRIDE-TM, 2008 – 2009: Entwicklung der Datenverarbeitung für Satellite Tracking, Beobachtungen; Dr. S. Pogrebenko  
Unter EU FP6 EXPRoS, 2006 – 2008: Entwicklung der VLBI-Datenerfassung u.a. Elektronik, Software, Protokolle für e-VLBI Datentransfer, gleichzeitig auch Arbeit am M.Sc. unter M.Sc. J. Ritakari und Prof. M. Hallikainen.
- 2003            **Helsinki Institute of Physics**, CERN-Sommerpraktikum, 2003/06–2003/08.
- 1998 – 2006    Studium, gleichzeitig verschiedene Arbeitsprojekte bei **Eaton Powerware**, **Elisa/IBM**, an der **Universität Helsinki**, **Helsinki University of Technology**, und an der **Deutschen Schule Helsinki**.